2D Nanocarbons: Functional Aspects and Device Fabrication

A Thesis

Submitted for the Degree of

Doctor of Philosophy
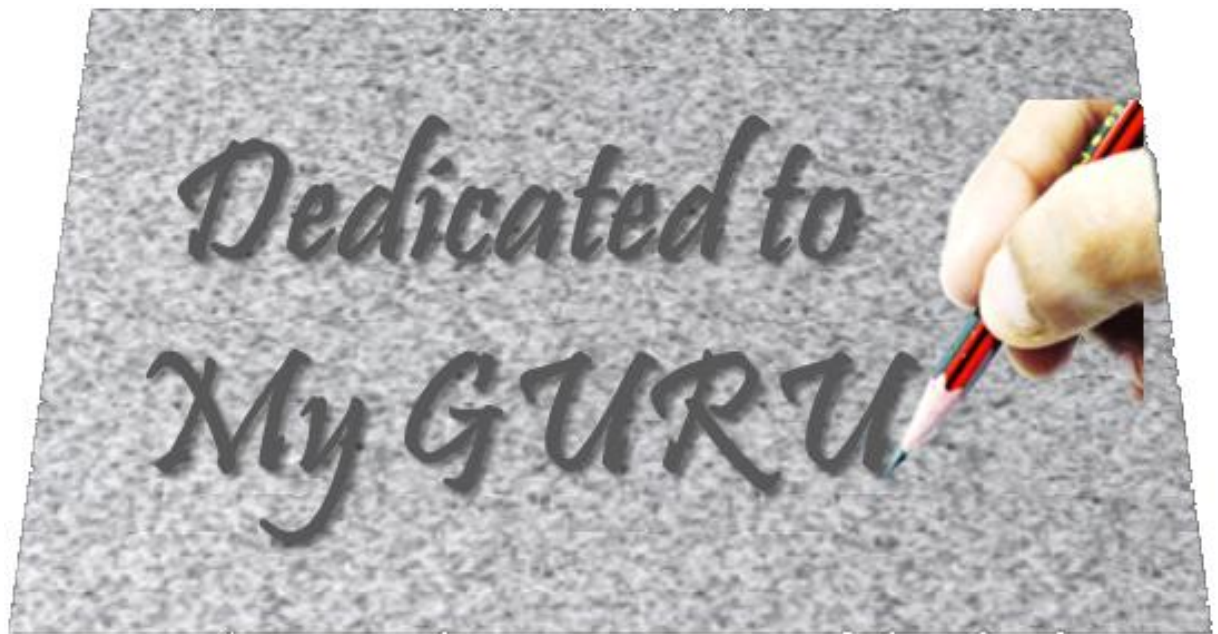
By

NARENDRA KURRA

Chemistry and Physics of Materials Unit

Jawaharlal Nehru Centre for Advanced Scientific Research

(A Deemed University)

Bangalore - 560064 (INDIA)

APRIL 2013

Dedicated to
My GURU

DECLARATION

I hereby declare that the thesis entitled "**2D Nanocarbons: Functional Aspects & Device Fabrication**" is an authentic record of research work carried out by me at the Chemistry and Physics of Materials Unit, Jawaharlal Nehru Centre for Advanced Scientific Research, Bangalore, India under the supervision of Professor **G. U. Kulkarni** and that it has not been submitted elsewhere for the award of any degree or diploma.

In keeping with the general practice in reporting scientific observations, due acknowledgment has been made whenever the work described is based on the findings of other investigators. Any omission that might have occurred due to oversight or error in judgment is regretted.

Narendra Kurra

CERTIFICATE

Certified that the work described in this thesis titled "**2D Nanocarbons: Functional Aspects & Device Fabrication**" has been carried out by **Narendra Kurra** at the Chemistry and Physics of Materials Unit, Jawaharlal Nehru Centre for Advanced Scientific Research, Bangalore, India under my supervision and that it has not been submitted elsewhere for the award of any degree or diploma.

Professor G. U. Kulkarni

(Research Supervisor)

ACKNOWLEDGEMENTS

Firstly, I would like to thank my research supervisor *Professor G. U. Kulkarni* for his constant guidance throughout this research journey. I am very grateful to him for suggesting such an interesting project and encouraging me towards new explorations. His simple way of thinking a research problem and further his participation in doing the experiments with me, made me understand crucial and critical things about the research. I never forget those days when Sir used to do experiments with me in the late nights and also imparted me a lot of experimental skills in designing scientific problems besides the style of writing a manuscript. He always inspires me by giving examples of famous personalities like Swami Vivekananda. He has also taken care of me in my personal life and supported me during tough situations. Many thanks to you sir, for giving me an opportunity and freedom to play with various instruments in the Nanolab. All-in-All, he is my **GURU** and I am going to dedicate my thesis to my Sir, **Prof. G. U. Kulkarni.**

Prof. C. N. R. Rao, a constant source of inspiration and it is always a great opportunity to listen to encouraging words about research by the legend. I learned more about him through my research supervisor, who himself is a great disciple of Prof. Rao. My mentor used to take his example, saying how different as an individual he is to be so great and used to motivate us in doing a better science. I also received immense support from Professor M. R. S. Rao, President, JNCASR, which I gratefully acknowledge.

It is a pleasure to thank all my collaborators; Prof. Ronald G. Reifenberger, Prof. Timothy Fisher Dr. Adina Scott and Dr. Gyan Prakash - Purdue University, Prof. N. Chandrabhas & Mr. Srinu Bhadram - CPMU for fruitful collaboration.

I thank all the faculty members of CPMU, TSU and NCU for their cordiality, especially my teachers, Prof. G. U. Kulkarni, Prof. Umesh Waghmare, Prof. A. Sundaresan, Prof. M. Eswaramoorthy, Prof. K. S. Narayan, Prof. S. Balasubramanian, Prof. S. M. Shivaprasad, Prof. T. K. Maji, Prof. S. K. Pati and Prof. S. Ranganathan (IISc) for their courses. I thank Dr. S. Vidhyadhiraja and Prof. Rama Govindarajan for useful discussions.

Timely and ready assistance and also friendly attitude from technical staff, Mr. Srinath and Mr. Srinivas is acknowledged. I am very thankful to Dr. S. Basavaraja (AFM), Mrs. Usha (TEM), Mrs. Selvi (FESEM) and Mrs. Suma (Confocal microscopy), Mr. Anil (XRD), Mr. Mahesh (SEM), Mr. Kishore (XPS), Dr. Karthik (TEM), Mr. Vasu (UV, IR, PL, TGA) and Mr. A. Srinivasa Rao for their invaluable technical assistance. Ms. Vanitha, Mr. Sunil, Mr. Moorthy, Mr. Gowda, Mr. Dilip and Mr. Peer are acknowledged for their assistance.

I am grateful to my past and present labmates, Mallik, Ritu, Ganga, Umesh, Kiruthika,

Preface

The thesis work pertains to functional aspects of 2D nanocarbons and their use in fabrication of devices. It is organized into five parts.

Part I introduces the concept of nanoscale materials, their important properties including nanocarbons. The thesis work deals with 2D nanocarbons in the form of graphene, nanocrystalline graphene, turbostratic graphene and amorphous carbon platforms and exploitation of these novel properties in realizing devices.

Part II pertains to Electron beam induced carbonaceous deposition (EBICD) as a source to obtain functional amorphous carbon platforms. The chemical and electrical properties of EBICD have been studied systematically in detail. EBICD has been employed as a local dielectric in carbon nanotube circuits. EBICD could be transformed into a conducting form via thermal treatment. EBICD layers were employed as carbon feedstock for the selective growth of nanocrystalline graphene which was employed as an active material in fabricating field effect transistors and infrared detectors.

Part III deals with Atomic force microscope bias lithography on carbon surfaces. The nucleation of the attoliter water droplets and their evaporation has been studied using EBICD as a platform under a positive tip bias in tapping mode. Further, by changing the conditions, the surface of the EBICD could be modified electrochemically. Reversible charge patterns could be written on the EBICD surfaces. On the graphite surface, using a negatively biased AFM tip, mesoscopic graphitic islands have been fabricated and the charge storing properties have been investigated.

Part IV presents the electronic and optoelectronic properties of graphene and turbostratic graphite. Graphene ribbons have been obtained through laser ablative patterning and studied for their electrical properties. Few layer graphene films have been grown from residual hydrocarbons and solid polymer sources in presence of Ni catalyst layer by thermal treatment. The infrared photoresponse behavior of these films has been investigated. On the other hand, bulk graphitic films exhibit bolometric response towards the infrared radiation due to heating effects. Pencil-traces on paper produce turbostratic graphite which has rotationally disordered graphene layers leading to the electronic decoupling among the layers. Passive devices such as resistor-capacitor filters could be made by employing pencil-trace as resistor and ion gel as dielectric. Electric field effect has been derived from pencil-traces with the aid of high specific capacitance of the ion gel.

Part V presents the fabrication of electrode materials for supercapacitors. Pd hexadecylthiolate was used a precursor which upon mild thermolysis in focused sun light, produced a highly conducting Pd nanoparticle/carbon composite. Due to autocatalytic nature of the nc-Pd/C, dipping the substrate in neutral permanganate solution, produced deposits of nanoscale MnO_2. Many supercapacitors have been made out of these electrodes, which showed energy densities ~ 80 Wh/kg and power densities ~ 30 kW/kg.

Table of Contents

PART V: Solar baked electrodes for the fabrication of high performance supercapacitors

ACRONYMS

0D	Zero dimensional	dia	Diameter
1D	One dimensional	DNA	Deoxy-ribonucleic acid
2D	Two dimensional	DOF	Depth of focus
3D	Three dimensional	DOS	Density of states
AC	Alternating current	DPN	Dip-pen nanolithography
AFM	Atomic force microscopy	EBL	Electron beam lithography
AFMEN	AFM-assisted electrostatic nanolithography	EBICD	Electron beam induced carbonaceous deposition
AFMNL	AFM nanolithography	ED	Electron diffraction
A-z curve	Amplitude-distance curve	JV	Current density-Voltage
		LAO	Local anodic oxidation
BMIMOSU	Butylmethylimidazolium octylsulfate	LCD	Liquid crystal display
		LED	Light emitting diode
CA	Contact angle	LER	Line edge roughness
C-AFM	Conducting atomic force microscopy	LIL	Laser interface lithography (Holographic lithography)
CD	Compact disc		
CNTs	Carbon nanotubes	LMCT	Ligand-to-metal charge-transfer
CV	Cyclic voltammetry		
DDA	Discrete dipole approximation	LTPS	Low temperature deposited polysilicon
DC	Direct current	MEF	Metal-enhanced fluorescence
DI	Deionised		
MEMS	Microelectromechanical systems	MFM	Magnetic force microscopy
MESFET	Metal semiconductor field effect transistor	MGIs	Mesoscopic graphitic islands

MLCT	Metal-to-ligand charge-transfer	PDMS	Polydimethylsiloxane
MNGP	Metal nanowire grating pattern	PEDOT:PSS	Poly(3,4-ethylenedioxythiophene): poly(styrenesulfonate)
MOF	Metal-organic frameworks	PET	Polyethylene terephthalate
MOSFET	Metal–oxide–semiconductor field-effect transistor	PL	Photoluminescence
		PMMA	Poly(methyl methacrlylate)
MP	Melting point	ppm	Parts per million
MRI	Magnetic resonance imaging	PVDF	Poly vinylidene fluoride
µ-stripes	Microstripes	PSI	Phase shifting interferometry
M-Thiolates	Metal Thiolates	PVA	Poly vinyl alcohol
MWNT	Multi walled carbon nanotube	PVD	Physical vapor deposition
NA	Numerical aperture	QD	Quantum dot
NAND		RC	Resistor-capacitor
Not AND		REM	Replica molding
NEM	Nanoentrapment molding	RF	Radio frequency
NEMS	Nanoelectromechanical systems	RIE	Reactive ion etching
		RR	Rectification ratio
NIL	Nanoimprint lithography	RT	Room temperature
NIR	Near field infrared spectroscopy	SAED	Selected area electron diffraction
NSOM	Near field scanning optical microscopy	SAMs	Self-assembled monolayers
NW	Nanowire	SAXS	Small angle X-ray scattering
OP	Optical profiler		
OOP	Out of plane (in Raman)	SD	Secure digital
PC	Polycarbonate		

SEF	Surface enhanced fluorescence		TERS	Tip enhanced Raman scattering
SEM	Scanning electron microscopy		TFT	Thin film transistor
SERS	Surface enhanced Raman scattering		TGA	Thermogravimetric analysis
SFIL	Step-and-flash imprint lithography		TCR	Temperature coefficient of resistance
SP	Surface Plasmon		UV	Ultraviolet
SPL	Scanning probe lithography		UV-vis	Ultraviolet-visible
SPR	Surface plasmon resonance		UHV	Ultra-high vacuum
STM	Scanning tunneling microscopy		VLS	Vapor-liquid-solid
STEM	Scanning transmission electron microscopy		VSI	Vertical scanning interferometry
STS	Scanning tunneling spectroscopy		VSM	Vibrating sample magnetometer
SWNT	Single walled carbon nanotube		XAFS	X-ray absorption fine structure
TEM	Transmission electron microscopy		XPS	X-ray photoelectron spectroscopy
			XRD	X-ray diffraction

PART I
Introduction

I.1 Nanoscale

The etymological basis of prefix "Nano" can be traced back to Greek "nan(n)os" or Latin "nanus", meaning "Dwarf". According to the dictionary definitions, "Nano" refers to "one-billionth" which means to designate "extreme smallness". Thus, the word "Nano" indicates something of the order of 10^{-9} (one billionth), for example, the diameter of a single walled carbon nanotube is of the order of 10^{-9} m, which is 1 nanometer. The strand width of the human hair is about 100 μm, equals to ~100,000 nanometers. Comparison of various natural and man-made nano and micron sized systems is shown in Figure I.1. Nanoscience is about studying the properties of nanoscale objects, whose physical dimensions (at least in one dimension) are in the range of 1-100 nm [1, 2].
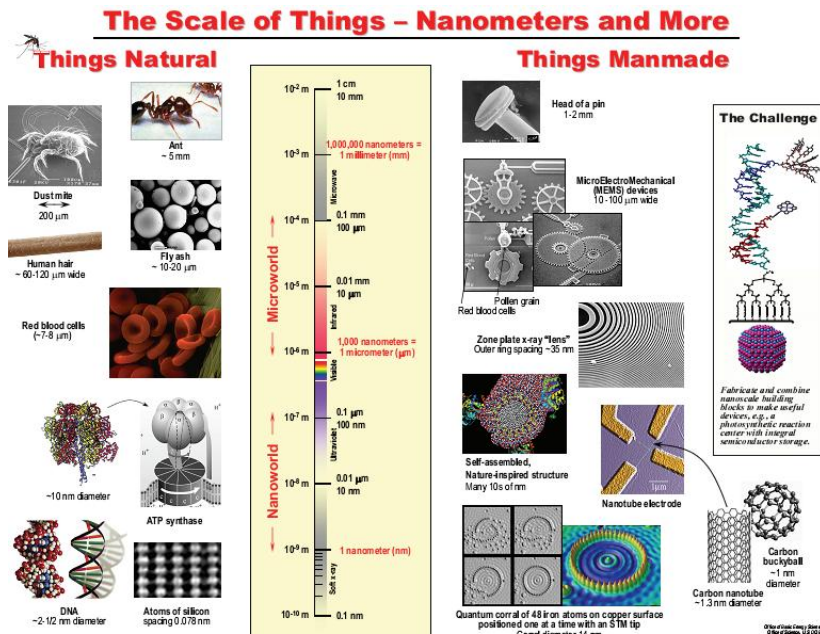
Figure I.1 Comparison of the objects at micro and nanoscale which are either manmade or natural [reproduced from ref. 3].

Nanoscience is about the exploration of the extraordinary properties, functionality and phenomena of the objects at the nanoscale. The applied stream of nanoscience is nanotechnology which deals with the manipulation, control and integration of nano-objects for designing the nanoscale architectures [1, 2]. Nanoscale bridges the atomic and

macroscopic worlds. The first record of atomistic theory (atom was considered as an indestructible particle of matter) was proposed by the Indian sage "Kanada", almost 2600 years ago. Nanoscience has a rich historical background from ancient Roman times (4th century A. D.), when the roman glass makers have fabricated colored glasses which essentially consist of colloidal particles of gold and silver dust. The magnificent cup, Lycurgus cup, kept in British museum, exhibits beautiful colors such as red and green for the transmitted and reflected light illumination (see Figure I.2a). This apparent dichroism is due to interaction of light with the embedded nanometals in the glass matrix of the cup [4]. Thus, the Lycurgus cup was actually a nanocomposite material, has been fabricated without the knowledge of nanoscience.

Figure I.2 (a) The apparent dichroism of Lycurgus cup towards the direction of light illumination and (b) gold sol prepared by Michale Faraday. Inset, bulk gold is in yellow color [reproduced from ref. 4, 5].

During the middle ages (5-15th centuries), it was customary to stain glass windows by incorporating metallic constituents (nanoparticles). The field of colloidal science was introduced by Thomas Graham during 19th century and Richard Zsigmondy had even estimated particle sizes of sols using an ultramicroscope [1, 2].

Michael Faraday, a great scientist of his time and treated as the father of modern nanoscience, has prepared the gold sol in the laboratory in 1857. Based on his observations, he stated that "the divided state of the metal" was responsible for the various colors of the gold sol such as ruby, green and violet or blue unlike the yellow color of the bulk gold (see Figure 1.2b) [5]. Thus, history is abundant with the examples making use of

intriguing properties of nanophenomenon in various fields such as fabrication of colored glasses, photography and catalysis, etc. For example, nanoscopic gold has been used in catalysis for the oxidation of carbon monoxide to carbon dioxide unlike the bulk gold which is noble and inert [6].

The modern spirit of nanotechnology was catalyzed through the visionary talk by the famous physicist Richard Feynmann in his lecture "There's plenty of room at the bottom" (American physical society, 29th December 1959) [7]. In his pioneering speech, he has emphasized on the creation, manipulation and controlling the things on a small scale. He justified his statement using an illustration about biosystems with many functional elements at nanodimensions [8]. "*The biological example of writing information on a small scale has inspired me…a biological system can be exceedingly small. Many of the cells are very tiny, but they are very active; they manufacture various substances; they walk around; they wiggle; and they do all kinds of marvelous things-all on a very small scale. Also they store information…in DNA molecules in which approximately 50 atoms are used for one bit of information. Consider the possibility that we too can make a thing very small that does what we want that we can manufacture an object that maneuvers at that level!*" He has also suggested miniaturization by introducing the concept of nanotechnology in which the fabrication of nano-objects may be possible via top-down and bottom-up approaches. His vision was to write the entire 24 volumes of Encyclopedia Britannica on the head of a pin and ultimately in terms of small bits to record 24 million books in a space width of 1/200 of an inch. The subsequent silicon revolution and microfabrication technology, made a path towards the growth of nanotechnology field. Invention of scanning probe techniques (1980s), capable of imaging with atomic resolution besides the precise manipulation of nanostructures, allowed researchers to understand nanoprocesses. The discovery of nanocarbons such as fullerenes and carbon nanotubes (around 1990s) was considered to be the starting point of the "*Nano age*" which further fast-tracked the quest to make other materials in similar dimensions besides exploring their technological aspects. In a nutshell, chemical and physical pathways for the synthesis of nanomaterials, the application of quantum mechanics for explaining the phenomenon at the nano and atomic world, detailed understanding of biological functions and developing powerful instrumentation resulted in the explosion of the nanoscience field as we see today [1, 2].

Eric Drexler has elaborated some of these ideas in his technical book *Nanosystems* [9].

I.2 Nanomaterials and classification

The physical dimensions of an object can be defined along X, Y and Z axes. The first criterion for a material to be called as a nanomaterial is that, at least one of its characteristic dimensions should be in the nanometric (1-100 nm) range [1, 2]. Besides having nanometric dimensions, the properties of a nanomaterial should be different when compared to its bulk counterpart. The characteristic dimension is the one which decides the properties of the nanomaterial. This is because when the characteristic dimensions of an object become comparable to the mean free path of the electrons in it, the electrons begin to feel confined (bound system) and therefore, the properties of the solid undergo a dramatic change critically depending on the number of atoms and electrons, in contrast to the average properties arising from the large scale periodic arrangement of atoms in the bulk state. On macroscopic length scales, the properties of the materials (physical, electronic and other properties) can be successfully explained based on classical laws. On the other extremes, i.e., at the atomic and molecular length scales, the classical laws begin to fail, quantum mechanics takes over in order to explain the properties and the phenomena. Nanoscale is the regime which is the bridge between the macroscopic and atomic scales where the properties become size dependent, primarily due to large surface area to volume ratio and quantum confinement. According to Siegel, nanomaterials can be classified into 0D, 1D and 2D materials based on their characteristic dimensions (see Figure I.3)[10, 11].
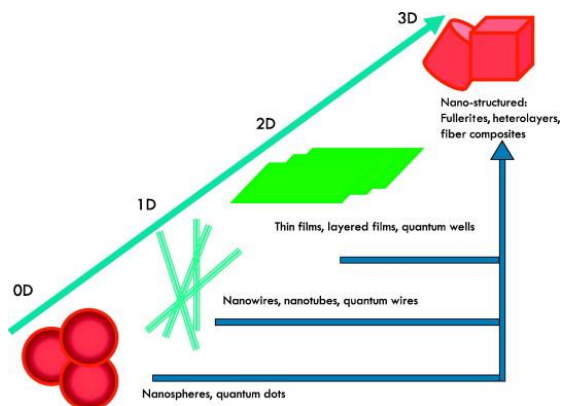
Figure I.3 Classification of the nanomaterials into 0D, 1D, 2D and 3D materials [reproduced from ref. 10].

A zero dimensional (0D) material is confined in all three dimensions (width, length

and thickness) with the characteristic dimensions of three, examples include fullerenes, quantum dots and nanoparticles. For a one dimensional (1D) nanomaterial, confinement is in only two dimensions (width and diameter) with macroscopic third dimension (length). Carbon nanotubes, nanowires and nanorods are considered as 1D nanomaterials. If the confinement is in only one dimension (thickness), the material is treated as 2D material where the length and width are of macroscopic dimensions. Thin films of different materials, graphene, silcene, inorganic chalcogenides such as MoS_2, WS_2, etc. are the typical examples for the 2D nanomaterials. If there is no confiment in any one of the dimensions, the material is treated as a 3D material. However, a 3D material with nanometric pores and structures, is called as nanostructured material. For example, zeolites, porous carbons and molecular sieves are of 3D in nature but they have nanoscopic structures and pores. Nano Porous materials are in high demand due to their potential applications in various fields of research which include purification, catalysis, gas storage and energy storage devices [12]. Thus, it is not the scale effect but the properties at the nanoscale that are intriguing and important.

I.3 Why are the properties of nanomaterials different compared to bulk?

As the size of the material goes down to nanometric dimensions, the surface area to volume increases which leads to enhanced reactivity besides the quantum confinement which introduces the discretization of energy levels. Thus, the properties of the nanomaterials are size dependent.

I.3.1 Surface area to volume ratio

The high surface area of a nanomaterial can be illustrated by taking the example of a cube with an edge length of 1 m whose surface area is given by 6 m^2 (see Figure I.4). When the cube is fragmented into the smaller cubes of 8 and 27 with the same volume, the surface area increases by twice and thrice, respectively (see inset of Figure I.4). Further, the surface area increases by orders of magnitude after chipping down the bulk material into nanometric dimensions, eventually ending up with high surface area to volume ratio as compared to the surface area available with a non-porous bulk cube. The fraction of atoms on the surface of a particle (P_s, percentage) can be estimated using the simple relation,

$$P_s = 4N^{-1/3} \; x100 \ldots\ldots(I.1)$$

where N is the total number of atoms in the particle. The variation of the surface fraction of

atoms with the number of atoms of a particle is shown in Figure I.4. The fraction of surface atoms becomes less than 1% only when the total number of atoms is in the order of 10^7, which for a typical metal would correspond to a particle diameter of 150 nm. Thus, at the nanoscale, the enhanced reactivity due to enormous surface area, finds applications in heterogenous catalysis [14].
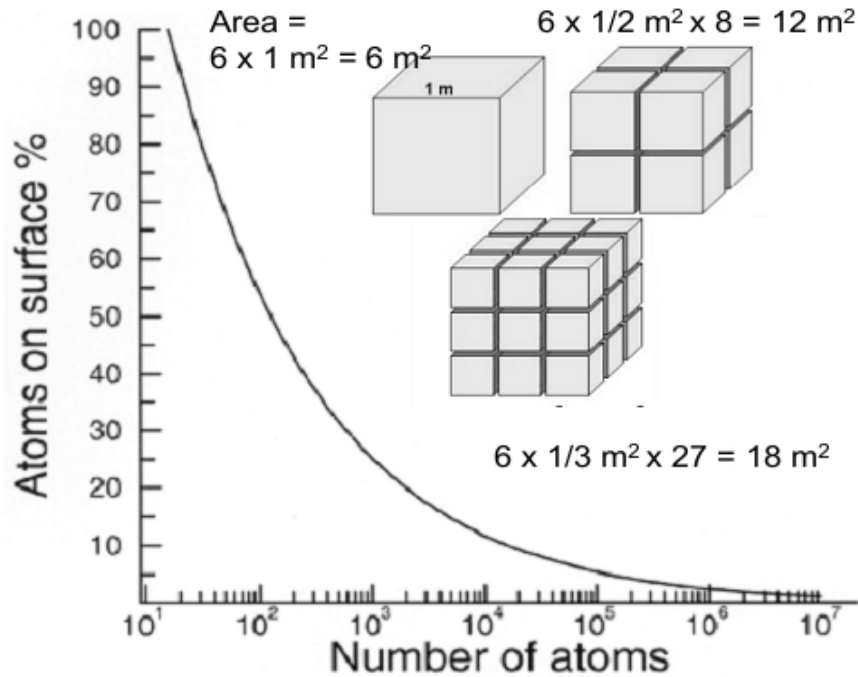
Figure I.4 Plot showing the dependence of the percentage of the surface atoms with respect to the number of atoms in a particle. The calculation of the percentage of atoms is made on the basis of the above equation in the case of metal particles [reproduced from ref. 13].

I.3.2 Quantum confinement

Bulk materials have extended band structures and as the size decreases, the spacing between the levels increases which can be described qualitatively using particle in a box model. The spacing between the energy levels is inversely proportional to the dimensions of the material (see below equation).

$$\Delta E_n = (2n+1)h^2/8mL^2 \ldots\ldots\ldots(I.2)$$

Where h is Planck's constant, m is the electron mass, L is the dimension of the material and n is the quantum number. For example, for a 1 mm conductor, the spacing is given by 4.5×10^{-12} eV while for 5 nm conductor, this corresponds to 0.179 eV. Thus, the energy quantisation couldn't be noticed in the case of macroscopic conductors as the thermal energy of the electrons is in the order of 25 meV at room temperature [15].
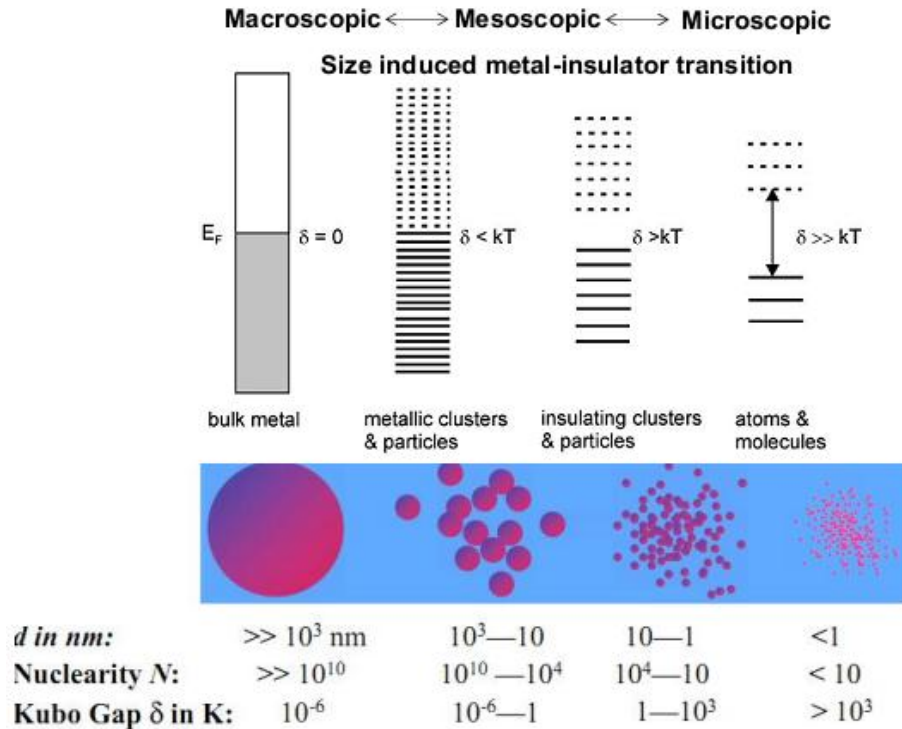
Figure I.5 Evolution of the band structure and the density of states with increasing number of atoms (from right to left) [reproduced from ref. 16].

In the case of atoms and molecules, the energy levels are quantized due to minimized interactions among them (hydrogen atoms and molecules), which is evident from spectroscopic studies. When the interactions are set in, the band structure starts evolving which leads to the extended band structures (as in metals or semiconductors). The contribution of electronic states by the atoms in a solid, increases the width of the bands leading to the extended band structures in a solid. As the number of contributing atoms increases, the density of states (DoS) within a band increases proportionally. This evolution of band structure with size is shown in Figure I.5. The typical width of a band would be around a few eV. The average spacing between consecutive energy levels is specified by the Kubo gap (δ), usually measured in terms of meV. The magnitude of δ varies inversely with nuclearity (the number of atoms). As the Kubo gap increases, there is a decrease in the DOS at the Fermi level. When the gap is less than thermal energy (k_BT), there would not be any discreteness in the energy. Kubo gap is given by the following equation

$$\delta = 4E_F/3n_e \ldots\ldots\ldots(I.3)$$

where, E_F is the Fermi level and n_e is the number of valence electrons.

Electron transport at nanoscale depends on the relationship between the sample dimensions (L) and three important characteristic length scales [1].

(i) Electron mean free path (L_{fp}), defined as the average distance an electron travels before it collides inelastically with impurities or phonons.

Electron transport is said to be diffusive if $L > L_{fp}$ and ballistic if $L << L_{fp}$.

(ii) The phase coherence length (L_{ph}), which is the distance after which the phase memory of electrons or electron coherence is lost due to dynamic scattering events.

For high mobility semiconducting heterostructures, L_{fp} and $L_{ph} \sim 10$ μm.

(iii) The electron Fermi wavelength (λ_F), defined as the wavelength of the electrons that governs the electrical transport.

The conductance (G) is said to be quantized ($G \sim e^2/h$) if $L \sim \lambda_F$

Quantum corrals are the closed structures of single atoms, fabricated by Eigler et al., who have observed the confinement of surface electronic wavefunctions by creating artificial atomic structures. They have arranged Fe atoms on a Cu(111) surface in the form of a quantum stadium as shown in Figure I.6. The standing wave pattern of the electrons was observed, due to interference effect of the confined electronic wavefunctions. This was the first experimental mapping of quantum confinement and thanks to the invention of scanning probe microscopes to probe out the electronic wavefunctions of the atoms.
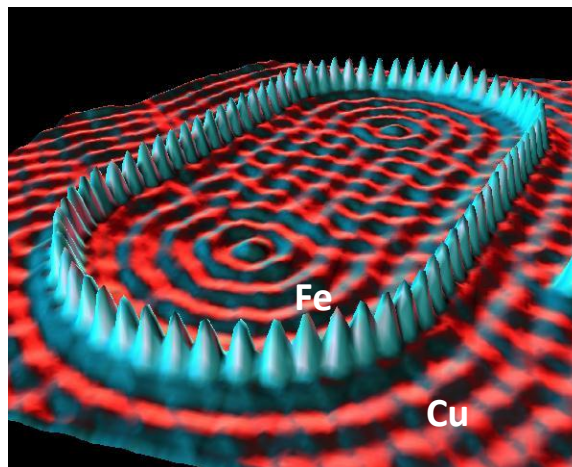
Figure I.6 Experimental evidence for the confined electronic wavefunctions in a quantum corral [reproduced from ref. 17].

I.3.3 Density of states (DoS) of Nanomaterials

Density of states (DoS) of a system describes the number of states per interval of energy at each energy level that are available to be occupied by electrons [18]. A high DoS at a specific energy level means that there are many states available for occupation. A DoS of zero means that no states can be occupied at that energy level. In general, DoS is an average value over the space and time domains occupied by the system. The DoS of a solid with electrons confined to one, two and three dimensions, named as 2D, 1D and 0D nanomaterials respectively, in comparison with the 3D material is shown in Figure I.7.
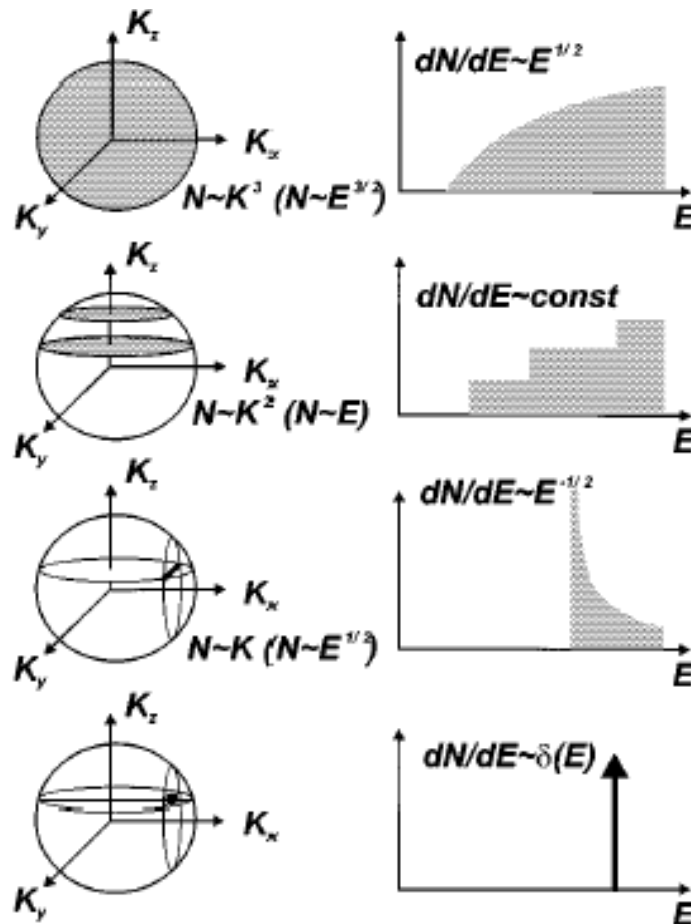
Figure I.7 DoS of the charge carriers in 3D, 2D, 1D and 0D materials [reproduced from ref. 19].

$$DoS = \frac{dN}{dE} = \frac{dN}{dk}\frac{dk}{dE} \quad \dots\dots\dots\dots(I.4)$$

$$N(k) = \frac{k\,space\,vol}{vol\,per\,state}$$

$$= \frac{4/3\pi k^3}{(2\pi)^3/V} \quad \dots\dots\dots\dots(I.5)$$

N(k) depends on the dimensionality of the system and the relation between the DoS and the energy for 0D, 1D, 2D in comparison with the 3D is given in the below table.

Table I.1-DoS of for materials of different dimensionalities

Structure	Degree of Confinement	$\dfrac{dN}{dE}$
Bulk Material	0D	$\sqrt{E}$
Quantum Well	1D	1
Quantum Wire	2D	$1/\sqrt{E}$
Quantum Dot	3D	$\delta(E)$

I.4 Size-dependent properties

I.4.1 Thermal properties – Melting point
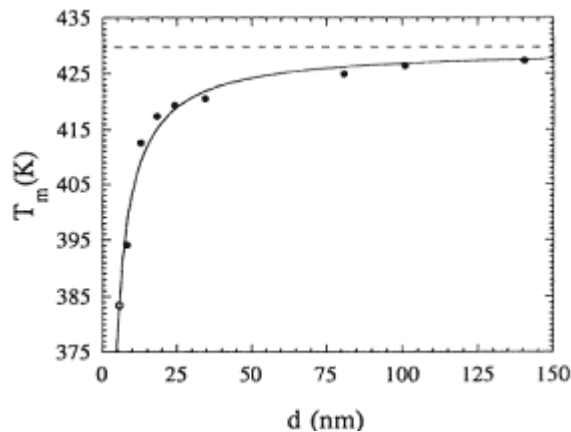
Figure I.8 Lowering of melting temperature with decreasing particle diameter. The melting point of the bulk material is represented with the broken line [reproduced from ref. 21].

The surface of a material has unsaturated bonds compared to the bulk due to lesser number of neighbouring atoms. Unlike the atoms in the bulk, the atoms on the surface have lesser cohesive energies due to low mean coordination number (number of nearest neighbours). As the size of the material is reduced to nanodimensions, the fraction of surface atoms increases (lower stabilisation energy) which have lesser cohesion energies, leading to the lowering of melting point compared to the bulk material (Figure I.8). In the year, 1871, W. Thomson [20] proposed the relation between the melting point and the radius of a particle according to the equation given below, which is known as Gibbs–

Thomson equation.

$$\frac{T_m - T^*{}_m}{T^*{}_m} = \frac{\Delta T_m}{T^*{}_m} = \frac{2V_m(l)\gamma_{sl}}{\Delta H_m r}$$ ....(I.6)

where T_m is the melting point of the cluster with radius r, T_m^* that of the bulk, $V_m(l)$ is the molar volume of the liquid, γ_{sl}, the interfacial tension between the solid and the liquid surface layer, and ΔH_m is the bulk latent heat of melting.

I.4.2 Optical properties

The optical properties of the nanomaterials, especially the fascinating colors of metal nanoparticles have been realised by the Roman glass makers for the fabrication of colored glasses (stained glass windows) [22]. The optical properties of the "nanomaterials" usually differ from that of their bulk counterparts which is something to do with absorption, scattering and emission phenomenon, become dominant at the nanoscale. In the case of bulk metals, due to metallic luster, the light falling on the surface gets reflected which is not the case for the metal nanoparticles where the absorption of light is observed due to a phenomenon called localized surface plasmon resonance. According to the Lorentz-Drude model, the free electrons in metal are treated as a sea of negatively charged entities surrounding the core of positively charged nuclei, called as "plasma electrons" [23]. The electric field component of the electromagnetic radiation, displaces the free electrons which will get restored to their original positions by the coulombic electrostatic attraction from the nuclei. This causes the oscillation of the plasma electrons which get modulated according to the electric field of the electromagnetic radiation, and the electron cloud coherently oscillates over the surface with a resonance frequency 'ω_p'. when the frequency of this oscillation matches with that of the incident radiation, the resonance condition is achieved, resulting in the intense absorption, termed as "surface plasmon resonance (SPR)" absorption (Figure I.9).

The frequency of oscillation of metal nanoparticles depends on the parameters such as number density of electrons, effective mass of the electron, the size and shape distribution of the charge. Thus, the optical properties of noble metal nanoparticles can easily be tuned by varying the size, shape and dielectric environment. Typically, the surface plasmon absorption band for spherical Au nanoparticles having diameter of ~ 20

nm is observed at around ~ 520 nm [24]. On increasing the diameter of the Au nanoparticle from 20 to 80 nm, SPR band shifts from 520 to 550 nm which is attributed to the electromagnetic hindrance and varying dielectric function with size. Theoretically, the dependence of the maximum of plasmon resonance band on the nanoparticle diameter, was estimated by adopting Mie theory and discrete dipole approximation method [25].
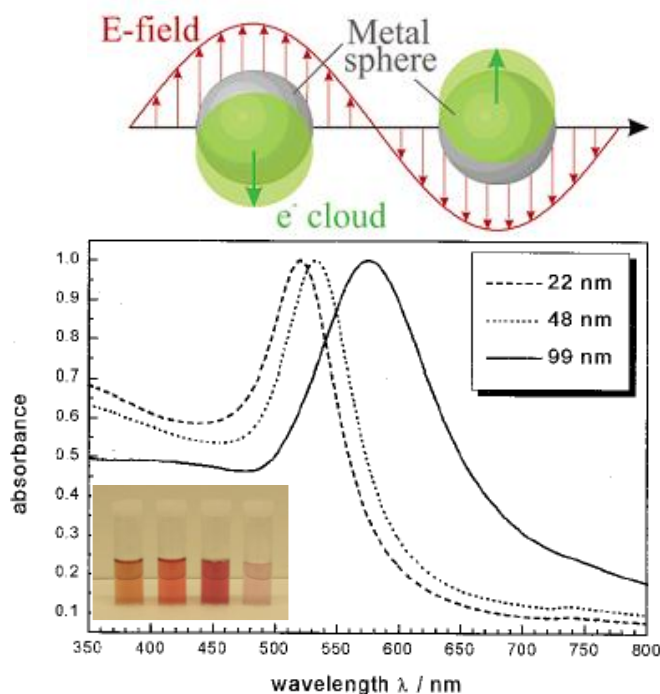
Figure I.9 Schematic showing the oscillation of the conduction electrons in presence of electromagnetic radiation. The SPR absorption spectra correspond to the different sizes of the AuNPs. Inset shows the different colors of the AuNPs of varied sizes [reproduced from ref. 23].

When the shape of the nanoparticle changes, the surface electron density changes accordingly which can be manifested in the absorption properties [25]. For example, in the case of Au and Ag nanorods, two surface plasmon bands were observed due to splitting of the dipolar resonance into oscillations along the transverse and longitudinal axes [26]. The longitudinal surface plasmon band shifts to longer wavelengths with increase in the aspect ratio, while the position of transverse surface plasmon band remains more or less unaffected. In the case of nanoplates and prisms, the surface plasmon modes will be different and the observed resonance peaks can be attributed to the in plane and out-of-plane dipolar as well as quadrapolar resonances.

In a semiconductor nanoparticle, due to quantum confinement of both electrons and

holes in all three dimensions, the effective band gap increases compared to that of bulk semicondutor. As the size of the quantum dots gets smaller, both the optical absorption and emission peaks shift towards lower wavelengths (higher energies). The emission maximum depends up on the band gap which can be controlled through the size of the quantum dots [27]. This has been illustrated using the well-known example of CdSe quantum dots showing different colors corresponding to the varied size of the quantum dots (Figure I.10). The traditional Indian Rangoli was filled with different colors corresponding to the emission colors of different sized CdSe quantum dots.
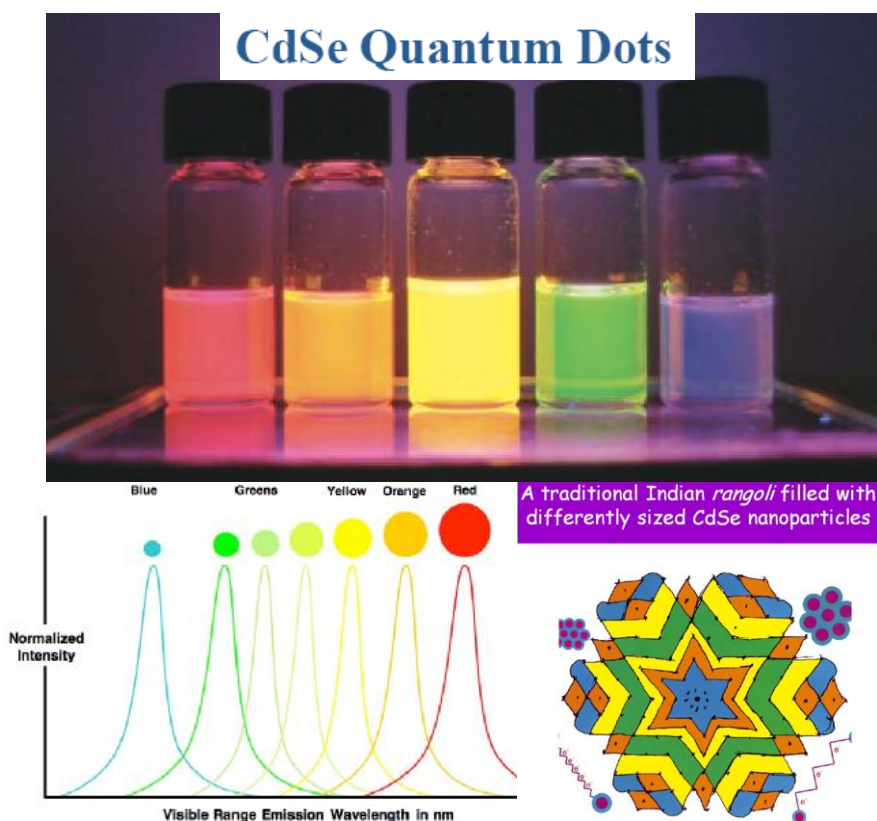
Figure I.10 Top: Photograph showing the beautiful colors emitted by CdSe QDs of different sizes. Emission spectra as a function of size. Indian Rangoli filled with the colors emitted by CdSe QDs of varied sizes [reproduced from ref. 16, 27].

Besides the fundamental interesting optical properties of nanostructures, the localized optical properties have been utilized for developing single molecule spectroscopy. For instance, when an electromagnetic wave is interacting with the nanoparticle or the plasmonic nanostructure, the local electric fields (E) get enhanced by E^4, leading to the enhanced Raman scattering of molecules in their vicinity, which is

known as Surface Enhanced Raman Scattering (SERS) [28]. The measured enhancement factors were of the order of 10^4 to 10^{15}, and even single molecules have been detected using this technique [29]. The colossal enhancement in SERS can be attributed to two mechanisms namely electromagnetic and chemical enhancements [30]. The electromagnetic enhancement is a physical phenomenon which arises due to the localized SP resonance modes, increases the E-field by orders of magnitude locally, giving rise to the enhancement in the Raman signals. The chemical enhancement results from the interactions between the molecule and the nanoparticle due to charge transfer interactions. The typical signal enhancement factors of 10^5-10^8 were observed, which can be explained based on electromagnetic mechanism while the chemical enhancement factors were typically of the order of 10-10^3 [31].

I.4.3 Electronic properties

When the size of a material decreases to nano and atomic dimensions, the energy levels become quantized unlike the continuum states in a bulk material. The natural consequence of the reduction in the size is the observation of size induced metal-insulator transition [32]. Generally, quantum confinement manifests when the size becomes comparable to de Broglie wavelength of conduction electrons in the case of metals whereas the size should be comparable to exciton Bohr radius in the case of semiconductors [33].
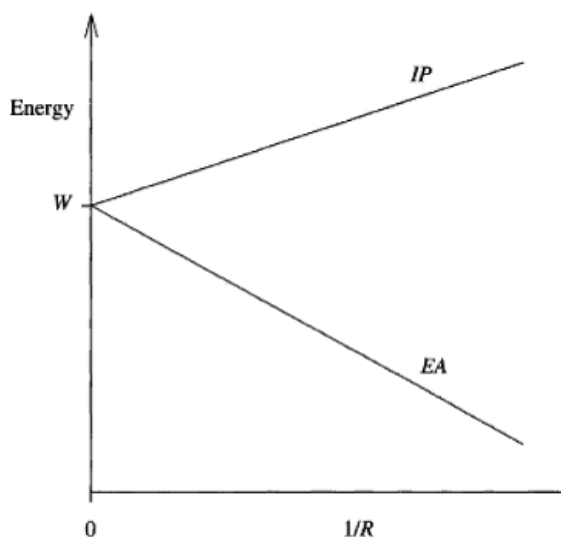
Figure I.11 Variation in the ionisation potential (IP) and electron affinity (EA) of a cluster with respsect to its radius predicted by Liquid drop model [reproduced from ref. 34].

The energy required to move an electron from the Fermi level to the vacuum level, is called the workfunction of the metal. When the size becomes small, the energy required to remove or add an electron is termed as ionization potential (IP) and electron affinity (EA), as in the case of molecules. The variation of the IP and EA with respect to the cluster size was predicted based on Liquid drop model (see Figure I.11). The difference between these two energies is called charging energy (U), which depends on the diameter and chemical identity of the material.

The charging energy (U) can be related to the capacitance (C) by the following equation

$$C= U/2e………(I.7)$$

where e is the electronic charge.
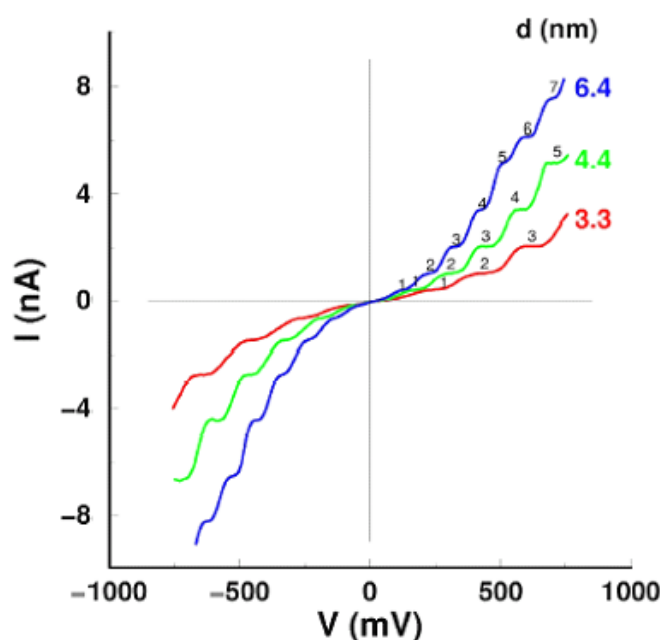
Figure I.12 I-V spectra of Pd nanocrystals of different sizes exhibiting Coulomb staircase phenomena [reproduced from ref. 36].

Typically, for a metal cluster covered with organic ligands, capacitance would be of the order of atto Farads ($\sim 10^{-18}$ F). When electrons are allowed to tunnel through a potential barrier into the cluster, the capacitance changes sufficiently to block the entry of the next electron till an observable change in the potential of the charging field is applied. This phenomenon has been observed in the current-voltage characteristics in the form of

Coulomb gap and Coulomb staircase (see Figure I.12, U ~ 100 meV). Due to self capacitance effects, nanocrystals can be employed in fabricating single electron devices such as supersensitive electrometers and memory devices. As a proof of concept, single-electron transistors have been fabricated out of one or few nanocrystals at the gap between electrodes [35].

1.4.4 Magnetic properties

As the surface energy increases with decreasing particle size, below a critical size, magnetic transitions are often observed due to switching of polarization directions of domains spontaneously. For instance, at nanoscale, the material tends to exhibit paramagnetic behavior despite its ferromagnetic nature in its bulk form [37]. The paramagnetic behavior of the nanoparticle would be different when compared with the conventional paramagnetism and hence it was referred as superparamagnetism. The coercivity field (i.e., the intensity of the applied magnetic field required to reduce the magnetization of that material to zero after the magnetization of the sample has been driven to saturation) of a nanoparticle strongly depends on its size. Thus, if the particle is large; it supports multidomain structure, magnetization reversal occurs through the domain wall motion and thus the coercivity is low. In a single-domain particle the change of direction of magnetization can occur only by coherent rotation of spins, which results in a higher coercivity compared to that of multi-domain particles (Figure I.13).
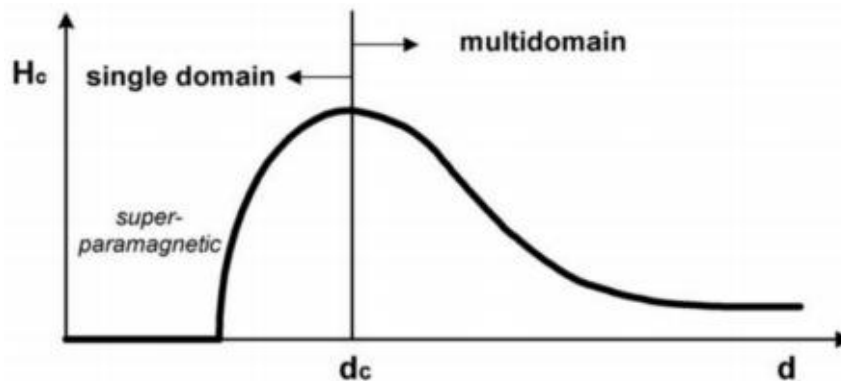
Figure I.13 Particle coercivity Hc versus size, d. The largest coercivity is observed at the particle size d_c corresponding to the transition from multidomain to single domain structure (reproduced from ref. 39).

When the size of the particle is reduced further, the coercivity falls off due to progressively increasing thermal fluctuations and thus leads to superparamagnetism. Thus,

superparamagnetic nanoparticles rapidly respond to an applied magnetic field but exhibit negligible residual magnetism and coercivity. These features make superparamagnetic nanoparticles very attractive for a wide range of applications [38]. Self-assembly of large complex nanoparticle structures provides an attractive strategy to controllably increase magnetization while retaining superparamagnetic characteristics.

I.5 Synthesis of Nanomaterials

The synthesis of nanomaterials can be categorized into three general ways such as top-down, bottom-up and hybrid methods (see Figure I.14).

I.5.1 Top-down approach
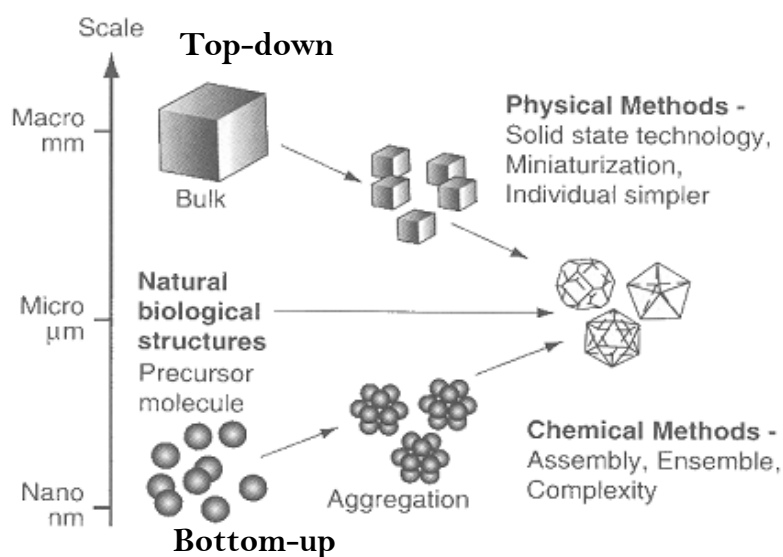
Figure I.14 Schematic representation of the top-down and bottom-up processes for the synthesis of nanomaterials [reproduced ref. 41].

Top-down approach is a physical technique which involves chipping down the bulk material into nano species, mostly followed by physicists. Top-down methods employ physical energy in the form of mechanical, thermal and high energy sources for synthesizing the nanomaterials. Mechanical methods include cutting, milling and machining; high energy sources includes electric arcs, lasers, solar flux, electron beams and plasmas; thermal includes pyrolysis, sintering techniques; in order to prepare nanomaterials via top-down approach. Lithography is also a top-down approach which uses photons, electron/ion beams and sharp probes for sculpting the nanostructures from the bulk materials. Natural processes such as erosion, etching (etching of silicate rocks by

carbonic acid from environment), volcanic activity, forest fires, digestion of food and biological decomposition, come under the category of top-down method [40].

I.5.2 Bottom-up approach

Bottom-up methods are mostly chemical methods followed by chemists and biochemists which involve the assembly of atoms and molecules leading to the formation of nanospecies. Nature highly follows the bottom up methods. Self assembly is the prominent approach for the assembly of nanomaterials to derive useful functionality. Bottom-up methods involve reactions in various phases such as gas, liquid and solid besides the biological route.

The formation of the clusters and thin films of specific materials by chemical vapor deposition (CVD), atomic layer deposition (ALD), molecular beam epitaxy (MBE), metal-organic chemical vapor deposition (MOCVD), etc come under the category of bottom-up approach. For example, synthesis of CNTs and graphene from hydrocarbon sources by CVD method is a bottom-up approach where the carbon radicals stitch together leading to formation of 1D nanotubes and 2D sheets. Synthesis of nanomaterials by liquid phase methods are guided by the intermolecular interactions which are also called secondary interactions. Secondary interactions include hydrogen bonding, π-π interactions, hydrophobic interactions, van der Waals forces, etc. Self assembly is a spontaneous process which is the basis for the supramolecular chemistry in which the morphology of the molecular assemblies can be tailored through controlling the secondary interactions. Formation of colloids, electrolytic and electroless deposition on the autocatalytic surfaces also come under the category of bottom-up methods. Natural processes such as photosynthesis in which plants synthesize carbohydrates using CO_2 and H_2O in chlorophylls is a bottom-up approach [40].

Hybrid methods involve both top-down and bottom-up approaches for the formation of a nanomaterial. Though, sometimes the synthesis method appears to be top-down but the microscopic mechanism suggests that the process is a bottom-up synthesis method. For example, while synthesizing CNTs by laser ablation, initially the carbon plasma gets created which is a top-down process while assembly of this plasma leading to the formation of CNTs is a bottom-up process.

I.6 Nanocarbons

I.6.1 Carbon

Carbon (Latin, "*Carbo*" means coal) is the most fascinating, versatile and unique element in the periodic table. It belongs to group 14 in the periodic table with atomic number of 6 and exhibits tetravalency. Carbon has catenation property, due to which it can form bonds with itself or with other elements leading to the generation of millions of organic compounds. Carbon combines with the other lighter elements such as H, O and N to form the functional biological molecules such as amino acids, carbonhydrates and nucleic acids etc. Molecules as such do not have life but they can organize in a complex manner which constitute the life. Thus, carbon is the basic building block for all forms of life on the Earth [42].

I.6.2 Bonding

In the atomic ground state, carbon has 6 electrons with electronic configuration of $1s^2\, 2s^2\, 2p^2$. Because the 2p orbitals ($2p_x$, $2p_y$, $2p_z$) are 4 eV higher in energy compared to the 2s orbital, it is energetically favourable to excite one electron from the 2s orbital to the 2p orbital, leading to the formation of four bonds. The hybridization of carbon include sp^1, sp^2, sp^3 which lead to linear, trigonal and tetrahedral bonding [43].

Graphite (sp^2 bonding) and diamond (sp^3 bonding) are the two well-known old crystalline allotropes of carbon with a huge contrast in the physical properties [44]. Graphite is a conductor with semimetallic nature while diamond is an insulator with a band gap of 5 eV. Graphite is soft, acts as a lubricant while diamond is hard, being used as abrasive. Besides the crystalline carbon allotropes, amorphous carbon with both sp^2 and sp^3 bondings together, makes a rich family of carbon based materials. Thus, it is possible to have various forms of carbon starting from the conducting graphite to semiconducting amorphous carbon to the insulating diamond like carbon. Thus, the electronic properties of the carbon can be controlled through the bonding which can be tailored based on the synthesis conditions. Graphite is the thermodynamically stable form of carbon while diamond is considered to be metastable [44]. The activation energy barrier for diamond to get converted into graphite is 0.02 eV per atom which is very high; it takes billions of years for the phase transformation to happen under standard temperature and pressure conditions [44].

Due to its flexible bonding capabilities, various young avatars of carbon have been discovered in the form of 0D fullerenes (1985), 1D carbon nanotubes (1991) and 2D graphene (2004) each generating increasing excitement among researchers. Several other exotic allotropes have also been discovered, such as lonsdaleite, glassy carbon, carbon nanofoam and linear acetylenic carbon (carbyne). Thus, carbon can have numerous incarnations based on the bonding and morphology with diverse physical properties [45, 46].

I.6.3 Graphite

Graphite (Greek "*graphein*" means to draw or write), is naturally found on earth in the form of minerals in metamorphic rocks such as marble, schist, and gneiss. Graphite is a layered material with planar structure and the carbon atoms in each layer are arranged in a honeycomb lattice with covalent bonding (C-C bond distance of 0.142 nm). These layers are stacked together via weak van der Waals forces (the distance between planes is 0.335 nm) along the c-axis. The two known forms of graphite, hexagonal (ABABAB..stacking) and rhombohedral (ABCABCABC..stacking) have very similar physical properties. Graphite is an anisotropic material and hence the properties such as electronic, thermal and mechanical would be different from inplane to that of out of plane. Graphite is being used in many applications starting from employing in making simple pencils as a writing implement, as a lubricant to a coolant in the nuclear reactors [47].

I.6.4 Fullerenes

Fullerenes were discovered in the year 1985 by Smalley, Kroto and Curl, through mass spectrometry analysis of the plume generated from laser ablation of a graphite source. A higher abundance in the mass spectrum was found corresponding to 60 carbon atoms forming a closed structure, resembling a foot ball with 12 pentagons and 20 hexagons. Another fairly common fullerene is C_{70}, but fullerenes with 72, 76, 84 and even up to 100 carbon atoms are commonly obtained [48].

I.6.5 Carbon Nanotubes

Carbon nanotubes are cylindrical graphitic tubules, 1D nanomaterials. Single walled carbon nanotubes, typical diameter of 1 nm, can be semiconducting or metallic depending on the diameter and helicity [49]. Rolling up of the two, three or few layers of graphite result in forming double, triple and few walled carbon nanotubes. Multiwalled

carbon nanotubes contain multi layers of graphite which exhibit metallic nature. owing to their extraordinary thermal conductivity, mechanical and electrical properties; carbon nanotubes have been employed in variety of applications [49].

I.6.6 Graphene

Graphene is considered as the mother of all graphitic forms (see Figure I.15). All graphitic forms can be obtained from graphene, for example, it can be wrapped into a OD material, rolled into a cylindrical form (1D material), stacked together to form 3D graphite. Initially, it was thought that the 2D materials are unstable due to Peierls instability which can not be isolated. But in 2004, Geim and Novoselov from Manchester have isolated graphene using a scotch tape technique successfully [50-52]. They won the Nobel prize in physics in 2010 for their ground breaking experiments on this wonder 2D material.
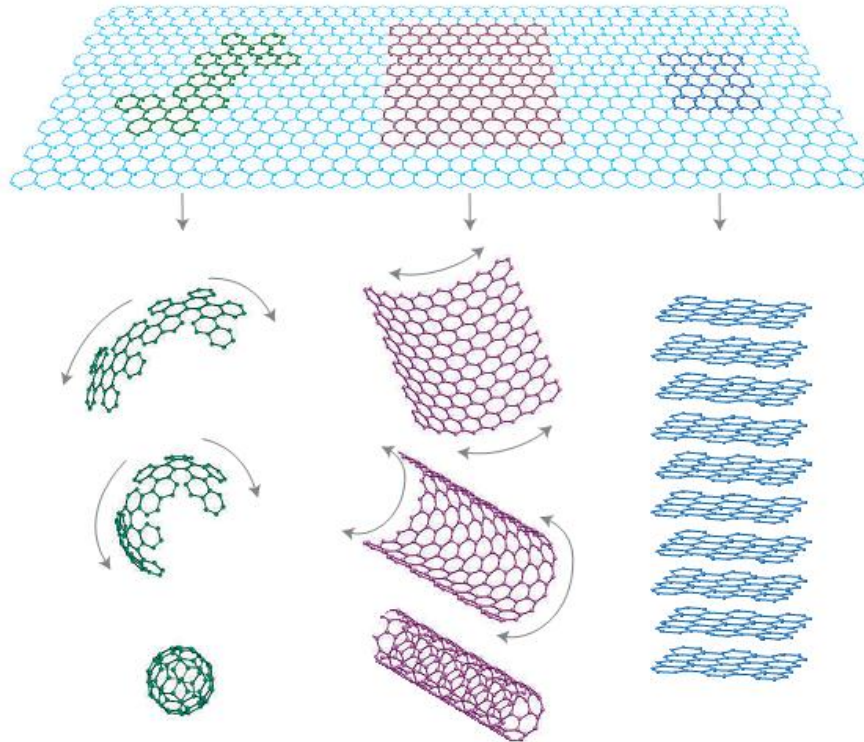
Figure I.15 Mother of all graphitic forms. Graphene is a 2D building material for carbon materials of all other dimensionalities. It can be wrapped up into 0D buckyballs, rolled into 1D nanotubes or stacked into 3D graphite [reproduced from ref. 50].

Graphene is a semi-metal with zero band gap and it was in 1947, Wallace had found that the E–k relation is linear for low energies near the six corners of the two-dimensional hexagonal Brillouin zone, leading to zero effective mass for electrons

and holes in graphene (see Figure I.16). Due to this linear dispersion relation at low energies, electrons and holes near these six points, two of which are inequivalent, behave like relativistic particles which have been described by the Dirac equation for Fermions. Hence, the electrons and holes are called Dirac Fermions which obey Dirac equation with a Fermi velocity $v_F \sim 10^6$ m/s, and the six corners of the Brillouin zone are called the Dirac points [53]. Graphene exhibits ambipolar electric field effect and absorbs only 2.3% of the incident visible light. Graphene, also exhibits the quantum Hall effect. Graphene is mechanically stiff and chemically inert. Thus, due to its intriguing electronic and optoelectronic properties, graphene has become a hot topic of research during the last decade.
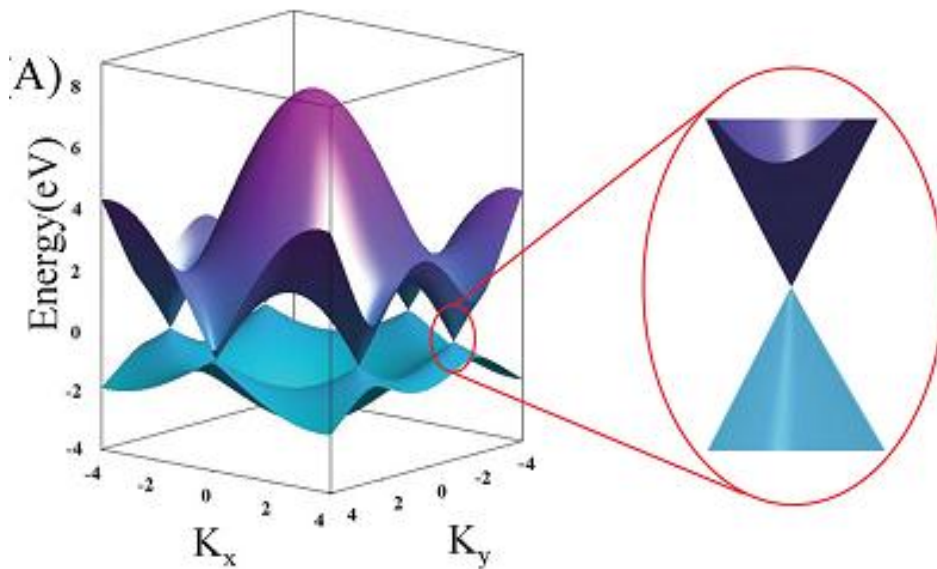
Figure I.16 The band structure of graphene in the honeycomb lattice. The enlarged picture shows the conical band structure close to one of the Dirac points [reproduced from ref. 53].

I.6.7 Turbostratic Graphite

Most graphite samples are obtained after annealing hydrocarbon sources at high temperatures (above 3000 K) and pressures. Highly oriented pyrolytic graphite (HOPG) is a synthetic graphite, obtained through annealing of hydrocarbons at high temperatures while applying the stress. The manner in which the graphene layers get stacked, the graphite material can be classified broadly into two categories. Bernally stacked graphite (ABABAB stacking) has the registry of the carbon atoms in the top and bottom graphene layers. Turbostratic graphite looks very similar to graphite except that the adjacent planes

are out of registry with one another. This results in an increase in the interlayer spacing, which can increase from 0.335 nm to more than 0.345 nm. The random stacking of graphene layers resulted from exfoliation, could possess the turbostratic nature. The rotational disorder and random stacking among graphene layers could lead to the electronic decoupling among the graphene layers (see Figure I.17). Thus, the turbostratic graphite is treated as 2D graphite [54]. The rotational disorder can be measured through the mosaicity which is a measure of the angle of mis-orientation of top graphene layers with respect to the bottom layers. Lower the mosaicity, lesser is the rotational disorder along the c-axis. Raman spectroscopy is also a good tool for finding the stacking of the graphitic layers along the c-axis. The shape of the 2D band indicates the stacking order of the graphite layers along the c-axis. For turbostratic graphite, 2D band is seen as single peak where as for Bernally stacked graphite, it is seen as a peak with a shoulder at lower wave number.

(A) **Turbostratic**   (B) **Bernal graphite**

$d_{002} \geq 3.440 \text{ Å}$ $d_{002} = 3.354 \text{ Å}$
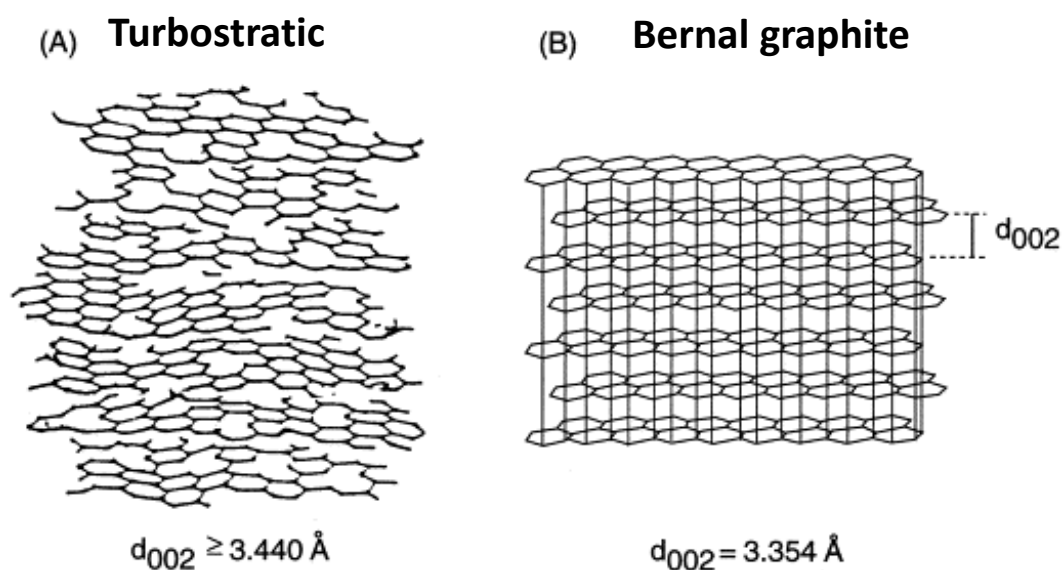
Figure I.17 A schematic representation of a hexagonal turbostratic graphite as compared to a three-dimensional Bernal-stacked graphite lattice [reproduced from 54].

I.6.8 Nanocrystalline graphene

Besides graphene, its derivatives have also become popular in the recent years due to their interesting properties. For example, graphene is a zero band gap semiconductor and the band gap can be introduced through lateral confinement of charge carriers by carving graphene nanoribbons (GNRs) [55]. Graphene in the form of quantum dots fluoresce and the color can be tuned depending on the size [56]. Nanocrystalline graphene contain the

domains of graphene with the sizes of the order of 10-100 nm with the interconnectivity among the domains. They find applciations in the fields of electronics and photovoltaics [57].

I.6.9 Raman spectroscopy-Nanocarbons

Raman spectroscopy has been extensively used as a tool for studying vibrational, rotational and other low frequency modes of molecular systems. Raman scattering is due to inelastic scattering of photons by phonons resulting in change of polarization. Since polarisability is a function of interatomic distance, Raman spectra become very sensitive to the changes in the local bond lengths, bond angles to provide unique information unlike other spectroscopy techniques. It is very easy, fast and non-destructive way of probing vibrational and structural aspects of molecules to materials under ambient conditions [58].
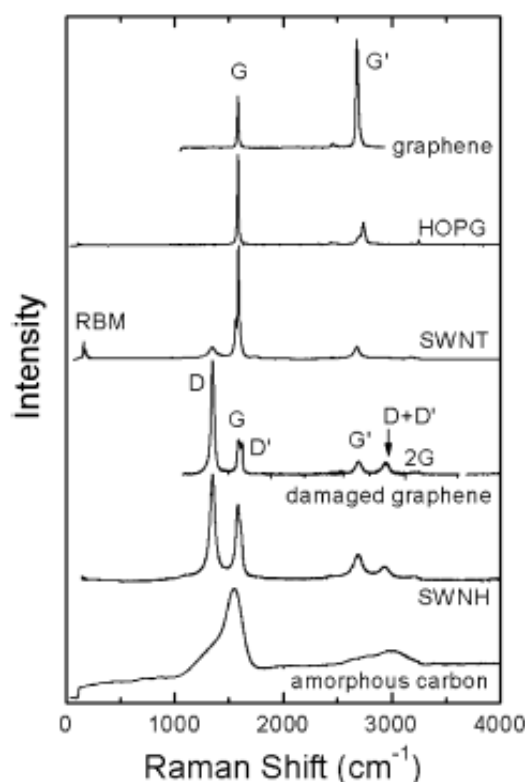
Figure I.18 Raman spectra from different types of sp^2 nanocarbons [60].

Raman has become an important structural and electronic characterization tool for various carbon materials as it is sensitive to the local changes in bonding and molecular morphology (see Figure I.18). In the case of graphitic materials, it can provide information about sp^2 crystallite size, the presence of sp^2-sp^3 hybridization, doping effects, edge

structure, strain, number of graphene layers, nanotube diameter, chirality, curvature, and finally the metallic vs semiconducting behavior. As the π-electrons of the sp^2 carbon can easily be polarized by visible photons which make the Raman technique sensitive to sp^2 sites. It is a very sensitive and versatile tool for knowing about defects, stacking and finite sizes of crystallites parallel or perpendicular to the hexagonal axis of graphitic materials. Raman spectroscopy is one of the most sensitive and informative technique to characterize disorder in the sp^2 carbon lattice. In graphene related materials, the Raman spectrum predominantly consists of three peaks which are named as D, G and 2D bands [59, 60]

D band: It is also called defective band, which arises due to breathing motion of six atom rings and requires a defect for its activation (see Figure I.19). Any phonon mode satisfying k=q/2 (where k is the wave vector for the electronic transition excited by incident photon and q is the phonon wave vector) condition gives rise to the D peak with A_{1g} symmetry; involve phonons near the k zone boundary. This mode is forbidden in perfect graphite and only becomes active in the presence of disorder. Typically, the D band position is found to be at 1350 cm^{-1} and it changes with excitation energy. The dispersion of D band is proportional to the order in the sp^2 carbon lattice. The intensity and integrated area of D band reveals the presence of disorders such as defects, grain boundaries, and functional groups in the sp^2 carbon lattice. Lower the D band; higher is the electronic quality of the graphitic lattice.

D band (A_{1g})   G band (E_{2g})
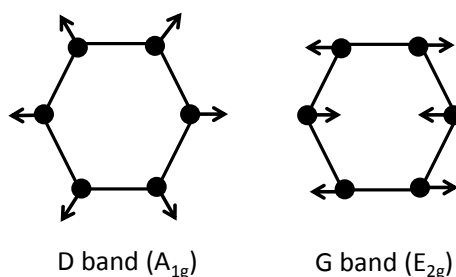
Figure I.19 schematic representation of D and G bands.

G band: It is also called graphitic band, arises due to in-plane bond stretching motion of pairs of sp^2 carbon atoms (see Figure I.19). G band doesn't require the presence of six fold rings unlike D band and it occurs at all sp^2 sites. The position of G band is at 1580 cm^{-1}, related to the zone center phonons with E_{2g} symmetry. G band doesn't disperse in graphitic

samples and disperses in more disordered carbon, where dispersion is proportional to the degree of disorder. The position and FWHM of the G band changes with increasing number of defects in the graphitic systems.

2D band: It is the overtone of the D band, reveals the stacking order and periodicity along the c-axis. Though the D band is absent in some locations of a graphite sample, the 2D band is always seen. The position of 2D band is at 2700 cm^{-1}, arises due to non-center zone boundary phonons and its origin can be explained by double resonance Raman phenomenon [60]. The position and shape of the 2D band gives information about the number of layers and type of stacking. For a single layer, the 2D band is single, sharp Lorenzian peak with FWHM 20-30 cm^{-1}. For few and multi layers; FWHM and number of peaks of 2D band increases. For turbostratic graphite where the electronic coupling along the c-axis is not good, we observe a single 2D band even for a multi-layer graphene with FWHM of 80-100 cm^{-1} (e.g. graphene grown by CVD on metal surfaces). Typically, in the case of turbostratic stacking, the FWHM of 2D band is atleast 20-30 cm^{-1} higher as compared to the Bernal type of stacking for a given number of layers. The 2D band for single layer graphene and turbostratic graphite look similar, the latter is considered as 2D graphite. As the disorder in the sp^2 lattice increases (the probability of inelastic scattering of photons increases), one phonon assisted D band processes will increase compared to the two phonon assisted 2D band processes. This competition between Raman allowed and defect induced peaks, leads to the decreasing intensity of the 2D band at the cost of increasing D band intensity. The 2D band becomes absent for the highly disordered graphene systems and only disorder free graphene layers will contribute to the intense G and 2D bands [61].

I_D/I_G ratio: The ratio of the intensity of D and G bands (I_D/I_G) is proportional to the abundance of six-fold aromatic rings, or in other words, the sp^2 carbon cluster area in amorphous deposit. This ratio gives us the in-plane crystallite size (L_a) of the sp^2 carbon lattice which is given by

$$L_a(nm) = 560/E^4_{laser}(I_D/I_G)^{-1}\ldots\ldots(I.8)\ [59]$$

Where E_{laser} is the laser excitation energy in eV

Typical I_D/I_G ratio for high quality graphene samples is in the order of 0-0.05,

defected graphene samples 0.5-2.

I_G/I_{2D} **ratio:** This ratio provides us the number of graphene layers.

For a single layer, ratio is in the range of 0.2-0.4, FWHM of 2D band, 25-35 cm^{-1} and 2D band position is at 2690 cm^{-1}. For few and multi-layer samples, the ratio is in the range of 0.5-4, with increase in the FWHM to 50 cm^{-1} and beyond, the position of 2D band will be upshifted to 2700 cm^{-1} as compared to the single layer [62].

I.7 Micro and Nanolithography

Lithography (in latin, *litho = stone, graphein = writing*) is a surface patterning technique, which comes under the category of top-down approach. Lithography was first introduced in 1798 by Alois Senefelder as a printing tool for transferring geometric shapes on a mask to the surface of a desired substrate. The patterning can be achieved using photons, electrons, ions or even sharp probes. Various lithography techniques have emerged based on the source employed, which are discussed below. Nanolithography is useful in patterning periodic arrays, gratings and also fabricating nanodevices. Basically, the lithography techniques are broadly classified into serial and parallel techniques [63].

I.7.1 Photolithography

This technique utilizes the exposure of the UV light on a photoresist through a photomask containing desired pattern. Depending on the exposure conditions, polymer chains of photoresist may get either broken into smaller oligomers or get crosslinked in the exposed regions. After dipping in a developer solution, if the material from the exposed regions get washed away, it is called a positive tone resist. In the case of negative tone resist, the exposed regions will get crosslinked and remain intact while the unexposed regions get washed away during the developing stage. Thus, the patterns on the photoresist can be used as a protective layer in subsequent etching or deposition processes to create desired patterns on the substrate [64].

Photolithography can be performed in three different ways, namely contact printing, proximity printing and projection printing (see Figure I.20). The placement of the photomask either in contact or in proximity to the photoresist followed by exposure of the UV light to record the patterns on the surface of the photoresist. In contrast, a projection printing system (so-called 'stepper') utilizes an optical lens system to project a deep-UV pattern from an excimer laser (wavelength of 193 or 248 nm) on the photoresist enabling

pattern size reduction by 2-10 times. It is capable of fabricating high-resolution patterns as small as few tens of nanometers (~50 nm) at a high throughput (~50 wafers/hr). However, it requires a sophisticated optical lens system and precise control systems of temperature and position resulting in a very expensive setup. Thus, it has been employed in manufacturing of advanced ICs and CPU chips. In recent years, immersion lithography, resolution enhancement technology and extreme-UV lithography have been developed to improve the lithography resolution of projection printing.
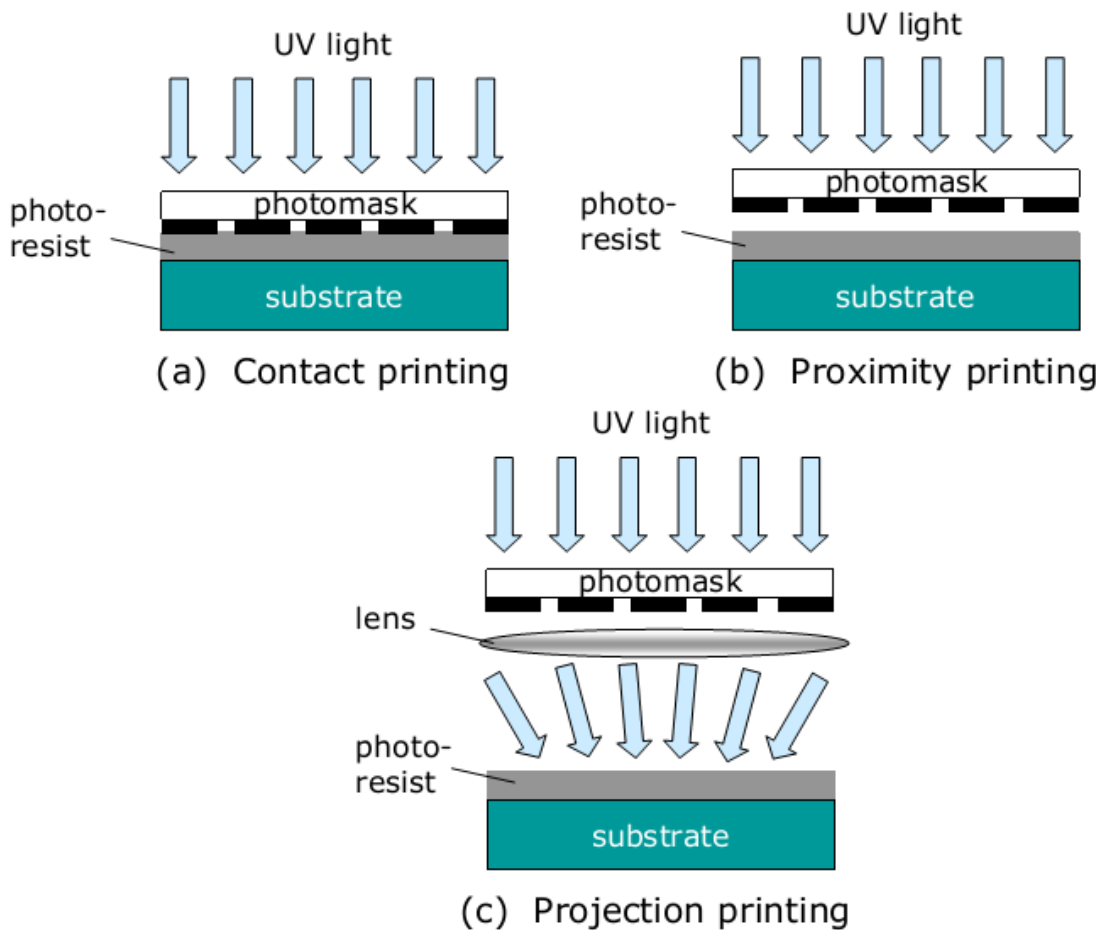
Figure I.20 Schematic illustration of three forms of photolithography: (a) contact printing (b) proximity printing and (c) projection printing [reproduced from ref. 65].

I.7.2 Electron beam lithography

Electron beam lithography (EBL) utilizes an electron beam instead of photons to achieve high resolution patterns due to small wavelength and a small probe size. It is a serial technique, capable of creating finer features for the fabrication of high density packaging. The process steps involved in EBL are similar to that of photolithography.

Poly(methyl methacrlylate) (PMMA) has been the most widely used and high resolution positive tone resist and hydrogen silsesquioxane (HSQ), a relatively new resist material, is a high resolution negative tone resist. One of the most important parameters of the EBL process is the resolution of a resist [66]. It is defined as the smallest line width which can be consistently patterned. Lower the molecular weight of the polymeric resist, higher is the resolution. The resolution is ultimately decided by the relation between the probe diameter and the interaction volume of the polymer. For any given polymer, the interaction volume is always greater than the probe diameter because of proximity effects, causing the higher widths for the defined features in comparison to the probe diameter (see Figure I.21). Due to proximity effects, the resist will get re-exposed by the secondary and back scattered electrons. The resolution is also limited by another factor which is swelling of the polymer in the developing solvent, leading to the higher feature size than expected [67, 68]. To suppress the proximity effect, higher electron beam energy can be used. Primary beam scattering occurs when electrons in the beam elastically collide with atomic nuclei in the material and their trajectory is subsequently altered, commonly described as two sub processes, namely, forward scattering and backscattering.
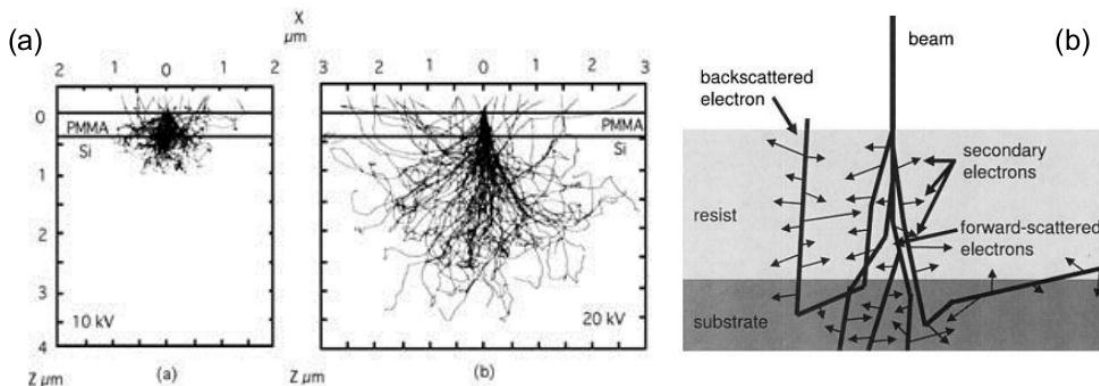
Figure I.21 Monte Carlo simulation of electron scattering in resist on a silicon substrate at (a) 10 kV and (b) 20 kV (reproduced from ref. 67]). (b) Schematic illustration of the various processes that influence the point-spread function. An electron beam traveling through a resist film can interact with particles both elastically (producing forward scattering and beam broadening) and inelastically (producing secondary elections) [reproduced from ref. 68].

Thus, the photolithography and electron beam lithography involve multiple steps such as baking, exposure, developing and lift-off for the creation of final patterns. Hence, direct write lithography techniques have been employed for fabrication of the surfaces in a single step.

I.7.3 Direct write lithography techniques

I.7.3a Electron beam induced deposition (EBID)

Focused electron beam induced deposition (EBID) is a direct write lithography technique that allows the fabrication of patterns on a substrate induced by electron beams (e-beams). EBID of metal deposition has been employed as a glue or nanosolder for interconnecting the nanoscale features. Precursors used in EBID process include contamination (carbon species from the residual gas in the electron optical system), metal-organic precursors (for instance, $W(CO)_6$ or trimethyl-platinum-cyclopentadienyl (Me_3PtCp)), or inorganic precursors (for instance, WF_6 or XeF_2).
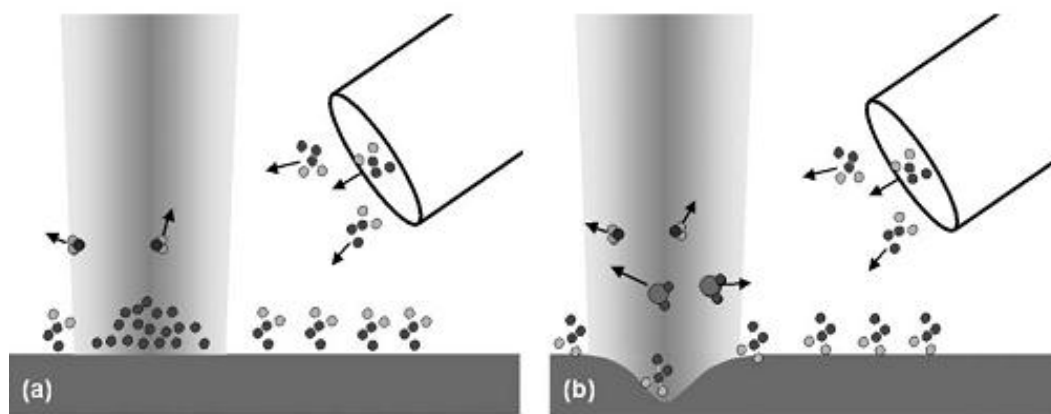
Figure I.22 A schematic drawing of (a) electron beam induced deposition and (b) etching [reproduced from ref. 69].

EBID of metal deposition results in the formation of metal nanocrystals embedded in the amorphous carbon matrix whch can be made conducting by post treatments. EBID has been employed to create structures either on planar or nonplanar surfaces besides the fabrication of three-dimensional (3D) structures. Apart from deposition, the e-beam can also be used to induce other effects such as local etching or heating (see Figure I.22). Together, these processes come under the category of focused e-beam induced processing (FEBIP) [70].

Electron beam induced carbonaceous deposition (EBICD) is a technique to pattern carbonaceous species in a direct manner with the aid of residual hydrocarbons in the vacuum chamber, or by supplying through pump oil. The irradiation of primary electron beam on the sample surface, generates the secondary electrons (energy of 5-50 eV) which induce the crosslinking of the hydrocarbon species, leading to the stitching of

carbonaceous species on to the surface. These carbonaceous deposits were found to be chemically robust, structurally amorphous and electrically insulating, employed as etch resist for the fabrication of semiconductor nanostructures and also as a dielectric in the fabrication of metal-insulator-metal diodes [71-73].

I.7.3b AFM nanolithography

The invention of scanning probe techniques namely STM (1981) and AFM (1986), capable of imaging atomic and nanoscale features, proliferated the rapid progress of the nanotechnology field. Soon after, in 1990's, nanolithographies based on scanning probes were developed for manipulation and modification of surfaces at nanoscale to study various fundamental quantum mechanical phenomenon experimentally [74, 75].

Compared to STM, AFM nanolithography is being widely employed for the modification of surfaces locally by application of either mechanical force or voltage bias [76]. The relative ease of conversion of a force microscope into a modification tool has prompted a fascinating variety of atomic and nanometer-scale modification approaches. Those approaches involve the interaction of a sharp probe with a local region of the sample surface. Mechanical, thermal, electrostatic and chemical interactions, or several combinations among them, are currently exploited to modify surfaces at the nanoscale with probe microscopes (see Figure I.23). Force assisted lithography involves the local deformation of material surfaces via elastic or plastic deformations, mostly used for patterning polymer surfaces [10]. Typical examples of force assisted nanolithography includes, indentation and plowing where a rigid AFM tip is used to mechanically modify a soft sample surface by applying certain load in the range of hundreds of nanoNewtons [76].

Resistively heated AFM probe (temperature of ~400 ºC) along with the application of mechanical force, was employed to write a data bit by scanning over a polymer surface. Here, the combined effect of heat and mechanical force of the tip is the reason for the polymer flow, which can be of potential use in writing data bits in a storage medium [77]. Dip pen nanolithography (DPN) is a direct write lithographic technique in which various functional molecules can be patterned onto the substrate surface, mediated through the water meniscus formed at the tip-sample interface (see Figure I.23b). DPN has been used extensively to pattern a wide variety of inks such as small organic molecules, polymers,

bio-molecules, colloids and metal ions onto surfaces with nanoscale resolution [78]. In the case of bias-assisted AFM nanolithography, the water meniscus formed between the tip and the sample acts as a nanoelectrolyte and the localized electric field (10^8 V/m to 10^{10} V/m) causes the dissociation of water molecules into the oxidative species (OH⁻, O⁻) which could oxidize the surface locally, called as local anodic oxidation (LAO). Besides the LAO, sometimes the biased AFM tip could cause other phenomenon such as electrostatic attraction, electrochemical deposition as well as nanoscale explosion and shock wave propagation [75, 76]. Local anodic oxidation (LAO) is a standard method used for the fabrication of nanosized oxide structures which have been employed as dielectric layers, etch masks and templates for specific affinity of the functional molecules. Thus, AFM based lithography techniques could be used for selective functionalization and patterning of the surfaces besides the fabrication of complex quantum devices and high density flash memories [75-78].
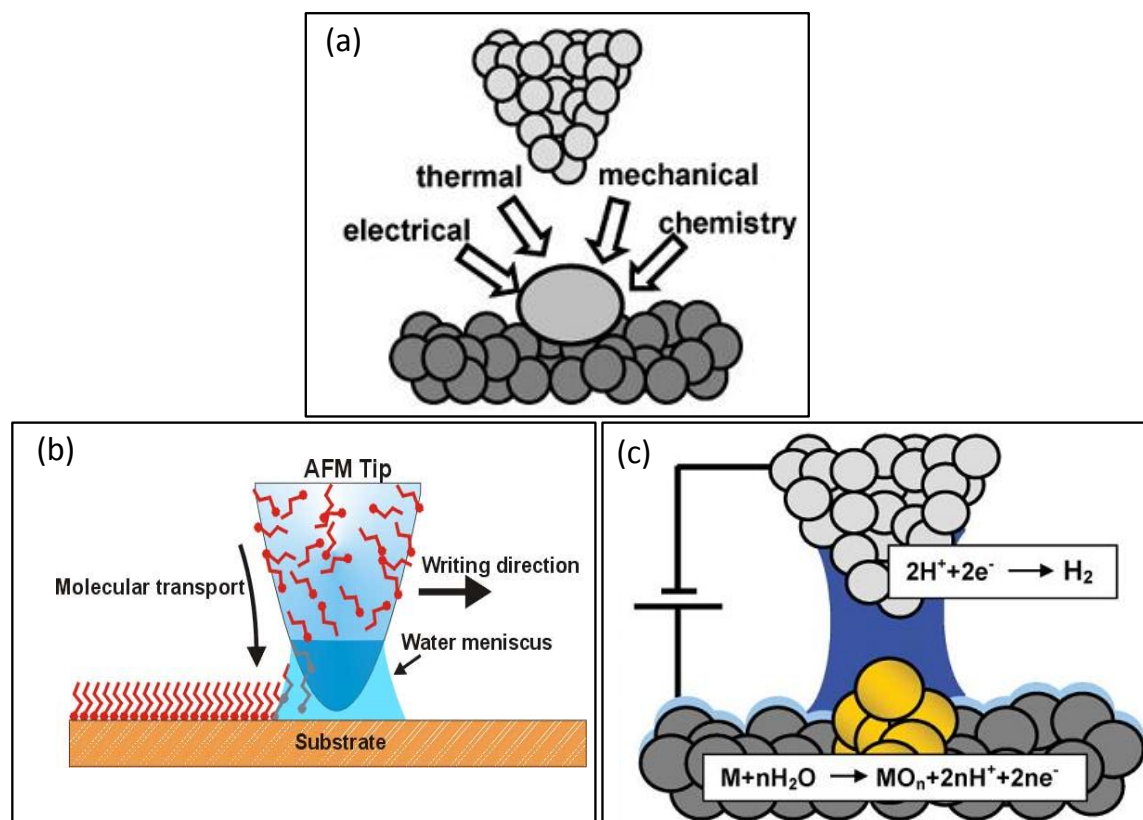
Figure I.23 (a) Schematic of some common mechanisms to modify surfaces with scanning probe nanolithographies. (b) Schematic showing the DPN lithography technique (c) local anodic oxidation through a nanoelectrochemical cell [reproduced from 75, 78].

I.7.3c Laser interference ablative patterning

Laser interference lithography is a technique in which a single laser beam is split into two beams using optical elements followed by setting up the interference patterns where the periodic modulation in the laser intensity, is used for creating periodic patterns over a large area on the sample surface (see Figure I.24a). This technique has been widely employed for patterning various kinds of materials including metals, semiconductors, polymers, etc [79]. Carbon nanotube films have also been patterned using laser interference ablation technique (see Figure I.24b) [80]. Near field phase mask lithography employs a phase mask in contact with the sample surface and the helps in modulating the parallel beam to create periodic structures over a large area [81].
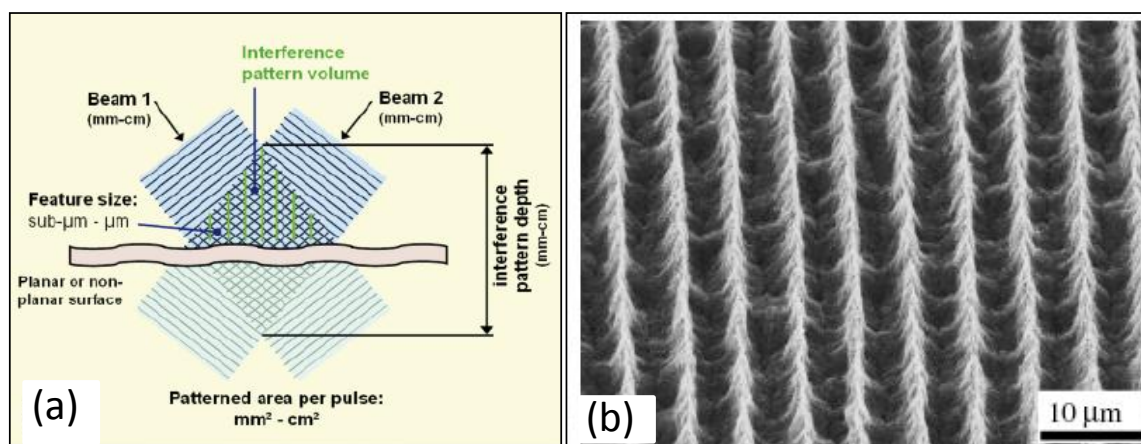
Figure I.24 (a)Schemtatic diagram showing the laser interference lithography. (b) periodic patterns of the carbon nanotube films created using laser interference ablative patterning [reproduced from 79, 80].

I.8 Nanodevices and applications

Nanotechnology essentially leads to miniaturisation of electronic devices. Moore, co-founder of intel has predicted that the number of transistors on a chip can double or triple every 18 months, known as Moore's law [82].

Augmented by the prediction of Moore that the number of transistors on a chip started growing exponentially with time, there has been a greater thrust towards miniaturization of devices and the existing silicon technology pose several practical problems when the thickness comes below 40 nm. This boosted the development of nanotechnology and molecular electronics and current research focuses mainly on electronic properties of nanomaterials.

Buckminsterfullerene, C_{60}, a spherical organic solid with unsaturated π-molecular orbitals, has a rich electronic and vibrational structure. The derivatives of fullerenes have been found to be good electron acceptor systems in the excited state and have been employed in fabricating acceptor-donor based solar cells [83].

Interesting electronic properties exhibited by carbon nanotubes (CNTs) are due to the inherent folding of graphitic sheets in 1-dimensional nature [84]. Electronic structure of CNTs has been well investigated and major contribution is from the π-derived electronic states. Calculations and experimental studies show that CNTs can be as good conductors as copper, although the degree of helicity together with the number of six-membered rings per turn decides their electronic properties. Electron transport in metallic CNTs occurs ballistically with quantized conductance over long nanotube lengths, enabling them to carry high currents with essentially no heating. Hence, they can carry high current densities and field effect transistors and logic circuits have been demonstrated by employing cross-wire configuration of CNTs. The variation in the conductivity on adsorption of gases or attachment of molecules inherent to the material of the nanotube or nanowire is utilized in sensing action [85]. One of the most important applications of CNTs that is already commercialized is its field emission property with low emission threshold potentials and high local field due to their sharp tip. They have longer lifetimes and are exploited in flat panel displays [85].
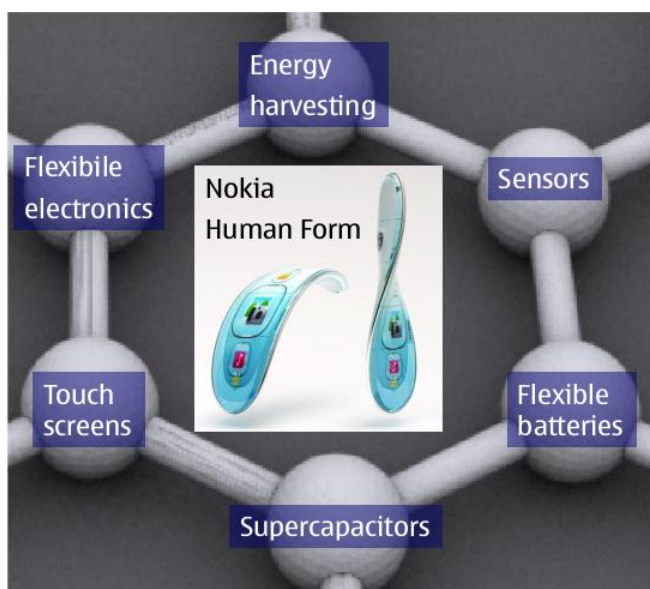
Figure I.25 Graphene based flexible and transparent nanodevices [reproduced from ref. 86, 87].

Graphene, 2D nanoallotrope of carbon, is considered to be potential candidate material for post-silicon electronics due to intriguing electronic and optoelectronic properties [50]. Due to absence of sizable band gap, graphene FETs suffer from poor on/off ratios and absence of saturation currents, limits them for digital applications. By carving graphene nanoribbons with widths of sub 10 nm, introduces band gap of 500 meV, exhibits good on/off ratio but the mobility values are degraded. Still efforts are in progress towards achieving high on/off ratios in the graphene based FETs without sacrificing mobility [88]. Graphene, due to its optical transparency and conducting nature, has been employed as a transparent conducting electrode in solar cell applications. Ultrafast graphene based photodetectors have been fabricated. Due to high electrical conductivity, large surface area and good electrochemical stability, graphene and its derivatives are the potential candidates in fabricating energy storage devices [89]. Thus, graphene is a potential candidate material for the fabrication of flexible and transparent electronic devices (see Figure I.25).

I.9 Nanotools-characterisation

Objects of interest can be evaluated either by seeing through eyes or touching with hands. As the human eye can visualize objects as small as 70 μm and the dimensions lower than this could be visualized after enlarging the image under a microscope. The microscopes are broadly classified into three categories, namely optical, electron and probe microscopes [90].

I.9.1 Optical Microscope

An optical microscope consists of a simple lens system for magnifying the small objects. The objective lens first creates an image of the object in the intermediate image plane which further can be magnified through another lens, the eye-piece. The resolution of the optical microscope is limited by diffraction. The Abbe-Rayleigh criterion states that, for a wavelength λ, the smallest distance d_{min} resolvable between two point sources as deduced from diffraction theory is given by the following relation

$$Resolution\ (d_{min}) = 0.612\lambda/n\ sin\alpha\ldots\ldots(I.9)$$

where NA = n ×sinα is called numerical aperture of the objective lens, n is the index of refraction in the object space, and α half the maximal angle under which the objective lens collects light from the object. The numerical aperture should be as large as possible due to

the following reasons

i) the spatial resolution improves for larger NA (using oil-immersion lenses)

ii) the collection efficiency, i.e. the brightness of the image, increases very quickly with NA, quadratically for small apertures [91].

I.9.2 Electron Microscopes

To overcome the resolution limitations of the optical microscopes, electron beams came into play in place of optical beams. In 1927, de Broglie proposed the concept of wave-particle duality and the wavelength of the electrons is given by the following equation

$$\lambda = h/mv = 1.22/E^{1/2} \ (\lambda \ is \ in \ nm, \ E \ is \ in \ eV)\ldots\ldots\ldots(I.10)$$

For example, electron beam energy of 100 keV has a wavelength of 4 pm (ignoring the relativistic effects) [92].

I.9.2a Transmission Electron Microscope (TEM)
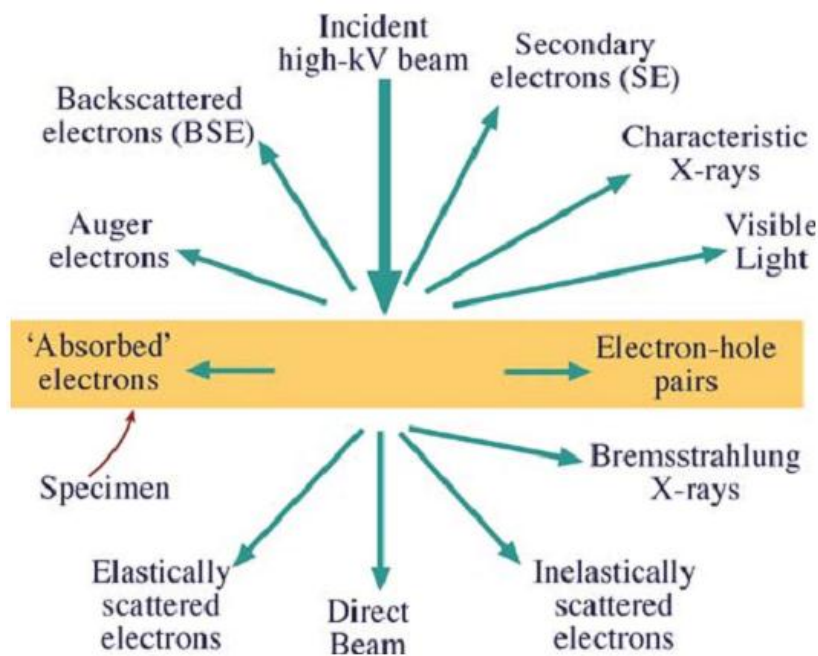
Figure I.26 Signals generated when a high-energy beam of electrons interacts with a thin specimen. Each signal would give different information about the sample under investigation. The directions shown for each signal do not always represent the physical direction of the signal, but indicate, in a relative manner, where the signal is strongest or where it is detected [reproduced from ref. 92].

The first ever electron microscope was built in transmission mode by Ruska and Knoll in 1930s. In the modern version, a beam of electrons is transmitted through an ultra-thin specimen and an image formed from the interaction of the electrons transmitted through the specimen, is detected by an area sensor such as a CCD camera. The focusing of electron beam can be achieved by using a set of electromagnetic lenses and a resolution of the order of 0.2 nm has been achieved. The electron diffraction pattern provides information about the local crystallinity (defects in the form of dislocations, grain boundaries, etc), an essential characteristic for controlling the materials properties. This requires extensive instrumentation such as electron optics, vacuum system ($\sim 10^{-9}$ Torr) and high accelerating voltages (~ 300 keV). TEM is routinely used in nanoscience research for imaging nanostructures and to understand local structure and can be integrated with other techniques like electron energy loss spectroscopy and energy dispersive X-ray spectroscopy to get information on the local chemical composition [92].

The interaction of the primary electron beam with the specimen generates various kinds of signals such as secondary electrons, backscattered electrons, X-rays, etc are shown in Figure I.26. Much information about sample surface, composition and structure can be gained by harnessing the scattered beam.

I.9.2b Scanning Electron microscope (SEM)

In SEM, the focused electron beam scans across the sample surface in a raster fashion, generates the secondary and backscattered electrons, detected by the detectors to generate the topography of the sample surface. The elastic scatterning produces backscattered electrons (energy > 50 eV) and inelastic scattering produces secondary electrons (energy < 50 eV), X-rays and also Auger electrons. These signals are obtained from specific emission volumes within the sample and can be used to examine many characteristics of the sample. X-rays emitted are characteristic of the elements present in the sample, hence can be used to study the chemical composition and is called energy dispersive X-ray spectroscopy. The Auger electrons can be used to map local chemical composition of nanostructures with good spatial resolution and is called scanning auger microscopy and spectroscopy [93].

Backscattered and secondary electrons are utilized in imaging surface topography. Topography contrast arises because the number and trajectories of backscattered electrons

and the number of secondary electrons depend on the angle of incidence between the beam and specimen surface. The backscattered image can provide a contrast of the chemical composition in terms of variation in atomic number. Due to large depth of focus of electron beams, 3D images can be acquired. Although the probe beam diameter can be made to 1 nm and high currents can be generated using field-emission electron sources, the ultimate resolution depends on the interaction volume of the sample from where the scattered beams are generated. The instrumentation has advanced to such an extent that even biological samples can be imaged without metal coating under low vacuum conditions and also scanning TEM is possible with the present day FESEMs.

1.9.3 Scanning Probe Microscopes (SPMs)

The fundamental principle of all SPMs is based on the interaction between a sharp tip and the sample surface for measuring the topography and the other local physical properties [94].

I.9.3a Scanning tunneling microscope (STM)
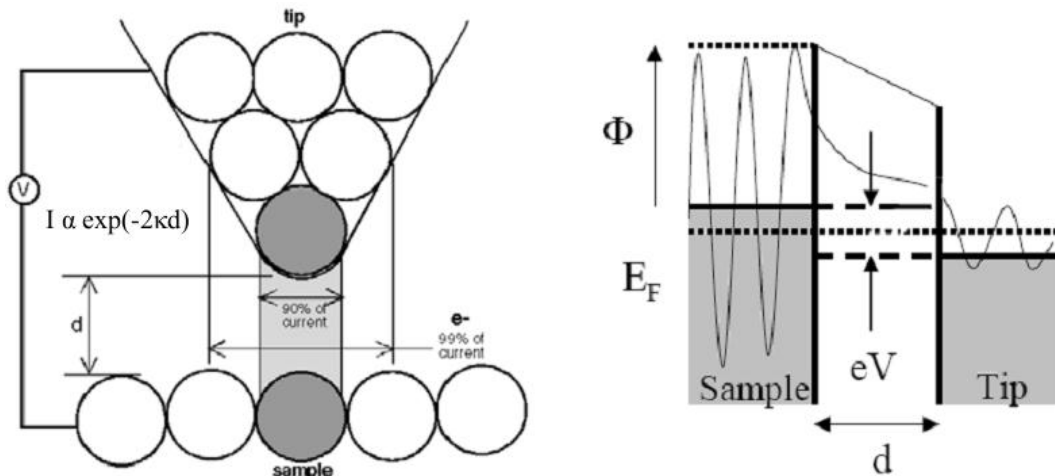
Figure I.27 Schematic showing the dependence of the tunneling current on the tip-sample separation. Tunneling of the electronic wavefunctions between the tip and the sample [reproduced from ref. 95].

STM is based on measuring the tunneling current between the sharp conducting tip and the conducting sample (see Figure I.27). The mapping of the tunneling current at each pixel of the sample surface (xy-palne) according to the z-coordinate produces topography and the contours of the electron density maps. The magnitude of the tunneling current

related to the tip-sample separation is given by the following equation

Tunnelling current, I $\propto$ exp(-2kd)……(I.11)

where d is the distance between tip and sample surface and $\kappa=(2m\varphi)^{1/2}/\hbar$

φ being the DOS at the Fermi level of the tip (for a small bias applied to the sample). This exponential dependence of tunnel current makes the STM as sensitive probe for atomic information. STM can image the surface of the sample with sub-angstrom precision vertically, and atomic resolution laterally.

STM can also give information about the local density of states (LDOS) which is also called scanning tunneling spectroscopy (STS). Reconstructions and the electronic properties of the conducting sample surfaces can be studied. For mapping the electronic density of the atoms of a surface, one needs to minimize the perturbations from the thermal drift and the effects of the ambient environment. For better results, STM is operated in the ultra high vacuum at low temperature conditions. Binnig and Rohrer were honoured with the Nobel prize in Physics in 1986, shared by Knoll for the discovery of the electron microscope.

I.9.3b Atomic force microscope
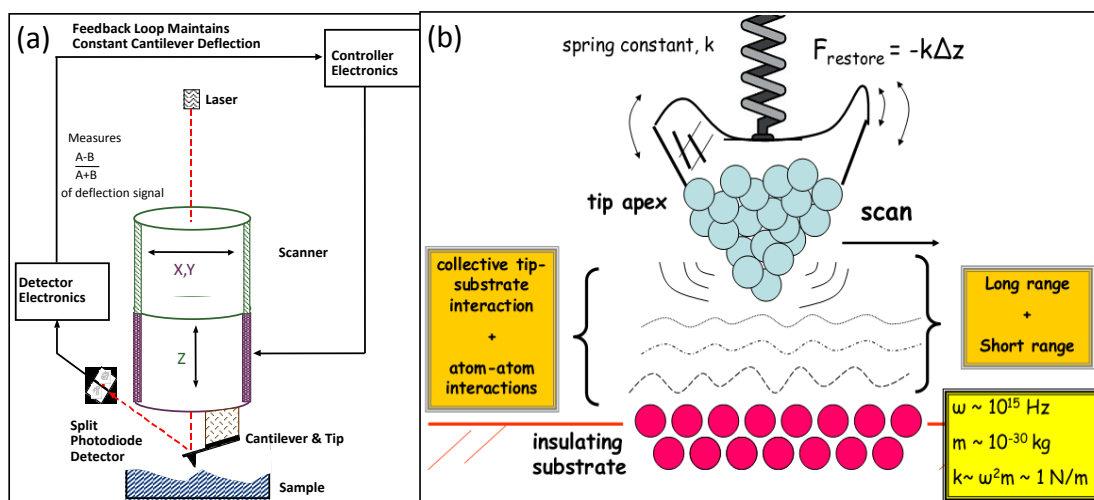
Figure I.28 (a) Schematic for the AFM layout. (b) cantilever restoring force against the tip-sample interaction forces [reproduced from 96, 97].

As STM is limited to conducting or semiconducting samples, an alternate technique was proposed based on measuring forces between the cantilever and the sample surface. This technique was developed by Binnig, Quate and Gerber in the year 1986, called

Atomic Force Microscope (AFM). AFM is a mechanical technique and can be used for insulating as well as for conducting samples. The layout for an AFM is shown in Figure I.28a. The cantilever and tip assembly is called the probe, mounted on a piezo scanner with three independent electrodes for controlling the movement of the probe along the X, Y and Z-axes. A laser beam falls on the back side of the cantilever and reflects back to the quadrupole photodetector. The deflection of the cantilever depends on the spatial variation of forces on the sample surface, which gets recorded by the photodetector and further this signal gets feeded to the feedback circuit which guides the controller to control the tip movement without getting crashed on the sample surface. The cantilevers are designed with specified spring constants according to the mode of operation. Typically, two kinds of forces are encountered during the operation of AFM which include repulsive and attractive van der Waals forces depending on the position of the tip from the sample surface besides the chemical and capillary forces (see Figure I.28b).
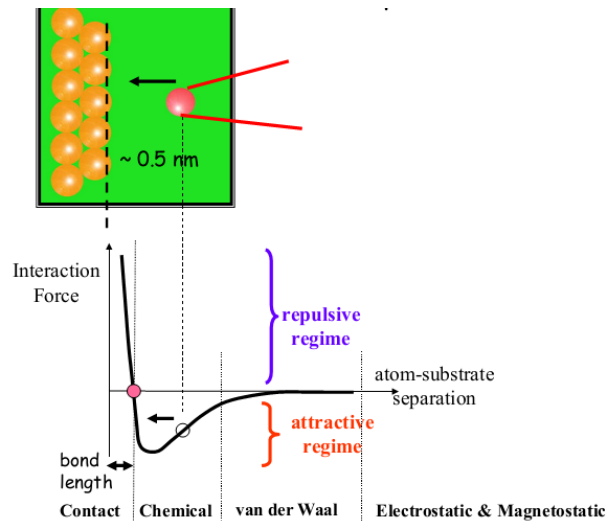
Figure I.29 Lennard-Jones potential to explain the various operating force according to the tip-sample separation [reproduced from ref. 97].

The tip-sample interaction forces are given by Lennard-Jones potential (see Figure I.29). AFM can be operated in static (contact) and dynamic modes. In the contact mode, repulsive interactions between the tip and the sample provides the information about the topography. As the tip is always in contact with the sample surface while imaging, there will be a local pressure of the order of GPa (Pressure = Force/area = nN/nm^2). To minimize the local deformations of the sample surfaces, dynamic modes were invented such as

tapping and noncontact modes. In dynamic modes, the probe vibrates at its resonance frequency and the effective spring constant of the cantilever changes according to the force gradients felt from the sample surface. Typically, dynamic modes are used for imaging soft samples such as polymers, bio-molecules, etc. Besides imaging, AFM has also been extensively used for probing local mechanical, electrical and magnetic properties, etc. Thus, in general, various kinds of forces can be mapped out from the sample surface to extract various local properties such as mechanical, electrical, magnetic, etc, come under the category of scanning probe force microscopes. AFM has also been employed as a local tool for manipulation, modification of the surfaces locally [97].

I.9.4 Characterisation techniques-specifications

Several spectroscopic and microscopic techniques have been used to characterize the prepared samples reported in this thesis. In the following paragraphs, the details of instruments used and the sample preparation methods are described.

Scanning electron microscope (SEM):

Scanning electron microscopy (SEM) measurements were performed using a Nova NanoSEM 600 equipment (FEI Co., The Netherlands). Energy dispersive spectroscopic (EDS) mapping was performed using EDAX Genesis V4.52 (USA) attached to the SEM column. The EDS mapping was performed at 10 kV (energy window, 10 eV) with a beam current of 1.1 nA, the dwell time per pixel being 25 µs. STEM (scanning transmission electron microscopy) and low vacuum imaging were performed on the same instrument using STEM and helix detectors respectively. Electron beam lithography (EBL) was performed under high vacuum conditions, typically 10^{-6} Torr. Before patterning, the sample was well grounded to avoid any charging while patterning, as charging can broaden the patterned feature. The patterns were created using a e-beam write software available with the instrument. The e-beam energy was varied between 5-30 kV. For fine structures, higher kVs were employed whereas for larger area patterning, lower kVs were preferred. The patterning was performed in parallel mode. The beam current was varied between 91 pA to 24 nA. The dwell time, i.e., exposure time per pixel was varied from 0.1- 50 µs. Number of passes was varied from 1-16000. EBICD was performed using residual hydrocarbons of the vacuum chamber (pressure of 10^{-6} Torr) at a working distance of 3-4 mm. Selected regions on the substrate were exposed to e-dosages of 0.7-2.5 C cm^{-2} at 10

kV in the patterning mode, large area depositions are made by raster scanning of the e beam in the TV mode. e-dosage increases with increasing time of exposure and number of passes and its formula is given by

Area dosage = (beam current*dwell time*number of passes)/area per pixel....(I.12)

For working in low vacuum environment, the pole piece was mounted with low vacuum detector (LVD) and the chamber was filled with water vapor at a chamber pressure of 0.4 Torr.

Transmission electron microscope (TEM):

Transmission electron microscopy (TEM) measurements were carried out with a JEOL-3010 instrument operating at 300 kV (λ= 0.0196 Å) and selected area electron diffraction (SAED) patterns were collected at a camera length 20 cm (calibrated with respect to the standard polycrystalline Au thin film). Samples for TEM were prepared by depositing a drop of the nanomaterial on a holey carbon copper grid, allowing it to dry in a desiccator overnight. Carbonaceous platforms have been synthesized on a holey carbon film supported by a Cu TEM grid. This grid was used for TEM and selected area electron diffraction (SAED) analysis. Vacuum annealed EBIC deposits and nc-graphene on the SiO_2/Si surface were transferred to holey carbon film of the Cu TEM grid by lifting with a PMMA layer. 50 μL of 3 wt% PMMA (M_w ~996 kDa, Sigma-Aldrich) was drop-coated on the annealed EBIC patterns followed by curing at 180 °C for 5 minutes. The underlying SiO_2 was etched away using buffer oxide etchant (6:1 40% NH_4F and 49% HF) overnight and the floating PMMA films carrying nc-graphene were thoroughly washed in water. The support PMMA film was placed on the TEM grid and then dissolved away in acetone to leave behind nc-graphene on the grid which was subsequently dried [98]. Pencil powder has been dispersed in chloroform solvent followed by drying over the holey carbon film of the Cu TEM grid in order to look at the nature of the graphite.

Atomic force microscopy (AFM):

Atomic force microscopy (AFM) experiments were carried out using Veeco Dimension 3100 SPM with Nanoscope-IV controller and Veeco diInnova SPM with Nanodrive controller. Tapping and contact (lateral force) mode imaging was carried out using standard etched Si or Si_3N_4 cantilevers, respectively. The scanner was calibrated using a standard Pt coated Au grid with a pitch of 1 μm. Both height and

deflection/amplitude information were recorded at a scan rate of 1 Hz, and stored in a 512x512 pixel format. Both intermittent contact (dynamic AFM) and direct contact scanning modes were used. Images were processed using the Nanoscope version 7.15 software. During the lithography, the feedback is turned off, and the lateral specific movements and the Z-position of the tip were adjusted using the "Nanoman Software". The depth of the trenches has been controlled by the experimental conditions such as mode of operation, tip bias, amount of the force (Z- position) and relative humidity (RH). Metalized Pt/Ir coated Si cantilevers with a nominal spring constant of 2.2 N/m and resonance frequency of 75 kHz (Veeco Model, SCM-PIT) were used for tapping mode AFM. For contact mode work, Pt/Ir coated Si cantilevers (Veeco Model SCM-PIC) with a nominal spring constant of 0.2 N/m and resonance frequency of 16 kHz were used. In some cases, conducting atomic force microscopy (cAFM) was performed on this device using Pt/Ir coated Si tips (SCM-PIC) operating in contact mode on diInnova SPM. The conducting tip is brought into contact with the substrate until a preset loading force is reached. The bias voltage on the sample is then varied while the resulting current is measured. For this reason, it is important to use clean tips to minimize unwanted contact resistance effects. Electrostatic Force Microscopy (EFM) was performed in two pass mode where in the second pass the tip is lifted by the scan height defined by the user to record electrostatic signals only. The magnetic force microscopy (MFM) was performed using a magnetic coated (Co/Cr coated) Si tip. It was magnetized vertically along the tip axis, thereby allowing detection of the perpendicular component of the stray field emanating from the sample surface with a spatial resolution of ~50 nm.

Optical and stylus profiler:

For film thickness measurements, a Wyko NT9100 (Veeco, USA) optical profiler (OP) and a stylus profiler Dektak 6M (Veeco, USA) were used. In OP, the vertical scanning interferometry (VSI) for roughness of samples more than 160 nm and phase shifting interferometry (PSI) mode for roughness of samples less than 160 nm were employed with a field of view and objective lens magnifications from 0.5x – 2x and 5x – 50x respectively.

Raman spectroscopy:

Raman spectra of carbon materials were recorded in the backscattering geometry

using a 532 nm excitation from a diode pumped frequency doubled Nd:YAG solid state laser (model GDLM -5015L, Photop Swutech, China) and a custom-built Raman spectrometer equipped with a SPEX TRIAX 550 monochromator and a liquid nitrogen cooled CCD detector (Spectrum One with CCD3000 controller, ISA Jobin Yvon) [99]. Temperature dependent Raman studies were done using a heating stage (Linkam THMS 600) equipped with a temperature controller (Linkam TMS 94). Raman measurements were performed using LabRAM HR apparatus (Horiba, USA) with an excitation wavelength of 632.8 nm and 5 mW.cm^{-2}. Signal accumulation was performed for 10 s with a spot size of ~1 μm.

X-ray photoelectron spectroscopy (XPS):

X-ray photoelectron spectroscopy (XPS) was carried out with OMICRON spectrophotometer (1x10^{-10} Torr vacuum) with nonchromatic X-ray source of Al Kα (E =1486.6 eV). Samples for XPS (solid substrates) were mounted on the stub using high vacuum compatible Ag paint and dried in a vacuum.

UV-Vis and IR:

UV-visible spectra were recorded using a Perkin-Elmer Lambda 900 UV/vis/NIR spectrophotometer. The photoluminescence (PL) spectra were taken with different excitation wavelength from the spectroflurometer. PL was measured on Perkin- Elmer LS55 Luminescence spectrometer. Fourier transform infrared (FTIR) measurements were done using a Bruker IFS66v/s spectrometer with a resolution of ~ 2 cm^{-1}.

Optical and confocal microscopes:

The optical images were procured with the microscope of Laben, India with a zoom-in lens of 100x. The images were captured using pixel link software. The confocal images were taken by using a Zeiss LSM 510 laser scanning confocal microscope at different excitation wavelengths.

X-ray diffraction (XRD):

Powder X-ray diffraction measurements were performed using a Siemens Seifert 3000TT diffractometer employing Cu Kα (λ = 1.5406 Å) radiation. Samples were prepared by depositing the materials in the form of films on glass slides and typical scan rate was 1 deg.min^{-1}. The X-ray tube was set at 40 kV and 30 mA. With a receiving slit of 0.3 mm wide and a scintillation counter as detector, the θ -2θ scans were performed.

High-purity silicon powder was used as an internal standard. The coherently diffracting crystallographic domain size (D) of the nanoparticles was calculated from X-ray diffraction (XRD) line broadening after subtracting the contribution from the Cu Kα component (Rachinger correction) and correcting for the instrumental width. The integral line width was used in the Scherrer formula [128] to calculate dXRD of the high intensity peak.

$$D = 0.9\lambda/\beta\cos\theta\ldots.(I.13)$$

where λ is the wavelength of the X-ray beam, β is the angular width at the half-maximum intensity and θ is the Bragg angle [100].

Laser ablative patterning:

A frequency tripled pulsed Nd:YAG laser (Quanta-Ray GCR-170, spectra-Physica, USA. λ=355 nm) of energy 100 mJ/pulse, with a pulse width of ~ 10 ns was used in the single shot mode for the ablation of HOPG. The laser beam was partially defocused towards the HOPG using a 90º TIR prism and a lens with a focal length of 30 cm. All the experiments were performed in ambient conditions of pressure and temperature. The laser fluence was varied from 1.1 to 4.2 J cm^{-2}. Aluminum layer on the commercially available compact disk and digital video disks (Sony CD-R, DVD-R) was peeled off using a sharp tweezers followed by cleaning in isopropanol and ethanol solvents to remove the dye. The disks were cut into 15x15 mm^2 pieces for use as optical mask. A commercial TEM grid of type G200HS obtained from Ted Pella Inc., USA with a strand width of 15 μm was used as a shadow mask.

Contact angle (CA):

For contact angle measurements, a Rame´-Hart digital contact angle (CA) goniometer was used to measure the surface wetting properties of hierarchical Pd films at room temperature. A deionized (DI) water droplet (3 μL) was deposited gently on the sample surface using an automatic pipette, and a photograph of the water droplet was taken immediately with the goniometer camera. CA values were given by the DROP image advanced software measurement; the CA values obtained from the software were also crosschecked with the CA values measured manually on the printed photograph of the water droplet. An average was taken after a few point measurements. For each point, a few images were recorded and measured. The typical error of the CA measurements is ±3°.

Electrical measurements:

Au metal (99.99% pure) was physically deposited by resistive heating using 12" vacuum coating unit, (12A4D, HindHivac system, Bangalore) under 10^{-6} Torr vacuum. In order to fabricate gap electrodes, 60 nm thick Au film was deposited on SiO_2/Si substrate by physical vapor deposition (PVD) (Hind Hivac, Bangalore) while using a carbon fiber (diameter, 6-9 µm) such as P100 as a shadow mask which defined the source-drain electrodes (top contacts) for the graphene and nc-graphene samples. Conductive Ag contacts (Ted Pella, USA) are made with hand directly on the pencil mark on the paper substrate.

Two probe electrical measurements were performed on Keithley 236 source-measure unit with a current compliance setting at 100 mA. Temperature dependent resistance measurements were done using a cooling/heating stage (Linkam THMS 600) equipped with a temperature controller (Linkam TMS 94) interfaced with the Keithley 236 source and measure unit. Four-probe resistivity measurements were done by using a physical properties measurement system (PPMS, Quantum Design). A Keithley-4200 semiconductor characterization system was used for measuring the transistor and capacitance characteristics.

IR photoresponse:

For photo response measurements, a Nd:YAG laser with a wavelength of 1064 nm (Quanta-Ray GCR-170, Spectra-Physics, USA) was used as IR source with maximum power output of 50 mWcm^{-2}. The resistance before and after illuminating with IR laser, was monitored using a digital multimeter (TestLink, India) with computer control. The resistance measurements were done by applying a constant bias of 10 mV. All the measurements have been carried out maintaining similar device configuration.

Electrochemical measurements:

The electrochemical properties of the nc-Pd/C films were investigated in two electrode configuration using 6M KOH, 1M Na_2SO_4, PVA/H_3PO_4 gel and 1M 1-butyl-3-methyl-imidazolium tetrafluoroborate (EMIMBF$_4$) in acetonitrile. The PVA/H_3PO_4 gel electrolyte was prepared as follows: 1 g of H_3PO_4 was added into 10 mL of deionized water, followed by 1 g of PVA powder. The whole mixture was heated to 85 °C under stirring until the solution became clear. A Whatmann filter paper (pore size of 220 nm,

NKK TF40, 40 μm) was used as a separator, sandwiched between two symmetric nc-Pd/C electrodes. Cyclic voltammetry and galvanostatic charge/discharge experiments were performed on the potentiostat equipment from Technoscience Instruments (Model PG 16250). The impedance spectra were recorded in the frequency range 1Hz to 1 MHz using CH Instruments 650 Electrochemical Station (Austin, TX, USA).

Function generator and Oscilloscope:

Function generator (8116A Pulse/Function generator 50 MHz, HP) was used to apply different voltage pulses from 10 Hz-50 MHz at amplitude of 1 V. The input and output signals are monitored using oscilloscope (DPO4104 Digital Phosphor Oscilloscope 1 GHz, Tektronix).

References

[1]   G. L. Hornyak, J. J. Moore, H. F. Tibbals and J. Dutta, *Fundamentals of Nanotechnology*, CRC Press, Boca Raton, FL, 2008.

[2]   T. Pradeep et al., A text book of Nanoscience and Nanotechnology, Tata McGraw Hill Education pvt Ltd, New Delhi, 2013.

[3]   http://science.energy.gov/~/media/bes/pdf/scale_of_things_26may06.pdf

[4]   H. Tait, Five thousand years of glass, The British Museum Press, London (1991).

[5]   M. Faraday, *Philosophical Transactions of the Royal Society of London*, 1857, **147**, 145.

[6]   M. Haruta, *Nature*, 2005, **437**, 1098.

[7]   R. P. Feynman, *Caltech Eng. Sci.*, 1960, **23**, 22.

[8]   R. P. Feynman, *J. Microelectromechanical Systems*, 1992, **1**, 60.

[9]   K. E. Drexler, *Nanosystems: Molecular Machinery, Manufacturing, and Computation*, Wiley, New York, 1992.

[10]   Siegel, R.W. 1994. Nanophasematerials. In Encyclopedia of applied physics, Vol. 11, G.L. Trigg, ed.Weinheim:VCH, pp. 1-27.

[11]   J. A. García-Calzón and M.E. Díaz-García, TrAC Trends in Analytical Chemistry, 2012, **35**, 27.

[12]   R. J. White, R. Luque, V. L. Budarin, J. H. Clark and D. J. Macquarrie, *Chem. Soc. Rev.*, 2009, **38**, 481.

[13]   http://www.uwgb.edu/dutchs/EarthSC202Notes/rockcycl.htm

[14]   Bond, G. C., *Heterogeneous catalysis*. 1987; p Medium: X; Size: Pages: 176.

[15]   C. Durkan, "Current at the nanoscale - an introduction to nanoelectronics" published in January 2008, Imperial College Press.

[16]   C. N. R. Rao, P. J. Thomas and G. U. Kulkarni, eds., *Nanocrystals: synthesis, properties and applications*, Springer, Heidelberg, 2007.

[17]   http://www.aip.org/png/html/corral.htm

[18]   Walter Ashley Harrison (1989). *Electronic Structure and the Properties of Solids*

[19]   R. M. Brydson and C. Hammond, in Nanoscale Science and Technology (R. W. Kelsall, I. W. Hamley, and M. Geoghegan, eds.), Wiley, New York, 2005.

[20]   W. Thomson, *Philosophical Magazine*, 1871, **42**, 362.

[21] E. Roduner, *Chem. Soc. Rev.*, 2006, **35**, 583.

[22] http://www.metmuseum.org/toah/hd/glas/hd_glas.htm.

[23] K. L. Kelly, E. Coronado, L. L. Zhao and G. C. Schatz, *J. Phys. Chem. B*, 2002, **107**, 668.

[24] N. N. Long, L. V. Vu, C. D. Kiem, S. C. Doanh, C. T. Nguyet, P. T. Hang, N. D. Thien and L. M. Quynh, *J. Phys.: Conference Series*, 2009, **187**, 012026.

[25] P. K. Jain, K. S. Lee, I. H. El-Sayed and M. A. El-Sayed, *J. Phys. Chem. B*, 2006, **110**, 7238.

[26] C. J. Murphy, T. K. Sau, A. M. Gole, C. J. Orendorff, J. Gao, L. Gou, S. E. Hunyadi and T. Li, *J. Phys. Chem. B*, 2005, **109**, 13857.

[27] http://nanocluster.mit.edu/research.php.

[28] P. L. Stiles, J. A. Dieringer, N. C. Shah and R. R. Van Duyne, *Ann. Rev. Anal. Chem.*, 2008, **1**, 601.

[29] M. J. Banholzer, J. E. Millstone, L. Qin and C. A. Mirkin, *Chem. Soc. Rev.*, 2008, **37**, 885.

[30] G. McNay, D. Eustace, W. E. Smith, K. Faulds and D. Graham, *Appl. Spectroscopy*, 2011, **65**, 825.

[31] S. E. J. Bell and N. M. S. Sirimuthu, *Chem. Soc. Rev.*, 2008, **37**, 1012.

[32] P. P. Edwards, R. L. Johnston & C. N. R. Rao in Metal Clusters in Chemistry, P. Braunstein, L. A. Oro, P. R. Raithby Eds, Wiley VCH, Weinheim(1999).

[33] B. Bhushan, ed., Springer Handbook of Nanotechnology, Springer, Berlin, 2004.

[34] R. L. Johnston, *Phil. Trans. R. Soc. Lond. A*, 1998, **356**, 211.

[35] D. L. Feldheim and C. D. Keating, *Chemical Society Reviews*, 1998, **27**, 1.

[36] P. J. Thomas, G. U. Kulkarni and C. N. R. Rao, *Chem. Phys. Lett.*, 2000, **321**, 163.

[37] D. L. Leslie-Pelecky and R. D. Rieke, *Chem. Mater.*, 1996, **8**, 1770.

[38] N. Bao and A. Gupta, *J. Mater. Res.*, 2011, **26**, 111.

[39] G. Schmid, *Nanoparticles, From Theory to Application*, WILEY-VCH Verlag GmbH & Co. KGaA, Weinheim, 2004.

[40] C. N. R. Rao, G. U. Kulkarni and P. J. Thomas & P. P. Edwards, *Chem. Soc. Rev.*, 2000, **29**, 27.

[41] R. M. Brydson and C. Hammond in Nanoscale Science and Technology, R. Keisall, I. Hamley, M. Geohegen Eds., Wiley VCH, England (2005).

[42] W. A. Fowler, *Rev. Mod. Phys.*, 1984, **56**, 149.

[43] L. Pauling, The Nature of the Chemical Bond, Cornell University Press, Ithaca, NY, 1960.

[44] B. C. Brodie, *Phil. Trans. R. Soc. A*, 1859, **149**, 249.

[45] http://afrodita.rcub.bg.ac.rs/~rzoran/Allotropes%20of%20carbon.htm.

[46] C. N. R. Rao et. al, "Graphene: The New Two-Dimensional Nanomaterial" *Angew. Chem. Int. Ed.* 2009, 48, 7752.

[47] Robertson, *J.Prog. Solid State Chem.*,1991, **21**, 199.

[48] Dresselhaus, M. S.; Dresselhaus, G.; Eklund, P. C. Science of Fullerenes and Carbon Nanotubes; Academic Press: New York, 1996.

[49] R. Saito, G. Dresselhaus, and M. S. Dresselhaus, Physical Properties of Carbon Nanotubes, Imperial College Press (1998).

[50] A. K. Geim and K. S. Novoselov, *Nat. Mat.*, 2007, **6**, 183.

[51] K. S. Novoselov, A. K. Geim, S. V. Morozov, D. Jiang, Y. Zhang, S. V. Dubonos, I. V. Grigorieva and A. A. Firsov, Science, 2004, **306**, 666.

[52] V. P. Gusynin and S. G. Sharapov, *Phys. Rev. Lett.*, 2005, **95**, 146801 .

[53] P. R. Wallace, *Phys. Rev.*, 1947, **71**, 622.

[54] B. K. Miremadi, K. Colbow, Sensors and Actuators B: Chemical, 1998, **46**, 30.

[55] M. Ezawa, *Phys. Rev. B*, 2006, **73**, 045432.

[56] L. Li , G. Wu, G. –H. Yang, J. Peng, J. Zhao and J.-J. Zhu, *Nanoscale*, 2013, **DOI:** 10.1039/C3NR33849E.

[57] Kalita et al., *RSC Advances*, 2012, **2**, 3225.

[58] http://bwtek.com/webinar/fundamentals-of-raman-spectroscopy/

[59] M. A. Pimenta, G. Dresselhaus, M. S. Dresselhaus, L. G. Canc¸ado, A. Jorioa and R. Saito, *Phys. Chem. Chem. Phys.*, 2007, **9**, 1276.

[60] M. S. Dresselhaus, A. Jorio, M. Hofmann, G. Dresselhaus and R. Saito, *Nanolett.*, 2010,**10**, 751.

[61] A. C. Ferrari et. al, *Phys. Rev. Lett.*, 2006, **97**, 187401.

[62] A. C. Ferrari and J. Robertson, *Phys. Rev. B*, 2000, **61**, 14095.

[63] R. F. Pease and S. Y. Chou, Lithography and other patterning techniques for future electronics, *Proc. IEEE*, 2008, **96**, 248.

[64] G. L. T. Chiu and J. M. Shaw, Optical lithography: introduction, IBM J. Res. Develop., 1997, 41, 3.

[65] http://www.mnems.eng.chula.ac.th/lab/review.pdf.

[66] C. Vieu, F. Carcenac, A. Pepin, Y. Chen, M. Mejias, A. Lebib, L. Manin-Ferlazzo, L. Couraud, and H. Launois, Electron beam lithography: resolution limits and applications,Appl. Surf. Sci., 2000, **164**, 111.

[67] D. F. Kyser and N. S. Viswanathan, Journal of Vacuum Science and Technology, 1975, **12**, 1305.

[68] B. Cord, J. Yang, H. Duan, D. C. Joy, J. Klingfus, and K. K. Berggren, Journal of Vacuum Science & Technology B: Microelectronics and Nanometer Structures, 2009, **27**, 2616.

[69] W. F. van Dorp and C. W. Hagen, *J. Appl. Phys.*, 2008, **104**, 081301.

[70] http://www.beilstein-institut.de/Bozen2010/Proceedings/Huth/Huth.pdf

[71] T. Djenizian, B. Salhi, R. Boukherroub, and P. Schmuki, *Nanotechnology*, 2006, **17**, 5363.

[72] N. Miura, H. Ishii, J. Shirakashi, A. Yamada, and M. Konagai, *Appl. Surf. Sci.*, 1997, **114**, 269.

[73] M. -F. Yu, O. Lourie, M. J. Dyer, K. Moloni, T. F. Kelly and R. S. Ruoff, Science, 2000, **287**, 637.

[74] D. Bonnell, *Scanning Probe Microscopy and Spectroscopy*; Ed.; Wiley-VCH: New York, 2000.

[75] R. Garcia, R. V. Martinez and J. Martinez, *Chem. Soc. Rev.,*2006, 35, 29.

[76] X. N. Xie, H. J.Chung, C. H. Sow and A. T. S. Wee, *Materials Science and Engineering R: Reports,* 2006**, 54**, 1.

[77] R. M. Nyffenegger and R. M. Penner, *Chem. Rev.*, 1997, **97**, 1195.

[78] K. Salaita, Y. H. Wang and C. A. Mirkin, *Nat. Nanotechnol.,* 2007, **2**, 145.

[79] M. Bieda, E. Beyer and A. F. Lasagni, *J. Eng. Mater. Technol.*, 2010, **132**, 031015.

[80] A. Lasagni, R. Cross, S. Graham and S. Das, *Nanotechnology,* 2009, **20**, 245305.

[81]   J. A. Rogers , K. E. Paul , R. J. Jackman, G. M. Whitesides, *J. Vac. Sci. Technol. B*, 1998, **16**, 59 .

[82]   Intel press release. http://www.intel.com/research/silicon/mooreslaw.htm

[83]   http://www.slideshare.net/anay_ict/fullerenes-applications

[84]   M. Endo, T. Hayashi, Y. A. Kim, M. Terrones and M. S. Dresselhaus, *Phil. Trans. R. Soc. Lond. A*, 2004, **362**, 2223.

[85]   P. M. Ajayan and O. Z. Zhou, M. S. Dresselhaus, G. Dresselhaus, Ph. Avouris (Eds.): Carbon Nanotubes, *Topics Appl. Phys.*, 2001, **80**, 391.

[86]   http://www.futurity.org/science-technology/graphene-combo-could-shrink electronics/.

[87]   P. Avouris, Z. Chen and V. Perebeinos, *Nat. Nanotechnol.*, 2007, **2**, 605.

[88]   K. S. Novoselov, V. I. Falʹko, L. Colombo, P. R. Gellert, M. G. Schwab and K. Kim, *Nature,* 2012*,* **490**, 192.

[89]   S. Gilje, Song Han, M. Wang, K. L. Wang, and R. B. Kaner, *NanoLett.*, 2007, **7**, 3394.

[90]   http://micro.magnet.fsu.edu/primer/anatomy/introduction.html

[91]   Pluta, Maksymilian (1988). *Advanced Light Microscopy vol. 1 Principles and Basic Properties*. Elsevier.

[92]   D. B. Williams& C. B. Carter, Transmission Electron Microscopy, PlenumPress, Newyork (1996).

[93]   J. Goldstein, D. Newbury, D. Joy, C. Lyman, D. Echlin et al., Scanning Electron Microscopy and X-ray Microanalysis, 3rd Edition, Springer Science and Business Media, Inc., USA (2003).

[94]   https://nanohub.org/resources/9598

[95]   S. N. Magonov & M. –H. Whangbo, Surface Analysis with STM and AFM, Wiley VCH, Weinheim (1996).

[96]   G. Binnig, C.F. Quate and C. Gerber, *Phys. Rev. Lett.*, 1986, **56**, 930.

[97]   R. Wiesendanger in Handbook of M icroscopy, Methods II, S. Amelinckx, D. Van Dyck, J. Van Landuyt, G. Van Tendeloo, Eds., Wiley VCH, Weinheim (1997).

[98]   L. Gao, W. Ren, H. Xu, L. Jin, Z. Wang, T. Ma, L.-P. Ma, Z. Zhang, Q. Fu, L.-M. Peng, X. Bao and H.-M. Cheng, *Nat. Commun.*, 2012, **3**, 699.

[99]   G. V. P. Kumar and C. Narayana, *Curr. Sci.*, 2007, **93**,778.

[100]   B. D. Cullity and S. R. Stock, Elements of X-Ray Diffraction, Prentice-Hall Inc., 2001.

PART II

Electron Beam Induced Carbonaceous Deposition - Fabrication, Characterization and Applications

Summary

Electron beam induced carbonaceous deposition (EBICD) derived from residual hydrocarbons in a vacuum chamber has many fascinating properties. The as-deposited carbonaceous deposits are comprised of several chemical functional groups; found to be chemically inert, structurally amorphous and electrically insulating as revealed by XPS, Raman, TEM and electrical measurements. Interestingly, EBIC patterns are found to be weakly blue fluorescent when excited with UV radiation, a property which owes much to sp^2 carbon clusters amidst sp^3 matrix. The insulating nature of the EBICD was confirmed through electrical measurements and the local dielectric properties of the EBICD were examined using conducting atomic force microscope (cAFM). Further, the EBICD was employed as local dielectric for CNTs. When performed at a CNT location on a Si substrate with low e-beam energy (10 kV), the deposition was taking place beneath the CNT. While higher beam energy (25 kV) aiding the deposition on the top surface of the CNT, in agreement with literature reports. The longitudinal current-voltage characteristics of CNTs were investigated using cAFM after inserting the dielectric carbonaceous layer beneath the CNT. By fixing one end of the CNT on the Ag/Si substrate using electron beam induced deposition of Pt (EBID-Pt) followed by depositing the carbonaceous layer in order to isolate the CNT from the bottom electrode. The I-V data from nanotubes of varying resistances have been collected using cAFM. Further, this technique was generalized to define local dielectric layers for few layer graphene and carbon nanospheres also.

EBICD was thermally treated to induce the graphitization in order to make it electrically conducting. Temperature-dependent Raman and electrical measurements have confirmed the graphitization of the EBICD through the decomposition of functional groups above 300 °C. These graphitized EBIC patterns were employed as channel material to fabricate field-effect transistors (FETs), which showed p-type behavior with typical hole

mobilities in the range of 0.2−4 cm^2/Vs. Further, the EBIC patterns were employed for the selective growth of nanocrystalline graphene (nc-graphene) in a transfer-free manner with the aid of Ni catalyst layer via vacuum annealing. The electrical nature of the nc-graphene was examined and the FETs based on nc-graphene showed p-type behavior, a typical hole mobility of ~90 cm^2/ Vs was obtained. The nc-graphene also proved to be suitable material for IR detection.

II.1 Introduction

Carbon is unique, exhibiting a variety of nanoallotropes. Starting from the discovery of the zero dimensional allotrope C_{60}, the saga of carbon nanotubes (1D) and more recently graphene (2D) is astounding. In hindsight, fullerenes and nanotubes may be viewed as single layers of sp^2 graphene rolled in different fashions [1, 2]. The way the dimensionality brings about diverse properties in carbon is something unparalleled [1-4]. While the electrical transport in these materials owes much to the prevalent sp^2 hybridization, an admixture of sp^3 carbon at corners and bends always induces defect levels in a given morphology which often are responsible for the observed interesting properties [2, 5]. For instance, C_{60} contains both hexagonal and pentagonal rings where the pentagonal rings (due to certain amount of sp^3 character) tend to avoid the delocalization of electrons, making an alkene-like electron deficient system exhibiting semiconducting properties [6]. Carbon nanotubes are considered as bucky tubes with cylindrical morphology, whose properties can be tuned from semiconducting to conducting depending on the tube diameter and chirality [7]. Graphene with lateral dimensions of more than 0.3 μm behaves as a semi-metallic system [8]. The edge states of graphene can be metallic or semiconducting depending on the edge configuration, namely zig-zag or arm chair respectively [9]. The graphene nanoribbons (widths ~ a few nanometers) show semiconducting properties with opening of a band gap due to edge scattering and quantum confinement [10]. These nanoallotropes find applications in photovoltaics, field effect transistors, sensors and supercapacitors etc [1-10].

The eldest cousin of these allotropes, amorphous carbon (a-C), is after all a mixture of sp^2 and sp^3 hybridized carbon atoms, exhibiting both diamond- and graphite-like properties depending on the sp^3/sp^2 ratio, higher the ratio better are the chemical stability, optical transparency and mechanical properties [11-13]. Thus, a-C structures have been

used as protective coatings for hard discs [14], and joint implants in the field of medicine [15]. Carbon deposits in the form of thin films are usually obtained by chemical vapor deposition [16], pulsed laser deposition [18], arc discharge methods [19] and sputtering [20]. The above methods involve high temperature and intense plasma conditions where the nature of the carbon produced depends on the deposition conditions and type of the precursor source [16-22]. While these techniques may offer control on the electrical properties of the carbon deposit, producing patterned carbon deposits with tunable electrical properties at desired locations is still challenging which may be required for establishing local dielectric platforms and active elements for the electronic devices.

Patterned deposition of carbonaceous species using an energetic electron beam has become popular in the recent years. Electron beam induced deposition (EBID) is direct write technique which offers a way to obtain patterned deposition of carbonaceous species. The carbonaceous deposition is usually performed by supplying the scanning electron microscope (SEM) chamber with a hydrocarbon source such as pump oil [23-25] or paraffin [26]. Even, residual hydrocarbons present in a low grade vacuum can also serve the purpose [27]. It is believed that when an electron beam is focused on to a substrate, it generates the secondary electrons from the sample surface which trigger the complex reactions among the hydrocarbon molecules in the proximity leading to the formation of carbonaceous deposits [23-27]. Raman spectroscopy measurements have shown that it is essentially hydrogenated amorphous carbon with more sp^2 than sp^3 character [26]. It is chemically robust and electrically insulating in nature. Although the exact chemical nature is yet to be established, its unique properties have been exploited. It has been used as an etch resist for micromachining [28, 29] and local dielectric in diode fabrication [25]. The deposit has also been employed as glue or a local solder in order to lower the electrical contact resistance and strengthen the mechanical characteristics [30-36] of CNT-CNT and CNT-AFM tip interfaces [37-40]. Even, high quality photonic crystals were fabricated through patterned carbonaceous deposits [41].

II.2 Scope of the present investigation

The present investigation deals with the fabrication and characterization of the EBICD obtained through high and low vacuum environments. It is known to be chemically complex but robust, structurally amorphous, and electrically insulating. In the present

study, the chemical nature of the EBICD has been studied systematically. The growth dynamics of the carbonaceous deposit on CNT surface has been studied [42]. However, under the conditions optimized in the present study, lower e-beam energy (10 kV) favored the carbonaceous deposition beneath the CNT while higher e-beam energy (25 kV) caused the carbonaceous deposition on the top of the CNT, the latter in agreement with the previous reports in the literature. The insertion of dielectric carbonaceous layer beneath the CNT enabled I–V measurement along the length of the nanotube using cAFM. This technique has offered a unique way of establishing local dielectric for the carbon nanotube and graphene, etc. The insulating EBICD was made conducting through thermal treatment under vacuum conditions. Further, the graphitized EBICD was employed as a channel material to fabricate field effect transistors which showed p-type with typical hole mobilities of 0.2-4 cm^2/Vs. EBIC patterns have been transformed into nc-graphene through thermal treatment in presence of thin Ni catalyst layer. Using this technique, nc-graphene has been grown selectively and also fabricated the FETs which showed a typical hole mobility of ∼ 90 cm^2/Vs. It has been shown that the nc-graphene could also be a potential candidate for the detection of infrared (IR) radiation.

II.3 Experimental Details

Si wafers ($\rho = 4 - 7$ Ω-cm) and SiO$_2$(300 nm)/Si substrates were cleaned by sonicating in acetone and isopropanol followed by a rinse in double distilled water for 2 minutes and dried by blowing nitrogen. Multiwall carbon nanotubes, 10 – 200 nm in diameter and 5 – 10 μm in length (Sigma Aldrich) were dispersed on the Si substrate by spin coating a 15 μL of the dispersant in dichlorobenzene (1 mg/5 mL) at 3000 rpm for 45 sec. This resulted in the wide spread of individual CNTs all over the surface [45]. The set up for cAFM consisted of a Multimode scanning force microscope attached to a Nanoscope IV controller (Digital Instruments, USA) and an external multimeter (Keithley 236) as the source and measurement unit for current-voltage characteristics. Au coated tip served as one electrode and the substrate as a second electrode, which was isolated from the scanner by proper insulation. The electrical noise was minimized by proper earthing of the instrument. Electric force microscopy (EFM) was carried out using a biased conducting tip (Pt/Ir) and scanning at a lift height of 30 nm.

Insulating EBICD was transformed into conducting carbon via vacuum annealing

(pressure = 4 x10^{-5} Torr) at a temperature of 500 ºC for 15 minutes. The selective growth of nanocrystalline graphene patterns were obtained via vacuum annealing of EBICD after depositing Ni catalyst layer (thickness, 10-40 nm) at chamber pressure of 6 x 10^{-6} Torr. Thermal treatment was done under vacuum conditions (pressure ~ 2 x 10^{-5} Torr) at different temperatures 600-1100 °C for 5-15 minutes.

II.4 Results and Discussion

II.4.1 Fabrication and characterization of EBICD
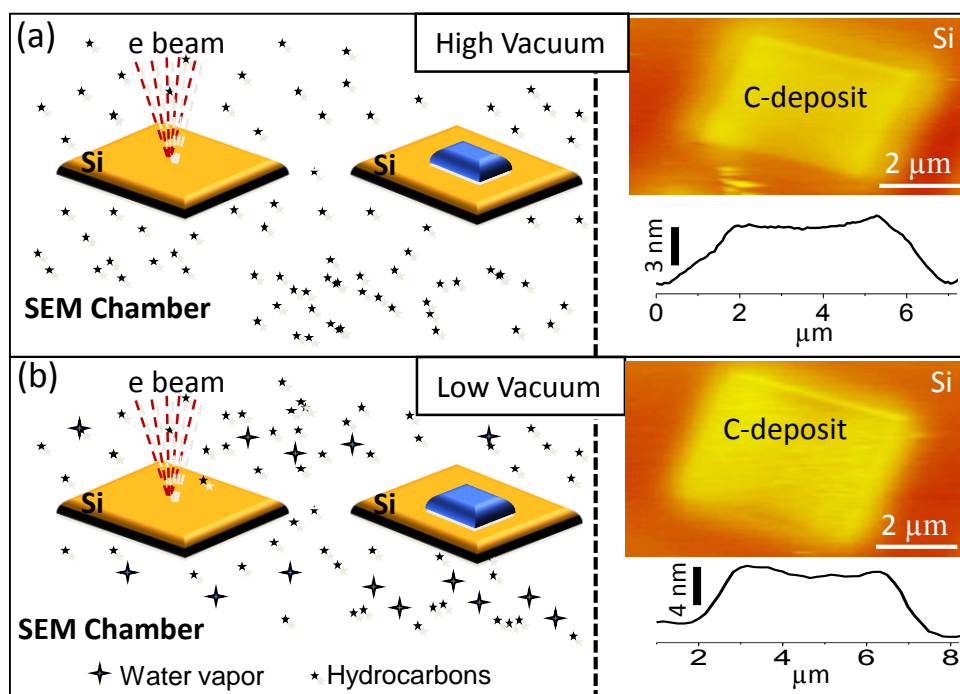
Figure II.1 The process of electron beam induced carbonaceous deposition (EBICD) in the SEM vacuum chamber. (a) and (b) schematic illustrations of the EBICD in high and low vacuum environments respectively. The corresponding AFM topography of the EBIC deposits on Si surface with z-profiles.

The fabrication and characterization of the EBIC deposits are discussed in this section. Schematic representations for the high and low vacuum environments of the SEM in order to fabricate EBIC deposits are shown in Figure II.1. Here, high vacuum corresponds to the vacuum chamber pressure in the range 10^{-4} to 10^{-6} Torr while low vacuum corresponds to a pressure of 10^{-1} Torr with the presence of water vapor. The latter is also called environmental SEM which is typically used for imaging insulating samples such as organic and bio materials where any charging can be neutralized by the water molecules. The SEM

vacuum chamber is pumped by a turbomolecular pump (entire pumping system is designed oil-free at a base pressure of 10^{-4} Torr), which is equipped with a nitrogen-purged bearing and is backed by a scroll pump. The residual gases such as water vapor and oxygen (possibly a little nitrogen) may exist in the vacuum chamber [47].
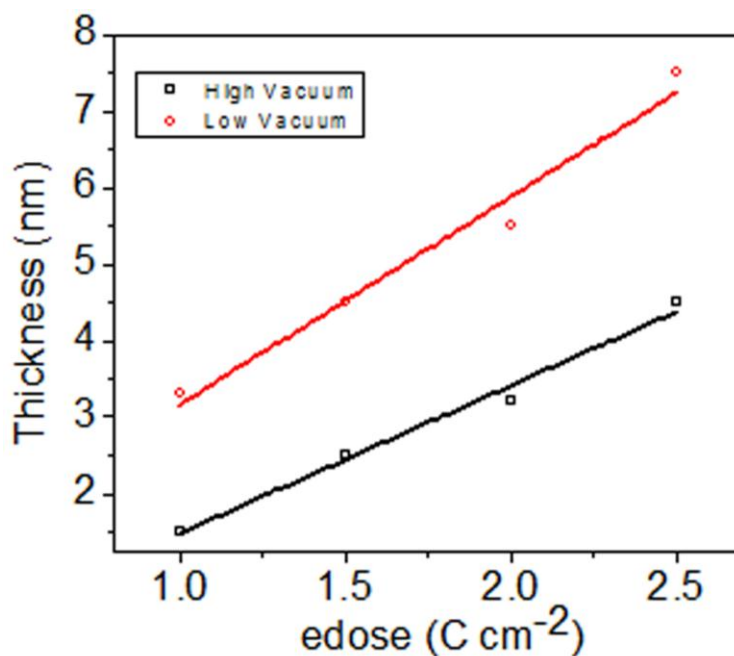
Figure II.2 Comparison of variation in the thickness of the carbonaceous deposits with e-dosage in high (squares) and low vacuum (circles) environments. This set of experiments was performed without breaking vacuum.

The hydrocarbon species in the form of residuals may originate from degassing of the sample holder and conducting glue etc. Secondary electrons generated from the substrate surface after the interaction of the primary e-beam, induce the crosslinking of hydrocarbon molecules leading to the formation of EBIC deposits. Though, the exact chemical reactions leading to EBICD are unclear, some of the aspects have been well discussed in the literature [24-42]. The deposition of the carbonaceous species on Si substrate has been performed in both high and low vacuum environments (see Schematic (a) and (b) in Figure II.1) with e-dosage of 2.5 C cm^{-2} at 10 kV beam energy. The corresponding AFM images of the EBICD along with the z-profiles are shown. The peripheral regions are of slightly higher thickness compared to the interior regions due to slightly larger e-dosages (see Figure II.1). The thickness was found to be 4.5 and 7.5 nm for the high and low vacuum deposits respectively.

The thickness of the carbonaceous deposits was controlled through e-dosage and also the residual pressure of the vacuum chamber (see Figure II.2). Thicker carbon deposits (~ 8 nm) were obtained under the low vacuum conditions and the thickness was varied from 3 to 7.5 nm with increasing the e-dosage from 1 to 2.5 C cm^{-2}. This is attributed to the additional ionic current generation due to ionization of the water molecules which induces the enhanced deposition of carbonaceous species. Under the high vacuum condition, the thickness of the carbonaceous deposits varied in a smaller range, ~1 to 4 nm. The slopes of the plots were found to be 2.7(3) and 1.9(2) nm/C cm^{-2} for the low vacuum and high vacuum environments respectively. The thickness and the chemical nature of the carbon deposits would depend on the quality of the vacuum chamber which is the source for the residual hydrocarbons [48].
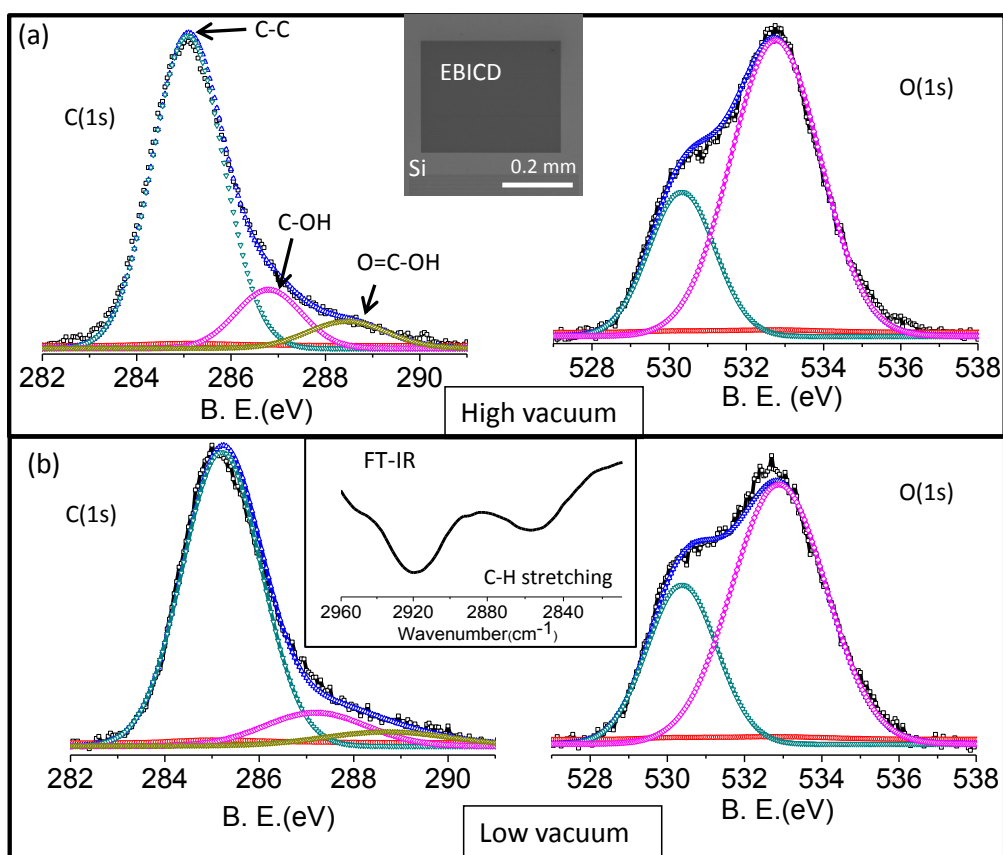
Figure II.3 C1s and O1s core-level spectra of the carbonaceous platforms deposited in high (a) and low (b) vacuum environments. The SEM image of the EBIC deposit over large area used for XPS measurement is shown in the inset. FTIR spectrum of carbonaceous deposit with the presence of C-H stretching vibrational modes (see inset of Figure II.3b). Curve fitting of the C1s and O1s spectra was performed assuming a Gaussian peak shape after appropriate background correction.

In order to examine the chemical nature of the carbonaceous deposits, X-ray photoelectron spectroscopy (XPS) measurements were performed (see Figure II.3). Figure II.3a shows the core level spectra of the deposits made in the high vacuum environment. The C1s spectrum has the main peak at 285.1 eV corresponding to C-C sp^3 species and additional peaks at 286.8 and 288.4 eV assignable to C-OH and O=C-OH species, respectively [49]. The O1s peak positioned at 530.3 eV is assigned to O=C-OH and that at 532.8 eV to C-OH groups. The C1s and O1s spectra for the carbonaceous deposits from the low vacuum environment are shown in Figure II.3b. The C1s spectrum shows the main peak at 285.2 eV and additional peaks at 287.2 and 288.7 eV corresponding to C=O and O=C-OH groups, respectively. Similarly, O1s contains two peaks at 530.4 and 532.9 eV due to O=C and O=C-OH; C-OH groups, respectively. The atomic ratio of carbon to oxygen was estimated to be 3:1 and 2.7:1 for the high and low vacuum deposits, respectively. From the above observations, it is clear that under low vacuum; the deposited carbon is relatively more oxygenated compared to that from the high vacuum deposition. The presence of hydrogen in the carbonaceous deposits was examined using infra-red spectroscopy (IR). The spectrum in the inset of Figure II.3b exhibits two vibrational modes at 2920 and 2856 cm^{-1} which correspond to the aliphatic C-H stretching modes [50].

As Raman spectroscopy is a structural characterization tool for carbon based materials [51], it was employed here to understand the structure of carbon in the EBICD. The optical micrograph in Figure II.4a shows the carbonaceous deposits on Au pads from both high and low vacuum environments. The Raman spectrum recorded on the carbonaceous platforms is shown in Figure II.4b. The positions of the D and G bands are found to be centered around 1389 cm^{-1} (FWHM, 274 cm^{-1}) and 1557 cm^{-1} (FWHM, 126 cm^{-1}), respectively (see Figure II.4b). In general, the G band relates to the bond stretching vibrations of sp^2 carbon atoms whereas the D band originates from the breathing motion of the six-fold aromatic rings. The ratio of the intensity of D and G bands (I_D/I_G) is proportional to the probability of finding six-fold aromatic rings which depends on the sp^2 carbon cluster area in amorphous carbon deposits [52]. The D and G bands being broad, is a clear signature of the amorphous nature of the carbon deposits (see Figures II.4b). The I_D/I_G ratio was found to be 0.57 for the EBIC deposits.
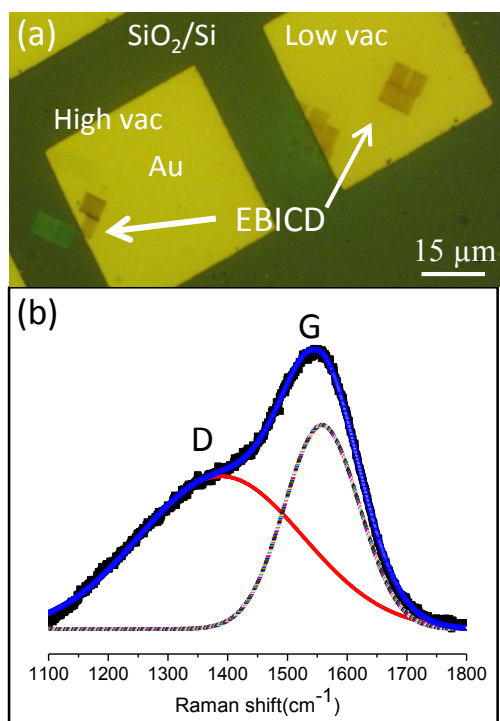
Figure II.4 (a) Optical micrograph of the carbonaceous platforms on the Au pads. (b) Raman spectrum recorded from EBICD. The overlapping D and G bands were deconvoluted by fitting two Gaussian peaks.
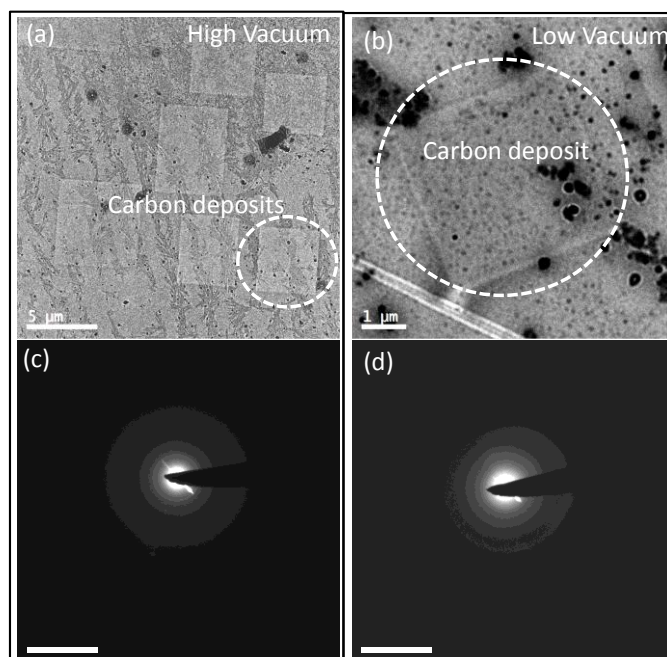
Figure II.5 TEM micrographs of the carbonaceous deposits on a holey carbon grid, deposited from (a) high and (b) low vacuum environments. The corresponding electron diffraction patterns from the interior of the carbonaceous platforms are shown in (c) and (d). The black dotted lines show the boundary of the carbonaceous platforms.

The micro structure of the carbonaceous deposits was examined using TEM (Figure II.5). The TEM micrographs of the carbonaceous deposits from the high and low vacuum are shown in Figures II.5a and b. The electron diffraction patterns from both types of deposits are diffused halos, indicating their amorphous nature (see Figures II.5c and d). These results are consistent with the previous reports based on Raman and TEM measurements [26].
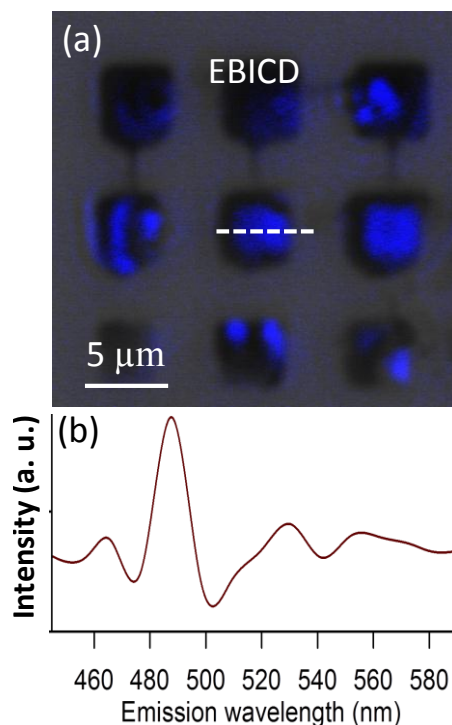
Figure II.6 (a) Confocal laser scanning image of the EBIC-deposits; the fluorescence map was obtained by exciting at 355 nm. (b) Emission spectrum of the EBICD with a emission maximum at 485 nm.

The emission map is shown in Figure II.6 (excitation, 355 nm), where the EBIC deposits are seen as blue fluorescent regions and the emission is non-uniform from the EBICD. This weak fluorescent nature arises due to the presence of the carbonyl, carboxyl and hydroxyl functional groups which goes well with the XPS analysis. The emission spectrum of the EBICD showed a peak at 485 nm (see Figure II.6b). Based on Raman measurements, the G band arises from the sp^2 carbon domains in the EBICD (see Figure II.4b). These sp^2 carbon domains are surrounded by the presence of functional groups which induces localization of electrons giving rise to isolated sp^2 clusters in the sp^3 carbon

matrix [53]. These clusters behave as luminescence centers or chromophores, fluorescence originates from the recombination of electron–hole (e–h) pairs within the localized small sp^2 carbon clusters embedded within the functionalized carbon sp^3 matrix.

II.4.2 Electrical characterization-EBICD as local dielectric for carbon nanomaterials

In order to investigate the electrical properties of the EBICD, Au contact pads (50 nm thick) were deposited on the carbonaceous platform using a shadow mask (~ 9 µm diameter). The I-V data shows a blockade region across zero bias (-2 V to +3 V) and beyond -3V, the curve is slightly asymmetric with current in the range of 20 nA (Figure II.7). The I-V behavior of the EBIC deposits (widths of 10 and 20 µm across length of 9 µm) between Au contact pads, confirms the insulating nature (see black and red curves in Figure II.7).
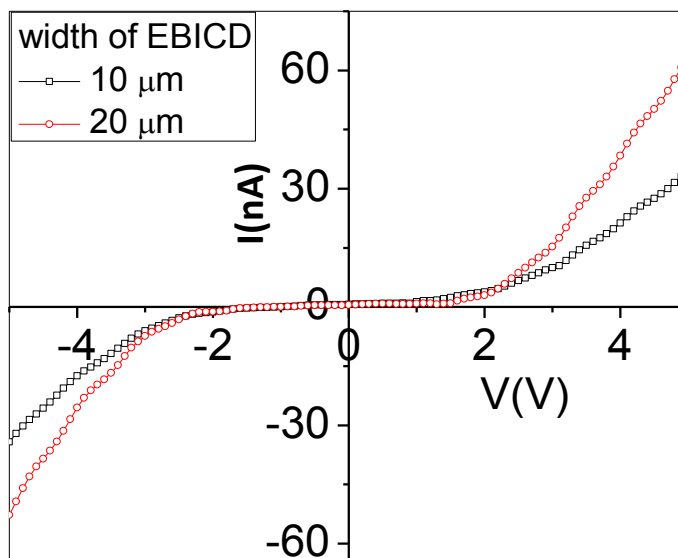
Figure II.7 Two probe I-V of the EBICD (high vacuum) on a glass substrate with a width of 10 µm (black curve) and 20 µm (red curve) with a length of 9 µm. I-V is non-linear with a current of 10 nA above 2 V, indicating the highly insulating nature of the EBICD.

The I-V characteristics of the EBICD obtained from low vacuum environment, showed blockade region across zero bias (-4 V to +10 V) and beyond -4V, the curve is slightly asymmetric with current in the range of 2-4 nA (Figure II.8). This implies that the EBICD obtained under low vacuum conditions was more insulating compared to that of high vacuum conditions.
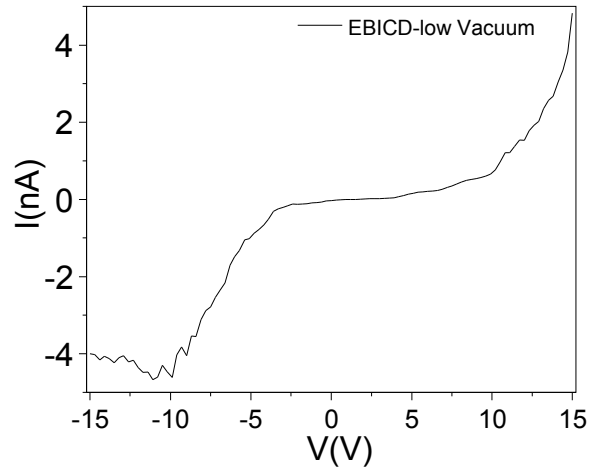
Figure II.8 I-V characteristics of the EBICD deposited under low vacuum conditions.

Further, the electrical behavior of the EBICD was investigated by employing cAFM where the AFM tip acts as a top electrode and Ag/Si substrate as bottom electrode.
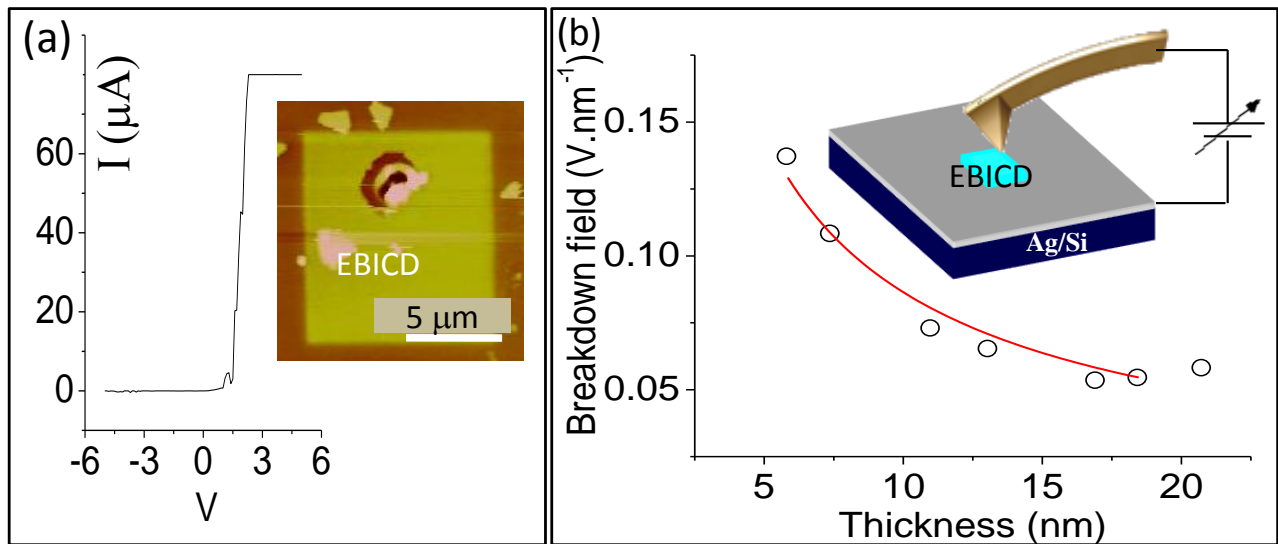
Figure II.9 (a) The current as measured by the conducting AFM tip in contact with the carbonaceous platform, against the applied bias. The current compliance was set to 80 μA. Adjacent AFM image shows rupturing of the carbonaceous platform due to electrical breakdown. (b) Variation of the breakdown field with the thickness of the carbonaceous platform. The inset shows a schematic diagram of the cAFM setup.

Conducting atomic force microscope (cAFM) tip was employed as a local top electrode. It was observed that on increasing the tip bias, a sudden increase in current was observed at a certain positive voltage which can be attributed to the electrical breakdown

of EBICD. In the example shown in Figure II.9a for a 25 nm thick EBICD platform, the electrical breakdown occurred at a tip bias of ~ +2.2 V. This aspect has been examined in detail on carbonaceous platforms of different thicknesses using the cAFM set up. The breakdown indeed leads to rupturing of the dielectric platform as apparent from the adjacent AFM image. This process was repeated for platforms of different thicknesses and in each case, the breakdown field was calculated. The variation of the breakdown field with the dielectric layer thickness (see Figure II.9b) was fitted to an empirical power-law of the form given by [54],

$$E_B(d) = \text{const} \times d^n \ldots\ldots(II.1)$$

The curve fitting of data yielded a value of $n \sim 0.75 \pm 0.01$. Typical values of n for dielectric films are in the range of 0.3-0.5 [55]. The observed higher value may arise due to non-ideal electrode configuration (one electrode being the AFM tip) as well as due to the possibility of high field emission from the tip.

Due to its insulating nature, EBICD has been used as a dielectric for the fabrication of metal-insulator-metal (MIM) diodes [25]. In order to study the nature of interaction of EBICD with the carbon nanotubes; CNTs were dispersed on a Si substrate. The process of carbonaceous deposition on a CNT is depicted in Figure II.10. Figure II.10a shows the SEM image of a CNT with ~200 nm diameter and several μms long.

At one end of the CNT under consideration, a rectangular region of carbonaceous deposition was produced (Figure II.10b) using an e-dose of 0.7 C cm^{-2}. On careful examination, it is rather not difficult to make out from the image that the CNT is located on top of the carbonaceous platform, instead of getting buried underneath. This is somewhat similar to the observation made in the case of Fe-Co-Ni nanoparticles, which were soldered by the carbonaceous layer from beneath [56]. Some deposition was observed on top as well. Unlike the case of nanoparticles, the CNTs in this case were found to roll away easily from their original positions even with minimal force of few nano Newtons applied during AFM scans, revealing that the interaction of CNT with the carbonaceous layer was rather weak (see Figure II.10c).
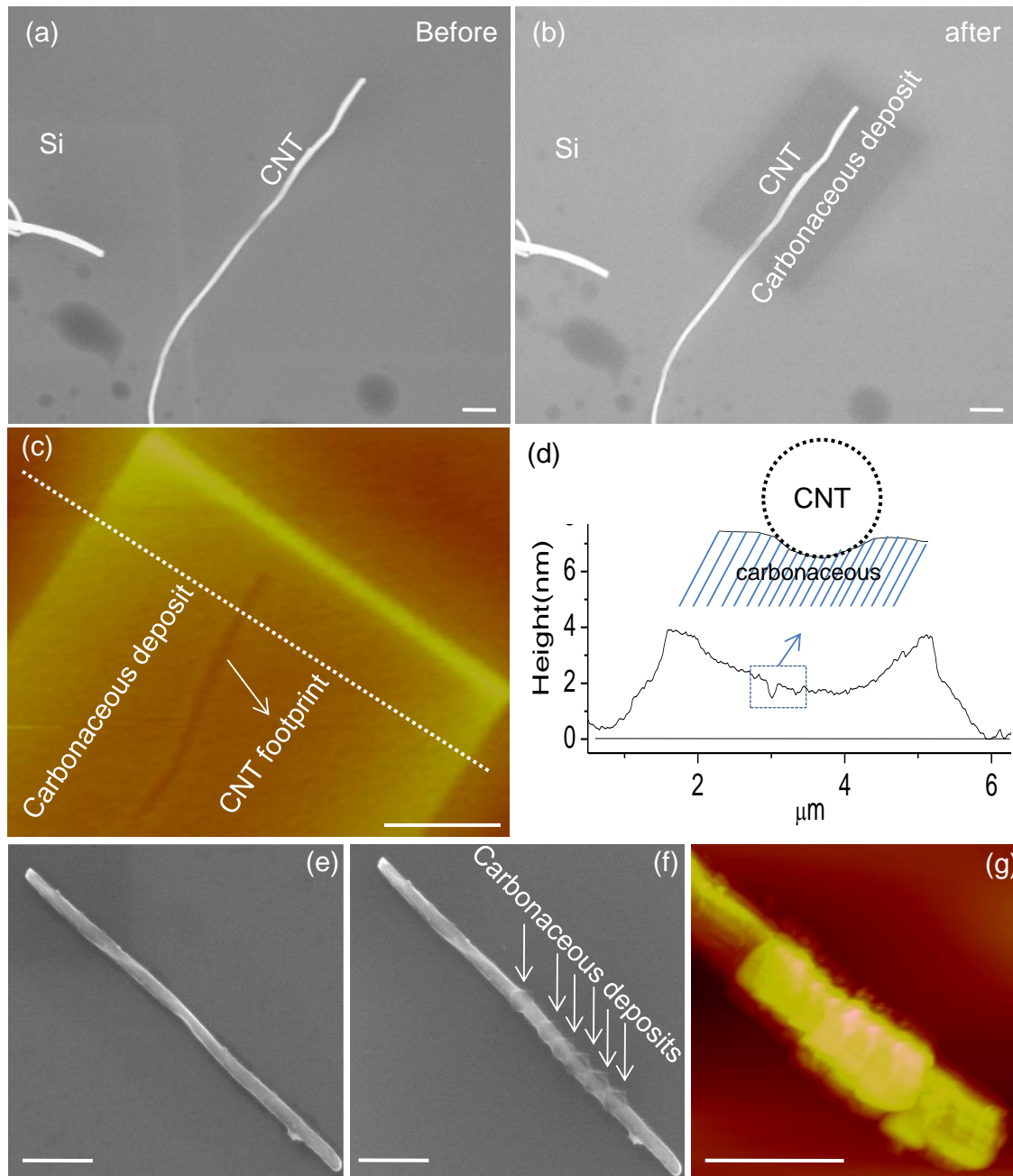
Figure II.10 (a) SEM image of a CNT on Si substrate. (b) Carbonaceous deposition (e-beam energy, 10 keV and e dose 0.7 C cm^{-2}) in the form of a black rectangular platform at one end of the CNT. (c) AFM scan leading to rolling of CNT away from the carbonaceous platform. The foot print of the CNT on the carbonaceous platform (thickness, 4 nm) can be seen. (d) AFM z-profile of the footprint. The top schematic illustrating the CNT on the carbonaceous platform before rolling away. SEM images of a CNT (e) before (f) after depositing the carbonaceous patterns (e-beam energy, 25 keV and e dose, 15.2 C cm^{-2}) on the CNT surface, and (g) the corresponding AFM image showing the carbonaceous deposition on top of the CNT. Scale bar, 1 μm.

However, the footprint of the CNT could be seen clearly. From the z-profile shown in Figure II.10d, the CNT footprint is 135 nm wide and 0.6 nm deep with nearly 1.4 nm of the deposit beneath. It appears that there is some contribution from the tip convolution to the width of the footprint (the tip radius being ~ 30 nm). The platform is somewhat non-uniform in thickness, something which is commonly observed during the EBID of carbon [26]. The footprint in Figure II.10c closely follows the shape of the CNT as seen in Figure II.10b. When the 10 kV e-beam was focused to a spot (instead of scanning) right on top of the CNT, no deposition has occurred. Thus, under the deposition conditions using low e-beam energies, the carbonaceous deposition seems to dewet from the CNT surface effectively lifting it on top. This observation is unique in this study. It required higher e-beam energy (25 keV) to produce the carbonaceous deposition wetting the CNT surface on top (Figures II.10e, f and g), as has also been observed by many others [42].
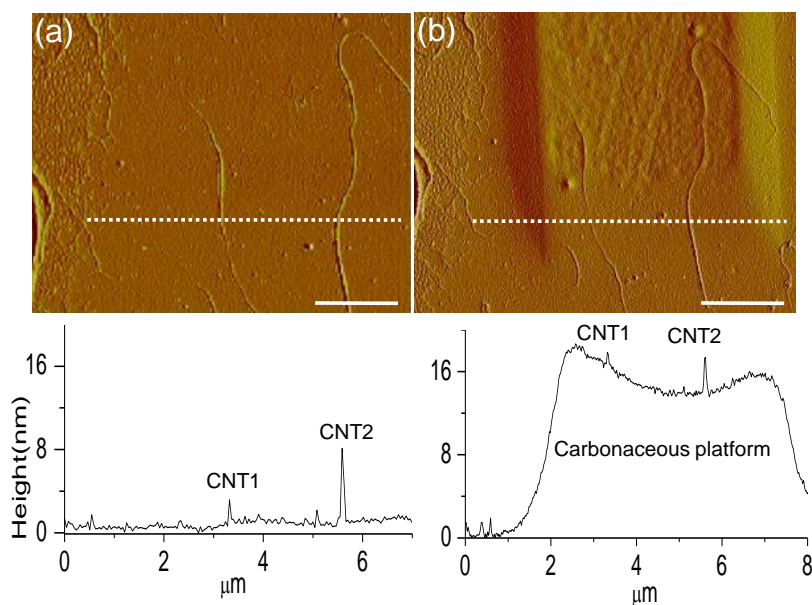
Figure II.11 AFM amplitude images of two thin CNTs on the Si substrate prior to (a) and after (b) the carbonaceous deposition. The corresponding height profiles are shown below. Scale bar, 2 µm.

When thin CNTs (diameter ~ 3-10 nm) were used, AFM measurements could be done without causing any displacement from the raised carbonaceous platform (e-dose, 3.0 C cm^{-2}) (Figure II.11). It is interesting to note that the overall shape of the CNTs was unaltered during the deposition. From the z-profiles shown under Figures II.11a and b, it can be seen that nearly half of the tube diameter is immersed in the carbonaceous platform,

the latter being ~16 nm high. The CNTs being very thin, the footprint on the platform can be quite comparable to the diameter. Because of this, they would remain firm during AFM scans. Importantly, this experiment shows that the CNTs could be repeatedly lifted to the top surface of the carbonaceous platform.
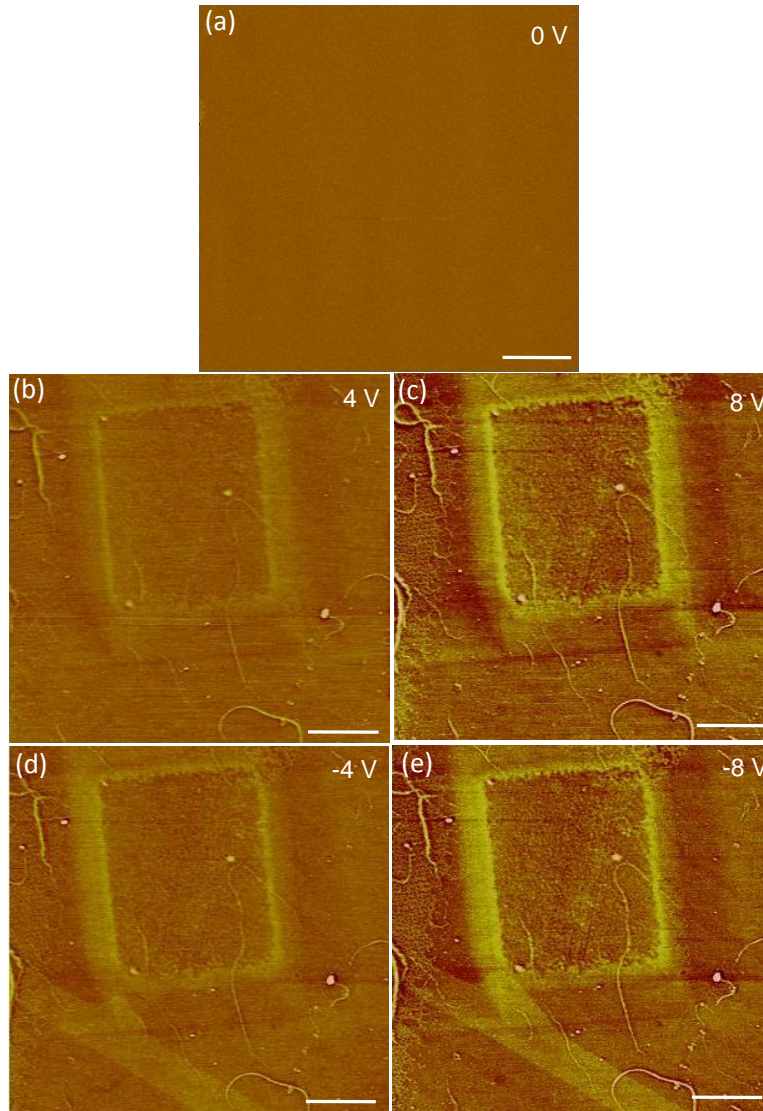
Figure II.12 EFM phase images (corresponding to the amplitude image in Figure II.11b) were obtained with tip bias of (a) 0 V, (b) 4 V, (c) 8 V and (d) -4 V, (e) -8 V, Scan lift height of 30 nm was used throughout. Scale bar, 2 μm.

EFM measurements were performed on the raised CNTs at a lift height of 30 nm and at different tip voltages of 0, 4 and 8 V (Figure II.12). Corresponding to the amplitude image in Figure II.11a, the zero bias phase image in Figure II.12a is featureless, while those

obtained with 4 and 8 V bias (Figures II.12b and c, respectively), show increasing contrast of the CNT on the carbonaceous deposit. The EFM phase images for the negative tip bias polarity (-4 and -8 V) are shown in Figures II.12d and e. Importantly, the carbonaceous deposit itself exhibited a weak signal in EFM, implying its dielectric nature. The tip-bias-dependent phase behavior seen here is typical of a conducting species like CNTs.

The longitudinal electrical transport of the CNTs was investigated by selectively lifting individual CNTs using the dielectric carbonaceous layer. As the CNT was only loosely bound as noted earlier (Figures II.10c and d), a method was followed where a desired CNT was first located and one end of the CNT was fixed to a Ag coated Si substrate by depositing Pt on top from a metal-organic precursor using the EBID process. This formed one electrode for the CNT.
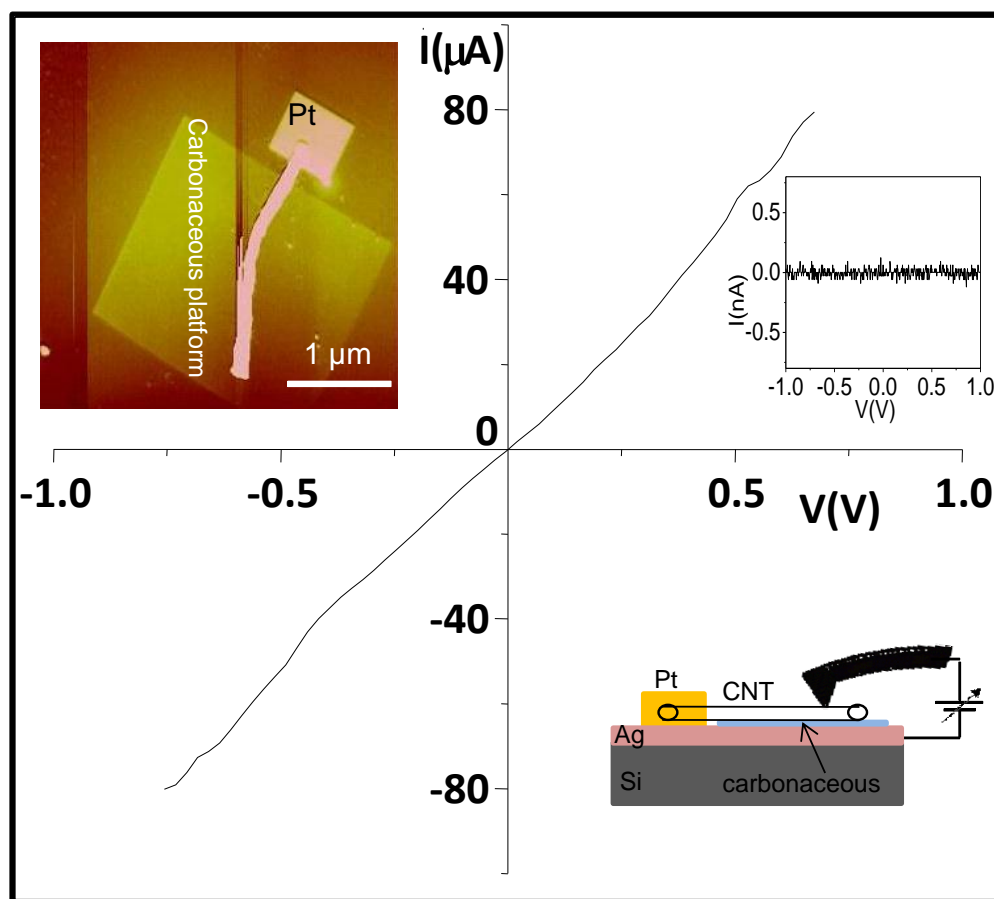
Figure II.13 I-V characteristics of a CNT using cAFM. The AFM image of the circuit is also shown (top- left). The streak in the middle is perhaps due to movement of the CNT while scanning. The I-V data from the carbonaceous platform away from the nanotube is shown in the inset. The schematic illustrating that the I-V measurement along the CNT length is shown (down-right).

After pumping away the precursor and introducing water vapor to 0.4 Torr, the carbonaceous deposition was then carried out (10 kV) to cover the rest of the length of the CNT so that it got almost entirely lifted on top of the carbonaceous platform of 10 nm thick (Figure II.13). The I-V measurement using cAFM in the central region of the nanotube showed a nearly linear behavior with a resistance of ~ 44 kΩ, typical of a MWNT. It may be noted that the resistance measurement was along the length of the nanotube but not across its diameter, as the tube was lying on the dielectric carbonaceous platform. Indeed, there was no current when the tip was positioned directly on the carbonaceous platform, away from the CNT (see inset in Figure II.13). As the raised CNT was electrically accessible, its surface must be devoid of the carbonaceous species from the deposition, affirming complete dewetting. These observations are in line with the results shown in Figures II.10-12.

Further, the carbonaceous deposition was employed to evaluate the longitudinal electrical behavior of the CNTs through depositing 10 nm thick EBICD beneath them (see Figure II.14). For the two CNTs under consideration, the carbonaceous deposition was carried out such that a 2 μm region in the middle was left free for micro-Raman measurement. The I-V measurement in the case of CNT-i was nearly linear in contrast to the non-linear behavior found in CNT-ii (see Figure II.14a), indicating that the former was more metallic.
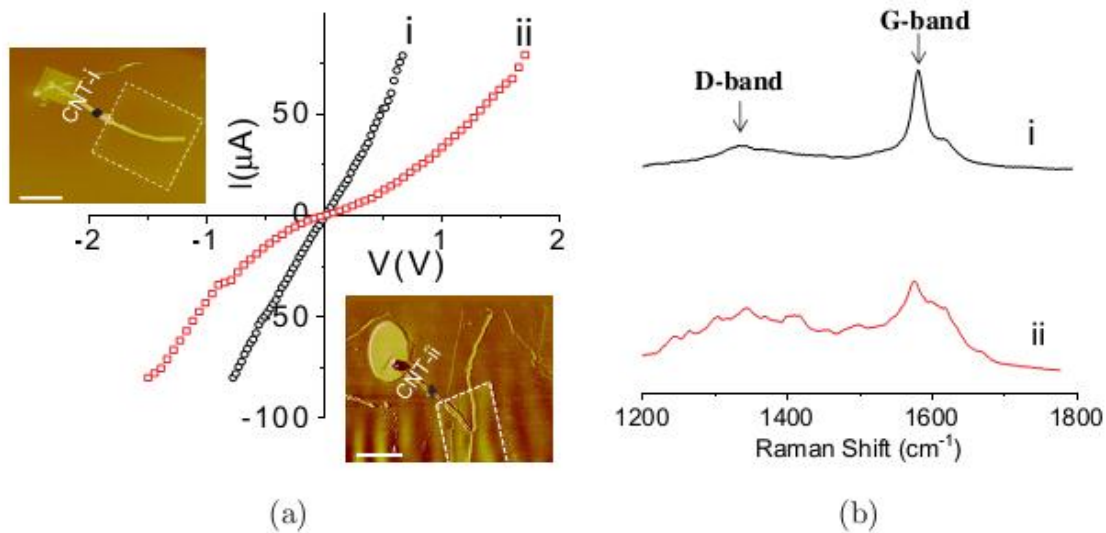
Figure II.14 (a) I-V characteristics of CNTs i and ii wired into a circuit using cAFM and corresponding AFM images have shown. (b) Raman spectra of the CNTs recorded at the black spots. Scale bar, 3μm.

In the corresponding Raman spectrum from CNT-i (see Figure II.14b), the intensity of the G band around 1560 cm^{-1} is relatively high compared to that of the D band at 1360 cm^{-1}. For CNT-ii, the spectrum is broad with D band intensity comparable to the G band. Clearly, the CNT-i is more crystalline [57, 58] which goes well with its electrical nature. Thus, the present technique allows a unique way of determining the electrical nature of CNTs randomly spread over a surface. Although the method employs cAFM to contact the CNT, it was unconventional in the sense that the electrical measurement here refers along the length of the tube lying on the dielectric carbonaceous platform.

A note on the nature of interaction between carbonaceous deposit and CNT surface is worthwhile. When a carbon source is deliberately introduced, the deposit produced can wet a carbon nanofibre surface and clamp it [39]. On the other hand, there are several studies which relied only on residual hydrocarbons. The deposit in these cases may come up below as well as on top [42] which has been used to stick two CNTs [33], to glue CNTs to electrodes [32] and AFM tips [31, 39, 40], or to clamp and freeze deformation in a CNT, while bending it by a nanomanipulator [34, 35]. EBICD has been used to clamp CNTs and form junctions [36]. In all the cases, the electron beam energy was above 25 keV. In this study, employing residual hydrocarbons in the presence of water vapor seems to make the deposition more facile. While the growth of the carbonaceous deposit below CNT is not altogether surprising, its dewetting nature is a novel observation. Indeed for 10 kV beam energy, no deposit is seen on the CNT surface! The hydrophobic nature of the CNT surface [59] may also play a role here. Under the low e-beam energy employed in this study, the secondary electrons generated from the substrate are causing the deposition beneath the CNT and the chemical nature of the carbonaceous species is perhaps quite different.

The unique observations of lifting on top of the carbonaceous platform and dewetting are not limited to CNTs (Figure II.15). Carbonaceous deposition was carried out on an isolated piece of few layer graphene (FLG) on a Si substrate as well as on carbon nanospheres of 80 nm diameter. As shown in Figure II.15a, the FLG feature (~3 nm) is seen on top of the carbonaceous platform (~4 nm) with a part of it touching the bottom Si. Similarly, from Figure II.15b, it was evident that the carbon nanospheres were seen on top of 40 nm thick carbonaceous platform.
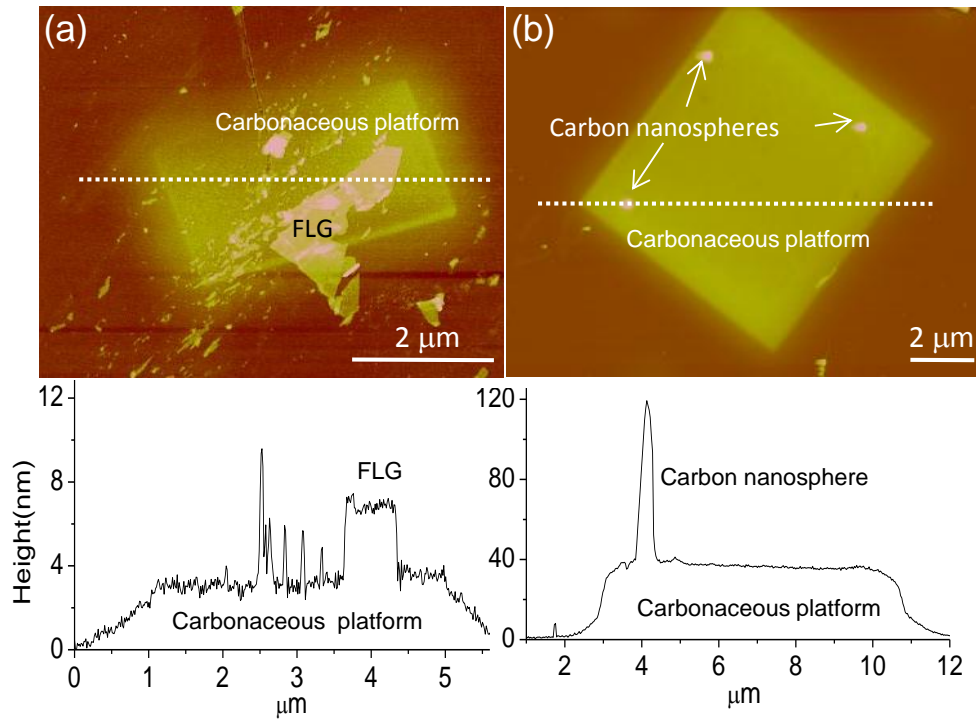
Figure II.15 (a) The AFM image with the corresponding height profile of the carbonaceous deposition (rectangular region) on a few layer graphene (FLG). The extraneous features are smaller chunks of the graphite. (b) The AFM image and the corresponding z-profile showing the lifting of carbon nanospheres on top of the carbonaceous platform.

II.4.3 Graphitization and electrical characterization of EBICD

As the pristine EBICD is insulating and it can be made conducting through thermal treatment. Raman spectroscopy was used as a tool to monitor the graphitization of the EBICD during heat treatment.

The evolution of D and G bands of Raman spectra of the EBICD after annealing at different temperature in air is shown in Figure II.16. At room temperature, the D band appears as a shoulder to the G band. As the temperature increases, the FWHM of both D and G bands decrease and peaks become prominent above 300 °C. The G band appearing at 1561 cm^{-1} at room temperature shifts gradually towards higher frequencies as the temperature is increased to a position finally at 1584 cm^{-1} at 500 ^{0}C, similar as observed by Dillon et al [60]. Defects introduced in the sp^2 carbon network soften the phonon band which is responsible for broadening of the peaks. The upshift of the G band together with its narrowing of the width indicates that the carbonaceous deposit becomes progressively defect free (decomposition of functional groups to form nano-crystalline graphite) at

higher temperatures [60]. As indicated in Figure II.16, I_D/I_G is 0.88 at room temperature and it increases with temperature to reach 1.05 at 500 °C. The thickness of the carbonaceous deposits decreased significantly (up to 20-30%) during heat treatment in air. The significant increase in the I_D/I_G ratio with temperature indicates that the growth of the sp^2 carbon clusters induce graphitic ordering in the carbonaceous deposits [51, 52].
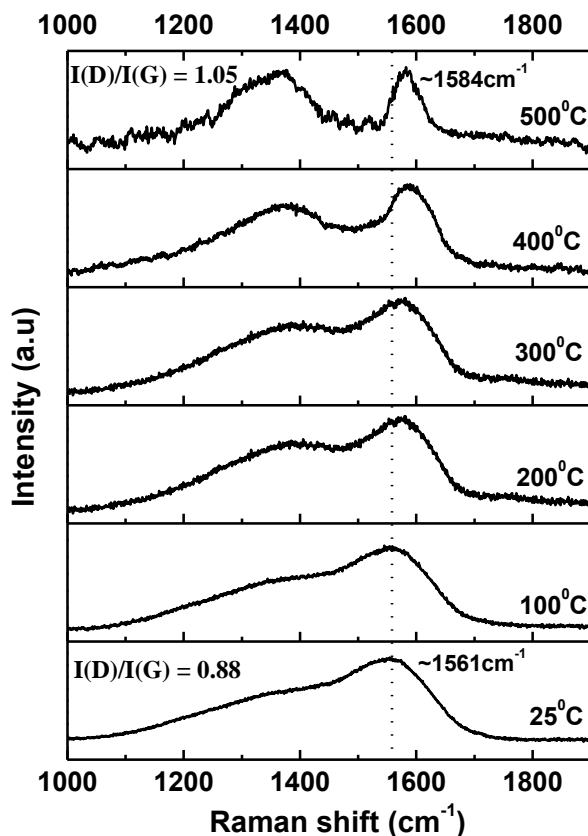
Figure II.16 Raman spectra of EBICD recorded at different temperatures.

It is well known that the thermal treatment in air, converts the solid EBICD into volatile CO and CO_2 gases. In order to prevent the volatilization, the samples were annealed under vacuum conditions at 500 °C for 15 minutes (pressure of 5×10^{-5} Torr). AFM topography shows the presence of nanoparticle domains in the EBICD after vacuum annealing (see Figure II.17a). The increase in the roughness of EBICD is due to decomposition of functional groups after the heat treatment (see Figure II.1b for the AFM topography of the EBICD). The similar behavior is reflected in the TEM analysis (see Figure II.17b). The nano domains are crystalline in nature as evidenced from the hexagonal electron diffraction pattern from the same region (see the inset in Figure II.17b). Therefore,

vacuum annealing of the EBICD leading to the formation of nano crystalline graphitic domains with typical crystallite sizes of 20-30 nm which is consistent with the sizes obtained from Raman studies.

The electrical nature of the pristine and thermally treated EBICD was investigated. The gold contacts (50 nm thick) were established on the carbonaceous platform using shadow mask technique (see inset in Figure II.17c). The I-V data (Figure II.17c) shows a blockade region across zero bias (-2 V to +3 V) and beyond -3V, the curve is slightly asymmetric with current in the range of 20 nA. This behavior is typical of the carbonaceous species produced by e-beam [27] which is usually insulating due to its amorphous state containing several functional groups. The carbonaceous deposits are thermally annealed under vacuum (5×10^{-5} Torr) at 500 °C for 15 minutes. The I-V data changed significantly (Figure II.17c), with current in the range of ~ 1 μA at a low bias of 1 V, which is at least three orders of magnitude higher compared to the pristine deposit [61]. The electrical nature of the pristine carbonaceous deposits has also been examined under ambient conditions with respect to temperature (see top inset in Figure II.17c). The current was monitored with time at a bias of 5 V with increasing temperature. Until 200 ºC, there is no change in the current but at 300 ºC; current value has increased by an order (0.1 μA to 1.3 μA). Further enhancement in the current (at least five times) was observed after heating the sample up to 400 ºC. This can be attributed to the graphitization of carbonaceous deposits above 300 ºC, supporting the temperature dependent Raman studies (Figure II.16) [60].

Thermal treatment can decompose the functional groups to induce graphitization in an otherwise insulating carbonaceous species. As discussed under Figure II.4, the as-deposited EBICD shows broad D and G bands, G band is centered around 1557 cm^{-1}(FWHM, 126 cm^{-1}) (see black curve in Figure II.17d). After vacuum annealing, the position of the G band is upshifted to 1599 cm^{-1} and the FWHM decreases to 76 cm^{-1} (see red curve in Figure II.17d). This upshift in the G band position and smaller FWHM are clear signatures for the growth of nanocrystalline graphitic domains in the carbonaceous deposits after vacuum annealing [52].
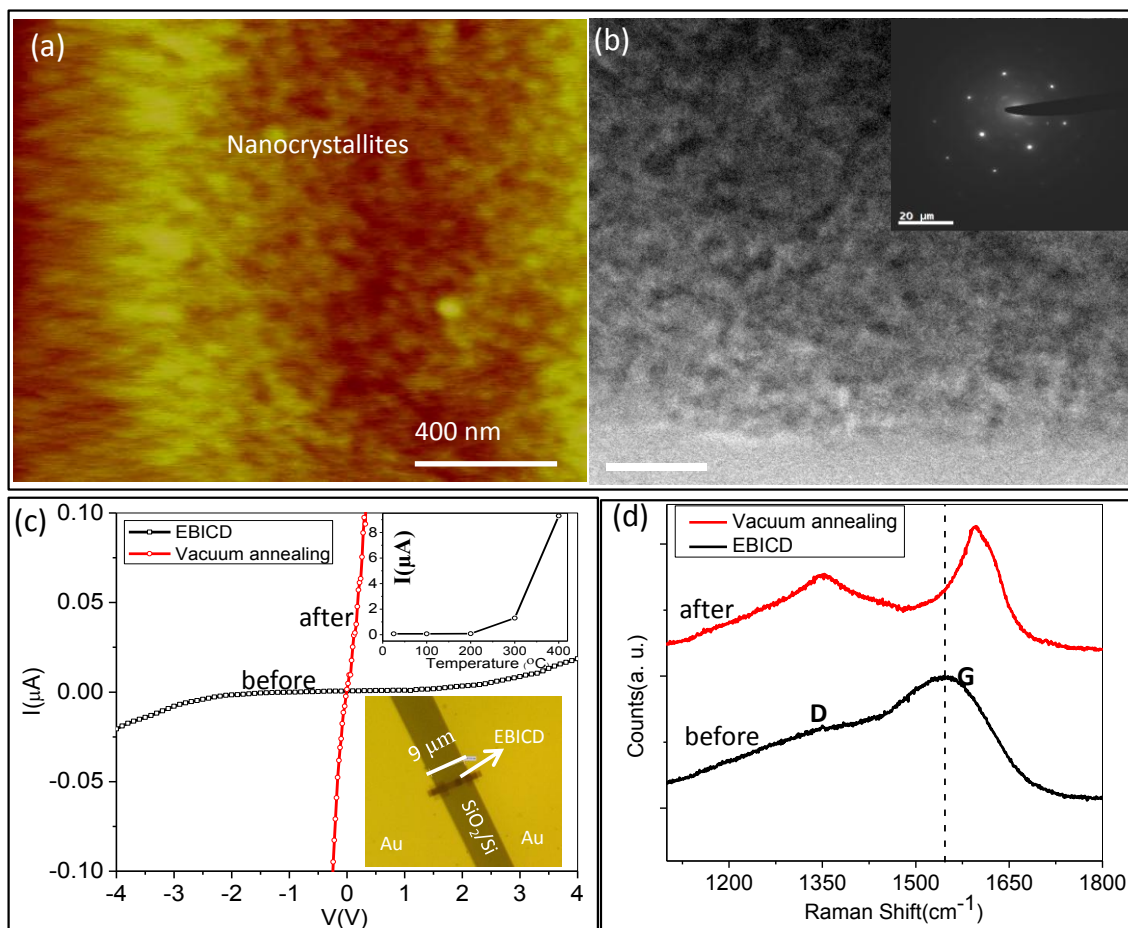
Figure II.17 (a) AFM topography and (b) TEM micrograph of the nanocrystalline domains of the carbonaceous platforms after vacuum annealing. Inset shows the hexagonal electron diffraction pattern from the same region. (c) Two probe I-V measurements of the EBICD between two Au electrodes on SiO_2/Si, before (black curve) and after (red curve) vacuum annealing at 500 ºC for 15 minutes. Top inset shows the increase in the conductance of EBICD with temperature under ambient conditions, bottom inset shows the optical micrograph of the EBICD across the gold pads. (d) Raman spectra for the EBICD before (black curve) and after (red curve) vacuum annealing.

Three terminal electrical transport measurements were performed on vacuum annealed EBICD deposits in the form of stripes between Au source-drain electrodes on SiO_2/Si substrates (Figure II.18). Figure II.18a shows the output characteristics (I_{DS} vs V_{DS}) with varying negative gate voltage (V_G). I_{DS} is increasing with negative V_G; demonstrating the p-type FET operation, similar to the amorphous carbon material deposited by other methods [62, 63]. Four such devices were tried and all exhibited p-type channel behavior with similar low operating voltages. The absence of saturation indicates that the conduction is by hopping rather than extended state transport, across the nanocrystalline

graphitic domains present in the amorphous carbon deposit.
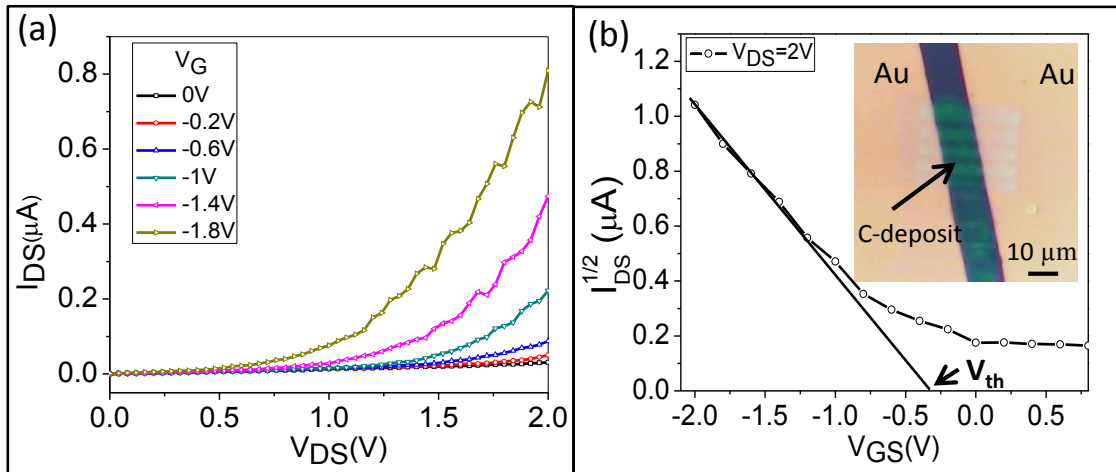
Figure II.18 (a) The output and (b) the transfer characteristics of thermally annealed carbonaceous patterns on a 300 nm SiO_2/Si substrate with Au source-drain electrodes.

Based on the transfer characteristics (Figure II.18b), the hole mobilities were calculated using following formula [64].

$$I_{DS} = (W/2L) \, C_i \, \mu \, (V_G - V_{th})^2 \quad [\text{for } V_{DS} \geq (V_G - V_{th})]....(\text{II.2})$$

where I_{DS} = source-drain current; W = width of the channel, 45 μm; L = length of the channel, 9 μm; C_i = capacitance per unit area, 12 nF cm^{-2}; μ = field effect mobility; V_G = Gate voltage, -0.4 V. A hole mobility of 4 cm^2/V.s was obtained with threshold voltage (V_{th}) of -0.3 V and current on-off ratio (I_{on}/I_{off}) of 20.
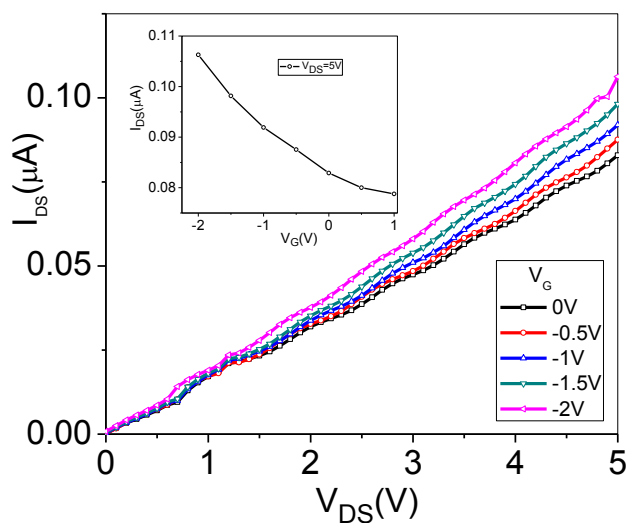
Figure II.19 Output characteristics of the thermally annealed EBICD with bottom Au contacts. Inset shows the transfer curve, p-type behavior with field effect mobility of 0.2 cm^2/V s.

The FET is also made with the bottom contacts to the thermally treated EBICD and the output and transfer characteristics are shown in Figure II.19. The channel current is increasing with increasing negative gate bias, which is also exhibiting p-type behavior with a hole mobility of 0.2 cm^2/Vs. The mobility values of the other two devices were found to be 1 and 2 cm^2/V.s. The varied mobility values in the thermally treated EBICD samples can be attributed to the configuration of the source-drain electrodes (top or bottom contacts), carbon-Au interface and the crystallite size of the graphitic domains.

II.4.4 Selective growth patterns of nanocrystalline graphene from EBICD

In order to transform EBICD into graphene like patterns, a Ni catalyst layer was deposited on the EBICD patterns followed by vacuum annealing and etching away the Ni layer in concentrated HNO$_3$ (see the schematic in Figure II.20a). The Raman spectrum of EBICD (~5 nm thick) on SiO$_2$/Si is shown in Figure II.20b. After deconvoluting the spectrum, D band appears as shoulder to the G band with the positions of the D and G bands centered around 1392 cm^{-1} (line width, 278 cm^{-1}) and 1559 cm^{-1} (line width, 128 cm^{-1}) respectively (see Figure II.20b). The D and G bands are broad with the absence of the 2D band at 2700 cm^{-1} (2D band region was not shown in the given spectrum), indicating that the EBICD obtained under given conditions (see inset of Figure II.20b for its optical image) is predominantly amorphous carbon [51, 52]. Upon Ni deposition followed by vacuum annealing at 1000 °C, due to solubility of carbon in Ni [65-68], the carbon atoms can diffuse through the metal and precipitate as nanocrystallites of graphene on the Ni surface (see the schematic in Figure II.20a). Raman spectra are recorded from the precipitated regions and it is observed that the D (1350 cm^{-1}) and G (1585 cm^{-1}) bands (see schematic in Figures II.20a and c) became significantly sharp (line widths of 90 and 40 cm^{-1} respectively) with the evolution of 2D band at 2690 cm^{-1}. It is noteworthy that the underlying patterns of nc-graphene remained intact on the SiO$_2$/Si substrate after etching away the Ni layer in conc. nitric acid (compare insets in Figures II.20c and d). The corresponding Raman spectrum (Figure II.20d) contained a D band with diminished intensity and a 2D band with slightly higher intensity.
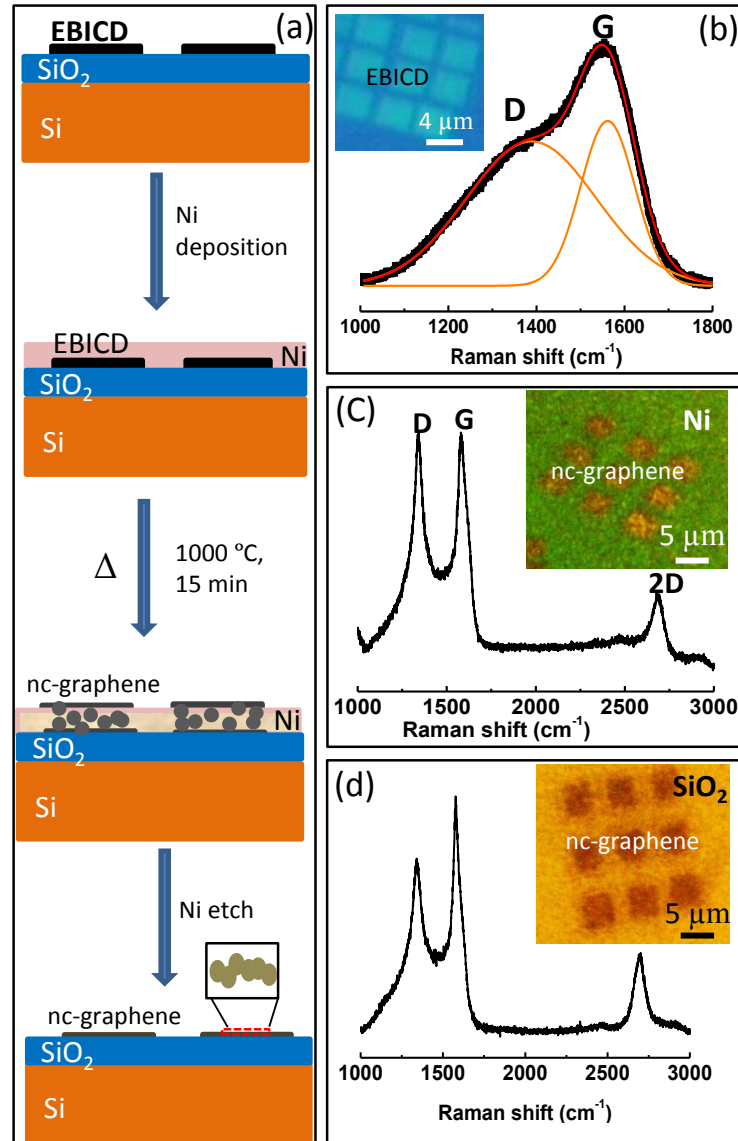
Figure II.20 (a) Schematic illustration of growth of nc-graphene patterns from the EBICD. Each stripe of EBICD is comprised of interconnected nanocrystalline domains of graphene after vacuum annealing in presence of Ni layer. Raman spectra for the as deposited EBICD (b), precipitated nc-graphene patterns on the Ni (b) and SiO$_2$/Si (c) respectively. The corresponding optical micrographs of the EBIC deposits, nc-graphene patterns before and after Ni etching are shown in the insets of (b), (c) and (d) respectively.

The I$_D$/I$_G$ ratio is found to be ~0.6 which corresponds to the average crystallite size of 30 nm [51, 52]. The crystallite size (L$_a$) is calculated using the following formula [52].

$$L_a(nm) = (2.4x10^{-10})\lambda^4(I_D/I_G)^{-1} \quad ....(II.3)$$

where λ is the excitation wavelength. Importantly, the evolution of the 2D band at ~ 2690 cm^{-1} as a single peak with line width of 70 cm^{-1} (see Figure II.20d) signifies the

turbostratic nature of the graphene layers produced by this method [69]. The 2D band intensity is somewhat lower due to the presence of intense D band [70, 71] but this is something typical of nc-graphene [72, 73]. The Raman spectrum looks similar to that of nc-graphene produced by various other methods in the literature. The I_G/I_{2D} ratio is in the range of 2.5-3.5 indicating the presence of regions containing few to multi-layer graphene [74].
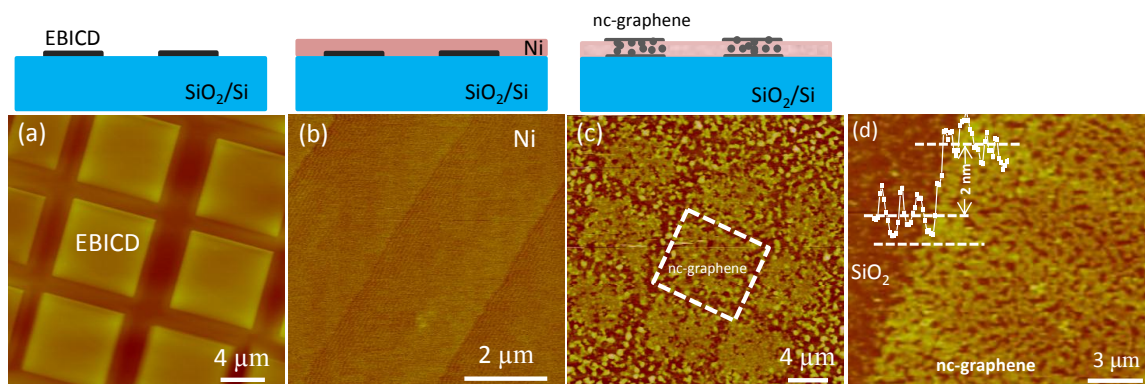
Figure II.21 The top schematic illustrates the process of precipitation of graphene from the EBICD patterns in presence of Ni catalyst layer after vacuum annealing. AFM topography of the EBICD patterns on SiO_2/Si (a), deposition of Ni film over the EBICD (b), precipitation of graphene patterns on the Ni surface after annealing (c). The average thickness of the nc-graphene is 1.5-2 nm, z-profile is shown in (d).

The AFM topography EBIC deposits (thickness, 10 nm) are shown in Figure II.21a. Nickel layer of 30 nm thickness was deposited over the EBIC deposits (see Figure II.21b), followed by annealing at 1000 ℃ for 15 minutes. The graphene has been precipitated over the Ni surface only from the regions of the EBICD (see Figure II.21c). The nickel layer has been etched away using conc. nitric acid and the patterns of nc-graphene remained intact on the SiO_2 surface. The high temperature treatment may be causing stress in the EBICD which lead to nanocrystallites rather than continuous graphene. It appears that during the annealing stage, around half of the thickness of EBICD gets vaporized or precipitated on the Ni surface and remaining amount will be intact as graphene on the SiO_2 surface. Interestingly, the precipitation of graphene occurred only in those regions on the Ni surface where there was a supply of carbon feedstock from the pre-defined EBICD patterns on the SiO_2 surface (see Figure II.21). The Raman spectra of evolution of nc-graphene growth at different temperatures (600-1100 ℃) for a particular thickness (30 nm) of Ni and constant

annealing time of 15 minutes are shown in Figure II.22a.
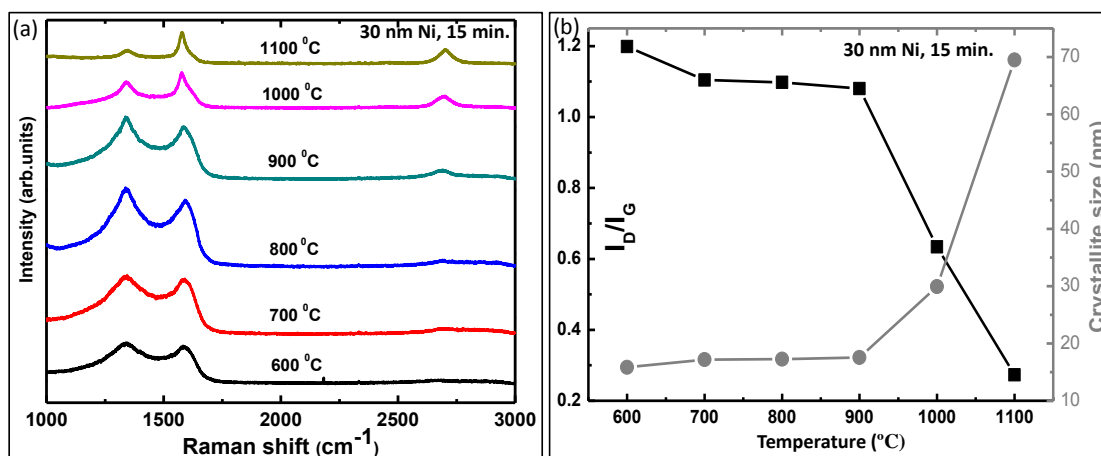
Figure II.22 (a) Raman spectra of the nc-graphene obtained after annealing at different temperatures from 600-1100 ºC (Ni thickness of 30 nm, annealing time of 15 minutes). (b) The crystallite size with I_D/I_G ratio at different annealing temperatures.
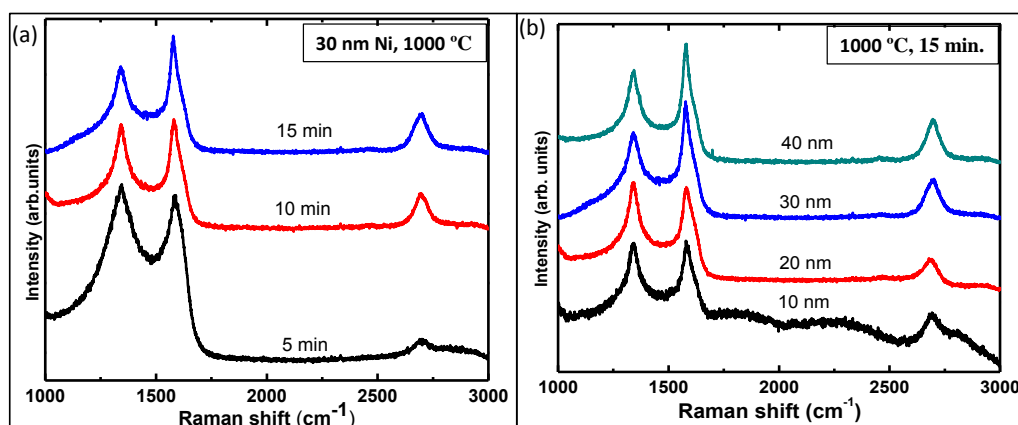
Figure II.23 (a) Raman spectra of the nc-graphene obtained at various annealing times (30 nm Ni, 1000 ºC). (b) Raman spectra of nc-graphene with various Ni thicknesses at annealing temperature of 1000 ºC for 15 minutes.

The I_D/I_G ratio is decreasing from 1.2 to 0.2 with increasing annealing temperature from 600 to 1100 ºC. The crystallite size is also increasing accordingly from 5 to 70 nm (see Figure II.22b). Hence, higher the annealing temperature, larger will be the size of the graphene crystallite.

The growth conditions as a function of annealing time were monitored for particular thickness (30 nm) of the Ni catalyst and constant annealing temperature (1000 ºC) (see Figure II.23a). The role of the thickness of the Ni catalyst layer was monitored in

the growth of nc-graphene at a temperature of 1000 ºC for 15 minutes (see Figure II.23b).
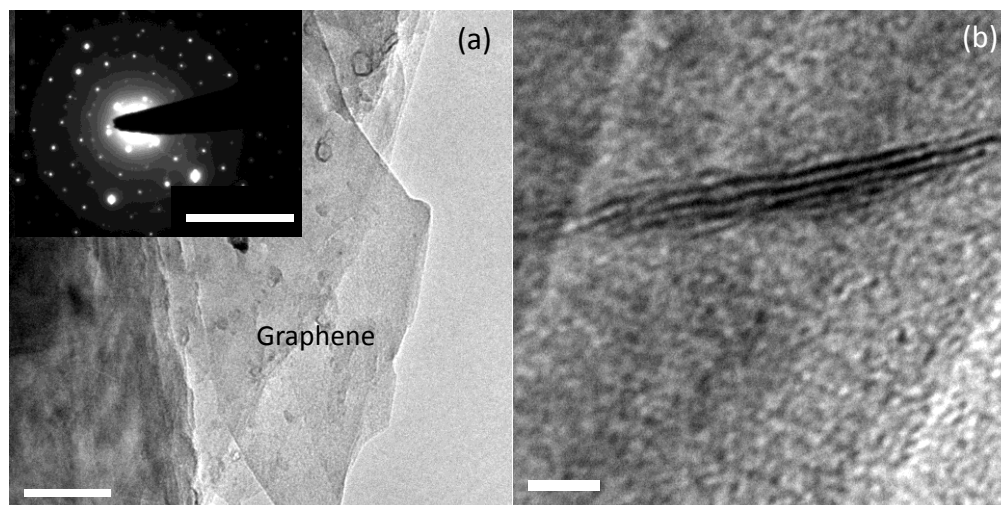
Figure II.24 (a) TEM micrograph of the nc-graphene transferred using PMMA and the inset shows the electron diffraction pattern, revealing the crystalline nature. (b) HRTEM showing 3-4 layers of graphene in nc-graphene.

In order to investigate the micro structure of the nc-graphene, these patterns were lifted off by PMMA via etching away the bottom SiO_2 in buffer oxide solution. Then, the PMMA was thoroughly washed with water and dissolved in acetone. The suspension was dropped onto the TEM grid followed by drying. The bright hexagonal pattern of the diffraction spots clearly indicate the crystalline nature of the nc-graphene (see Figure II.24a). The multiple electron diffraction spots arise due to the randomly oriented graphene layers along the c-direction. The high resolution TEM image shows 3-4 layers of the nc-graphene (see Figure II.24b).

In order to examine the role of Ni in catalyzing the growth of graphene crystallites, an experiment was carried out where Ni deposition was performed over the EBICD in a selective manner using a TEM grid as a shadow mask. The substrate was subjected to thermal treatment at 1000 °C for 15 minutes under vacuum conditions. This is found optimal as longer durations (>15 min) may lead to the decomposition of SiO_2 under vacuum conditions [12, 13].

The optical micrograph of the thermally treated EBICD between two Ni pads is shown in Figure II.25a. The AFM topography of precipitated graphene crystallites on the Ni surface (see inset of Figure II.25a), shows nanocrystalline domains of 20-30 nm wide.

Raman spectra were recorded from the different regions marked as 1, 2 and 3 as shown in Figure II.25b. The 2D band is seen in the spectrum recorded from the Ni/EBICD/SiO$_2$ sample (see spectrum 1) while it is absent in the case of EBICD/Ni/SiO$_2$ (spectrum 2, Figure II.25b) and EBICD/SiO$_2$ samples (spectrum 3, Figure II.25b). Moreover, the spectra '2' and '3' consist of broad D and G bands indicating the amorphous nature of carbon. Thus, it is evident that the Ni capping layer indeed plays a key role in crystallizing the amorphous carbon in EBICD into nc-graphene [68].
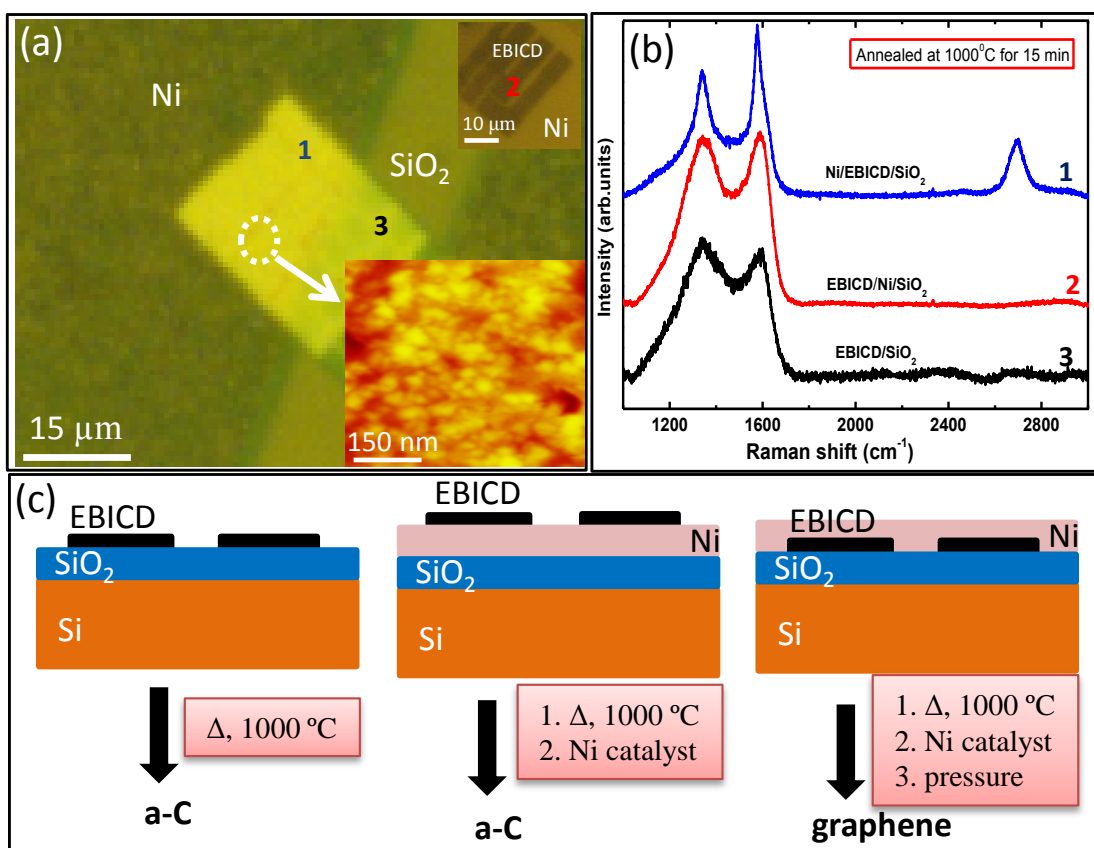
Figure II.25 (a) Optical micrograph showing the regions of precipitated nc-graphene on the Ni surface and amorphous carbon (a-C) on SiO$_2$ surface after vacuum annealing. Top right inset showing the optical micrograph of the annealed EBIC deposits on Ni surface. The bottom right inset shows the AFM topography of the nanocrystallites of graphene. (b) Raman spectra of the annealed samples of EBICD/SiO$_2$, EBICD/Ni/SiO$_2$ and Ni/EBICD/SiO$_2$ indicated with the curves 3, 2 and 1 respectively. (c) Schematic demonstrates the suitable conditions for the growth of graphene form EBICD.

Based on the above observations, the conditions favorable for the growth of graphene from EBICD can be explained as in the schematic in Figure II.25c. The EBIC deposition on SiO$_2$ or on Ni surface (Ni/SiO$_2$), followed by vacuum annealing, leads to the

formation of a-C (see spectra 3 and 2 of Figure II.25b). In the case of CVD grown graphene, it is customary to have the graphene grown over the metal catalyst [75]. However, this represents a scenario where there is constant supply of hydrocarbon in contrast to the present case, where the carbon source as EBICD is limited during annealing. When the Ni layer is deposited on top of EBICD, it results in the formation of graphene following thermal treatment. This provides a strong evidence that Ni is indeed playing two roles, namely, as a capping layer (to build enough pressure and prevent complete volatilization of hydrocarbon species during the heat treatment) and as a catalyst to induce the growth of crystalline sp^2 carbon (see Figure II.26). The contact of the Ni surface to the EBICD without the deposition may not induce the graphitization (see red spectrum, Figure II.26).
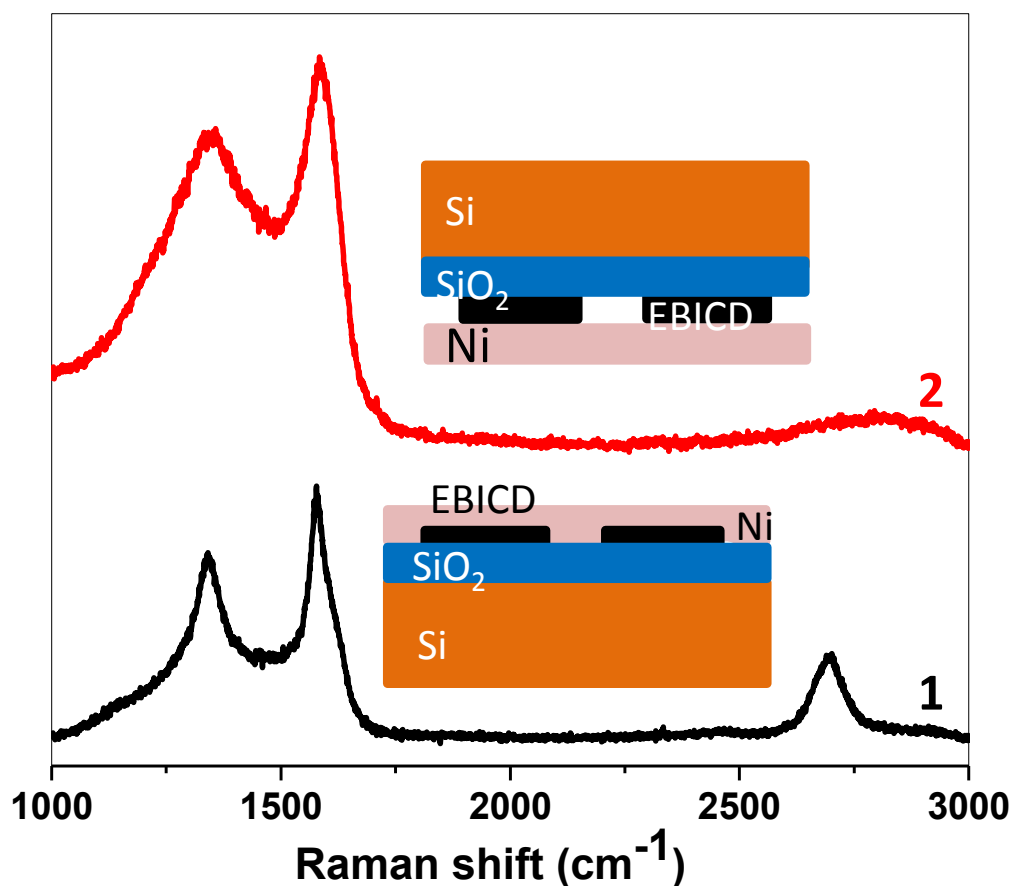
Figure II.26 Raman spectra of the annealed EBICD samples where the Ni is just in contact (red curve) and intimate contact (black curve).

II.4.5 Nanocrystalline graphene based FETs and photodetectors

The AFM topography and the Raman spectrum of the nc-graphene between the Au source-drain contacts are shown in Figure II.27a. Temperature dependence conductivity of the nc-graphene showed linear dependence which is typical of semi-metallic nature (see Figure II.27b). The enhanced electrical transport across the nanocrystalline domains of the graphene is clear from its nonexponential $\sigma(T)$ dependence, similar nature was also observed for the other semi-metallic systems such as nc-graphene obtained from the self-assembled monolayers after annealing at high temperatures [76]. The conductivity of the nc-graphene is varying linearly with temperature and this behavior can be attributed to the 2D weak localization. Transistor characteristics recorded on a device using a nc-graphene strip (24 µm wide) as active element are shown in Figures II.27c and d.
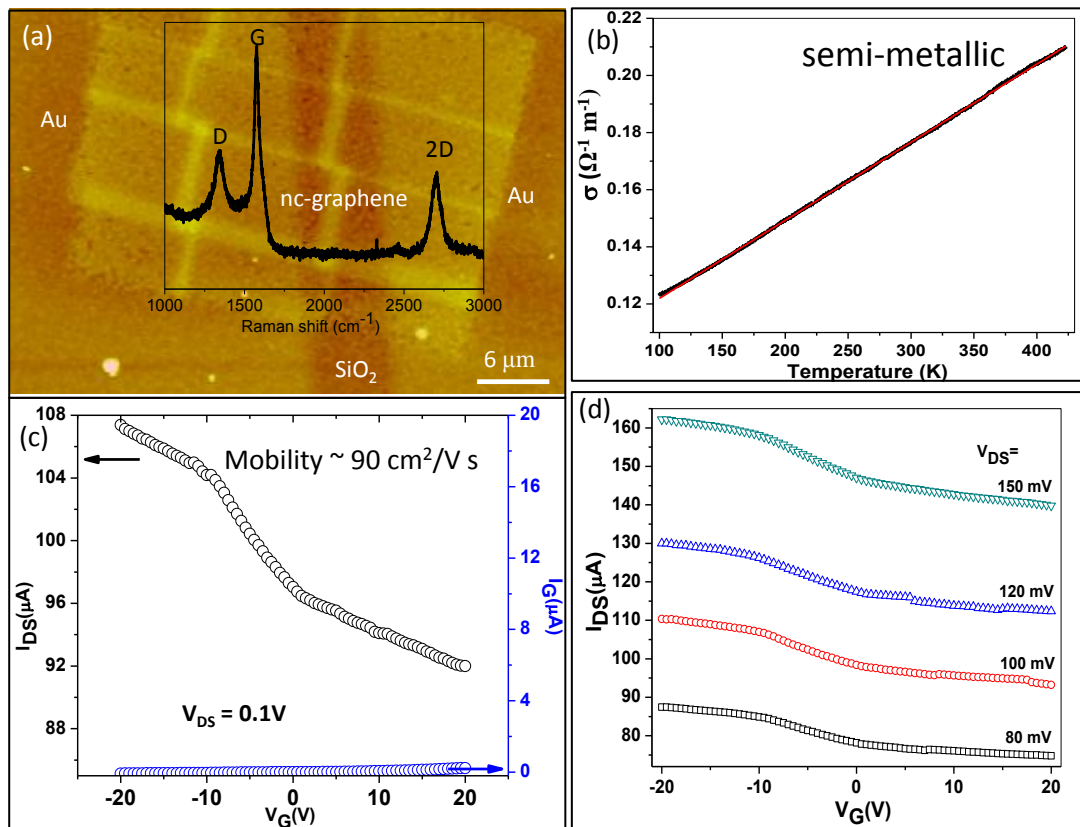
Figure II.27 (a) AFM topography of the nc-graphene (average thickness 1.5-2 nm) between Au source-drain electrodes. The corresponding Raman spectrum, revealing 4-5 layer graphene in the inset. (b) Conductivity versus temperature of the nc-graphene which was obtained after annealing at 1000 ºC for 15 minutes (30 nm thick Ni catalyst layer). (c) and (d) transfer characteristics of the nc-graphene derived from EBICD at different source-drain voltages (V_{DS} of 80, 100, 120 and 150 mV). Blue curve is for the gate leakage current.

In the output characteristics, the I_{DS} (source-drain current) versus V_{DS} (source-drain voltage) curve is linear indicating an ohmic contact between the nc-graphene pattern and the Au electrodes (not shown). This linear behavior is akin to graphene and nc-graphene produced by various methods with the absence of saturation in the currents [65-68, 76]. The transfer characteristics (Figure II.27c) reveal a p-type behavior with holes as charge carriers. The carrier (hole) mobility, μ, was estimated from the channel trans-conductance ($g_m = 4.6 \times 10^{-7}$ A/V) of the FET, $g_m = (dI_{DS}/dV_G) = (W/L)\mu C_o V_{DS}$ in the linear regime of the I_{DS}-V_G curve, where W/L is the width-to-length ratio of the channel and C_o is the gate capacitance per unit area [77]. The W/L for the given device is equal to 4. For 300 nm SiO$_2$, C_o is about 12 nF/cm^2 and based on this value, the hole mobility was derived to be μ_h ∼ 90 cm^2/V s. The gate leakage curve is shown as blue curve in Figure II.27c which is three orders of magnitude lesser as compared to the channel current. The transfer curves for the same device at different source-drain voltages are shown in Figure II.27d. The mobility of nc-graphene depends on the size of graphene crystallites (can be controlled through annealing temperature) and also the interaction of nc-graphene with the bottom SiO$_2$ surface [76, 78].
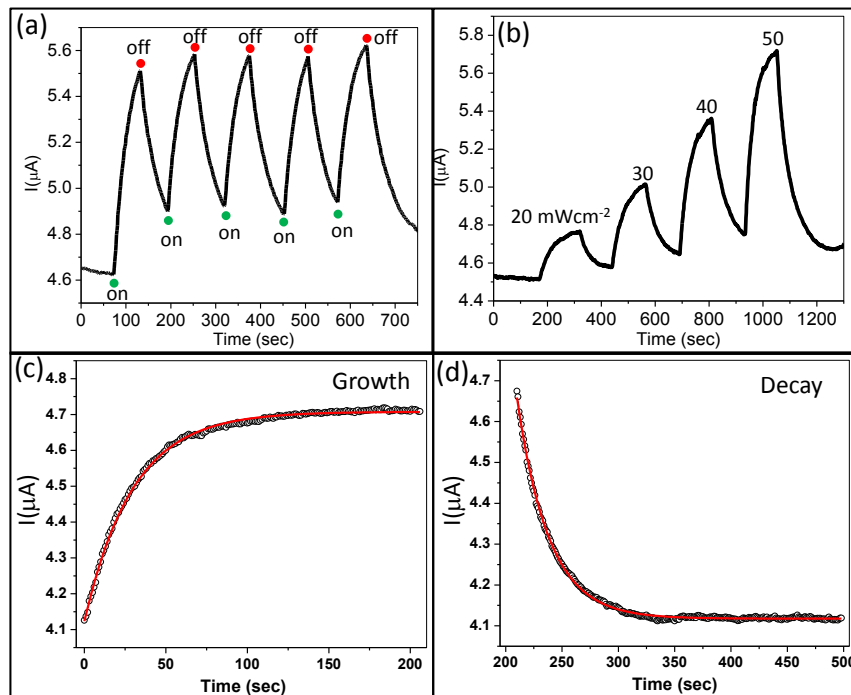
Figure II.28 (a) Photo-response curve for five cycles with turning on and off the IR laser. (b) The photo response behavior for different laser energies. (c) Growth and (d) decay of the photocurrent of the nc-graphene in response to turn on and off of the IR laser.

It has been shown that FETs based on large-area single or few-layers of graphene serve as ultrafast photodetectors [79]. Reduced graphene oxide and graphene nanoribbons have been shown as materials for IR photo detectors [80-82]. The photo-response of the nc-graphene (in 2 probe configuration) towards IR laser (1064 nm) is shown in Figure II.28.
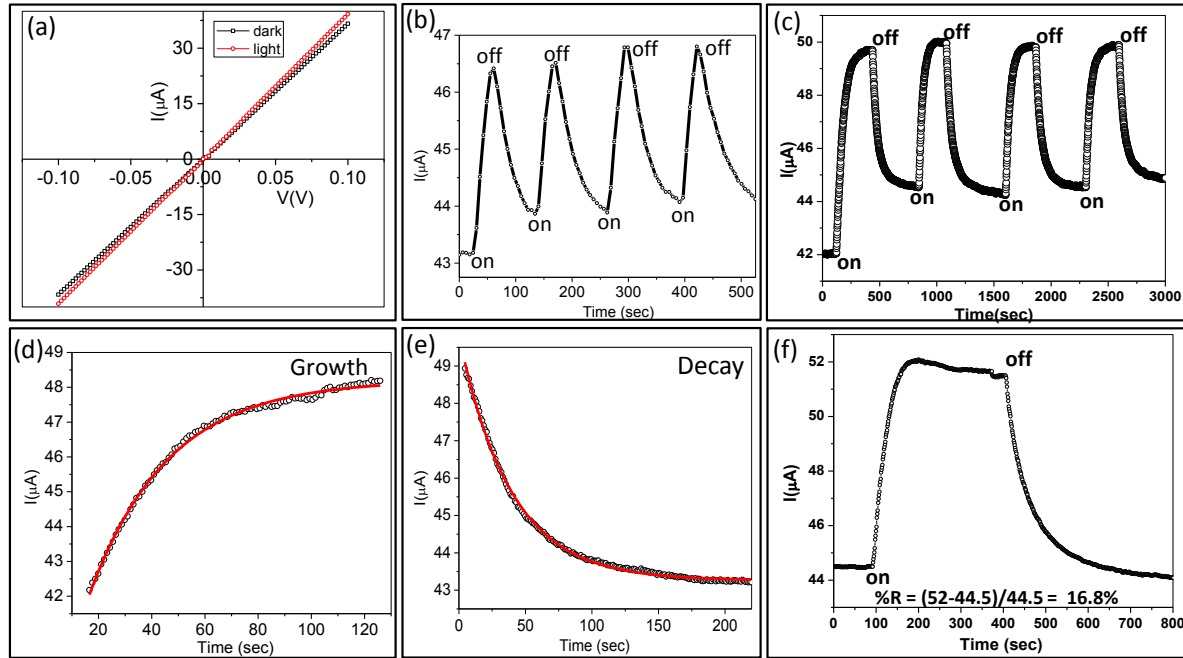
Figure II.29 (a) I-V characteristics of the nc-graphene in the dark (black curve) and illuminated by IR laser (1064 nm) (red curve). The increase in the current is due to absorption of IR radiation, leading to the formation of photoexcited charge carriers. (b) Photo-response curve for four cycles without saturation with respect to turning on and off the IR beam for every 60 seconds. (c) Few cycles with saturation in the photocurrent. (d) and (e) growth and decay of the photocurrent with respect to the turning on and off the IR beam respectively (time constant are found to be 48 and 50 seconds respectively) . (f) Photoresponse of the circuit calculated from one cycle after dividing base current with the difference in the saturated and base current values.

The change in the current was monitored (Figure II.28a) while turning the IR laser on and off repeatedly for five times with a time interval of 60 seconds. Accordingly, there was increase and decrease in the current as the laser beam was turned on and off, respectively. The increase in the base current for every cycle is due to thermal effects after illuminating with the IR beam besides the photoexcitation [80-82]. The photo-response was found to be 23%, calculated after dividing the dark current with change in the current due to IR illumination [79-82]. The photocurrent increased linearly with increasing the laser power (see Figure II.28b). The time constants for the growth and decay of the photo current were

calculated after fitting with the exponential functions (see Figures II.28c and d) and they were found to be 28 and 30 seconds respectively. The time response is much slower for the nc-graphene when compared with the large area graphene which is of the order of pico seconds [79].

Another similar device based on nc-graphene showed a photo-response of 16% (Figure II.29). I-V characteristics of the nc-graphene in the dark (black curve) and illuminated by IR laser (1064 nm) (red curve) is shown in Figure II.29a. The increase in the current is due to absorption of IR radiation by the nc-graphene, leading to the formation of photoexcited charge carriers. The temporal photoresponse with respect to turning on and off the IR beam for every 60 seconds was shown in Figures II.29b and c. The growth and decay of the photocurrent was fitted to exponential functions which were giving rise to the time constants of 48 and 50 seconds, respectively (see Figures II.29d and e). The photoresponse was calculated by dividing base current with the difference in the saturated and base current values (see Figure II.29f). The slower response times of the nc-graphene when compared with the large area graphene devices can be attributed to the presence of disorder and interfaces in the nc-graphene [80]. The scattering of the charge carriers by the traps and boundaries can also lead to a slower time response.
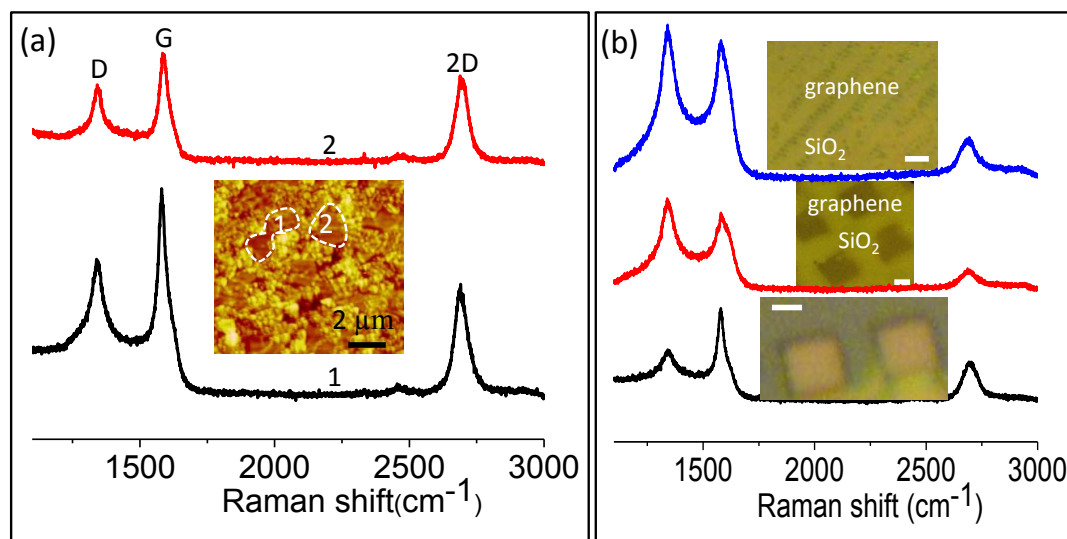
Figure II.30 (a) Raman spectra of the few layer graphene obtained from PMMA after thermal treatment in the presence of Ni capping layer. Inset shows the AFM topography of the graphene flakes over SiO_2/Si. (b) Raman spectra of the graphene patterns on SiO_2/Si obtained from the pre-patterned PMMA films via laser interference, shadow mask and electron beam lithography techniques followed by thermal treatment using Ni catalyst layer. Inset shows the optical micrographs of the graphene patterns. Scale bar, 5 μm.

The formation of graphene and nc-graphene from the films and patterns of PMMA is described in Figure II.30. PMMA films (thickness =10 nm) have been formed on SiO_2/Si substrates through spin coating. A frequency tripled pulsed Nd:YAG laser (Quanta-Ray GCR-170, spectra-Physica, USA. λ=355 nm) of energy 100 mJ/pulse, with a pulse width of ~ 10 ns was used in the single shot mode for the ablative patterning of PMMA [83]. The laser beam was partially defocused towards the PMMA using a 90º TIR prism and a lens with a focal length of 30 cm. All the experiments were performed in ambient conditions of pressure and temperature. The laser fluence was maintained at 1.1 J cm^{-2}. Commercially available compact disk (Sony CD-R) was cleaned with isopropanol and ethanol solvents to remove the dye and Al layer was peeled off using sharp tweezers. The disks were cut into 15x15 mm^2 pieces for use as optical mask. A commercial TEM grid of type G200HS obtained from Ted Pella Inc., USA with a strand width of 15 μm was used as a shadow mask.

Once these films have been patterned via laser interference, shadow mask and electron beam lithography techniques. A piece of compact disc (CD) is placed on top of the PMMA, followed by laser ablation leading to the formation of the 1 μm stripes of PMMA. Another sample of the PMMA film has been patterned by placing TEM grid as a shadow mask followed by laser ablation. Since PMMA is an e-beam resist, it can be patterned by exposing e-beam at higher dosages (e dosage of 1 mC/cm^2) leading to the crosslinking of the polymer chains followed by developing in acetone. Now the above substrates were deposited with a nickel layer of 30 nm thickness followed by vacuum annealing at 1000 ºC for 15 minutes. After etching away the Ni in conc. nitric acid, patterns of graphene remained intact on SiO_2 surface. The Raman spectra of the nc-graphene patterns are shown in Figure II.30b. The presence of 2D band signifies the crystalline nature of obtained graphene. The intensity of D band is high for patterns of nc-graphene compared to the films which is attributed to the incorporation of defects due to laser and e-beam irradiation. I_D/I_G ratio is found to be 1-1.2 and I_G/I_{2D} ratio is 2-3. This indicates that the each pattern region is composed of few to multi-layer graphene.

As evident from this study, the simple method of EBICD which enables nano patterning without the need of an external carbon source can be extended with a following step of vacuum annealing to produce a-C patterns, which serve as active elements in FET

devices. Instead of vacuum annealing, the graphitization of the carbonaceous deposits can also be achieved through Joule heating by passing high currents. This form of a-C may find applications in resistive switching memory where the resistance states can be controlled through the ratio of sp^2/sp^3 carbon bonding through partial graphitization. By introducing suitable organometallic precursors in vacuum during EBICD, the electronic properties of the carbonaceous deposits can be varied through local doping and a-C based p-n junctions can be realized for designing All-carbon based nanoelectronic devices [76]. It is noteworthy to mention that the nc-graphene showed less mobility ($\sim$ 90 cm^2/Vs) when compared with the crystalline carbon nanomaterials (carbon nanotubes, graphene and graphene nanoribbons) produced by various synthesis methods (mobilities >1000 cm^2/Vs). But mobilities of nc-graphene are much higher as compared to a-C based devices. Moreover, nc-graphene produced in this method exhibits higher mobility compared to the nc-graphene produced by other methods (see Table II.1). There are other factors such as density of defects in nc-graphene domains and the electronic coupling among the domains as well as with the source-drain electrodes, which may have a strong influence on the mobility and photo-response behavior. The present investigation has the following merits such as, firstly, it does not require a hydrocarbon source to be connected and consumed in the process; the source is 'vacuum' itself. Degassing and residuals in vacuum can be an ample supply of hydrocarbon. EBICD is a direct way of patterning residual hydrocarbon species into carbonaceous deposits which further can be transformed into graphene patterns with the help of catalytic Ni layer through thermal treatment. This technique offers to obtain graphene patterns with less number of processing steps over the graphene derived from other solid carbon sources in the literature [65-68]. EBICD can withstand even harsh acid and base environments. On the other hand, most polymers suffer from the solubility issues while processing and patterning them on a given substrate. For example, the growth of graphene from PMMA was also demonstrated through thermal treatment in the presence of Ni catalyst layer (see Figure II.30). PMMA requires additional steps for processing and patterning which is not the case for EBICD, although both processes finally lead to similar quality of graphene.

Table II.1 Synthesis of nc-graphene by various methods and their functional applications-examples from literature.

S. No.	Method of synthesis	Carbon source and conditions	Substrates	Applications	Reference
1.	Remote plasma enhancement chemical vapor deposition (r-PECVD)	Pure Methane, 550 ℃ 2h-4h	SiO$_2$/Si, glass, Quartz	Transparent conducting films	Zhang et al. NanoRes. 4, 315, 2011.
2.	Chemical Vapor deposition (CVD)	Methane, H$_2$ 325 ℃-825 ℃ 1h-10 s	MgO	Characterization	Mark et al. Acs Nano, 4, 4206, 2010.
3.	Thermal annealing	Self-assembled monolayers, 1000 ℃, 30 min.	Au surface followed by transferring onto SiO$_2$	FETs, ambipolar (0.01, 0.02, 0.2, 0.5 cm^2/Vs). Max mobility 40 cm^2/Vs Increase in the electrical transport with the growth of graphene crystallites	Turchanin et al. Acs Nano, 5, 3896, 2011.
4.	Carbon molecular beam epitaxy	Pyrolytic carbon, 1100 ℃	Sapphire	Hall effect measurements, Nanocrystalline graphite, mobility ~1 cm^2/Vs	Jerng et al. J. Phys. Chem. C 115, 4491, 2011.
5.	Thermal annealing	SiC, Ni 1100 ℃, 30 s	SiO$_2$	Characterization	Hofrichter et al. Nano lett., 10, 36, 2010.
6.	CVD	C$_2$H$_2$, Ar 750 ℃, 60 min.	Glass	Transmittance of the graphene films on glass	Lee et al. Appl. Phys. Lett., 98, 183106, 2011.
7.	CVD	CH$_4$, H$_2$ 1000 ℃, 30-60 min.	SiO$_2$	FETs, mobility ~ 40 cm^2/Vs	Sun et al., J. Appl. Phys. 111, 044103, 2012.
8.	Microwave assisted surface plasma CVD	C$_2$H$_2$, Ar Power 1.2 kW, 70-120 s	Si, Glass, SiO$_2$	Photovoltaics	Kalita et al., RSC Advances, 2, 3225, 2012.
9.	Thermal annealing	Photo resist pattern, liquid Ga, 1000 ℃	SiO$_2$	FET, mobility ~10^{-3} cm^2/Vs	Fujita et al., J. Vac. Sci. Technol. B, 28, C6D1, 2010.

The other advantage of converting EBICD into graphene is that the thickness of graphene can be well controlled through the initial thickness of EBICD (which in turn can be controlled through e-dosage conditions). The lateral dimensions of the EBICD can be tuned from millimeter to nanometer range using focused and flooded electron beams respectively. The graphene features of different geometrical shapes can also be realized using this technique. By depositing Ni at specific locations on EBICD, one can have domains of nc-graphene and a-C in a desired fashion which may have interesting electronic applications. This technique offers transfer-free growth of graphene on insulating surfaces. Though, the graphene produced in this method is nanocrystalline in nature, the quality of graphene can be improved by coating higher thickness (300 nm) of Ni [65-68].

II.5. Conclusions

The nature of the carbonaceous deposit produced by EBICD is known in the literature. The present study has brought out additional features of the carbonaceous deposit produced by EBICD namely, the weak blue fluorescing nature due to presence of functional groups and the porous nature of the carbonaceous deposit obtained in presence of moisture (low vacuum deposition). The insulating nature of the EBICD was exploited as local dielectric for the fabrication of CNT and graphene circuits. Following one step vacuum annealing, it has been effectively converted to patterned a-C which in turn served as an active channel material in field effect transistors. The FET devices are of p-type behavior with mobilities in the range of 0.2-4 cm^2/Vs. The operating voltages are rather low (~ 2 V). The EBICD has also been transformed into patterns of nanocrystalline (nc) graphene on SiO_2 substrate directly through vacuum annealing using Ni capping layer. Thus patterned nc-graphene has been effectively employed as an active channel material in field effect transistors. The FET devices exhibit p-type behavior with a mobility of ~ 90 cm^2/Vs. Nc-graphene was found to be sensitive to IR radiation and showed a photo response of 23%. Thus, the insulating and conducting nature of the pristine and the treated EBICD may envisage applications in all-carbon electronics [84].

References

[1]   K. Geim and K. S. Novoselov, *Nat. Mater.,* 2007, **6**, 183.

[2]   M. S. Dresselhaus, G. Dresselhaus and P. C. Eklund Science of Fullerenes and Carbon Nanotubes (Academic Press, New York, **1996**).

[3]   J. Robertson, *Prog. Solid State Chem.*, 1991, **21**, 199.

[4]   J. Robertson, *Pure Appl. Chem.*, 1994, **66**, 1789.

[5]   D. Wei and Y. Liu, *Adv. Mater.*, 2010, **22**, 3225.

[6]   J. W. Mintmire, B. I. Dunlap and C. T. White, *Phys. Rev. Lett.*, 1992, **68**, 631.

[7]   A. M. Rao, E. Richter, S. Bandow, B. Chase, P. C. Eklund, K. A. Williams, S. Fang, K. R. Subbaswamy, M. Menon, A. Thess, R. E. Smalley, G. Dresselhaus and M. S. Dresselhaus, *Science*, 1997, **275,** 187.

[8]   K. S. Novoselov, A. K. Geim, S. V. Morozov, D. Jiang, Y. Zhang, S. V. Dubonos, I. V. Grigorieva and A. A. Firsov, *Science*, 2004, **306**, 666.

[9]   Y. – W. Son, M. L. Cohen and S. G. Louie, *Phys. Rev. Lett*., 2006, **97**, 216803.

[10]   X. L. Li, X. R. Wang, L. Zhang, S. W. Lee and H. J. Dai, *Science*, 2008, **319**, 1229.

[11]   P. Zhang, et al., *J. Vac. Sci. Technol. A*, 2002, **20**, 1390.

[12]   M. G. Beghi, et al., *Appl. Phys. Lett.*, 2002, **81**, 3804.

[13]   S. J. Bull, *Diamond Relat. Mater.*, 1995, **4**, 827.

[14]   B. Petereit, et al., *Surf. Coat. Technol.*, 2003*, **648**, 174.

[15]   A. Grill, *Diamond Relat. Mater.*, 2003*, **166**, 12.

[16]   W. Zhang and Y. Catherine, *Surf. Coat. Technol.*, 1991*, **47**, 69.

[17]   A. A. Voevdin and M. S. Donley, *Surf. Coat. Technol.*, 1996*, **82**, 199.

[18]   A. A. Onoprienko and I. B. Yanchuk, *Powder Metall. Met. Ceram.*, 2006**, 45**, 190.

[19]   B. Rother, et al., *J. Mater. Res.*, 1991*, **6**, 101.

[20]   J. Robertson, *J. Mater. Sci. Eng. R.*, 2002, **37**, 129.

[21]   F. Rossi, B. Andre, A. V. Veen, P. E. Mijnarends, H. Schut, M. P. Delplanke, W. Gissler, J. Haupt, G. Lucazeau and L. J. Abello, *Appl. Phys.*, 1994, **75**, 3121.

[22]   L. D. Urso, G. Compagnini and O. Puglisi, *Carbon*, 2006*, **44**, 2096.

[23]   H. W. P. Koops, E. Munro, J. Rouse, J. Kretz, M. Rudolph, M. Weber, and G. Dahm, *Nucl. Instrum. Methods Phys. Res. A*, 1995, **363**, 1.

[24]   C. Schossler, J. Urban and H. W. P. Kopps, *J. Vac. Sci. Technol. B*, 1997, **15**, 1535.

[25]   N. Miura, H. Ishii, J. Shirakashi, A. Yamada and M. Konagai, *Appl. Surf. Sci.*, 1997, **114**, 269.

[26]   W. Ding, D. A. Dikin, X. Chen, R. D. Piner, R. S. Ruoff, E. Zussman, X. Wang and X. Li, *J. Appl. Phys.*, 2005, **98**, 014905.

[27]   K. Narendra, T. Vijay Kumar and G. U. Kulkarni, *J. NanoSci. Nanotechnol.*, 2011, **11**, 1025.

[28]   T. Djenizian, B. Salhi, R. Boukherroub and P. Schmuki, *Nanotechnology*, 2006, **17**, 5363.

[29]   N. Morita, N. Kawasegi and K. Ooi, *Nanotechnology*, 2008, **19**, 155302.

[30]   A. Bachtold, M. Henny, C. Terrier, C. Strunk, C. Schönenberger, J. P. Salvetat, J. M. Bonard, and L. Forró, *Appl. Phys. Lett.*, 1998, **73**, 274.

[31]   Q. Chen, S. Wang and L. -M. Peng, *Nanotechnology*, 2006, **17**, 1087.

[32]   P. Rice, T. Mitch Wallis, S. E. Russek and P. Kabos, *Nano Lett.*, 2007, **7**, 1086.

[33]   Y. G. Wang, T. H. Wang, X. W. Lin and V. P. Dravid, *Nanotechnology*, 2006, **17**, 6011.

[34] M. Wang, J. Wang, Q. Chen and L. –M. Peng, *Adv. Funct. Mater.*, 2005, **15**, 1825.

[35] M. Wang, L. –M. Peng, J. Wang and Q. Chen, *Adv. Funct. Mater.*, 2006, **16**, 1462.

[36] F. Banhart, *Nanolett.*, 2011, **6**, 329.

[37] T. Fujii, M. Suzuki, M. Miyashita, M. Yamaguchi, T. Onuki, H. Nakamura, T. Matsubara, H. Yamada and K. Nakayama, *J. Vac. Sci. Technol. B*, 1991, **9**, 666.

[38] H. W. P. Koops, J. Kretz, M. Rudolph, M. Weber, G. Dahm and K. L. Lee, *Jpn. J. Appl. Phys. Part 1*, 1994, **33**, 7099.

[39] M. –F. Yu, O. Lourie, M. J. Dyer, K. Moloni, T. F. Kelly and R. S. Ruoff, *Science*, 2000, **287**, 637.

[40] S. Kim, J. Kim, M. Berg and A. de Lozanne, *Rev. Sci. Instrum.*, 2008, **79**, 103702.

[41] M. –K. Seo, J. –H. Kang, M. –K. Kim, B. –H. Ahn, J. –Y. Kim, K. –Y. Jeong, H. –G. Park and Y. –H. Lee, *Opt. Express*, 2009, **17**, 6790.

[42] K. Rykaczewski, M. R. Henry and A. G. Fedorov, *Appl. Phys. Lett.*, 2009, **95**, 113112.

[43] N. W. Parker *et al.*, *Proc. SPIE,* 2000, **713**, 3997.

[44] G. V. Pavan Kumar and C. Narayana, *Curr. Sci.*, 2007, **93**, 778.

[45] D. S. Kim, D. Nepal and K. E. Geckeler, *Small*, 2005, **1**, 1117.

[46] H. –J. Shin, et al., *Adv. Mater.*, 2011, **23**, 4392.

[47] P. Roediger, et al., *J. Vac. Sci. Technol. B*, 2009, **27**, 2711.

[48] D. D. Kulkarni, K. Rykaczewski, S. Singamaneni, S. Kim, A. G. Fedorov and V. V. Tsukruk, *ACS Appl. Mater. Interfaces*, 2011, **3**, 710.

[49] S. J. Yumitori, *Mater. Sci.*, 2000, **35**, 139.

[50] K. S. Subrahmanyam, P. Kumar, U. Maitra, A. Govindaraj, K. P. S. S. Hembram, U. V. Waghmare and C. N. R. Rao, *Proc. Natl. Acad. Sci. U.S.A.*, 2011, **108**, 2674.

[51] M. A. Pimenta, G. Dresselhaus, M. S. Dresselhaus, L. G. Cancado, A. Jorio and R. Saito, *Phys. Chem. Chem. Phys.*, 2007, **9**, 1276.

[52] A. C. Ferrari and J. Robertson, *J. Phys. Rev. B.*, 2000, **61**, 14095.

[53] G. Eda, Y. –Y. Lin, C. Mattevi, H. Yamaguchi, H. –A. Chen, I. –S. Chen, C. –W. Chen, M. Chhowalla, *Adv. Mater.*, 2010, **22**, 505.

[54] J. J. O'Dwyer, The Theory of Electrical Conduction and Breakdown in Solid Dielectrics (Clarendon: Oxford, 1973).

[55] A. D. Milliken, A. J. Bell and J. F. Scott, *Appl. Phys. Lett.*, 2007, **90**, 112910.

[56] A. V. Moskalenko, D. J. Burbridge, G. Viau and S. N. Gordeev, *Nanotechnology*, 2007, **18**, 025304.

[57] R. A. DiLeo, B. J. Landi and R. P. Raffaelle, *J. Appl. Phys.*, 2007, **101**, 064307.

[58] S. R. C. Vivekchand, A. Govindaraj, M. M. Seikh and C. N. R. Rao, *J. Phys. Chem. B*, 2004, **108**, 6935.

[59] B. A. Kakade and V. K. Pillai, *J. Phys. Chem. C*, 2008, **112**, 3183.

[60] R. O. Dillon, J. A. Wollam, *Phys. Rev. B*, 1984, **29**, 3482.

[61] K. Rykaczewski, M. R. Henry, S. –K. Kim, A. G. Fedorov, D. Kulkarni, S. Singamaneni and V. V. Tsukruk, *Nanotechnology*, 2010, **21**, 035202.

[62] L. Liao, M. Zheng, Z. Zhang, B. Yan, X. Chang, G. Ji, Z. Shen, T. Wu, J. Cao, J. Zhang, H. Gong, J. Cao and T. Yu, *Carbon*, 2009, **47**, 1841.

[63] P. G. Collins, K. Bradley, M. Ishigami, A. Zettl, *Science*, 2000, **287**, 1801.

[64] M. L. Chabinyc, J. –P. Lu, R. A. Street, Y. Wu, P. Liu, B. S. Ong, *J. Appl. Phys.*, 2004, **96**, 2063.

[65] Z. Yan, Z. Peng, Z. Sun, J. Yao, Y. Zhu, Z. Liu, P. M. Ajayan and J. M. Tour, *ACS Nano*, 2011, **5**, 8187.

[66] Z. Peng, Z. Yan, Z. Sun and J. M. Tour, *ACS Nano*, 2011, **5**, 8241.

[67] H. –J. Shin, et al., *Adv. Mater.*, 2011, **23**, 4392.

[68] S. –J. Byun, H. Lim, G. –Y. Shin, T. –H. Han, S. –H. Oh, J. –H. Ahn, H. C. Choi and T. –W. J. Lee, *Phys. Chem. Lett.*, 2011, **2**, 493.

[69] L. M. Malard, M. A. Pimenta, G. Dresselhaus and M. S. Dresselhaus, *Phys. Rep.*, 2009, **473**, 51.

[70] L. G. Cancado, A. Jorio, E. H. M. Ferreira, F. Stavale, C. A. Achete, R. B. Capaz, M. V. O. Moutinho, A. Lombardo, T .S. Kulmala and A. C. Ferrari, *Nano Lett.*, 2011, **11**, 3190.

[71] A. Jorio, M. M. Lucchese, F. Stavale, E. H. M. Ferreira, M. V. O. Moutinho, R. B. Capaz and C. A. Achete, *J. Phys.: Condens. Matter.*, 2010, 22, 334204.

[72] J. Sun, N. Lindvall, M. T. Cole, T. Wang, T. J. Booth, P. Bøggild, J. Teo, K. B. K. Liu and A. Yurgens, *J. Appl. Phys.*, 2012, **111**, 044103.

[73] C. M. Lee and J. Choi, *Appl. Phys. Lett.*, 2011, **98**, 183106.

[74] A. C. Ferrari, et al., *Phys. Rev. Lett.*, 2006, **97**, 187401.

[75] C. A. Di, D. C. Wei, G. Yu, Y. Q. Liu, Y. L. Guo and D. B. Zhu, *Adv. Mater.*, 2008, **20**, 3289.

[76] A. Turchanin, D. Weber, M. B¨uenfeld, C. Kisielowski, M. V. Fistul, K. B. Efetov, T. Weimann, R. Stosch, J. Mayer and A. G¨olzh¨auser, *ACS Nano*, 2011, **5**, 3896.

[77] Y. B. Tang, et al., *Nano Lett.*, 2009, **9**, 1374.

[78] K. I. Bolotin, K. J. Sikes, J. Hone, H. L. Stormer and P. Kim, *Phys. Rev. Lett.*, 2008, **101**, 096802.

[79] F. Xia, T. Mueller, Y. –M. Lin, A. Valdes-Garcia and P. Avouris, *Nature Nanotechnol.*, 2009, **4**, 839.

[80] S. Ghosh, B. K. Sarker, A. Chunder, L. Zhai and S. I. Khondaker, *Appl. Phys. Lett.*, 2010, **96**, 163109.

[81] B. Chitara, L. S. Panchakarla, S. B. Krupanidhi and C. N. R. Rao, *Adv. Mater.*, 2011, **23**, 5419.

[82] V. Ryzhii, V. Mitin, M. Ryzhii, N. Ryabova and T. Otsuji, *Appl. Phys. Exp.*, 2008, **1**, 063002.

[83] N. Kurra, A. A. Sagade and G. U. Kulkarni, *Adv. Funct. Mater.*, 2011, **21**, 3836.

[84] P. Avouris, Z. Chen and V. Perebeinos, *Nat. Nanotechnol.*, 2007, **2**, 605.

Part III

Atomic Force Microscopy bias nanolithography on carbon surfaces

Summary

This study explores the atomic force microscopy (AFM) bias nanolithography on carbon surfaces. A variety of local electrochemical and physical modifications have been observed under controlled experimental conditions adopted. Carbonaceous platforms can be produced on Si substrates by the technique called electron beam induced carbonaceous deposition (EBICD), discussed in the part-II. AFM bias lithography in tapping mode with a positive tip bias resulted in the nucleation of attoliter water on the EBICD surface under moderate humidity conditions (35-50%). This is essentially electrocondensation of water leading to charged droplets, as evidenced from the electrostatic force microscopy (EFM) measurements. The droplets are highly corrugated and evaporate rather slowly taking several tens of minutes. While the lithography in contact mode with a negative tip bias caused the electrochemical modifications such as anodic oxidation and etching of the EBICD under moderate (45%) and higher (60%) humidity conditions respectively. Finally, reversible charge patterns are created on these EBICD surfaces under low (30%) humidity conditions and investigated by means of EFM.

Electrochemical oxidation and etching of highly oriented pyrolytic graphite (HOPG) has been achieved using biased atomic force microscopy (AFM) lithography, allowing patterns of varying complexity to be written on the top layers of HOPG. The graphitic oxidation process and the trench geometry after writing was monitored using intermittent contact-mode AFM. Electrostatic force microscopy reveals that the isolated mesoscopic islands formed during the AFM lithography process become positively charged, suggesting that they are laterally isolated from the surrounding HOPG substrate. The electrical transport studies of these laterally isolated finite-layer graphitic islands enable detailed characterization of electrical conduction along the c-direction and reveal an unexpected stability of the charged state. Utilizing conducting atomic force microscopy,

the measured I-V characteristics revealed significant non-linearities. Micro Raman studies confirmed the presence of oxy functional groups formed during the lithography process.

III.1 Introduction

Atomic force microscopy (AFM) is a powerful characterization tool for imaging the surface morphology with atomic and molecular resolution [1]. As AFM relies on the local tip-sample forces, it has been employed to study a variety of materials which include conducting, semiconducting and even insulating samples [1, 2]. In addition to surface characterization, AFM has been used to modify the substrate surfaces locally either by application of force or bias [3]. In force assisted AFM nanolithography, the force applied on the tip is larger than for normal AFM imaging which may bring local physical modifications to surfaces via elastic or plastic deformations. Mechanical indentation, scratching, plowing and nanomanipulation come under the category of force assisted AFM nanolithography where the tip-sample interactions are of mechanical in nature [4, 5]. Nanoscale patterning using AFM based surface wetting is well known in the form of dip-pen nanolithography (DPN) [6]. DPN is a direct write lithographic technique in which an AFM tip is inked with molecules of interest. A narrow gap capillary is formed between the AFM tip and the surface which in the ambient atmosphere, leads to the formation of a water bridge, enabling transport of molecules from the tip to the surface, even without an electric field. A vast variety of inks made of small organic molecules, colloids, polymers, biological molecules, and metal ions have been patterned onto surfaces of interest with nanoscale resolution via the DPN process [6-8]. Unlike DPN where water is acting only as a solvent or mediator for molecules, electrochemical DPN utilizes this tiny water meniscus as a nanometer-sized cell in which metal salts can be locally electrochemically reduced into metals and deposited on the surface. Thus, for instance, metallic patterns of Pt, Pd, Cu, Ag and Ge have been fabricated using this technique [9]. The water meniscus which forms at the tip-sample interface has also been employed as an electrolyte to set up a nanoelectrochemical cell under a biased AFM tip. The applied voltage bias of few volts would generate an electric field of 10^9-10^{10} V/m which induces the ionization of water molecules, leading to the generation of oxidative species (OH$^-$, O$^-$) which cause the oxidation of material surfaces locally, known as local anodic oxidation (LAO) [10].

LAO has been employed to fabricate nanoscale oxide features on various materials which include metals, semiconductors and even sometimes insulators [3, 10]. In the case of polymeric films deposited on conductive substrates, the intense fields (10^8-10^9 V/m) can cause dielectrophoretic manipulation of a thin polymer film softened locally due to joule heating to its glass transition temperature [11]. Below the characteristic dielectric breakdown voltage of the polymer, mass transport to the tip takes place producing stable protruded patterns [11-13] or features which decay with time [13], while at higher voltages the polymer can get ablated, producing trenches [12]. Nanoscale explosion and shock wave propagation were also observed in case of polymers and semiconductor surfaces under higher humidity and bias conditions [14]. Besides the above mentioned local chemical modifications, AFM bias lithography has also been employed to write charge patterns on the electret films [15], polymers [16], and fluorocarbon films [17] and recently $LaAlO_3$/$SrTiO_3$ interfaces [18]. Thus, AFM bias lithography became an effective tool to cause various kinds of local modifications depending on the material surface and operating conditions.

AFM based local electrochemical reactions could be exploited to carve the carbon nanostructures precisely in a desired fashion. Carbon layers can either be oxidized or etched at a rate that depends on the strength and polarity of the applied bias, tip scan velocity, tip-sample force, and relative humidity. It is therefore not surprising that scanning tunneling and atomic force microscopes have been used to pattern graphene nano ribbons from graphene flakes [19, 20]. A number of other scanning probe nanofabrication approaches have reported work on HOPG with a variety of empirical observations and proposed etching mechanisms [21-24]. AFM has also been used to fabricate single-wall carbon nanotube charging devices and to cut multi-walled carbon nanotubes [25, 26]. Graphene nanodevices were fabricated in the form of nanoribbons, nanorings and quantum dots using AFM bias lithography and further investigated their electrical transport behaviors [27-30]. AFM bias lithography has also been employed to modify the various amorphous carbon films locally [31, 32]. Hence, it is always interesting to modify carbon surfaces via electrophysical/chemical ways to derive local functionality.

As this study is about AFM bias lithography, a brief note on the basic modes of performing lithography is in order. AFM bias lithography can be performed either in contact or dynamic modes (see Figure III.1). During the contact mode operation, as the tip is in intimate contact with the sample surface, the normal force remains same throughout. Once, the voltage bias is applied, it results the electrolytic dissociation of the water meniscus giving rise to the constant ionic current during the lithography process (see Figure III.1a). When contact mode is used, the tip-substrate force is preset to a value of 5-10 nN. But in the tapping mode, as the tip is half the time in contact with the sample surface, a normal force varies periodically. Upon application of bias, the ionic current profile will look similar to that of the normal force profile (see Figure III.1b). Under the given experimental conditions, it is possible to estimate theoretically the peak tip-substrate force when the tip comes into intermittent contact with the HOPG substrate. Using the VEDA AFM simulation tool [23], the tip-substrate force estimated to be approximately 6 nN (see Figure III.1c).
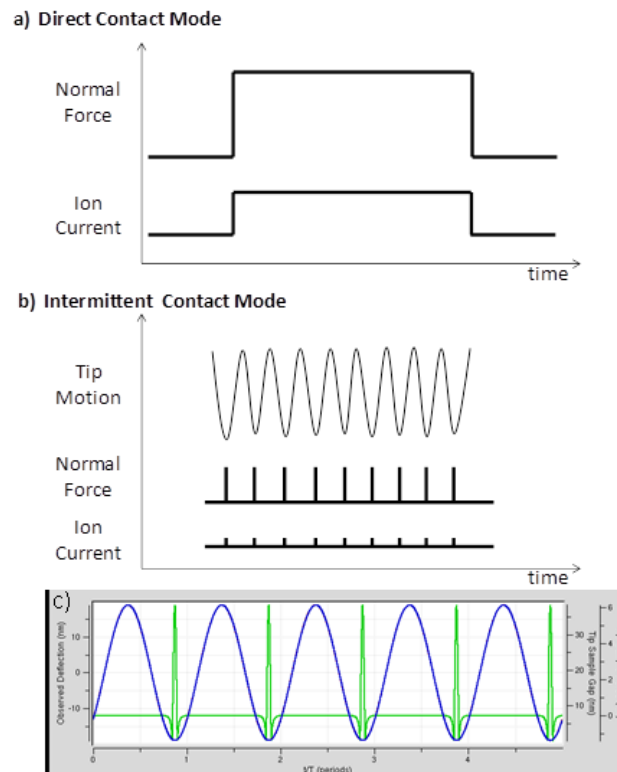

Figure III.1 A schematic diagram showing the difference between (a) contact mode bias lithography and (b) intermittent contact bias lithography. (c) peak force plot for the intermittent contact bias lithography, simulated using VEDA software tool.

III.2 Scope of present investigation

In most of the AFM based lithography techniques, either water mediates an interaction or a reaction, but need not be part of the final product itself; its presence is often inferred only from the tip-surface interaction forces [34, 35]. Indeed, there are many experimental as well as theoretical reports on water bridge formation, relating to cantilever dynamics and meniscus forces [36-38]. Water meniscus formation between a tip and a surface has been directly visualized using environmental SEM [39, 40]. Only under high humidity conditions on a highly hydrophilic surface (such as mica) stable water droplets can be deposited from an AFM tip [41]. Else, the droplets disappear instantly, not accessible to the present day AFM, which takes typically several minutes for imaging [42]. The present investigation is about how a biased AFM tip on carbonaceous platform is able to induce charged water condensation which could be imaged through its evaporation for several minutes. The carbonaceous platforms are created by the exposure of focused electron beam on a surface in the presence of abundant residual hydrocarbons within the scanning electron microscope (SEM) chamber. The unique and diverse surface properties of EBICD have been reflected by employing AFM bias lithography under different operating conditions such as mode of operation, tip bias polarity and humidity. A positively biased AFM tip in the tapping mode under moderate humidity conditions (40-45%) could nucleate the attoliter water on the EBICD surface. The carbonaceous platforms are chemically robust and electrically insulating which can preserve the charge and minimize the effects of electrolytic decomposition, particularly at high tip voltages. Besides water condensation, electrochemical oxidation, etching and charge writing have also been observed on these carbonaceous platforms under specified experimental conditions. Lithography in the contact mode with a negative tip bias bring in the electrochemical modifications such as anodic oxidation and etching of the EBICD under moderate (45%) and higher (60%) humidity conditions respectively. Reversible charge patterns are created on these EBICD surfaces under low (30%) humidity conditions in contact mode.

AFM bias lithography on conducting carbon surfaces such as highly oriented pyrolytic graphite (HOPG) resulted in the electrochemical oxidation and etching, allowing

patterns of varying complexity to be written into the top layers of HOPG. This technique was utilized to carve isolated graphitic regions, named as mesoscopic graphitic islands (MGIs). EFM reveals that isolated mesoscopic islands formed during the AFM lithography process become positively charged, suggesting that they are laterally isolated from the surrounding HOPG substrate. The electrical transport studies of these laterally isolated finite-layer graphitic islands enable detailed characterization of electrical conduction along the c-direction and reveal an unexpected stability of the charged state. Using cAFM, the measured I-V characteristics revealed significant non-linearities. Micro Raman studies confirm the presence of oxy functional groups formed during the lithography process.

III.3 Experimental details

The HOPG used in our experiments was purchased from NT-MDT, ZYB grade and was characterized by a mosaic spread of ~0.8°. Before scanning, a clean HOPG surface was freshly prepared by stripping away a few layers using the conventional sticky tape technique.

Silicon substrates of 1x1 cm^2 dimensions are cut from the n-type Si wafer ($\rho = 4 - 7$ Ω.cm) followed by cleaning through sonication in acetone, ethanol and double distilled water for 5 minutes. Electron beam induced carbonaceous deposition was performed in the environmental mode making use of the residual hydrocarbons present in the vacuum chamber of SEM. AFM imaging and bias lithography were performed at room temperature employing a Dimension 3100 SPM with a NS-IV controller (Veeco, USA). Both intermittent contact (dynamic AFM) and direct contact scanning modes where used. During the lithography, the feedback is turned off, and the lateral specific movements and the Z-position of the tip were adjusted using the "Nanoman Software". The depth of the trenches has been controlled by the experimental conditions such as mode of operation, tip bias, amount of the force (Z- position) and relative humidity.

Metalized Pt/Ir coated Si cantilevers with a nominal spring constant of 2.2 N/m and resonance frequency of 75 kHz (Veeco Model, SCM-PIT) were used for tapping mode AFM. For contact mode work, Pt/Ir coated Si cantilevers (Veeco Model SCM-PIC) with a nominal spring constant of 0.2 N/m and resonance frequency of 16 kHz were used. Where

required, Sader's method was used to measure the precise spring constant of the cantilever [43]. Typically, a set point in the 5-10 nN range is used during contact mode lithography. In intermittent contact scans, the free amplitude cantilever oscillation was set to 35-47 nm when the tip is far from the substrate. Tapping mode imaging and lithography were performed with a set point amplitude ratio of 50-60%. The tip-substrate force was estimated using the VEDA AFM simulation tool [33]. Unless stated otherwise in the text, the tip velocity used while electrochemically writing a feature was 0.5 μm/s. A bias voltage could be applied to the metalized AFM tips using the AFM controller electronics and a controllable negative tip bias ranging up to -12V was applied duringlithography with the substrate at ground potential. The majority of the experiments were carried out in a clean room under ambient conditions (relative humidity = 30-50%, temperature = 22 ℃).

EFM was performed using a biased conducting tip coated with a 20 nm layer of Pt/Ir evaporated on top of a thin 3 nm Cr adhesion layer. The electrostatic force was detected as a phase shift in the cantilever response with respect to the diether piezo drive signal as measured after performing a topographic line scan and then lifting the tip by an additional height of 60 nm. For a cantilever operating near resonance, a fixed bias voltage applied to the tip causes an attractive (repulsive) electrostatic force producing a frequency shift to lower (higher) frequencies and resulting in a negative (positive) phase shift of the cantilever that depends on the magnitude of the electrostatic force gradient. By adjusting the voltage on the tip until the phase shift vanishes, it is possible to estimate both the magnitude and polarity of the electrostatic potential difference between the tip and a local region on the substrate.

Another useful technique employed in this study is conducting atomic force microscopy (cAFM) using Pt/Ir coated Si tips operated in contact mode on an Innova AFM (DiInnova, Bruker). The conducting tip is brought into contact with the substrate until a preset loading force is reached. The bias voltage on the sample is then varied while the resulting current is measured. This technique provides useful information about the local I(V) characteristics of a sample under study, but the data include any unknown contact resistance that may develop between the tip and substrate. For this reason, it is important to use clean tips to minimize unwanted contact resistance effects.

III.4 Results and Discussion

III.4.1a Tip-substrate interactions

It is necessary to examine the nature of tip-substrate interactions under the experimental conditions employed in order to exercise the optimized or favorable cases to achieve desired local modifications. The contribution of the electrostatic force during the AFM bias lithography can be estimated by taking into account two contributions: (i) the electrostatic force (F_{tip}) that develops between the tip apex and the substrate and (ii) the electrostatic force exerted by the cantilever (F_{cant}) due to the applied bias [44]. For the tip apex, the electrostatic force was modeled by using a planar capacitor model

$$F_{tip} = \frac{\varepsilon_o A V^2}{2d^2}$$ …………. (III.1)

where ε_o is the dielectric constant, A is the effective tip-substrate contact area, V the applied bias voltage, and d the gap between the tip and the sample. Assuming a reasonable value for the contact area A of 240 nm^2 (tip radius, 20 nm) and a minimum tip-substrate air gap d of 0.5 nm, a bias voltage of 8 V produces an additional applied force of 250 nN.

The cantilever force F_{cant} is calculated in much the same way, but a small tilt angle α is included to account for the tilt between the cantilever and the sample surface [44]. For small angles ($\alpha \approx 20°$), F_{cant} can be described by:

$$F_{cant} = \frac{\varepsilon_o b \ell_c V^2}{2\left(\ell_t^2 + \ell_c \ell_t \tan \alpha\right)}$$ ……….. (III.2)

where b and ℓ_c are the width and length of the cantilever, respectively, and ℓ_t is the length of the tip. For the cantilevers used here (Veeco SCM-PIT intermittent contact: $\ell_c = 225\pm25$ μm, $b = 50\pm5$ μm, $\ell_t = 12.5\pm2.5$ μm or Veeco SCM-PIC contact: $\ell_c = 450\pm45$ μm, $b = 28\pm5$ μm, $\ell_t = 12.5\pm2.5$ μm), The estimated forces are less than 3 nN at an applied bias voltage of 8 V. Based on these estimates, the dominant force during intermittent contact nanolithography is ~250 nN due to the electrostatic force between the tip apex and the

grounded substrate. For a nominal tip radius of ~10 nm, this force can easily exert pressures greater than a few tens of GPa in the tip-contact region. The mode of AFM operation (direct contact or intermittent contact) has great influence over the electrochemical etching process because the modification to the surface relies on a variety of parameters that include the duration and strength of electric field, the ionic current in the tip-sample gap, and the tip scan velocity.

III.4.1b Condensed water bridges formed between tip and substrate

The water bridge that forms between the tip and substrate plays a crucial role in any AFM-based nanolithographic process and for this reason; it is useful to review some of the underlying principles and the standard equilibrium theory that are believed to describe its formation. The general principles underlying the formation of the water bridge seems clear enough. The molecular structure of water at the interfaces determines the wetting phenomena such as hydrophilicity and hydrophobicity which are fundamental in biology and in materials sciences [45].

All surfaces when exposed to humid air quickly acquire a thin layer of water molecules with a thickness (h) that depends on relative humidity (RH). The thickness of the water layers measured under controlled conditions can be inferred from attenuated total reflection-infrared (ATR-IR) spectroscopy, transmission Fourier transform IR, ellipsometry, X-ray photoelectron spectroscopy (XPS), and mass up-take measurements. The fractional coverage can be described by a Brunauer, Emmett and Teller (BET) model for multilayer adsorption with an adjustable constant to describe the strength of the water-substrate interaction [46]. ATR-IR measurements indicate the mean thickness of water layers on SiO_2 substrates that are on the order of ~1nm thick at relative humidity near 50% [47, 48].

When a spherical tip comes into close proximity to a substrate, the surface water layers coating the tip and substrate merge to form a water bridge with an air-liquid interface that assumes a characteristic crescent shape (see Figure III.2). The crescent-shaped curvature of the water meniscus is of fundamental interest since it reflects the strength of molecule-molecule interactions within the liquid. An expenditure of energy in the form of work is necessary to move a molecule from the interior of the liquid water bridge toward the water-air interface. If a water molecule moves from the liquid (molecular

density of $\sim 3 \times 10^{22}/cm^3$) into the vapor (molecular density of $\sim 2 \times 10^{19}/cm^3$), work must be expended to overcome a net inward force of attraction due to the vastly greater number of water molecules in the liquid. This work adds additional potential energy to molecules on the surface, making their potential energy greater than those embedded in the interior of the liquid. However, in stable equilibrium, the system must have a minimum in potential energy. In order to achieve this condition, the water-air interface minimizes its surface area, thereby minimizing the number of high potential molecules at the surface. Thus, in equilibrium, the shape of the interfacial surface of the water bridge is said to be a minimal surface bounded by fixed arbitrarily-shaped boundaries that are imposed by the geometry of the tip apex and the substrate. A minimal surface develops with a shape governed locally by the principle of area-minimization. The final result is an interface having the smallest area consistent with the largely unknowable, fixed boundary conditions.
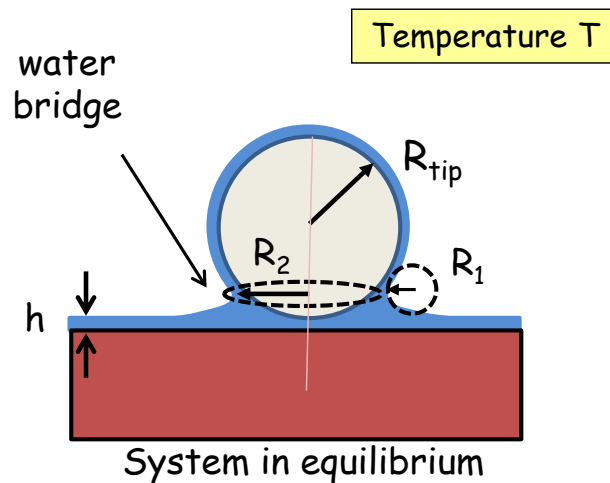
Figure III.2 A diagram schematically illustrating the water bridge that forms when a spherical tip is brought close to a flat substrate. The case when the tip is in contact with the substrate is illustrated.

The standard theory of liquid interfaces predicts a pressure difference across the liquid-vapor interface of the water bridge given by the Young-Laplace equation

$$\left(P_{in} - P_{out} \right) = \gamma \left(\frac{1}{R_2} + \frac{1}{R_1} \right) \quad \ldots\ldots\ldots \text{(III.3)}$$

where γ is the surface tension of water at room temperature (γ=0.072 J/m^2 for bulk water) and R_1, R_2 are the radii of the curved surface (in meters) along any two orthogonal directions. The Young-Laplace equation relates the pressure discontinuity at a given point on a curved interface to the product of the local value of surface tension and the mean curvature $\left(\dfrac{1}{R_2}+\dfrac{1}{R_1}\right)$ of the interface. Since $|R_1|$ is typically much smaller than $|R_2|$, the sign conventions for the radii of curvature dictate that the internal pressure inside the water bridge is less than the pressure of the ambient vapor. Again, according to the standard theory of liquid interfaces, any curvature in a liquid causes a change in the equilibrium vapor pressure of the liquid from the vapor pressure existing over a flat liquid surface at the same temperature. This effect is traditionally described by the Kelvin equation

$$\frac{R_{gas}T}{V_{mol}}\ln\left(\frac{P^c_{vap}}{P^f_o}\right)=\gamma\left(\frac{1}{R_1}+\frac{1}{R_2}\right)=P_{Laplace} \quad\ldots\ldots\ldots\ldots \text{(III.4)}$$

where R_{gas} is the universal gas constant (R_{gas}=8.314 J/(K·mol)), T is the absolute temperature in Kelvin, V_{mol} is the molar volume (V_{mol} (H$_2$O) = 18 cm^3/mol for bulk water), P^c_{vap} is the vapor pressure of water above the curved surface, and P^f_o is the vapor pressure of water measured above a flat surface. Equilibrium water vapor saturation (relative humidity) is assumed to set the ratio $\dfrac{P^c_{vap}}{P^f_o}$. The right hand side of the equation contains geometric terms already defined above. According to this theory, when the water bridge forms, R_1 and R_2 dynamically change until equilibrium with $\dfrac{P^c_{vap}}{P^f_o}$ is established and the Kelvin equation is satisfied. For water at room temperature, the constant $\gamma V_{mol}/R_{gas}T$ = 0.52 nm and this constant sets the length scale for the effective radius R_{eff} defined as

$$\frac{1}{R_{eff}}\equiv\frac{1}{R_1}+\frac{1}{R_2}=\ln\left(\frac{P^c_{vap}}{P^f_o}\right)\bigg/0.52 \quad\ldots\ldots\ldots \text{(III.5)}$$

Even though the volume of liquid in the water bridge is quite small, in equilibrium, when vapor evaporation and vapor condensation equilibrate, the water bridge will stabilize once R_{eff} satisfies the equation given above for a specified humidity.

Lastly, the non-zero Laplace pressure difference, $P_{Laplace}$, defined above acts over the lateral area of the liquid neck which has an area approximately equal to $\pi R_2{}^2$. This develops an additional, uncontrollable capillary adhesion force of ~10-50 nN that pushes the tip toward the substrate whenever the water bridge forms [47, 49, 50]. This additional adhesive force must be added to any tip-substrate attractive force while executing nanolithography.

While the standard theory discussed above enjoys a long history, is widely cited, and is generally accepted, it is nevertheless worthwhile to review how expectations match AFM-based liquid bridge experiments and whether bulk values for the various parameters like surface tension can be used to adequately describe the properties of small liquid bridges. Furthermore, using the water bridge to perform local electrochemistry requires an electric field between the tip and substrate, a factor not included in the above discussion. In the following sections, recent experimental evidence regarding the formation and dimensions of the water bridge between an AFM tip and a substrate will be summarized. The nascent meniscus formed by a tip at its closest contact with the substrate is independent of the tip geometry and wettability. In general, the meniscus becomes smaller when the temperature is raised.

III.4.1c Estimation of water meniscus

Figure III.3 provides direct evidence for both long-range electrostatic interaction forces as well as water meniscus formation when the tip is biased. Useful information can be obtained by monitoring the cantilever deflection as the substrate is approached in both the direct and intermittent contact modes of operation. The biased AFM tip can enhance the condensation of water at the tip substrate interface due to electrostatic attraction of polarized water molecules, a process often referred to as field enhanced water condensation [51]. As a result, the biased AFM tip can experience two attractive forces, electrostatic and capillary. In Figure III.3a, the increase in lift-off force as the tip bias is increased indicates the formation of a water meniscus. The Z-hysteresis upon retraction increased from 93 nm to 150 nm as tip bias increased from 0 to -5V (see Figure III.3a). As

shown in Figure III.3b, evidence for long-range attractive electrostatic forces is evident from amplitude-displacement data at different tip biases using tapping mode AFM. Taken together, the data presented in Figure III.3 provide confirming evidence of bias-induced water condensation and long-range electrostatic interactions between the tip and substrate.
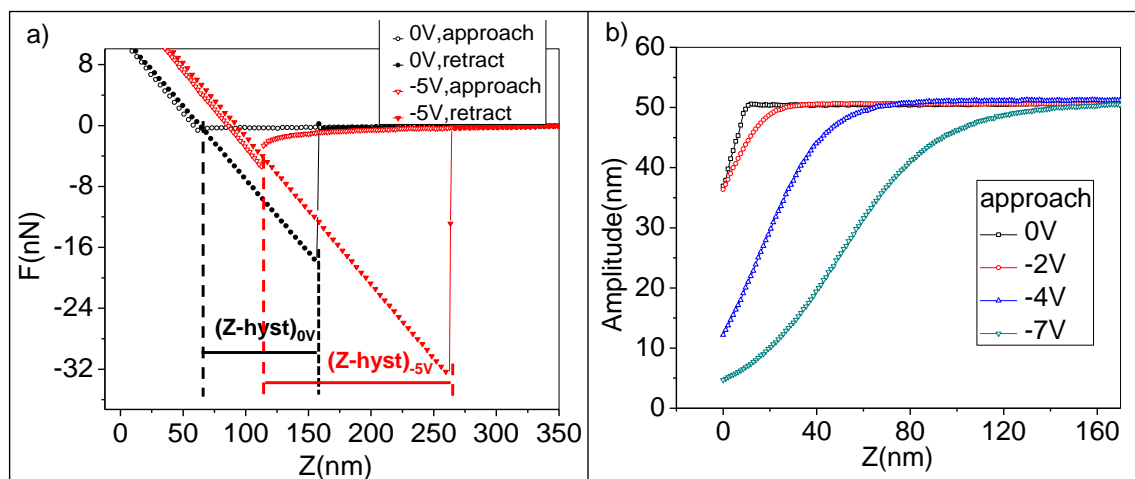
Figure III.3 Evidence for the formation of a water neck can be found in both the static and dynamic force and amplitude vs. displacement data.

III.4.2 Nucleation of water patterns under the electric field

The asymmetry of a water molecule leads to an electric dipole moment that lies in the symmetry plane of the molecule. The dipole moment points toward the more positive hydrogen atoms and has a measured magnitude of 6.2×10^{-30} C·m = 1.8 D, resulting in a very polar liquid with a high dielectric constant (κ=80). Water molecules can be easily manipulated or controlled *via* external applied electric fields. As an example, water molecules tend to become aligned in high electric fields. As a result, the molecular rotational kinetic energy decreases as well as the diffusivity. These effects change the free energy of condensation and facilitate the nucleation of ice layers on the surface of electrified wires [52].

The carbonaceous platforms on Si substrate were chosen for performing the AFM bias lithography. These carbonaceous platforms are created by the technique called electron beam induced carbonaceous deposition (EBICD). Briefly, the abundant residual hydrocarbon molecules in the scanning electron microscope vacuum chamber get adsorbed onto the substrate surface which gets cross-linked by the secondary electrons originated

from the substrate through complex reactions. Thus, the carbonaceous species could be stitched to form the EBIC platforms. Square shaped carbonaceous deposits (5 x 5 µm) were created on the Si substrate at e-beam dosages of 1.3 C/cm^2 with an accelerating voltage of 10 kV in the TV mode (area deposition mode) at a working distance of 4 mm (see scheme in Figure III.4).
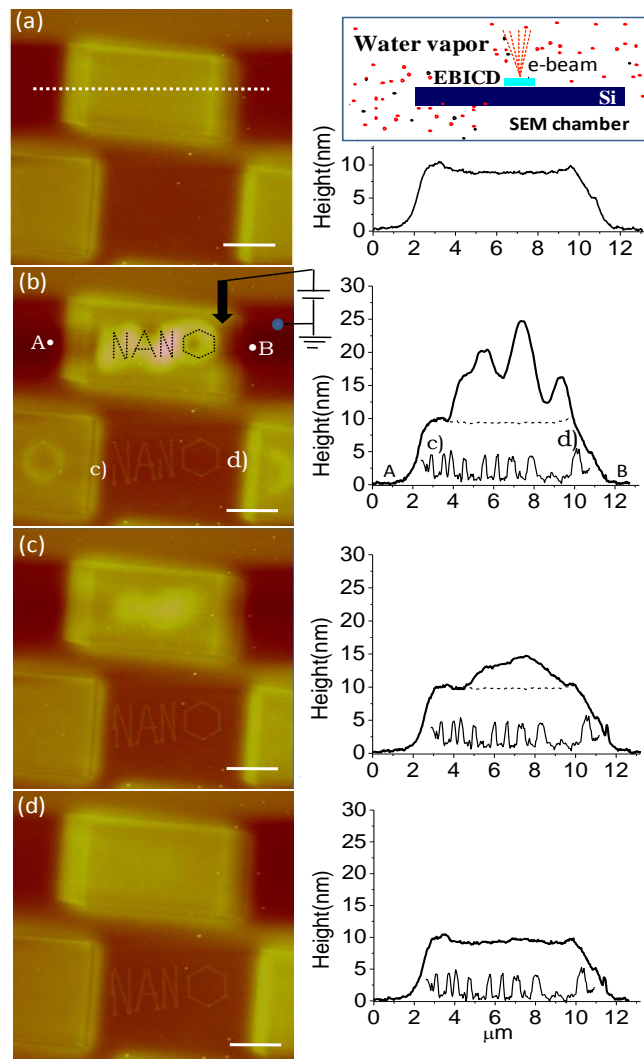
Figure III.4 AFM images (left side) and corresponding height profiles (right) illustrating the electro condensation process. The carbonaceous platforms on a Si substrate are shown in (a). The process for fabricating the carbonaceous platforms is shown schematically in the inset. (b) Shows the same region immediately after writing water patterns (NANO) on a carbonaceous platform with a positively-biased AFM tip. For comparison, `NANO' is also written using a standard local anodic oxidation (LAO) process employing a negatively biased. Over time, the water patterns dissipate, as shown in (c) and (d), whereas the LAO pattern remains unchanged. The images shown in b, c and d are recorded at elapsed times of 5, 20 and 35 minutes with respect to the image in a. The scale bar is 2 µm.

Following lithographic writing, the topography image showed a pattern, somewhat corresponding to the intended shape "NANO" (Figure III.4b). It is amazing that the raised pattern in some places is as high as ~15 nm above the carbonaceous platform (see between points A and B in Figure III.4b). The same tip with a negative bias produced typical LAO patterns on bare regions of the Si substrate (see between points C and D in Figure III.4b), where the height is only ~2.5 nm as expected [53]. Repeated AFM imaging of the region revealed that the raised structures exhibit a time dependent behavior (Figures III.4b-d). The image in Figure III.4c captured after a lapse of 15 minutes shows the patterned region diminishing in height as depicted in the adjoining profile. Interestingly, there was no trace of the raised pattern after 30 min as evident from the image in Figure III.4d; the corresponding height profile resembles closely that of the bare carbonaceous platform (see Figure III.4a). The LAO pattern on Si however remains unchanged (between points C and D in Figure III.4d). From the images shown in Figures III.4a and d, it is clear that the carbonaceous platform itself does not participate chemically but only witnesses temporary physical changes on the surface leading to the formation of raised features. These raised features, attributed to water condensation from the biased tip, evaporate subsequently, leading to reduced feature heights and eventual disappearance! The pattern being made of water is of low aspect ratio with blurred boundaries. It appears that this is an electro-condensation process induced by a biased AFM tip under moderate humid conditions (RH, 45%).
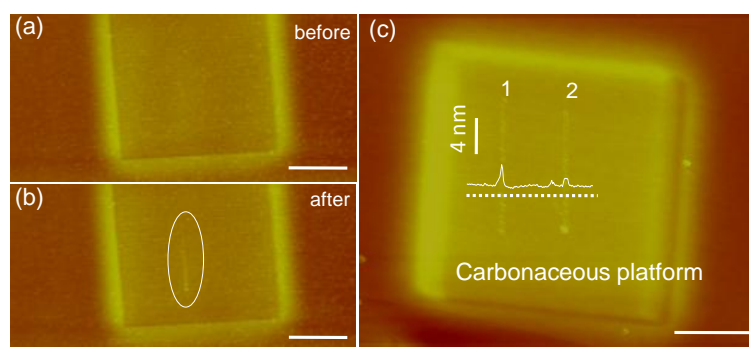
Figure III.5 AFM topographic image showing the carbonaceous deposition (a) before lithography (b) structure formation on the carbonaceous platform in contact mode(Tip V=+10V, S=0.5 µm/s) shown in marked area. (c) Negative tip bias induces the local chemical modification of carbonaceous layer, typical protruded features are of 1-2 nm in height shown with AFM z-profile. Lines 1 and 2 are created in contact and tapping mode respectively with a bias of -10 V, tip velocity= 1 µm/s. Scale bar, 2 µm.

While the lithography performed in the contact mode under similar conditions however, did not produce raised features but instead meek features (around 2 nm, see Figure III.5a and b) similar to previous reports on carbonaceous films [54]. Neither negatively biasing the tip helps the situation, be it contact or tapping mode (see Figure III.5c). Thus among other conditions, a positively biased tip in the tapping mode seem to be important to produce the water patterns.
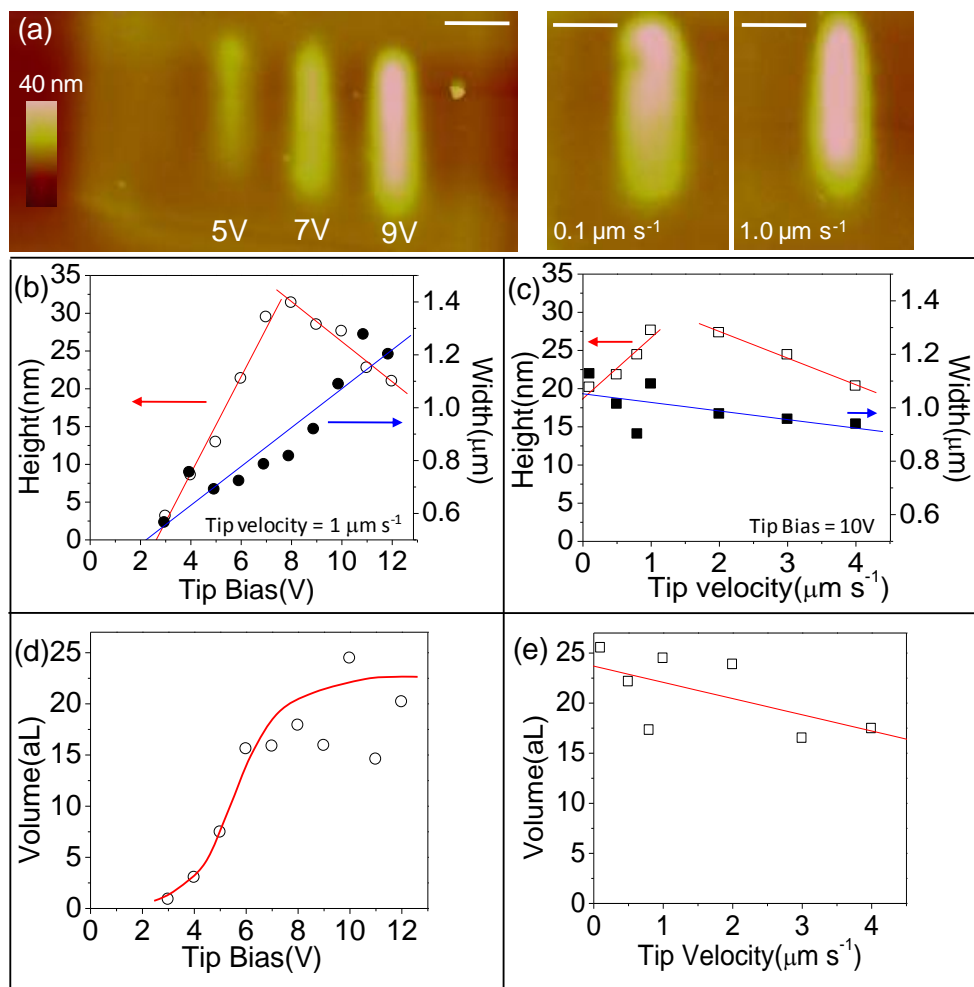
Figure III.6 The dimensions of the water pattern can be controlled by varying the writing conditions. The effects of tip bias (left) and tip velocity (right) during patterning were characterized. AFM images of representative 2 µm single-pass lines written under different conditions are shown in (a). The variations in water feature height and width with respect to tip bias and velocity are shown in (b) and (c), respectively. Similarly, the variations in volume are shown in (d) and (e), respectively.

The lithography process has been carried out at different tip voltages and velocities (Figure III.6). Figure III.6a is showing an example image scanned within the first minute

of drawing lines of water condensates at tip voltages of 5, 7, and 9 V, respectively (tip velocity=1 μm/s); increasing tip bias produced increasingly prominent water condensates. Below 3 V, no water condensation was observed. The z-profiles showed a linear increase in the height of the condensate for increasing tip bias but beyond 8 V, the height decreased (Figure III.6b). This trend is reflected in volume as well. The volume of water calculated using SPIP software [30], increases gradually up to 8 V (see Figure III.6c) and seems to settle thereafter to around ~20 aL. A higher voltage can bring about increased ionization of water molecules and ionic currents [31]. The scatter in volume data in Figure III.6c is therefore not surprising. The influence of tip velocity on the electro-condensation process is relatively less (Figures III.6d and e). The right images in Figure III.6a corresponding to 0.1 and 1.0 μm/s (tip voltage, 10 V) show only marginal differences. The height variation is between 20 - 27 nm with a change of trend around 1.0 μm/s. Greater dwell times at lower speeds can make the tip dump more water on the surface, while above 2 μm/s velocity, the water meniscus itself may become unstable. Such situations are quite common while performing DPN [6-8]. As regards water volume (Figure III.6e), it is difficult to decipher a definite trend due to data scatter, although a gradual decrease is evident.

At lower tip velocities or smaller areas, one may also expect effects due to ionization and joule heating. While drawing the circular and spot patterns, chemical modification of the carbonaceous layer takes place as the interaction time of tip is more with the surface species on a small area compared to the line patterns (see Figure III.7). Permanent local chemical modification of the EBICD surface was observed for the lower tip velocities (0.1-0.5 μm/s), seen as circular oxidized patterns in Figure III.7a. While increasing the tip velocity (up to 1μm/s), could lead to the nucleation of water (see Figure III.7b).
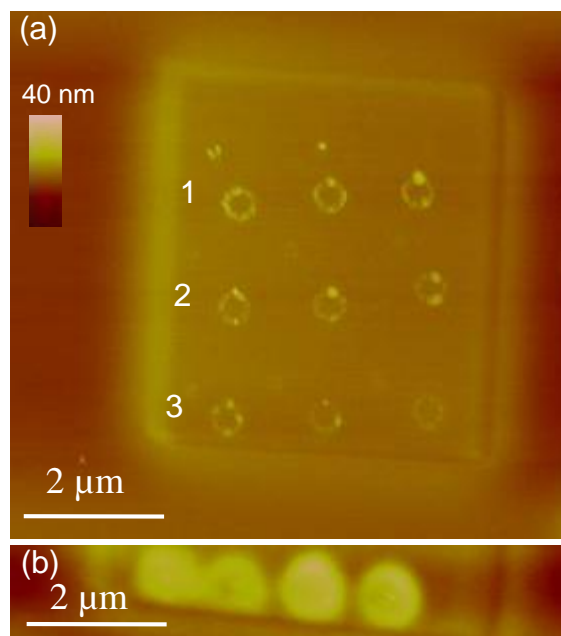
Figure III.7 (a) Circular rings shows the chemical oxidation of carbonaceous layer drawn a with a tip voltage of +10 V and at different tip velocities 0.1, 0.3 and 0.5 µm/s labeled as 1,2 and 3 respectively. (b) Series of rings drawn with a tip velocity of 1.0 µm/s and +10 V. Scale bar, 2 µm.
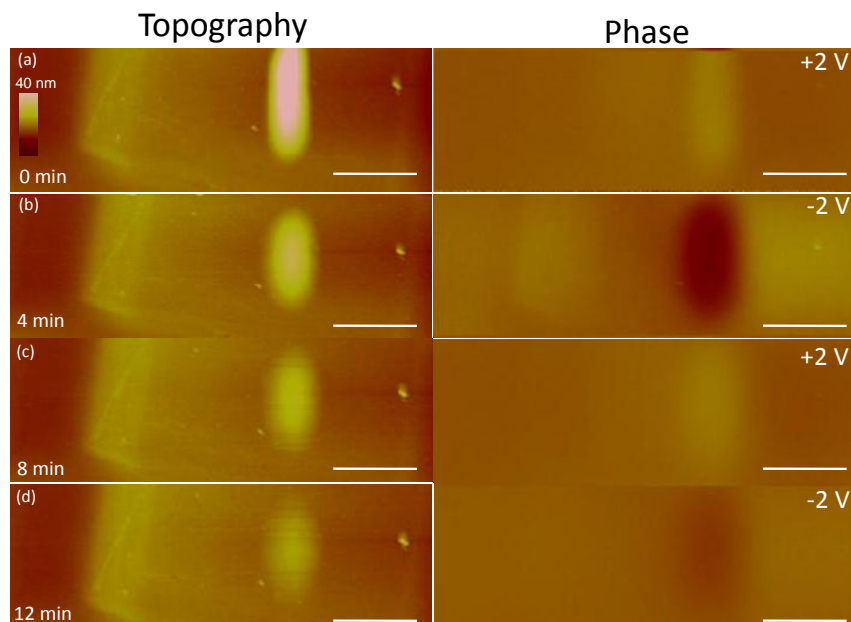
Figure III.8 Electrostatic force microscopy (EFM) was used to probe the charge and polarization within the water droplet. Topography images (left) and corresponding EFM phase images of a water feature as it evaporates are shown. (a) and (c) were taken with positive EFM tip voltage (+2V) whereas (b) and (d) where taken with negative EFM voltage (-2V). The reversal of contrast for different tip biases in EFM clearly indicates that the water droplet is charged. The local charge dissipates as the water evaporates. The scale bars correspond to 2 µm.

EFM was carried out on a water condensate at a tip lift height of 120 nm (Figure III.8). The phase image obtained with a tip bias of +2 V (Figure III.8a) shows a bright contrast corresponding to the water feature, whereas that in Figure III.8b recorded with -2 V tip bias showed a darker contrast. This color contrast relates to charge accumulation in the water condensate. A brighter contrast from positive bias data is taken to indicate positive charge accumulation in the condensate [55]. Figures III.8c and d show diminishing features due to water evaporation. The charge seems to dissipate locally as the molecules evaporate. Although the observation is qualitative, it certainly indicates the presence of electric charges on the condensed water features from the lithography process. The charge quantification was not attempted due to the temporal nature of the features.

It appears that a congregation of experimental parameters is at play to give rise to water condensation. In the tapping mode, there is no mechanical contact of the tip with the surface and the water bridge formation is not spontaneous. A certain threshold voltage (V_{Th}, ~ +3V in this case) is therefore required to induce the formation of a water bridge [56, 57]. The substrate also seems to play an important role. The carbonaceous species is dielectric [58], but its surface functionality is locally polarizable, a property which owes much to the presence of moisture during deposition using e beam. During the AFM lithography process, the deposited water carries positive charges from the positively biased tip (negative bias leads to no water condensation) which means that the substrate is polarisable only with positive charges. Contact mode lithography would be hopeless under these conditions. Higher voltage conditions are also not favorable as ionic currents would destabilize the condensed water droplets. This is more so with negative voltages [59], adding another reason to why negative tip voltages cannot induce electrocondensation in our studies.

Having realized positive charge accumulation in electrocondensed water on carbonaceous platform, the influence of negatively biased tip was investigated (Figure III.9). For this purpose, a large water drop was created on a carbonaceous platform as shown in Figure III.9a, by drawing closely spaced lines with 10 V tip bias. Although the topography is not quite even (discussed later), it enabled us to make further observations. The image in Figure III.9b obtained after patterning on the water feature with a − 10 V

biased tip, shows that water can be instantaneously evaporated locally. Although the intended pattern, 'K' is barely seen distinctly, water evaporation in the region is quite apparent. It appears that neutralization of the positive charge locally by the negatively biased tip leads to ionic current and joule heating causing instantaneous evaporation.
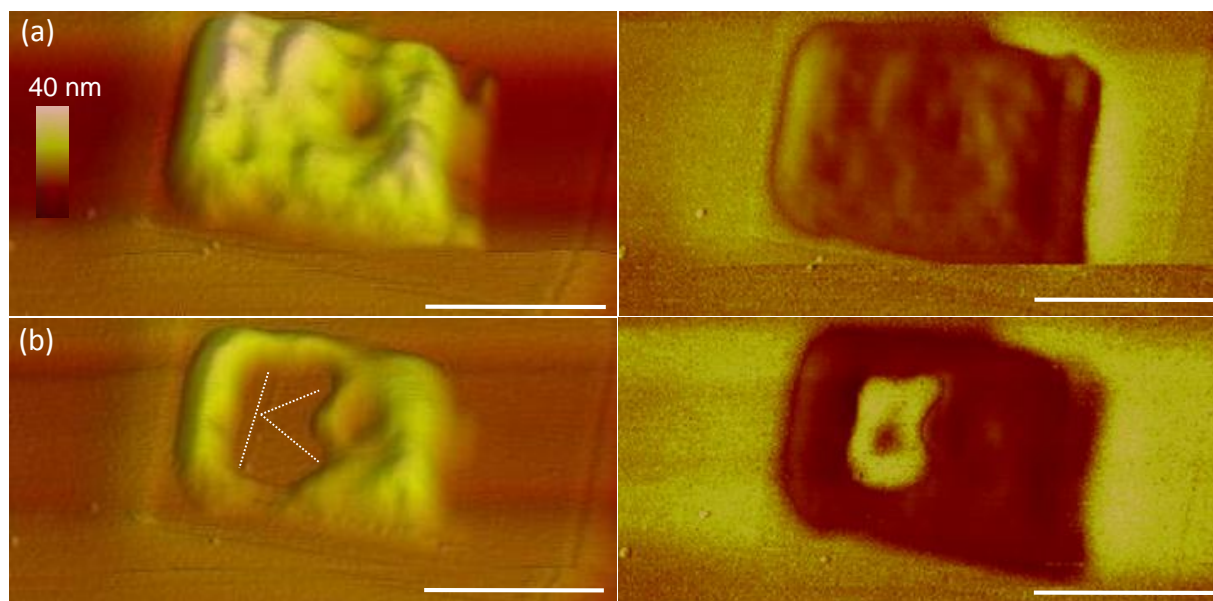
Figure III.9 3-dimensional AFM topography images of subtractive water patterning by tip-induced evaporation. (a) Shows a large water feature written at positive bias. By applying negative bias (-10V), it is possible to induce rapid evaporation, as shown in (b). The dotted line shows schematically the nominal feature (letter `K'). The corresponding phase images of (a) and (b) are shown in right side. The scale bar is 2 μm.

From the above observations (Figures III.4, 6, 8, 9), it is clear that a positively biased AFM tip can trigger the nucleation of water via electrocondensation. The implications of surface charge on the evaporation of droplets are striking. The time-dependent behavior of the water condensate is shown in Figure III.10 in terms of image contrast, z-profiles and volume. The water condensate was created with a tip bias of +10 V, indicated as 0 min in Figure III.10a. The gradual evaporation of the water condensate is observed through the images obtained after 8 and 16 minutes and complete evaporation after 24 minutes. Correspondingly, the height of water condensate decreases from 25 to 2 nm as shown by AFM z-profiles in Figure III.10b. There was also considerable smearing as seen from the width variation, ~ 0.5 to 2.5 μm. Figures III.10c and d contain trends in height and width variations respectively, for water condensates produced with different tip

voltages. A gradual variation in height is observed, where the different curves are seen lifted up depending on the initial height (Figure III.10c). The 8 V curve is on the top extending up to 38 min. On the other hand, the width variation is not found to be monotonous. The width increases in each case to a point beyond which it decreases, the turnaround time itself is found to increase with the tip voltage employed to create the water condensate. Interestingly, the low bias curves (4, 5, 6 and 8 V) group themselves with the initial width at ~ 0.5 µm. The 10 V and 12 V curves are much wider (see Figure III.10d). Similar trends are observed in the volume data (Figure III.10e).
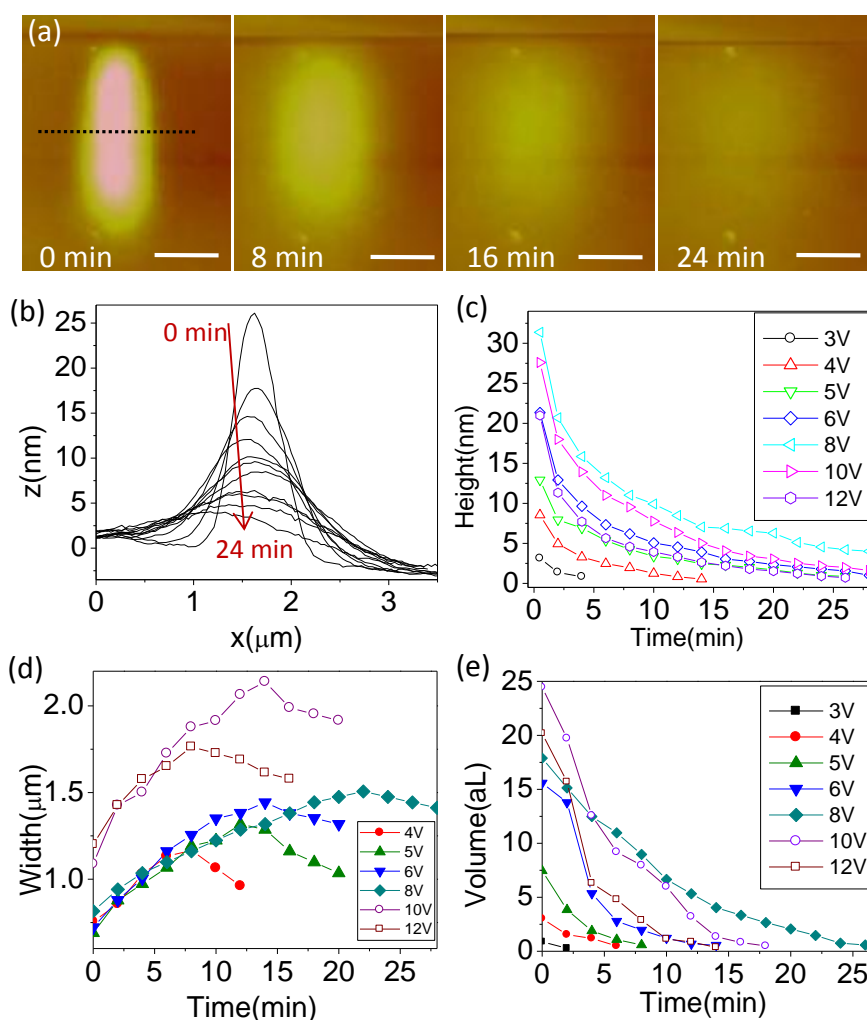
Figure III.10 Evolution of water feature size and shape during evaporation. A representative series of images taken at different times after writing are shown in (a). (b) Shows height profiles of an evaporating drop illustrating that the height decreases and the width increases over a period of 24 minutes. Height variation (c), width variation (d) and (e) volume variation of water condensates at different tip voltages. Scale bar 1 µm.

Thus, the water condensates created using lower tip biases evaporate rather quickly (within ~ 12 min), while those from above 8 V bias, exhibit an initial drop lasting 5 min and a more gradual evaporation during the following 20 min or so. The behavior with the 8 V curve is quite unique, an overall gradual evaporation going beyond 25 min.
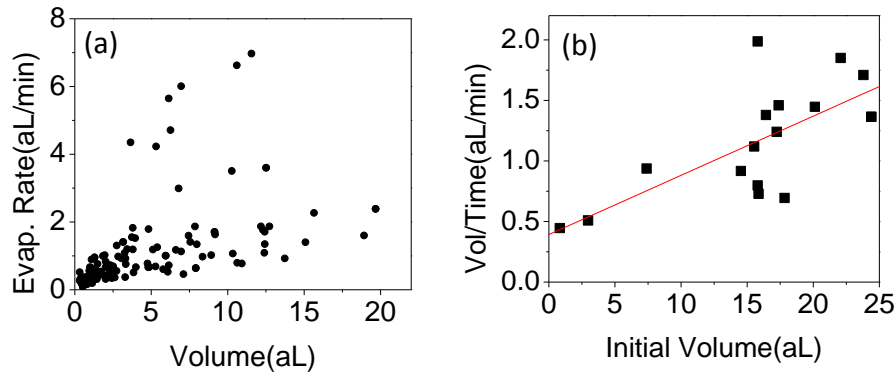
Figure III.11 (a) and (b) show the instantaneous and overall evaporation rates, respectively. Over time, the feature spreads as it evaporates.

The instantaneous and overall evaporation rates of the water condnesates are plotted in Figure III.11. The maximum evaporation rate is estimated to be 2 aL/min. The evaporation of macro or microdroplets of water is known to be a rapid process; the evaporation rate of a water droplet on PMMA surface under similar humidity conditions is typically 0.1 μL/min [60]. Assuming that trends in evaporation are independent of droplet size, attolitre volumes of water such as shown in Figure III.10a, should evaporate within picoseconds (10^{-12} sec)! In contrast, the aL quantities of water evaporate very slowly, indicating that physical mechanisms are quite different relevant only for nanoscale volumes [61, 62]. Besides, the droplets of water are highly charged and the dimensions are perhaps small relative to the screening lengths in water, which are typically on the order of a few hundred nms [63]. Since the carbonaceous platform serving as substrate for water is dielectric, the dissipation of charges is expected to be slow. It appears that water molecules require extraneous energy to leave the droplet surface [61, 62, 64, 65]. As a result, the evaporation is significantly slowed, enabling us to visualize the droplets on macroscopic timescale. Interestingly, the evaporation curves in Figure III.10e show that when the droplet volume is above 20 aL (see 10 V and 12 V curves in Figure III.10e), initial evaporation is fast (~ 5 min) and thereafter becomes gradual, much the same way micro

liter droplets would behave [60]. Smaller droplets (< 20 aL, see 8, 6, 5, 4 and 3 V curves in Figure III.10e), differ from this behavior in that their trends are relatively monotonic.
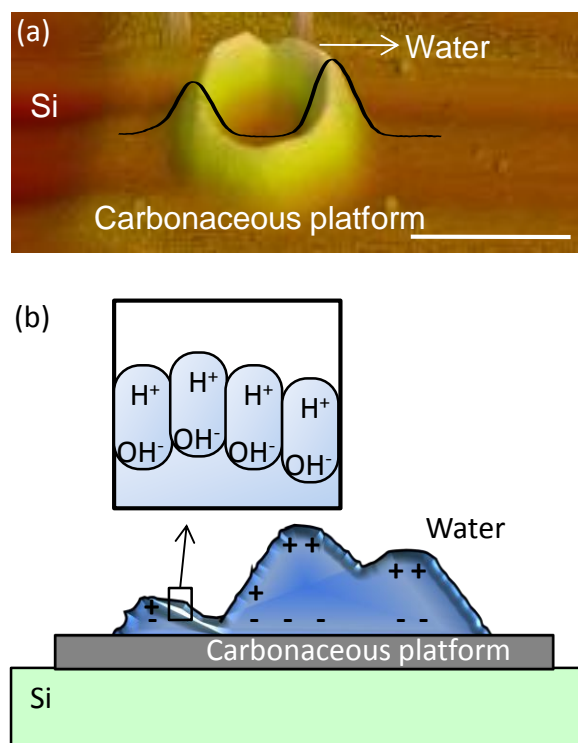
Figure III.12 (a) 3-dimensional image and corresponding line profile of a hexagonal water pattern showing the unusually sharp local water morphology that can be achieved using AFM-induced electrocondensation. The scale bar is 2 μm and the maximum height of the water feature is 27 nm. The schematic in (b) illustrates the presence of local tip-induced charge and polarization in the water which contributes to the anomalous droplet shapes and evaporation characteristics observed.

The electrocondensed water on the carbonaceous platform is different from standard droplets in yet another sense. One may recall the topography of the image shown in Figure III.9a, where the square water island is seen with highly uneven surface, a behavior foreign to bulk water. Another example is the topography image in Figure III.12a of a ring of water condensate, which did not show any tendency to collapse into a rounded droplet. The overlapping z-profile shows unusually sharp local morphology and corrugations of the water condensate.

This is illustrated with the schematic shown in Figure III.12b. Small volumes combined with localized charges arise due to alignment of water dipoles under the electric fields may attribute special properties different from the macroscopic behavior of water

condensates [62]. With time the hexagon is becoming a rounded droplet, demonstrating the evaporation phenomenon (see Figure III.13). The evaporation pattern for the water coral was recorded for every 2 minutes and the images are shown in Figure III.13.
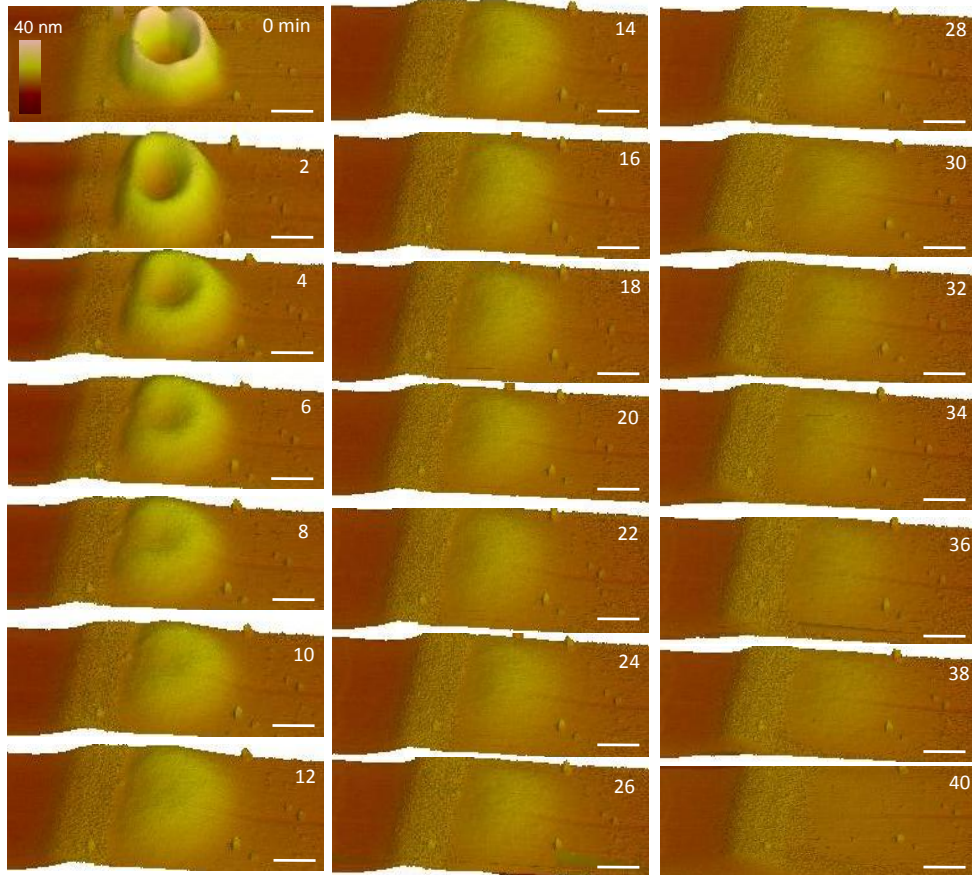
Figure III.13 The series of AFM images showing the evaporation of hexagonal water nanopattern with time (indicated in minutes at the top of right corner). Scale bar, 1 μm.

III.4.3 Local Anodic oxidation and etching

In order to study the influence of mode of operation, lithography was performed in contact mode. Figure III.14a shows the AFM topography of the EBICD (thickness ~ 10 nm) on the Si substrate. Lithography was performed by drawing lines from Si to the EBICD using negatively biased AFM tip (-10 V) at a relative humidity of 45%. At these conditions, the biased AFM tip initiates local anodic oxidation of both Si and EBICD, which can be seen as raised features which remained indefinitely (see Figure III.14b) [66, 67]. The inset shows a zoom-in-view of the grid pattern of oxide lines on the EBICD surface. The typical height of these features is 1.5-2 nm as determined from the

corresponding z-profile (see Figure III.14c). Further, the lithography was executed with a tip bias of -10 V at relative humidity of 60%. Lithography was performed on the set of EBICD platforms (thickness ~ 5 nm) on Si is shown in Figure III.14d. After performing the lithography, almost the entire region underwent modification. This is due to parallel spreading of oxidative species on the substrate surface under high humidity conditions [68, 69]. AFM z-profile analysis in Figure III.14f shows that ~ 2 nm of the EBICD got etched away during this process as the oxidative species transformed solid carbon into volatile CO and CO_2. The propagation of the shock waves can spread the oxidative species to a lateral distance of several µms generating oxide structures on the Si surface [68]. This behavior is also observed in polymer films under higher humidity conditions, where nanoexplosion under the tip apex and a shock wave propagation with a center cone and outer ring-like structures [68-70].
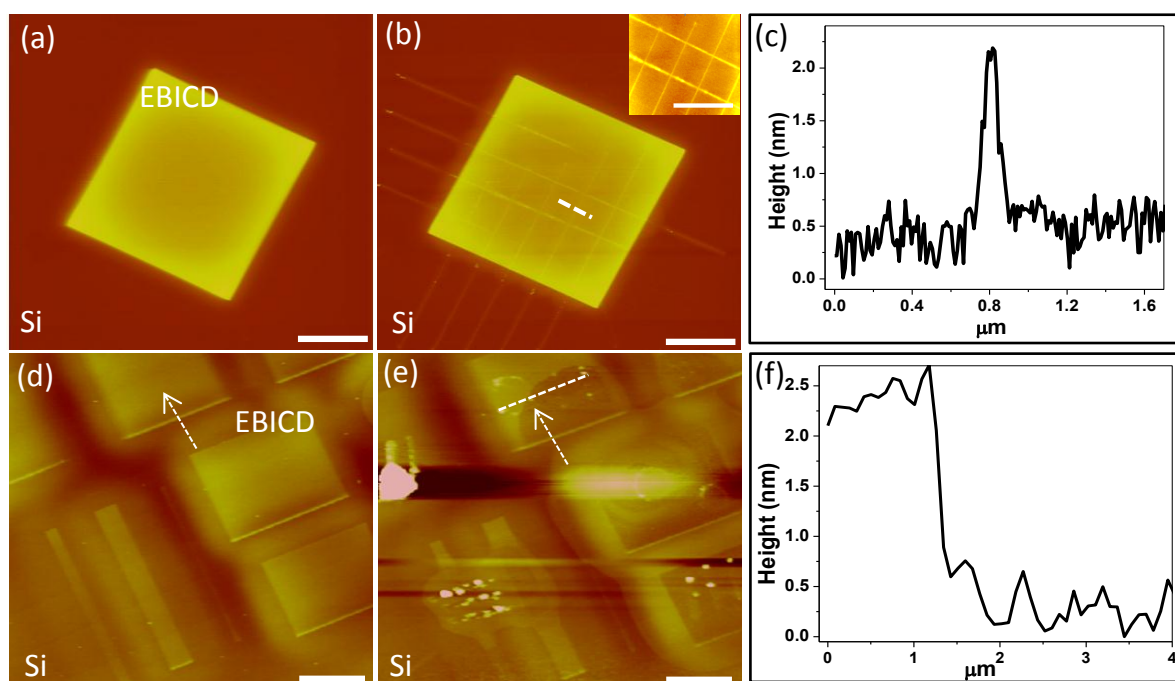
Figure III.14 Electrochemical modifications on Si and EBICD surfaces with a negatively biased AFM tip (-10 V) in contact mode. (a) AFM topography of the EBICD on Si. (b) oxide patterns in the form of lines on the Si and EBICD surfaces (RH=40-45%). Inset shows the grid pattern of oxide features on the EBICD surface. (c) z-profile for the oxide feature. AFM topography of the (d) EBICD platforms and (e) electrochemical etching of EBICD under high humidity (RH=60%) conditions. Scale bar, 3 µm. (f) AFM z-profile for the etched part of the EBICD platform with respect to the unmodified region.

III.4.4 Charge Patterning

Lithography was performed on the EBICD surface under lower humidity conditions (RH=30%) in the contact mode. Tip biases of +6 and -10 V are applied to write the lines on the top and bottom EBICD platforms respectively. No appreciable changes in the topography of the EBICD surfaces were seen before and after writing with the given tip biases (see Figures III.15a and b).
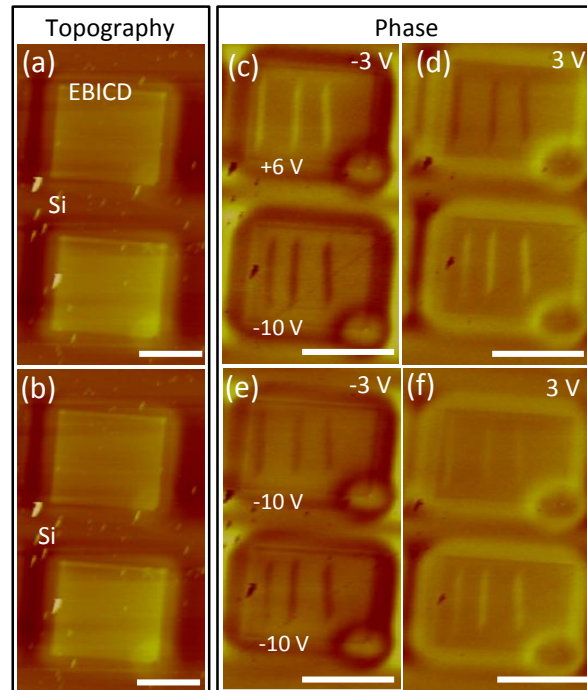
Figure III.15 (a) and (b) AFM topography of the EBICD platforms before and after charge patterning respectively. EFM phase images after writing three lines at V_{write} of +6 V (top), -10 V (bottom), read with V_{read}, -3 V (c), and +3 V (d), lift scan height of 120 nm. EFM phase images with V_{read} of (e) -3 V and (f) 3 V after rewriting with tip bias of -10 V on same patterns of the top EBICD platform. Scale bar, 3 μm.

EFM was performed in order to examine whether there exist any charge patterns which could not been seen in topography. To determine the sign of these surface charges, EFM phase images were recorded with V_{read} of -3 and +3 V, both at a lift scan height of 120 nm. The two bias polarities showed opposite contrast in the images. In EFM, attractive and repulsive force gradients result in the negative and positive phase shifts which give darker and brighter contrasts respectively. The three lines written with a V_{write} of +6 V on the top EBICD platform showed bright and dark contrasts for V_{read} of -3 and +3 V respectively (see Figures III.15c and d). On the other hand, the lines written with -10 V on

the bottom EBICD platform showed dark and bright contrasts for V_{read} of -3 and +3 V respectively (see Figures III.15c and d). This indicates that writing with the positive tip bias results in the negative surface charges and reverses for the negative tip bias writing. This observation was further confirmed by drawing lines with V_{write} of -10 V on the top EBICD platform only without rewriting on the bottom. Now the top and bottom platforms showed similar contrasts for the lines, indicating the possibility of reversible charging depending on the sign of V_{write} (see Figures III.15e and f).
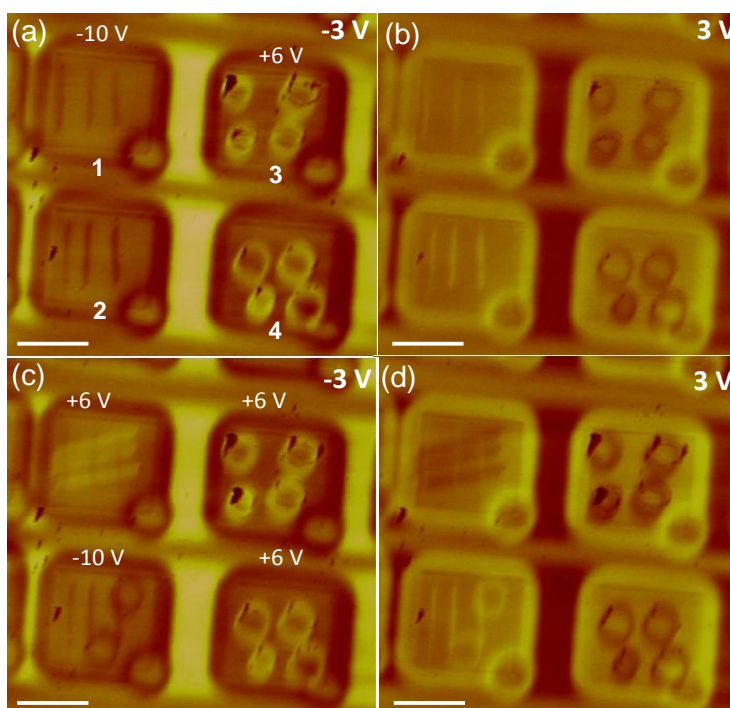
Figure III.16 (a) and (b) EFM phase images after writing three lines at V_{write} of -10 V (1 and 2 platforms), +6 V (3 and 4 platforms), read with V_{read}, -3 V and +3 V lift scan height of 120 nm. EFM phase images with V_{read} of (c) -3 V and (d) 3 V after rewriting with tip bias of +6 V and -10 V, indicated on the platforms. Scale bar, 4 µm.

The charges on the carbonaceous platforms can be erasable and rewritten. The same platforms (as in Figure III.15) were used for further writing process. AFM tip bias of -10 V and +6 V were used for writing on the carbonaceous platforms numbered 1, 2 and 3, 4 respectively. The EFM phase contrast seen according to the V_{write} used for the writing purpose (see Figures III.16a and b). Circles and cross lines are written and showed EFM phase contrast according to the V_{write} (see Figures III.16c and d).

A summary of the AFM bias lithography on the EBICD surface is presented in Figure III.17. The surface of EBICD stabilizes the water condensation under a positively biased AFM tip in tapping mode at a moderate humidity (45%). As the humidity decreased to 30%, the formation of reversible charge patterns were observe depending on the tip bias polarity guided by the water-cycle mechanism. These modifications are treated as electrophysical which do not involve any chemical modifications to the EBICD surface. After changing the mode of operation to contact mode, the negatively biased AFM tip induces the local anodic oxidation of the EBICD surface under moderate humidity (45%). Further, increase in the humidity up to 60% resulted in the lateral spreading of oxidative species (which is known in the literature as shock wave propagation) causing the electrochemical etching of the EBICD surfaces over microns range.
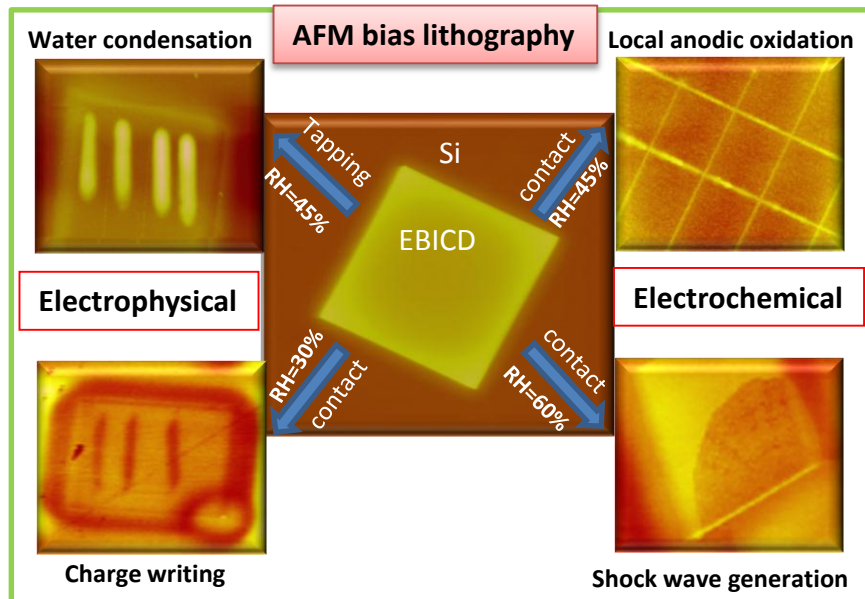
Figure III.17 AFM bias lithography on the EBICD surface under different conditions favoring the electrophysical modifications such as water condensation and charge writing and the electrochemical modifications such as local anodic oxidation and shock wave generation.

The charge patterning on the EBICD surface can be explained by the water-cycle mechanism [71] in which the electrochemical reactions are not favorable on these EBICD platforms rather only physical processes such as charge patterning is possible at low humidity conditions. Charge patterning involves no changes in the topography and only detected either through EFM or KPFM imaging. It is known that the negative and positive tip biases drive the OH^- and H^+ ions respectively towards the substrate surface, resulting in

charge deposition on the EBICD surface. Under low humidity conditions, the number of the oxidative ions are low enough not causing the local chemical modification but only resulting in the physical incorporation of charged ions such as OH^- and H^+, leading to the charge writing on the carbonaceous platforms.

The novel surface functionality of the EBICD surface is responsible for the tunable local modifications according to the operating conditions adopted. The electron beam inducing the complex reactions of residual hydrocarbons along with the moisture leading to the formation of stitched carbonaceous patterns. The carbon to oxygen ratio of the carbonaceous deposits is found to be 70:30 determined through XPS analysis. A local probe technique such as AFM was employed as to exploit the unique surface functionality of the EBICD surface. Firstly, EBICD was employed as a suitable platform for the condensation of water patterns and their stability under ambient conditions. This can be explained by the polarizable surface functional groups under the electric field from the AFM tip followed by subsequent electrostatic clamping of water molecules leading to the condensation of water features. The relaxation of polarized functional groups with time causes detachment of water molecules leading to the evaporation. Thus, the reversible polarization of surface functional groups allowed us to study the nature of water condensation under different tip bias conditions during tapping mode of operation. On the other hand, using a negative tip bias in contact mode, the local electrochemical modifications were observed. At moderate humidity, the oxidation of the EBICD surface was observed while at higher humidity the spreading of the oxidative species via shock wave propagation causing the electrochemical etching of the EBICD surfaces relatively over large areas conditions. Apart from these permanent chemical modifications, the charge patterns could be written on the EBICD surfaces under low humidity in contact mode. The charge patterns have been reversibly changed according to the sign of tip bias. As there is no change in the topography, the written charge patterns are imaged through EFM. Thus, this study brought out the important observations about the electrophysical processes such as water condensation, charge patterning and electrochemical modifications such as oxidation and etching of the EBICD surfaces by choosing the appropriate operating conditions.

III.4.5 Charge storage in mesoscopic graphitic islands (MGIs)

III.4.5a Local anodic oxidation

In 1990, Dagata and co-workers have observed the modification of a hydrogen-terminated silicon surface through application of a bias voltage between an STM tip and the surface [72]. The composition of the modified region was found to be silicon oxide, confirmed through secondary ion mass spectroscopy (SIMS). This phenomenon has been attributed to the local oxidation of the Si under the electric field from the STM tip. In 1993, similar observations were made by employing AFM which could cause the local oxidation of Si (111) surfaces. Since these early stuides AFM has been extensively used for the local oxidation of surfaces due to its ease of operation and speed.

Typically, conducting AFM tips such as Pt/Ir, Au, W_2C coated and heavily doped Si probes have been employed for the local oxidation of surfaces in contact and dynamic modes. Local anodic oxidation (LAO) is about the formation of a simple nanoelectrochemical cell in which AFM tip serves as a cathode, the water bridge formed between the tip and surface as electrolyte, and the substrate serves as the anode. LAO resembles conventional anodic oxidation except that the former relies on 10^4-10^5 water molecules while latter uses Avogadro's number of (6×10^{23}) electrolyte molecules. Another fundamental difference is that in LAO, the anode and cathode are separated by a few nanometer (~1-2 nm) distance where the application of nominal bias voltage of 10 V would generate an intense electric field ($E = V/d = 10$ V/nm), more than enough for the electrolytic dissociation of water to cause local chemical modifications. The high aspect ratio of the AFM tip further concentrates the electric field upon application of a bias voltage. Besides the electrochemical modifications, such extremely high electric fields can initiate various physical and chemical processes such as electrostatic charging, field emission, Joule heating, explosive discharge, nanoexplosion and shock wave generations [3]. As discussed in the previous section, the formation of a water bridge is usually formed either by mechanical contact between tip and sample surface or through the application of an electrical field in the case of dynamic modes of operation.
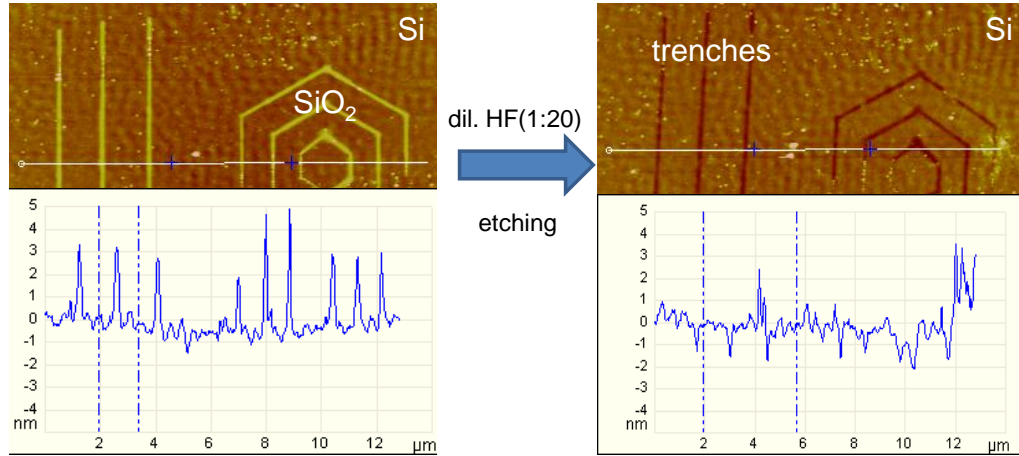
Figure III.18 Local anodic oxidation and etching of Si (100) surface and corresponding z-profiles.

Most of the initial LAO experiments were performed on Si surfaces to gain the basic understanding of the oxide growth kinetics and optimization of experimental parameters. The anodic oxidation of the semiconductors and metal surfaces can be explained through the following chemical reactions proposed by Sugimura and Nakagiri [73].

At anode: $M + nH_2O \longrightarrow MO_n + 2nH^+ + 2ne^-$ .... (III.6)

At cathode: $2H^+_{(aq)} + 2e^- \longrightarrow H_{2(g)}$

$2H_2O + 2e^- \longrightarrow H_2 + 2OH^-$
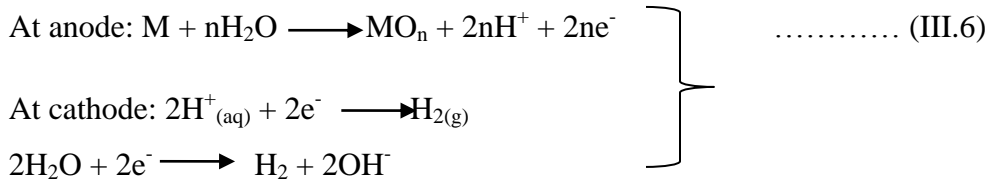
In the case of Si surface, after LAO as the resulted SiO_2 has more volume compared to Si, it forms a protrusion on the surface. Alternatively, depressions on Si can be formed through wet chemical etching of SiO_2 using dilute HF (see Figure III.18).

This LAO technique has been employed widely for the oxidation of various surfaces such as metals (Ti, Ta, AL, Mo, Ni, Nb), semiconductors (SiC, III-V semiconductors), dielectrics (Si_3N_4, perovskite films), self-assembled monolayers and carbonaceous films, etc. Mode of operation is very important during the lithography; it is found that during the contact mode lithography, due to continuous voltage bias, there is a buildup of space charge within the oxide during the growth. Whereas dynamic modes such as tapping and non-contact modes resulted in the high aspect ratio oxide features due to pulsing nature of the applied bias which minimizes the width of the meniscus.

Though much of the earlier reports are mainly focused on Si surfaces and to some extent various metal surfaces, due to recent interest in fabrication of carbon-based devices, SPM lithography has become a popular tool for realizing carbon nanodevices directly. The basic difference between the Si and C substrates is that Si can only be oxidized whereas carbon either can be oxidized or etched during the SPM lithography. As the electronic properties of carbon are very sensitive to the local electrochemical modifications, SPM lithography can offer the possibility of fabricating carbon nanodevices with tunable properties. In addition, SPM lithography provides a resist free method for fabricating carbon nanostructures. The advantages are far-reaching since the intrinsic electronic properties remain preserved, unlike other lithographic techniques such as electron beam lithography and photolithography which involve resist coating with multiple steps of chemical processing. Nanofabrication with scanning probe microscopes provides a widely accessible method for high resolution nanofabrication with a precision approaching atomic (0.1 nm) dimensions.

III.4.5b Relevant Electrochemical Reactions

AFM bias lithography was performed on the conducting carbon such as highly oriented pyrolytic graphite (HOPG). HOPG is a standard calibration sample for STM and cAFM due to its smooth surface. The local electrochemical reactions on HOPG may be partial or complete leading to the oxidation or etching of the graphene layers depending on the experimental conditions. A brief discussion is presented related to local electrochemical processes on the graphite surfaces. When a local electric field is applied between a tip and a carbon substrate in the presence of a water meniscus, a number of possible electrochemical reactions can take place to affect localized domains on the carbon substrate. The features produced can be either due to an oxidation or an etching process, which process dominates depends on the strength of the applied electric field and the duration of resulting ionic current. Oxidation produces raised oxide features while etching produces localized pits [74]. For the purpose of this study, the pits can be classified as either deep (depth greater than ~2 nm) or shallow (depth less than ~2 nm). In all cases, a permanent chemical modification of the carbon surface occurs that will impact the performance of any intended device. This distinction based on trench depth is important

because significant differences in electrical behavior between shallow and deep trenches are observed.

$$2H_2O + E\ field \rightarrow 2OH^- + 2H^+$$
$$C + 2OH^- \rightarrow CO_2 + 2H^+ + 4e^-$$
$$2H^+ + 2H^+ + 4e^- \rightarrow 2H_2$$

$$\overline{}$$

$$C + 2H_2O \rightarrow CO_2 \uparrow + 2H_2\ (Overall\ reaction)$$ ....(III.7)
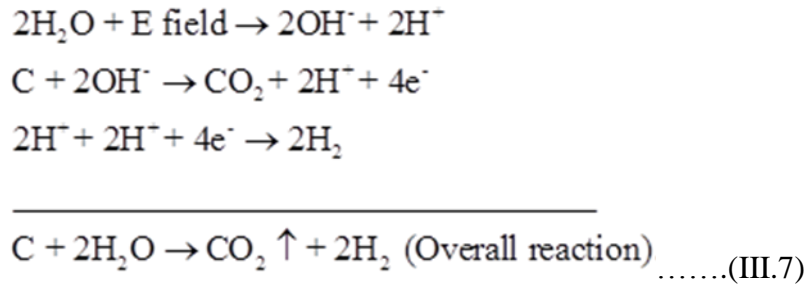
The chemical reaction to etch a carbon surface can be understood by converting solid carbon into gaseous CO and CO_2 through reactions mentioned above. Although this process is slow under normal conditions, it is accelerated by the high electric fields between the biased tip and carbon substrate. As a result, OH^- is driven toward the substrate, and the chemical reaction goes to completion with the end result that C atoms are removed to form trenches [75-77].

$$H_2O + E\ field \rightarrow OH^- + H^+$$
$$C + OH^- \rightarrow C\text{-}OH + e^-$$
$$C\text{-}OH \rightarrow C\text{-}O^- + H^+$$
$$C\text{-}O^- + H^+ + H^+ \rightarrow C{=}O + H_2$$

$$\overline{}$$

$$C + H_2O \rightarrow C{=}O\ (carbonyl) + H_2\ (Overall\ reaction).$$ .... (III.8)
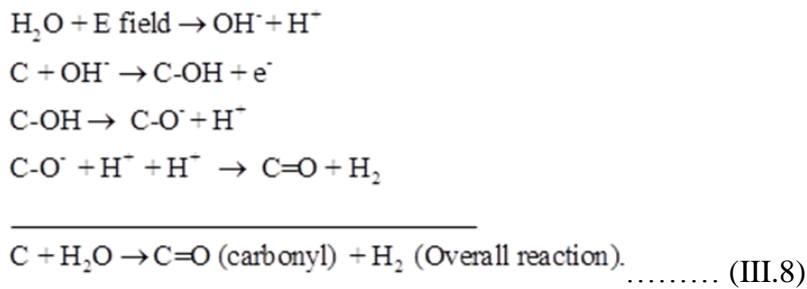
Under sufficiently low bias or when the electric field is applied for a sufficiently short period of time, carbon can be oxidized rather than etched. Even though, Pourbaix diagram shows the possibility of etching at low voltages, the chemical kinetics favor the oxidation of the carbon surface resulting in a raised surface feature rather than a depressed pit [78]. Hence, the conversion of C to gaseous CO and CO_2 is incomplete and only surface carbonyl, carboxyl and epoxy formation is expected (see Equation III.7).

Under practical conditions, both processes outlined above may occur in parallel, producing localized features that contain carbon atoms modified by oxy-functional groups due to incomplete reactions. The presence of such species is confirmed by Raman measurements (*vide infra*).

III.4.5c Geometric Characterization of Electrochemical Oxidation on HOPG

Figure III.19 summarizes the results of typical electrochemical oxidation and etching experiments performed on the topmost layers on an atomically flat HOPG substrate. In Figure III.19a, the observed patterns (lines and hexagons) were created through local anodic oxidation of the HOPG surface using intermittent contact mode under a relative humidity of 35% and a tip bias of -8 V. Under these conditions, protruded features were observed on the HOPG substrate. The typical height of these features was found to be 1-1.5 nm as determined from the corresponding z-height profile (shown in the line scan in below Figure III.19a).

Since the features are raised above the substrate, they were formed by electrochemically oxidizing the topmost graphitic layers (see Eq. III.8 in section III.4.5b). Under similar conditions (-8 V tip bias and 35% relative humidity), when the tip is in contact mode, local anodic etching of graphitic layers is observed (see Eq. III.7 in section III.4.5b and related discussion). Figure III.19b shows a sequence of line features created by scanning the biased tip at a velocity of 0.5 µm/s. This experiment demonstrates control of trench depth as a function of the bias applied to the tip. Bias voltages from -8.0 V to -6.8 V in steps of -0.2 V ('a' to 'g') were investigated. As deduced from the z-height profiles in Figure III.19b, a negative tip bias of -8V in contact mode etches a trench ~40 nm wide and with an apparent depth of 1.5 nm, suggesting the formation of a cut through ~4-5 carbon layers. This observation is comparable to that obtained by Jiang et al. [24] who ramped voltage pulses from 8 V to 5 V for a duration of 10 s in order to produce shallower cuts (less than 2 nm deep) through the HOPG layers. Figure III.19c demonstrates the reliability of localized electrochemical etching to form well-defined geometries in the top-most graphitic layers of HOPG. The formation of hexagonal islands of different sizes is demonstrated. After analyzing these images, it can be confirmed that the inner portion (marked as 'i' in Figure III.19c) of the hexagon forms a graphitic island that is laterally isolated from the surrounding infinite graphite substrate (marked as 'o' in Figure III.19c). For this reason, the inner region was referred to as a "mesoscopic graphitic island (MGI)."
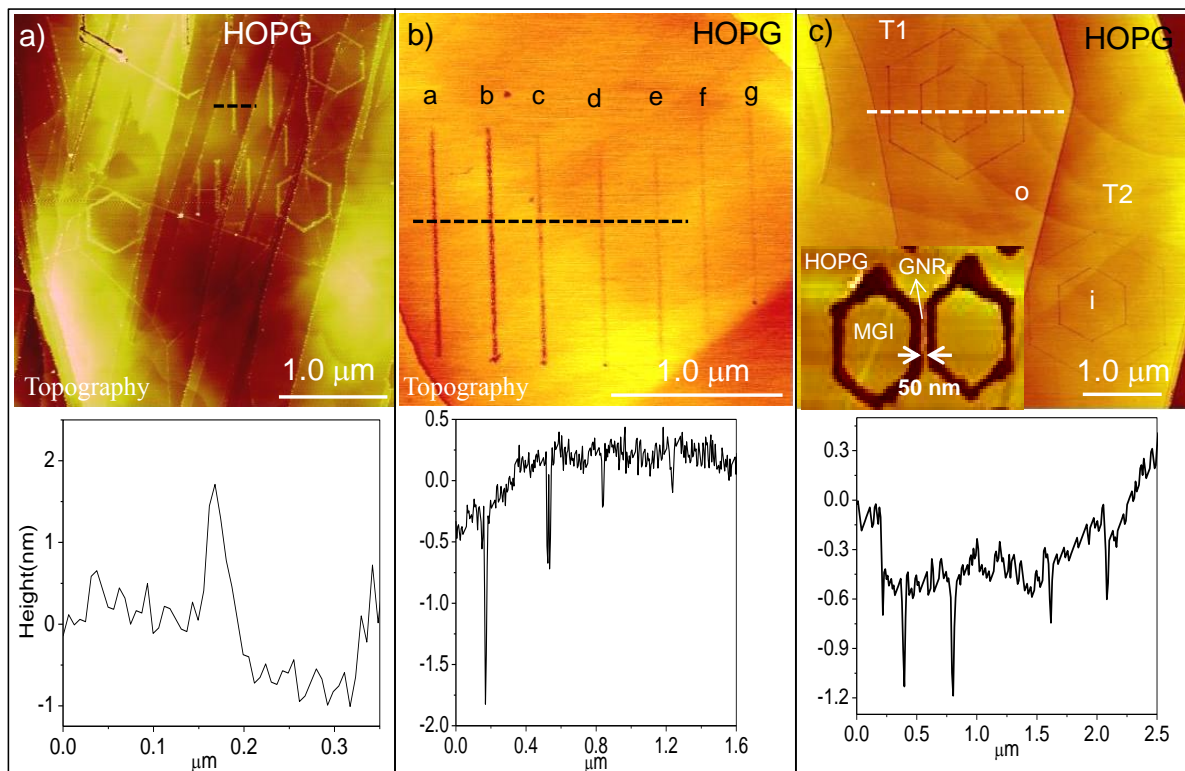
Figure III.19 Electrochemical oxidation and etching of graphitic layers with a negatively biased AFM tip. (a) Graphite oxide patterns in the form of lines and hexagons with heights of 1 nm obtained in intermittent contact mode with a tip bias of -8V. (b) AFM topography of the trench patterns labeled 'a' to 'g' were drawn in contact mode with biases ranging from -8 V to -6.8 V in steps of 0.2 V respectively. (c) Hexagonal island-like patterns are created at two locations on HOPG (marked as T1 and T2) by locally etching away layers of graphite with a tip bias of -8 V. Inset shows the narrow constriction of 50 nm ide separating two MGIs. The corresponding z-profiles are shown below for each image. A relative humidity of 35% was kept constant for this set of experiments.

III.4.5d Electrostatic Charging of MGIs with Deep Trench Perimeter

Because chemical modification of the graphitic layers is likely to result from electrochemical etching, systematic experiments were conducted to characterize the contact potential difference between MGIs and the surrounding HOPG substrate. Figure III.20 illustrates a typical electrostatic force microscopy (EFM) study of MGIs with varying size and trench dimensions. The AFM topography image in Figure III.20a shows MGIs with lateral dimensions of 500 nm (top pair of hexagons), 300 nm (middle pair) and 150 nm (bottom pair). Note that the perimeter around the upper right hexagon has intentionally not been completed, allowing the interior region of this partially formed hexagon to retain connectivity to the uppermost graphitic layers of the surrounding HOPG substrate. Trench depths were measured to be in the range of 2-5

nm. The corresponding EFM phase images (shown in Figures III.20b, c, d, e) were recorded with tip biases of 0, +3, -3, +5V using a lift height of 60 nm. Figure III.20b shows the EFM phase image recorded with a zero tip bias that reveals a small but measurable electrostatic signal presumably due to a work function difference between the tip and HOPG. Interestingly, this signal provides evidence for a small phase contrast *inside* the hexagonal MGIs, when compared with topography image in Figure III.20a.
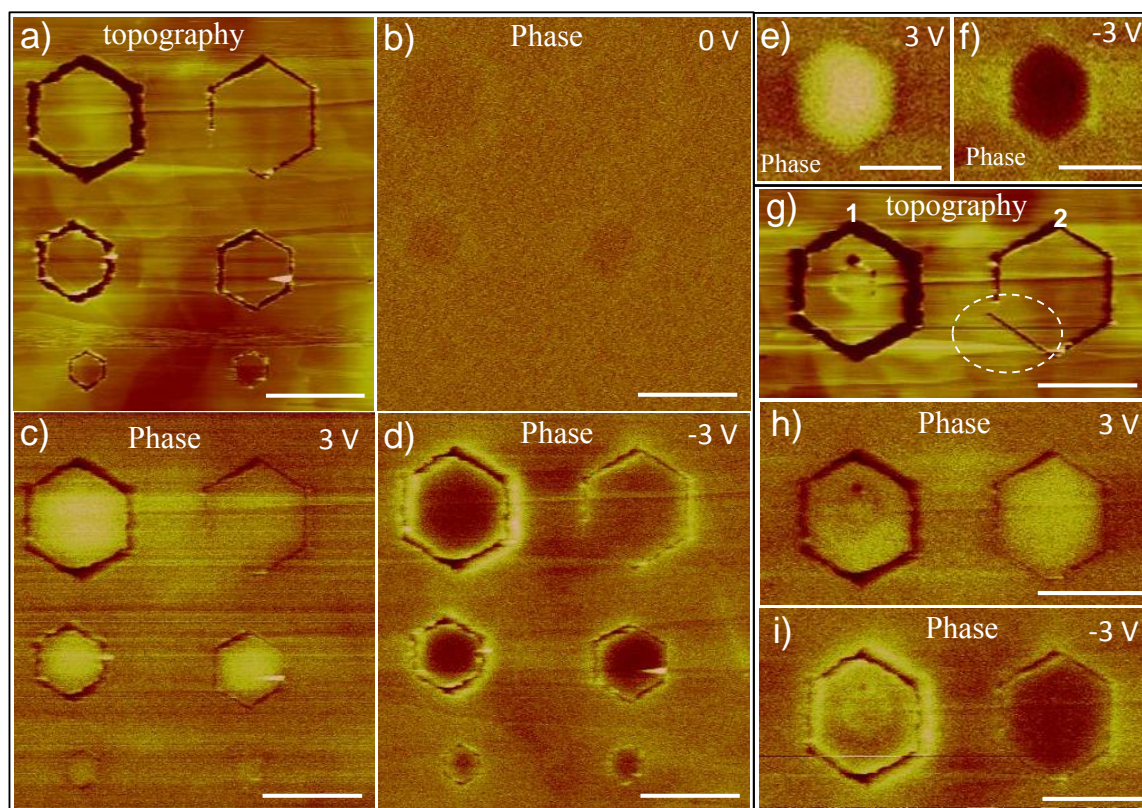
Figure III.20 EFM studies on MGIs with different lateral dimensions. (a) Topography image showing the MGIs with lateral dimensions of 500 nm (top pair of hexagons), 300 nm (middle pair) and 150 nm (bottom pair), depths of 2-5 nm. EFM phase images obtained with a tip bias of (b) 0 V, (c) 3 V and (d) -3 V. EFM phase images obtained with a tip bias of (e) 3V and (f) -3V for the MGIs defined under mild electrochemical conditions (g) Topography shows a small circle drawn inside of hexagon 1 and nearly complete etching of hexagon 2, with only a small bridge connecting the interior of the hexagon to the surrounding HOPG substrate. EFM phase images recorded with a tip bias of (h) 3 V and (i) -3 V. The lift height is maintained constant throughout as 60 nm. Scale bar, 0.5 μm.

It is noteworthy that the upper right partial hexagon does not exhibit this phase contrast because of continuity of the top graphene layers which allows charge equilibration between the partial MGI and the surrounding surface. The observations are more striking

with bias applied on the tip. In Figure III.20c, the EFM image recorded with a tip bias of +3 V, shows a positive phase shift of 0.4º from the interior of the hexagons with respect to rest of HOPG surface. This phase shift is similar irrespective of the size of the hexagon and is uniform throughout the inside region. The trench regions are seen darker due to attractive capacitive interactions irrespective of the tip bias polarity. Moreover, the upper right hexagon does not exhibit any difference in phase. Upon reversal of tip bias (to -3V), it was observed that a reversal of EFM phase contrast for the MGIs, confirming the electrostatic nature of the interaction producing the phase shift (shown in Figure III.20d). Analysis of this data suggests that the interior MGI regions are positively charged (see Figure III.20e). Further examination of the data in Figure III.20d provides evidence that the trench regions surrounding the hexagonal MGIs are oppositely charged with respect to the MGI interior. As mentioned above, the upper right partial hexagon imaged in Figure III.20a was intentionally cut on only five sides, allowing for electrical continuity between the interior of the partial-hexagon and the surrounding HOPG substrate. It is clear from the data in Figure III.20e that the EFM phase contrast is greatly diminished when the MGI interior is intentionally connected to the surrounding HOPG substrate.

From this set of experiments, it can be inferred that the local lithographic etching of HOPG with a biased AFM tip creates MGIs that appear to be electrically charged. It was also noted that the charge persists over extended periods of time (at least several hours) lapsed between the different experiments. The apparent charging of isolated MGIs was further investigated in a second set of experiments. In these experiments, modifications were made to the top pair of large hexagons previously shown in Figure III.20a. Specifically, a small 0.2 μm diameter circle has been electrochemically etched inside the hexagon marked 1 in Figure III.20g using a negative tip bias of -10 V. Subsequent EFM phase imaging with the tip biased at ±3 V (see Figures III.20h and i) reveals a reduction in the phase contrast when compared to Figures III.20c and d. A second modification was made to close the open side of the hexagonal MGI marked 2 in Figure III.20g. This modification reduced the electrical contact and further isolated the interior of the MGI from the surrounding HOPG. Only a small bridge of ~ 50 nm width (see Figure III.20g) now connects the interior of the MGI to the surrounding topmost layers of HOPG.

Significantly, a pronounced EFM phase contrast develops within the interior of the MGI as can be seen by comparing Figures III.20g and i with Figures III.18c and d. It is clear that the EFM phase difference across the interior of a hexagonal MGI can be controlled by the degree of isolation between the interior region and the surrounding HOPG substrate.
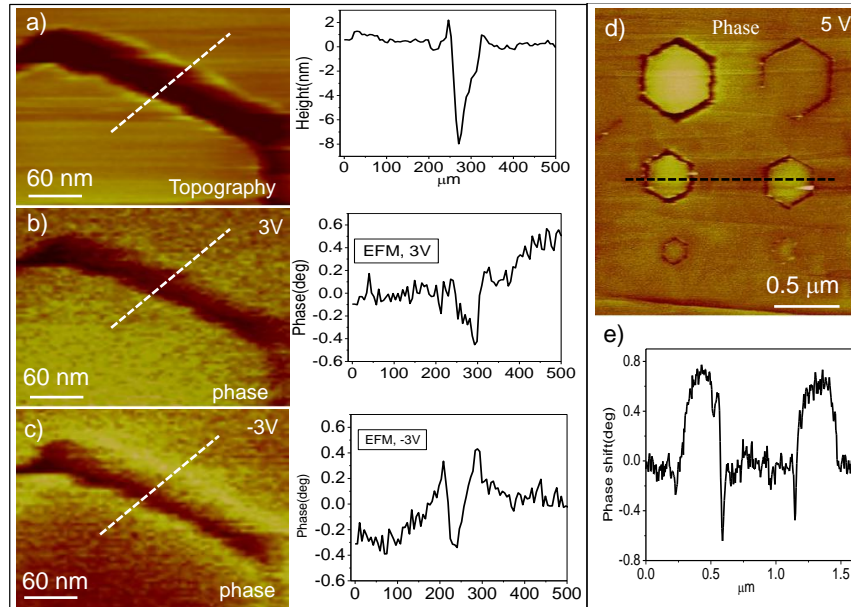
Figure III.21 The width of the trench was 60 nm from the topography (a), and the apparent width of the trench was decreasing to 50 nm and 40 nm for the EFM phase images recorded at tip bias of (b) 3V and (c) -3 V respectively. The corresponding profiles are shown. (d) The EFM phase image of MGIs with a tip bias of 5 V and (e) the phase shift of 0.7 ° shown in the profile.

The apparent width of the trench was lesser in the phase images when compared with the topography image (see Figures III.21a, b and c). This is due to the long- range nature of electrostatic forces and broadening of the potential distribution near the edges of the trench. This can also be inferred from the opposite phase shift that appears as a bright halo around the perimeter of the MGIs. This feature may not be due to AFM controller instability since this "opposite phase contrast" appears to be a unique characteristic of the MGIs surrounded by shallower trenches. Figure III.21d shows phase image of the isolated hexagonal MGIs when the tip bias is set to +5 V. The EFM phase shift in the interior of the MGIs is ~0.7° greater than the surrounding substrate (see Figure III.21e).

III.4.5e Electrostatic Charging of MGIs with Shallow Trench Perimeters
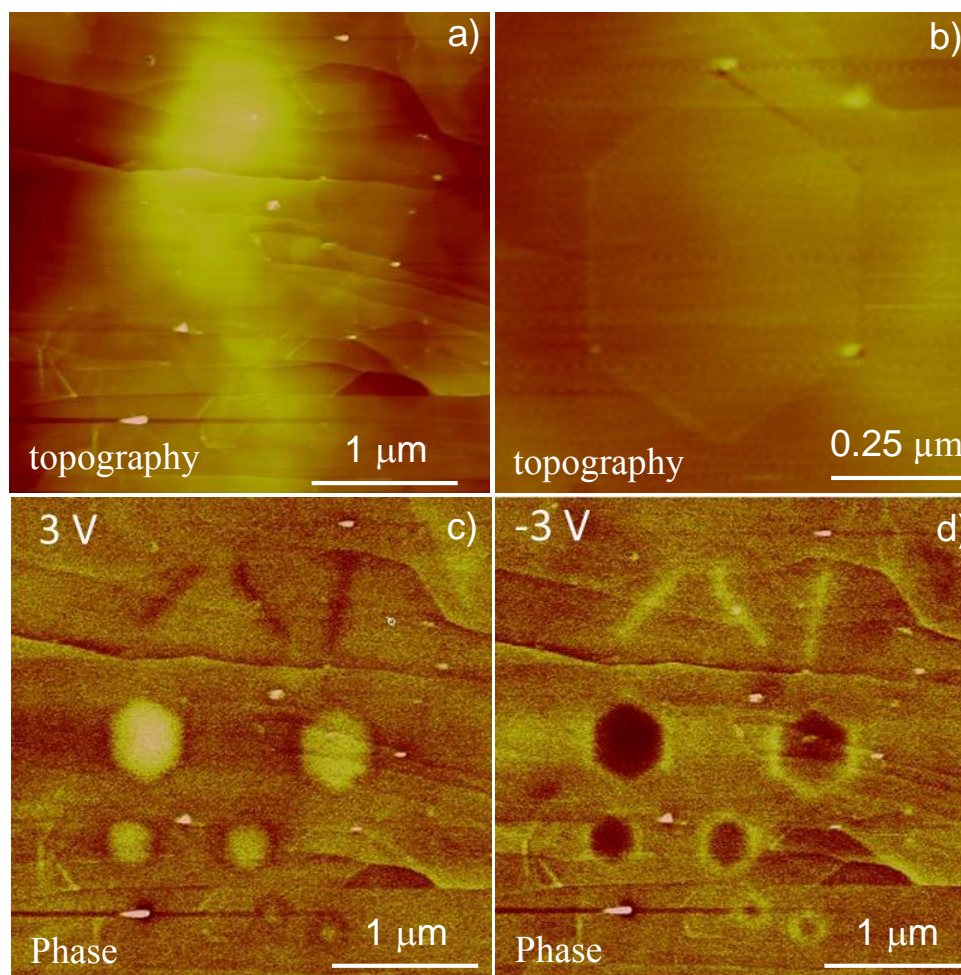
Figure III.22 (a) Topographic image recorded after mild electrochemical modification to form various patterns. The topographic features are barely visible due to presence of large number of steps at this location on HOPG. (b) Topography of an individual MGI with very mild features of perimeter. However, the location of these features is clearly revealed by comparing with EFM phase images obtained with a tip bias of (b) 0V, (c) 3V and (d) -3V respectively. The lift height is maintained constant throughout as 60 nm. The phase images clearly show patterns with reversal of contrast for the opposite polarity of the tip biases.

In order to further investigate the electrostatic charging, both straight lines and hexagonal MGIs were fabricated with interiors isolated from the surrounding HOPG by shallow trenches (depths of less than 1 nm). Figure III.22a illustrates the topographic image recorded after performing bias lithography. It appears featureless when imaged at this length scale due to the shallow depth of the trenches that were created. However, some of the sides of the hexagons are the raised surface oxidized features rather than trenches.

That location of HOPG contained a large number of steps, and therefore precise determination of trench depth is difficult. However, the observation of EFM phase contrast from the drawn features, indicating the delamination of the graphene layers because of the electrostatic pressure exertion form the oxyanions. Figures III.22b, c and d show the EFM phase image recorded with a tip bias of 0V, +3V, and -3V respectively. These images provide clear evidence for the reversal of EFM phase contrast for the interior of the MGIs, and again indicate that a net positive charge accumulates on the interior of the MGIs. This result is not only consistent with the observations inferred from Figure III. 20 but affirms that charge accumulation is possible even with MGIs defined by shallow trenches (or oxidation) Interestingly, the three straight lines etched into HOPG (as seen in the upper region of Figures III.22c and d) indicate an EFM phase contrast that is clearly opposite with respect to the MGI interiors.

This suggests that the trenches are negatively charged along their length, a result that is consistent with the formation of oxy-functional groups during electrochemical etching. While working with mild conditions in tapping mode, it was difficult to distinguish a shallow trench from a raised feature clearly, given the roughness the region develops following the process. The formation of a raised feature joined along by a shallow trench is also a possibility. However, it is quite clear that the perimeter of MGI in such a case comprises of an oxide species.

Table-III.1 The measured EFM phase shift values for the different dimensions of MGIs compared with that of HOPG background.

Specifications	Range of Phase shifts (degree)
HOPG background	0.03-0.06
Shallow trenches (1 nm deep)	0.1-0.3
Medium trenches (10 nm deep)	0.1-0.5
Very deep trenches (40 nm deep)	0.4-1.0

III.4.5f Electrical Characterization

In order to assess the degree of electrical isolation of the MGIs, the current-voltage characteristics were measured using conducting AFM (cAFM). First, as shown in Figure III.23a, hexagonal MGIs were created in a flat region of HOPG.
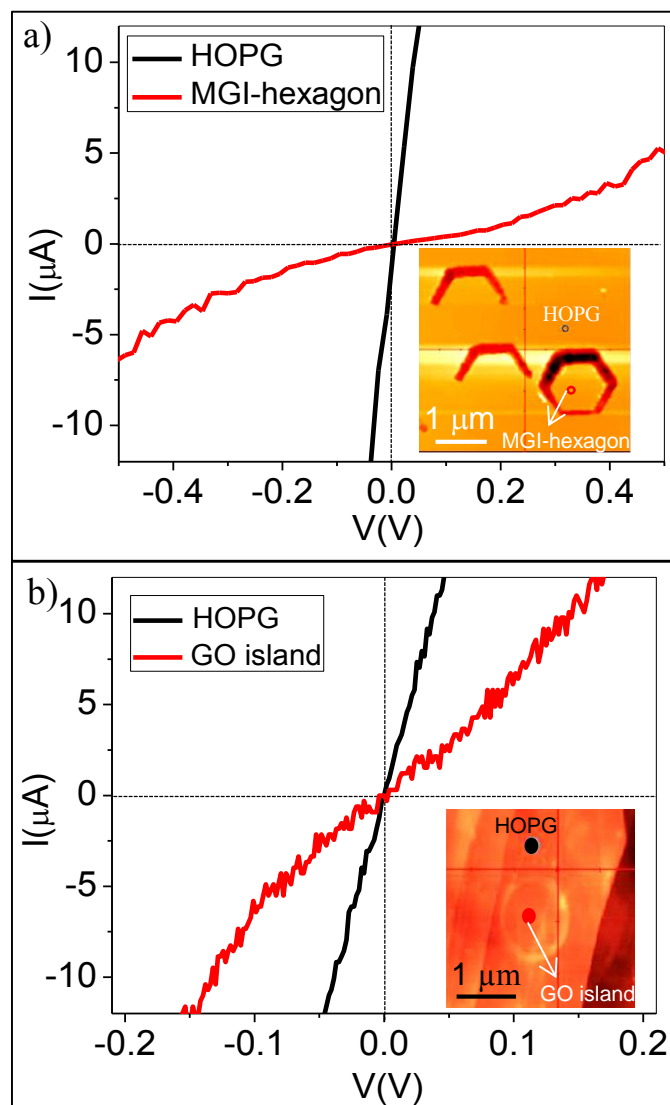
Figure III.23 conducting AFM (cAFM) studies on graphene oxide island. The black linear curve is typical of that found when the tip is loaded and positioned on flat HOPG with a contact resistance of 3.6 kΩ. The I-V from the interior of the graphene oxide island shown with red curve, contact resistance of 16 kΩ. The inset shows the AFM topographic image.

For the purposes of this study, both completely enclosed hexagons as well as half-hexagons were fabricated. When the tip is positioned on flat HOPG, the resulting I-V curves are linear as shown in Figure III.23b. Analysis of the slope of the I-V data near V = 0 gives a contact resistance of ~3 kΩ. Positioning near the half-completed hexagons shown in Figure III.23a produced similar I-V characteristics, indicating that the etching process alone did not significantly affect the electrical transport. However, when the tip is positioned within an isolated MGI-hexagon with a lateral dimension of 1 μm, separated

from the surrounding HOPG by a trench of depth 70 nm, a distinctly non-linear I-V behavior occurs. Analysis of the slope of the I(V) data near V=0 gives a contact resistance of ~200 kΩ. This is nearly 70 times that higher resistance compared to HOPG.

A number of I-V curves recorded inside and outside the hexagon reveals that I-V from anywhere inside the isolated hexagon is nonlinear, whereas linear I-V behavior is always observed with the tip positioned outside of the hexagon. The non-linear I-V recorded inside the MGIs suggests an electrical decoupling of the hexagonal islands from the surrounding HOPG substrate with a degree of electrical isolation that is ~70 times greater when compared to direct contact to the flat HOPG. Interestingly, current mapping on the MGIs has revealed that the edges on either side of the trench regions appear as brighter features, indicating their highly conducting nature due to localization of charge carriers, this observation is consistent with prior work [79]. Further experiments were conducted on the interior of an MGI separated from the surrounding HOPG by a raised oxide line, similar to that shown in Figure III.19a. These data are presented in Figure III.23b and indicate a factor of 4.4 increase in resistance as well as a slight non-linearity near V=0.
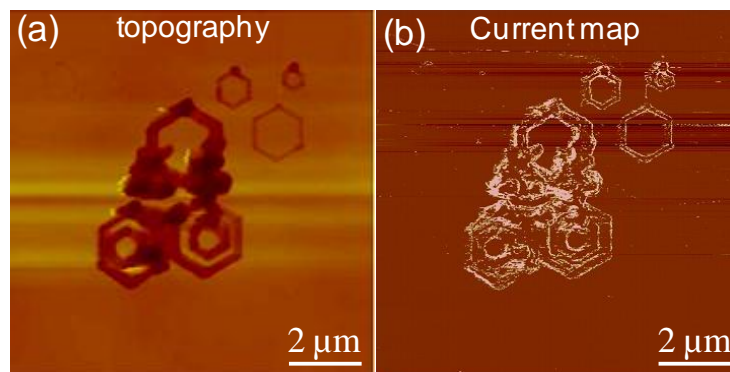
Figure III.24 (a) Topography of the hexagons with deep trenches and the corresponding current mapping image is shown in (b) with a sample bias of 1 V and tip was grounded. The perimeters of the trenches appear as brighter contrast, revealing the local higher conductance as compared to the rest of the HOPG.

Conducting maps of the MGIs were performed with a tip bias of 1 V and results are presented in Figure III.24. The current map in Figure III.24b shows that the edges of the MGIs were of brighter contrast as compared to the rest of the regions. The corresponding AFM topography is shown in Figure III.24a. The edge regions are of higher conducting

due to the a little overlap of the graphene layers with the bottom. This leads to the localization of the charge carriers, giving rise to the higher conducting edges.

III.4.5g Dissipation of charges through thermal treatment
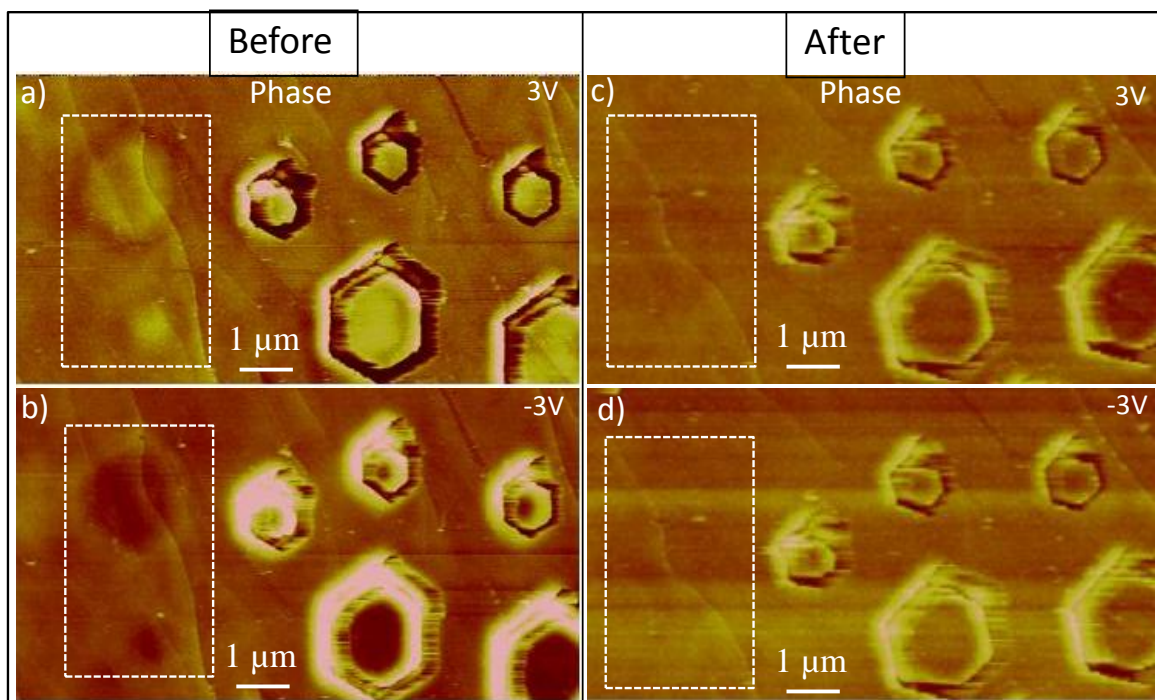
Figure III.25 Charge decay after the heat treatment. EFM phase images showed the reversal of the phase contrast in the interior of the hexagons before the heat treatment with a tip bias of (a) 3V (b) -3V respectively. The EFM phase images for the same after heating the sample at 200°C for 5 minutes, no reversal of the phase contrast. For the tip biases of (c) 3V and (d) -3V respectively.

The positive charge in the interior of the hexagons has been neutralized by contacting with a negatively biased tip (while drawing a circle inside of hexagon, see Figure III.20g). It was also found that thermal activation of charge carriers can also be used as a method to dissipate the charges. In a typical experiment shown in Figure III.25, EFM was recorded on a set of hexagons with different lateral and vertical dimensions before and after heat treatment to realize the process of dissipation of charges. Figures III.25a and b correspond to the EFM phase images recorded on the MGIs with different dimensions with tip biases of 3V and -3V, lift height of 120 nm respectively. As usual, the interior of the hexagons are positively charged (similar to Figures III.20 and 22). The hexagons with the shallow trenches are marked with the rectangular box. The sample was then heated to 200 °C for 5 minutes, followed by EFM mapping of the same area. Interestingly, the EFM

phase contrast after thermal treatment is the same, regardless of tip polarity (see Figures III.25c and d). One can easily observe from Figure III.25 that following heat treatment, there is no trace of charge in the interior of the hexagons defined by shallow trenches. This result clearly indicates a strong coupling of the layers after the heat treatment along the c-axis, which leads to the dissipation of the charges.

The I-V behavior reverts to a linear characteristic after heat treatment; with resistance values from MGIs comparable to the surrounding HOPG (see Figure III.26).
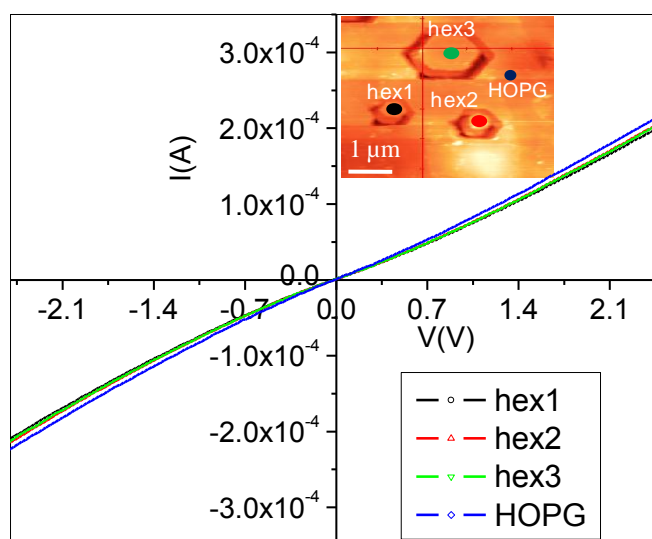
Figure III.26 Conducting AFM on different dimensions of the hexagonal MGIs after heating the sample at 200° C for 5 minutes. The similar behavior in the current-voltage characteristics from the interior regions of the hexagons as that of rest of HOPG (resistance near V=0 is 13 kΩ). The thermal treatment was helpful in reducing the potential barriers for the flow of charge carriers along the c-direction.

III.4.5h Micro-Raman Characterization

The Raman spectrum of HOPG (curve a in Figure III.27) has two major peaks at 1580 cm^{-1}(G -band) and 2690 cm^{-1} (2D band). The G band is due to in plane vibrations of sp^2 carbon network. The D band at 1330cm^{-1}, arises due to the presence of topological or functional defects which introduce the sp^3 carbons into the large sp^2 carbon network. Though the D band is not seen at all locations on a HOPG surface, its overtone (2D band) is seen as it is very sensitive to the stacking order of graphene sheets along c-axis [80]. During the AFM electrochemical oxidation of HOPG, the oxidative species (OH$^-$, O$^-$) react with the sp^2 carbon and convert to sp^3 with hydroxyl and epoxy functional attachments.

Spectrum 'b' recorded on an electrochemically etched trench of 200 nm width (Raman probe diameter, 1 µm) shows a broad D band at 1330 cm^{-1} and a small upshift in the G band position (to 1582 cm^{-1}). As shown in the inset of spectrum 'b', the shoulder at 1613 cm^{-1} clearly indicates the presence of oxy functional groups along with topological defects [80].
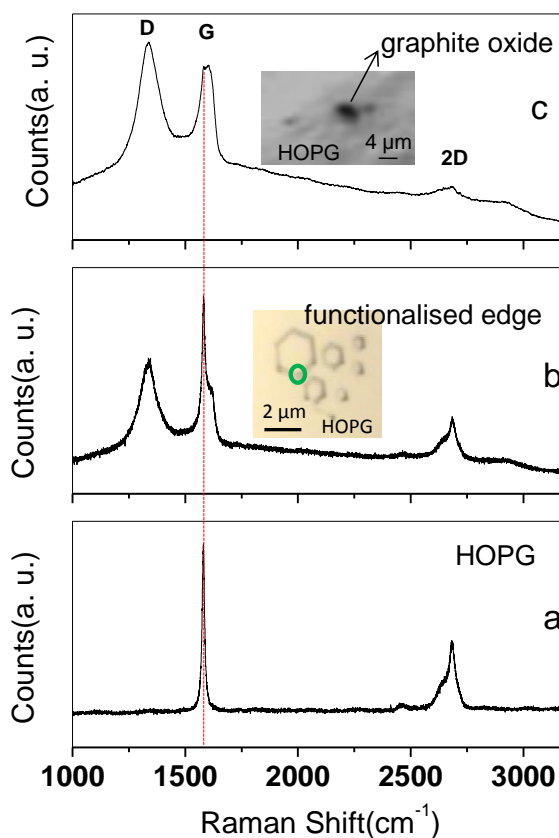
Figure III.27 Comparison of Raman spectra during the AFM electrochemical oxidation with that of HOPG. The evolution of D band, up shift in the position of G band and its broadening, signifies the attachment of oxy functional groups to the carbon lattice (plots 'b' and 'c' are compared against 'a'). The position of G band peak is indicated by a vertical line.

Large pits were also created on HOPG whose dimensions (diameter, 1-2 µm and depth 500 nm) are comparable to the micro Raman probe diameter. The spectrum 'c' is very different from the HOPG ('a') and the most salient differences are (i) a strong D band (~1330 cm^{-1}) with higher intensity as compared to the G band; (ii) a much broader G band whose position at 1595 cm^{-1} (an up shift of 15 cm^{-1} with respect to HOPG), signifies the oxidation of the graphite lattice (see spectrum 'c'). The shape of 2D band is very different

as compared to the spectra 'a' and 'b' and may reflect a disruption in c-axis periodicity due to the introduction of oxy functional groups during oxidation of graphitic layers.

III.4.5i Further discussion

Using a biased AFM tip, the electrochemical oxidation and etching of HOPG has been studied. By varying the tip bias voltage, lines or trenches have been written into the top layers of HOPG. The depth of the trenches can be controlled by adjusting the tip bias voltage. Using the lithographic capabilities inherent in AFM, patterns of varying complexity have been defined by writing trenches with specific geometry. Of particular interest is the formation of mesoscopic graphitic islands (MGIs) with an interior that is laterally electrically isolated from the surrounding HOPG substrate. Using EFM techniques, shallow trenches with a depth of ~ 2 nm or less are found to exhibit a pronounced negative charge distribution along their length, suggesting the presence of oxy-functional groups that form during the electrochemical etching. Subsequent micro-Raman examination of such electrochemically etched features provides direct evidence for the presence of such groups. Examination of the interior of MGIs by EFM indicates that a net positive charge is distributed uniformly across the island interior. The charge persists for many hours, suggesting that a permanent electrostatic polarization of a MGI interior has been produced. When the interior of a MGI remains partially connected to the surrounding HOPG substrate by a bridge, the positive charge distribution is greatly reduced. Experiments show that the net positive charge distribution can also be reduced by performing lithography in the interior of a closed hexagon (essentially contacting it) with a negatively biased tip. Taken together, these experiments suggest that the net negative charge distributed around the perimeter of a MGI is formed at least partially from electrons removed from the interior of the MGI.

Similar charge persistence has been reported for carbon nanotubes supported on insulating SiO_2 substrates [81]. After contact with a biased AFM tip, a nanotube could remain charged for many hours. Separate experiments were conducted to assess the degree of electrical isolation of a MGI from the surrounding HOPG substrate. The highly non-linear I-V data obtained when the MGIs are bounded by deep trenches (see Figure III.23a) suggests that current flow through the islands is indeed weakly coupled to the surrounding

HOPG substrate. Such a weak coupling could be produced by filamentary contacts bridging the topmost carbon layers to the surrounding HOPG substrate. Alternatively, the large resistivity ratio between the basal plane and c-axis directions in pyrolytic graphite is well known; measured values for the c-axis resistivity are ~100 times greater than for the basal plane [82]. If the top few layers of the MGI interior are well isolated laterally from the surrounding HOPG substrate, then current flow through the MGI will occur predominantly along the c-axis, with the result that a higher resistance might be expected. The fact remains that electrical current can flow through the islands, suggesting that the persistence of the interior charge distribution is likely the result of a permanent charge polarization that sets up in the top few graphitic layers in HOPG during the oxidative lithography process. Such a charge polarization will have deleterious effects on any electronic devices that may be formed using an AFM-based nanolithography process. On the other hand, it may have potential applications where charge localization and storage is desirable.

Because the exact quantitative estimation of charges is limited by self-capacitance effects induced by the tip-cone and cantilever of the scanning probe, an approximate parallel plate capacitor model was used to estimate the charges in the interior of the hexagons. Experiments were conducted to specifically determine the tip bias voltage at which the EFM phase contrast disappeared. When this condition is met, the tip voltage approximately equals the potential of the MGI. In a series of such experiments, it can be inferred that the interior of an MGI was charged to a potential of approximately +0.5 V. This result can be understood by considering the electrostatic potential V(z) that develops as a function of distance z above a disk of radius R with a uniform charge density σ. The solution of this problem is given by

$$V(z) = 2\pi\sigma \frac{1}{4\pi\varepsilon_o} \left[\sqrt{z^2 + R^2} - z \right]; \quad z > 0. \quad \text{............... (III.9)}$$

as z→0, $V(0) = +0.5V \sim \frac{\sigma}{2\varepsilon_0} R$. For the MGI used in this study, R=0.25 μm, implying charge densities σ≈+3.5×10^{-5} C/m^2 are present on the top surface of an MGI, roughly

equivalent to the permanent removal of ~40 electronic charges from the interior of the 0.5 μm diameter hexagonal island.

It is possible that during the formation of an MGI, a disruption in the c-axis periodicity from its nominal value of 0.35 nm has occurred. It has been reported that the pressure required to exfoliate graphite is ~0.4 MPa [83]. There are two possible forces that might initiate delamination: (i) electrostatic pressure on the topmost surface due to the electric field produced by the surface charge distribution σ and (ii) the capillary force exerted on the substrate upon liftoff when using a biased tip. Using values of σ inferred above, it is easy to decide that the electrostatic pressure is negligible. However, the ~ 32 nN liftoff forces, as inferred from Figure III.3a, can produce a pressure that exceeds that required to exfoliate graphite. This lift-off force is concentrated around the perimeter of the MGI and it may serve to delaminate the top-most graphitic layers as the tip is pulled away. Furthermore, the evolution of CO and CO_2 gases during lithography may also contribute to a disruption of the c-axis periodicity. Such delamination effects would further isolate the topmost layer(s) of graphite from the underlying substrate and may contribute to the observed non-linearity in I-V when measured along the c-direction. This observation further suggests that in addition to the lateral isolation produced by the trenches formed around the perimeter, there may be an additional isolation along the c-axis due to incorporation of oxy moieties inducing some charge localization in the top most layers of MGIs.

III.5 Conclusions

This study brings out a set of conditions required for electrophysical and chemical modifications on a dielectric EBICD surface using a biased AFM tip under different humidity conditions and mode of operation. The carbonaceous platforms on Si were created by the electron beam induced deposition using residual hydrocarbons along with water vapor at 0.4 Torr. The carbonaceous deposits contain functional groups such as carbonyl, carboxyl and hydroxyl etc. AFM bias lithography was performed under different conditions such as mode of operation, polarity of the tip bias and RH. Under an optimum RH of 40-45% favor the local anodic oxidation in either contact or tapping modes under a

negative tip bias. Further, higher humidity conditions (~60%) cause the spatial distribution of oxidative species due to shock wave generation. Under low humidity conditions (~ 30%), reversible charge patterns have been created depending on the tip bias polarity. Exclusively, positive tip voltages in the tapping mode at humidity of 40-45% favor the condensation of water on the carbonaceous platforms.

The electrochemical modifications (oxidation and etching) of HOPG surfaces have been realized during AFM bias lithography in contact and intermittent contact modes. The above phenomenon was utilized to fabricate MGIs that are laterally isolated from the HOPG substrate. The electrical properties of these MGIs were characterized using EFM and conducting AFM. The EFM studies have revealed that these MGIs are permanently polarized. The electrical transport through the interior of an MGI is non-linear as shown by conducting AFM experiments. These observations can be attributed to the local change of electronic structure by incorporation of oxy functional groups around the perimeter of an MGI during the lithographic process. The above study offers a facile method to create spatially confined graphene-like structure that could form the foundation of functional devices, namely mesoscopic graphitic islands. Further studies should focus on extraction and transfer of few-layer graphene from MGIs onto desired substrates such as boron nitride [84] in lieu of growing graphene on common substrates. This way, the advantages of pristine, suspended graphene can be preserved in lieu of the deleterious interactions with most substrates. In addition, the oxy functional groups at the trenches offer a means of decorating molecules of specific interest carrying suitable mating groups [85].

References

[1]   G. Binnig, C.F. Quate and C. Gerber, *Phys. Rev. Lett.*, 1986, **56**, 930.
[2]   D. Bonnell, *Scanning Probe Microscopy and Spectroscopy*; Ed.; Wiley-VCH: New York, 2000.
[3]   X. N. Xie, H. J. Chung, C. H. Sow and A. T. S. Wee, *Materials Science and Engineering R: Reports*, 2006, **54**, 1.
[4]   B. Cappella and H. Sturm, *J. Appl. Phys.*, 2002, **91**, 506.
[5]   Y. Sugimoto, M. Abe, S. Hirayama, N. Oyabu, Ó. Custance and S. Morita, *Nat. Mater.*, 2005, **4**, 156.
[6]   K. Salaita, Y. Wang and C. A. Mirkin, *Nature Nanotech.*, 2007, **2**, 145.
[7]   D. S. Ginger, H. Zhang and C. A. Mirkin, *Angew. Chem., Int. Ed.*, 2003, **43**, 30.
[8]   R. D. Piner, J. Zhu, F. Xu, S. Hong, C. A. Mirkin, *Science*, 1999, **283**, 661.

[9] Y. Li, B. W. Maynor and J. Liu, *J. Am. Chem. Soc.*, 2001, **123**, 2105.

[10] R. Garcia, R. V. Martinez and J. Martinez, *Chem. Soc. Rev.*, 2006, **35**, 29.

[11] S. F. Lyuksyutov, R. A. Vaia, P. B. Paramonov, S. Juhl, L. Waterhouse, R. M. Ralich, G. Sigalov and E.Sancaktar, *Nat. Mater.*, 2003, **2**, 468.

[12] T. Vijaykumar and G. U. Kulkarni, *Nanotechnology*, 2007, **18**, 445303.

[13] M. A. Reagan, D. Kashyn, S. Juhl, R. A. Vaia and S. F. Lyuksyutov, *Appl. Phys. Lett.*, 2008, **93**, 033109.

[14] X. N. Xie, H. J. Chung, Z. J. Liu, S. -W. Yang, C. H. Sow and A. T. S. Wee, *Adv. Mater.*, 2007, **19**, 2618.

[15] P. Mesquida and A. Stemmer, *Adv. Mater.,* 2001, **13**, 1395.

[16] L. Ressier and V. L. Nader, *Nanotechnology*, 2008, **19**, 135301.

[17] P. Mesquida, H. F. Knapp and A. Stemmer, *Surf. Interface Anal.,* 2002, **33**, 159.

[18] Y. Xie, C. Bell, T. Yajima, Y. Hikita and H. Y. Hwang, *Nano Lett.*, 2010, **10**, 2588.

[19] L. Tapaszto, G. Dobrik, P. Lambin and L. P. Biro, *Nat. Nanotechnol.*, 2008, **3**, 397.

[20] L. Weng, L. Zhang, Y. P. Chen and L. P. Rokhinson, *Appl. Phys. Lett.*, 2008, **93**, 093107.

[21] N. Yoshimizu, B. Hicks, A. Lal and C. R. Pollock, *Nanotechnology*, 2010, **21**, 095306.

[22] J. Park, K. B. Kim, J. -Y. Park, T. Choi and Y. Seo, *Nanotechnology*, 2011, **22**, 335304.

[23] J. G. Park, C. Zhang, R. Liang and B. Wang, *Nanotechnology*, 2007, **18**, 405306.

[24] Y. Jiang and W. Guo, *Nanotechnology*, 2008, **19**, 345302.

[25] D.-H. Kim et al., Phys. Rev. B., 2003, **68**, 113406.

[26] J. -Y. Park, Y. Yaish, M. Brink, S. Rosenblatt and P. L. McEuen, *Appl. Phys. Lett.*, 2002, **80**, 4446.

[27] S. Masubuchi, M. Ono, K. Yoshida, K. Hirakawa and T. Machida, *Appl. Phys. Lett.*, 2009, **94,** 082107.

[28] I. -S. Byun et al., *ACS Nano*, 2011, **5**, 6417.

[29] S. Masubuchi at al., *Nanolett.*, 2011, **11**, 4542.

[30] S. Neubeck, F. Freitag, R. Yang and K. S. Novoselov, *Phys. Status Solidi B*, 2010, **247**, 2904.

[31] T. Mühl and S. Myhra, J. Phys. D: Appl. Phys., 2007, **40**, 3468.

[32] P. S. Spinney et al., *Nanolett.*, 2007, **7**, 1512.

[33] J. Melcher, S. Hu, and A. Raman, *Rev. Sci. Instrum.*, 2008, **79**, 061301.

[34] T. Stifter, O. Marti and B. Bhushan, *Phys. Rev. B*, 2000, **62**, 13667.

[35] J. Jang, G. C. Schatz and M. A. Ratner, *Phys. Rev. Lett.*, 2004, **92**, 085504.

[36] J. W. van Honschoten, N. Brunets and N. R. Tas, *Chem. Soc. Rev.*, 2010, **39**, 1096.

[37] Nosonovsky et al., *Phys. Chem. Chem. Phys.*, 2008, **10**, 2137.

[38] M. Kohonen, N. Maeda and H. K. Christenson, *Phys. Rev. Lett.*, 1999, **82**, 4667.

[39] B. L. Weeks et al., *Langmuir*, 2005, **21***,* 8096.

[40] M. Schenk, M. Fu¨ting and R. Reichelt, *J. Appl. Phys.*, 1998, **84**, 4880.

[41] R. D. Piner et al., *Langmuir*, 1997, **13***,* 6864.

[42] A. Méndez-Vilas, A. B. Jódar-Reyes and M. L. González-Martín, *Small*, 2009, **5**, 1366.

[43] J. E. Sader, J. W. M. Chon and P. Mulvaney, *Rev. Sci. Instrum.*, 1999, **70**, 3967.

[44] T. Mühl, H. Brückl, G. Weise and G. Reiss, *J. Appl. Phys.*,1997, **82**, 5255.

[45] R. Garcia, R. V. Martinez and J. Martinez, *Chem. Soc. Rev.*, 2006, **35**, 29.

[46] A. L. Sumner et al., *Phys. Chem. Chem. Phys.*, 2004, **6**, 604.

[47] Asay and Kim, *J. Phys. Chem. B*, 2005, **109**, 16760.

[48] Asay and Kim, *J. Chem. Phys.*, 2006, **124**, 174712.

[49] B. Cappella and G. Dietler, *Surf. Sci. Rep.*, 1999, **34**, 1.

[50] He et al., J. Chem. Phys., 2001, **114**, 1355.

[51] Calleja et al., *J. Appl. Phys.*, 2002, **92**, 5539.

[52] T. Cramer, F. Zerbetto and R. García, *Langmuir*, 2008, **24**, 6116.

[53] F. Pérez-Murano, G. Abadal, N. Barniol, X. Aymerich, J. Servat, P. Gorostiza, F. Sanz, *J. Appl. Phys.*, 1995, **78**, 6797.

[54] A. Avramescu, A. Ueta, K. Uesugi and I. Suemune, *Appl. Phys. Lett*., 1998, **72**, 716.

[55] A. Verdaguer et al., *Appl. Phys. Lett.*, 2009, **94**, 233105.

[56] S. Gómez-Moñivas, J. J. Sáenz, M. Calleja and R.García, *Phys. Rev. Lett.*, 2003, **91**, 056101.

[57] G. M. Sacha, A. Verdaguer and M.Salmeron, *J. Phys. Chem. B*, 2006, **110**, 14870.

[58] N. Miura, H. Ishii, J. I. Shirakashi, A. Yamada and M. Konagai, *Appl. Surf. Sci.*, 1997, **113–114**, 269.

[59] S. F. Lyuksyutov, P. B. Paramonov, R. A. Sharipov, G. Sigalov, *Phys. Rev. B*, 2004, **70**, 174110.

[60] J. H. Kim, S. I. Ahn, J. H. Kim and W. C. Zin, *Langmuir*, 2007, **23**, 6163.

[61] C. Hock, M. Schmidt, R. Kuhnen, C. Bartels, L. Ma, H. Haberland and B.v. Issendorff, *Phys. Rev. Lett.*, 2009, **103**, 073401.

[62] V. Znamenskiy, I. Marginean and A. J. Vertes, *Phys. Chem. A*, 2003, **107**, 7406.

[63] C. D. Daub, D. Bratko, K. Leung and A. J. Luzar, *Phys. Chem. C*, 2007, **111**, 505.

[64] J. V. Iribarne and B. A. Thomson, J. Chem. Phys. 1976, **64**, 2287.

[65] G. F. Krymskiĭ and G. S. Pavlov, Dokl. Phys. 2008, **53**, 310.

[66] R. M. Nyffenegger and R. M. Penner, *Chem. Rev.*, 1997, **97**, 1195.

[67] D. Wouters and U. S. Schubert, *Angew. Chem. Int. Ed.*, 2004, **43**, 2480.

[68] X. N. Xie, H. J. Chung, Z. J. Liu, S. -W.Yang, C. H. Sow and A. T. S. Wee, *Adv. Mater.*, 2007, **19**, 2618.

[69] X. N. Xie, H. J. Chung, C. H. Sow, K. Adamiak and A. T. S. Wee, *J. Am. Chem. Soc.*, 2005, **127**, 15562.

[70] X. N. Xie, M. Deng, H. Xu, S. W. Yang, D. C. Qi, X. Y. Gao, H. J. Chung, C. H. Sow, V. B. C. Tan and A. T. S. Wee, J. *Am. Chem. Soc.*, 2006, **128**, 2738.

[71] N. Kurra, G. Prakash, S. Basavaraja, T. S. Fisher, G. U. Kulkarni and R. Reifenberger, *Nanotechnology*, 2011, **22**, 245302.

[72] J. Dagata, J. Schneir, H. H. Harary, C. J. Evans, M. T. Postek and J. Bennett, *Appl. Phys. Lett.*, 1990, **56**, 2001.

[73] H. Sugimura and n. Nakagiri, *Jpn. J. Appl. Phys.*, 1995, **34**, 3406.

[74] C. Kozlowski and P. M. A. Sherwood, *J. Chem. Soc. Faraday Trans.*, 1984, **80**, 2099.

[75] W. Mizutani, J. Inukai and M. Ono, *Jpn. J. Appl. Phys.*, 1990, **29**, L815.

[76] R. L. McCarley, S. A. Hendricks and A. J. Bard, *J. Phys. Chem.*,1992, **96**, 10089.

[77] M. Matsumoto, T. Manako and H. Imai, *J. Electrochem. Soc.*, 2009, **156,** B1208.

[78] T. R. Albrecht, M. M. Dovek, M. D. Kirk, C. A. Lang, C. F. Quate and D. P. E. Smith, *Appl. Phys. Lett*., 1989, **55**, 1727.

[79] S. Banerjee, M. Sardar, N. Gayathri, A. K. Tyagi and B. Raj, *Phys. Rev. B*, 2005, **72**, 075418.

[80] K. N. Kudin, B. Ozbas, H. C. Schniepp, R. K. Prud'homme, I. A. Aksay and R. Car, *Nano Lett.*, 2008, **8**, 36.

[81] M. Zdrojeka, T. Mélin, H. Diesinger, D. Sti´evenard, W. Gebicki and L. Adamowicz, *J. Appl. Phys.*, 2006, **100**, 114326.

[82] S. Ono and K. Sugihara, *J. Phys. Soc. Japan*, 1966, **21**, 861.

[83] X. Liang, A. S. P. Chang, Y. Zhang, B. D. Harteneck, H. Choo, D. L. Olynick and S. Cabrini, *Nano Lett.*, 2008, **94**, 67.

[84] C. R. Dean et al., *Nat. Nanotechnol.*, 2010, **5**, 722.

[85] L. P. David, J. C. Victor and P. B. Jr. Thomas, *Science*, 1994, **265**, 231.

Part IV

Graphene and turbostratic graphite: Electronic and optoelectronic properties

Summary

Graphene, the two dimensional crystalline allotrope of carbon, exhibits unique and extra-ordinary electronic [1-3], optoelectronic [4-6] and physical properties [7-10]. This study pertains to obtaining graphene by top-down (physical) and bottom up (chemical) approaches in addition to investigating electronic and optoelectronic properties. This part also includes a section on deriving the electric field effect from the pencil-traces and fabrication of resistor-capacitor (RC) filters.

The top-down method comprises of laser ablative patterning of highly oriented pyrolytic graphite (HOPG) using a near field transmitting phase mask in a single step and ultra-fast manner. Periodic arrays of lines are patterned on the HOPG surface over large areas by spatially modulating the laser intensity through the mask. Thus, the patterned surface serves as a source for multi- and few-layer graphene ribbons for transferring onto desired substrates using polydimethylsiloxane (PDMS) as the transferring agent. The transferred regions are contained with few-layer graphene (5-6 layers) ribbons as well as thick graphitic ribbons (30-40 nm), with widths ~ 1 μm and lengths of several micrometers. Raman, TEM and electrical measurements have confirmed that the transferred ribbons are highly crystalline in nature. Using combinations of shadow and transmitting phase masks, other patterns such as checker boards and diamond-shaped pits are produced.

Few-layer graphene (FLG) films have been grown via bottom-up (chemical) route with the aid of residual hydrocarbons and polymethylmethacrylate (PMMA) carbon sources. FLG films were directly grown on insulating substrates through thermal annealing in the presence of Ni catalyst. A comparative study of the infrared (IR) photoconductive and bolometric response from FLG to graphitic films obtained by different methods was investigated. FLG obtained from the residual hydrocarbons show IR photoresponse of 73% which is far higher compared to the FLG films (6-14%) obtained from CVD and scotch tape methods. The photoconductive nature of FLG films is due to the generation of

photoexcited charge carriers. On the other hand, the photoresponse of the bulk graphitic films is bolometric in nature where the resistance changes are due to thermal effects. The IR photoresponse from these graphitic films are correlated with the Raman peak intensities which are very sensitive to the nature of the FLG.

Pencil drawing on paper is essentially graphite with turbostratic nature, confirmed through Raman studies. The turbostratic graphite, which is essentially a 2D system due to electronic decoupling of the graphene layers, may have some electronic properties similar to those of graphene. Pencil drawings have been employed as resistor and an ion gel, 1-butyl-3-methyl-imidazolium octylsulfate mixed with PDMS as dielectric for the fabrication of paper based RC filters which showed a cut-off frequency of ~ 9 kHz. Ambipolar electric field effect was observed from the pencil-trace at low operating voltages with the aid of an ion gel as gate dielectric. The carrier mobilities were found to be ~ 106 and 59 cm^2/Vs for holes and electrons respectively. The mobility value showed only 15% variation among few devices tested, truly remarkable given the simplicity of the fabrication process.

IV.1 Laser ablative patterning of HOPG to produce graphene ribbons

IV.1.1 Introduction

Besides the high mobility of charge carriers in the *sp^2* carbon lattice, graphene also exhibits extraordinary properties such as quantum Hall effect and ambipolar electric field effect, which have promoted graphene to be key component in the future electronic devices [2, 11-13]. The ballistic transport of charge carriers in graphene, an important property of this 2D system, remains almost unaffected even down to sub micrometer lateral dimensions, say 0.3 μm at 300 K [1, 2]. Further, the electronic properties of graphene can be tuned from semi-metallic to semiconducting by reducing the lateral dimensions to a few tens of nanometers [14, 15]. It was demonstrated that graphene nanoribbons with lateral dimensions of sub tens of nanometers are semiconducting and the electronic properties are highly influenced by edge states and quantum confinement [14-16].

The reduction in the mobility of the charge carriers due to edge effects (see Table IV.1) may limit the usage of graphene in electronic applications [17, 18]. While it is important to restrict the thickness, it is also desirable to maintain the lateral dimensions of graphene big enough so that the edge effects are minimal [17, 19], unless such effects are desired for specific applications. There have been several attempts in the literature to

isolate the graphene sheets, 1-10 layers thick spreading over several micrometers, from graphite bulk crystals (HOPG) employing micro-mechanical cleavage [1-3, 20], chemical exfoliation [11, 21, 22], liquid-phase exfoliation [23, 24] and growth using chemical vapor deposition [25]. These methods produce randomly distributed graphene sheets on a given substrate and locating them for device fabrication is usually tedious. In order to exercise a control over the site specific placement of graphene, methods such as transfer printing [26, 27], electrostatic exfoliation [28] and site specific stamping of patterned graphite have been developed [29]. A combination of photolithography and reactive ion etching techniques, involving multiple processing steps has also been used for patterning HOPG; such methods are time consuming and expensive [26-29].

IV.1.2 Scope of the present investigation

Here, a resistless direct patterning method for HOPG is presented, which operates based on single laser pulses through a transmitting phase mask. This approach is different from the commonly used pulsed laser interference lithography. The latter is a well-established technique where two or more laser beams are made to interfere to produce periodic structures on surfaces of metals, polymers and amorphous-carbon films [30-32]. Recently, the carbon nanotube films have been patterned using this technique [33]. Unlike the laser interference lithography, which requires multiple beams with additional optical elements, single laser pulse based lithography using a near field phase shifting mask sounds equally promising. The light passing through a phase shifting mask diffracts in the far field and modulates the intensity in the near field according to its grating parameters [34]. This concept has been employed in photolithography to improve resolution [34, 35] which has been adopted for direct patterning by near-field ablation. Using this method, various types of patterns on HOPG surfaces have been produced, by ablating carbon to form periodic array of check boards, line gratings of ~ 1.1 μm wide and spacing of 450 nm over mm^2 area. Other shapes such as diamond or square pits have also been produced in large arrays. Using polydimethylsiloxane (PDMS) layer, the patterned regions were transferred onto different substrates and thus produce essentially multi or few layer graphene ribbons.

IV.1.3 Experimental Details

The HOPG used in the present experiments was purchased from NT-MDT, ZYB grade and was characterized by a mosaic spread of ~0.8°. Before patterning, a fresh surface was prepared by stripping away a few layers using the conventional sticky tape technique. Polycarbonate absorbs at 193 nm with an absorption coefficient of ~10^5 cm^{-1}. It absorbs only 15% at 355 nm and transmits 85% of the light (see Figure IV.1) [36].
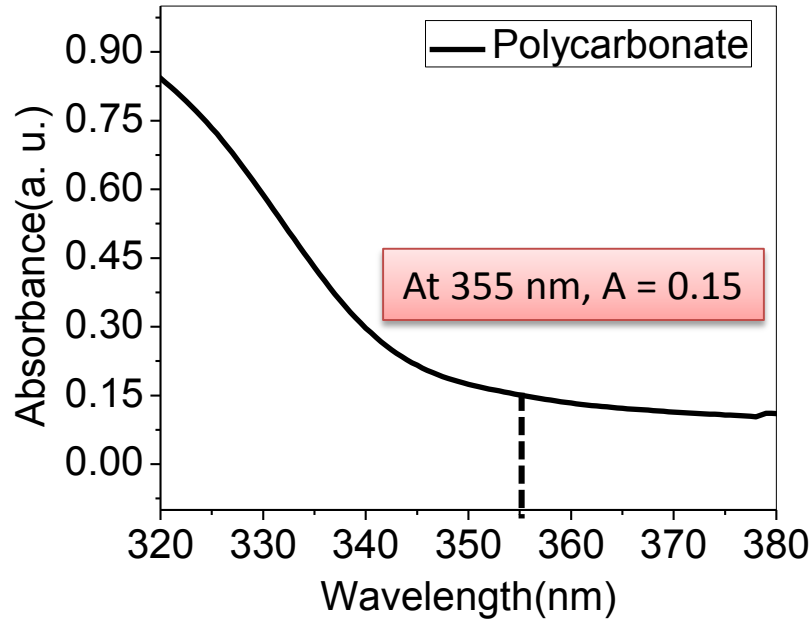
Figure IV.1 UV-Vis absorption spectrum for the polycarbonate, with absorption of 15% at 355 nm.

PDMS required for transferring the patterned graphene layers was prepared by mixing Sylgard 184 curing agent (Dow Corning) and its elastomer in the ratio of 1:5 by weight. The mixture is then degassed under vacuum for 30 minutes. A SiO$_2$ (300 nm)/Si wafers were cleaned by sonicating in acetone and isopropanol, dried by blowing dry nitrogen.

IV.1.4 Results and Discussion

The table below shows the dependence of the electronic properties of the graphene with respect to its lateral dimensions. Graphene exhibits ballistic transport up to a width of 0.3 μm and as the size decreases, the band gap opens up and scattering of charge carriers by the edges come into picture which cause the degradation in the mobility of the charge carriers (see Table-IV.1).
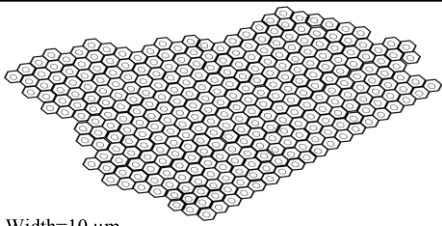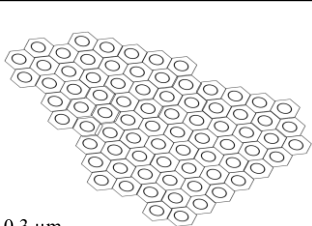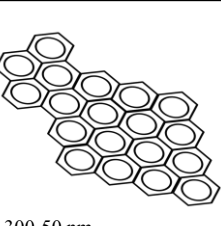
	Width=10 μm	1-0.3 μm	300-50 nm	50-5 nm
Edge effects	No edge effects Only phonon scattering	No edge effects Only phonon scattering	edge effects and phonon scattering	Edge effects dominating & Band gap opening
Mobility $(cm^2V^{-1}s^{-1})$	40,000 [1, 2]	40,000 [1, 2]	3,000-1,000 [14, 15]	200-10 [16, 19]
Band gap (eV)	0	0	0.05	0.3-1.0
Applications	Transparent conducting electrodes, solar cells	Nano electronics, space optimization	Field effect transistors	Field effect transistors

Table-IV.1 Dependence of electronic properties of graphene with respect to different lateral dimensions. The relevant references are indicated.

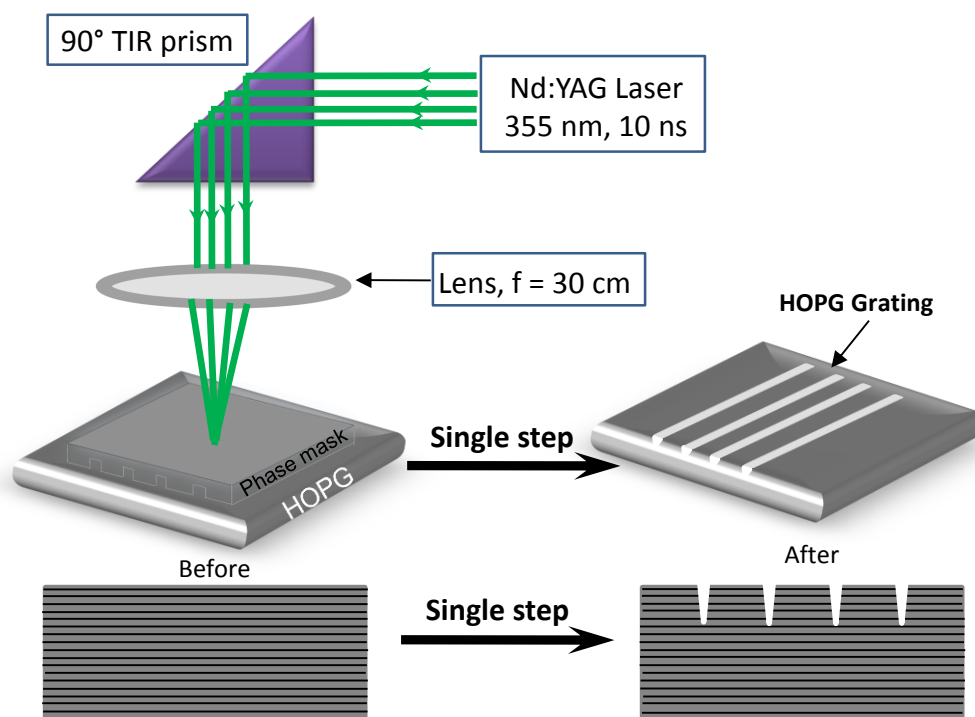## IV.1.4.a Pulsed Laser Ablative Patterning of HOPG

Figure IV.2 Direct laser interference patterning using a proximal transmitting diffraction grating. A schematic showing ultrafast, single step and large area direct fabrication of patterns on HOPG surface. The bottom panel shows a side view of the HOPG grating structure.

Figure IV.2 describes the direct patterning process of HOPG by laser ablation. A small (15 x 15 mm^2) piece of a compact disc (CD), composed of an array of parallel lines with a width of 1 µm, spacing of 500 nm and a height 180 nm, was used as a transmitting phase mask and kept in contact to the HOPG substrate (Figure IV.2) with no additional pressure. This assembly was exposed to a single shot of Nd:YAG laser (λ= 355 nm, ~ 100 mJ/pulse) in a Q-switch mode under ambient atmosphere. A 30 cm focal point lens was used and the diameter of the partially defocused laser beam was typically ~ 2 mm. A single shot of laser pulse was sufficient to produce the imprint of the phase mask on the HOPG surface (Figure IV.2).
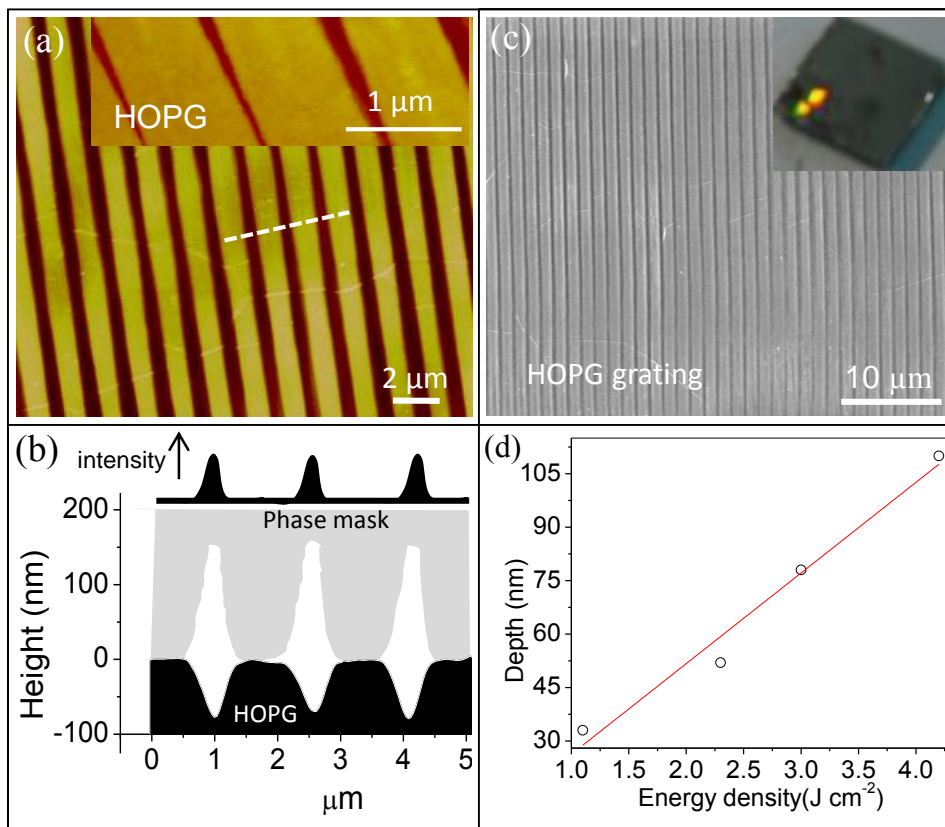
Figure IV.3 (a) AFM topography image of graphitic grating patterns on HOPG and inset is the magnified AFM image of the HOPG grating (b) The comparative AFM z-profiles of CD phase mask (gray) and patterned HOPG (black) in close proximity, a schematic of the spatially varying laser intensity pattern is shown on top (c) Typical SEM image of the patterned HOPG surface, and the inset shows the optical image of HOPG grating spots which diffract the light (d) Plot of depth of patterns with laser fluence (J cm^{-2}) used in the experiments.

AFM topography image of the periodic line arrays on HOPG (Figure IV.3a) showed parallel stripes with width of 1.1 µm separated by ~ 450 nm and height of ~ 80 nm. The

periodic unablated areas of HOPG are smooth as those regions are unaffected during the laser irradiation (see inset of Figure IV.3a). The AFM height profile of the phase mask when compared with that of the produced pattern (Figure IV.3b), shows that the width of the pattern is nearly the same as the relief feature (~ 1100 nm), but the trench depth is only ~ 80 nm, in contrast to 180 nm in the phase mask. This observation implies that the laser intensity gets amplified through land regions [35], thus causing periodic ablation of graphite surface (see schematic in Figure IV.3b). Figure IV.3c shows typical SEM image of the HOPG grating pattern over a large area. The optical photograph in the inset shows the grating action from the patterns exhibiting colors. The depth of laser ablation can be well controlled by adjusting the laser fluence (Figure IV.3d); the variation is as expected, linear at lower laser fluence [37]. A minimum depth of 25-30 nm was achievable with a Q-switch threshold fluence of 1.1 J cm^{-2} and is comparable to the skin depth of HOPG, typically 20 nm (absorption coefficient ~ 5×10^5 cm^{-1}) [37].

IV.1.4b Transferring of graphitic ribbons

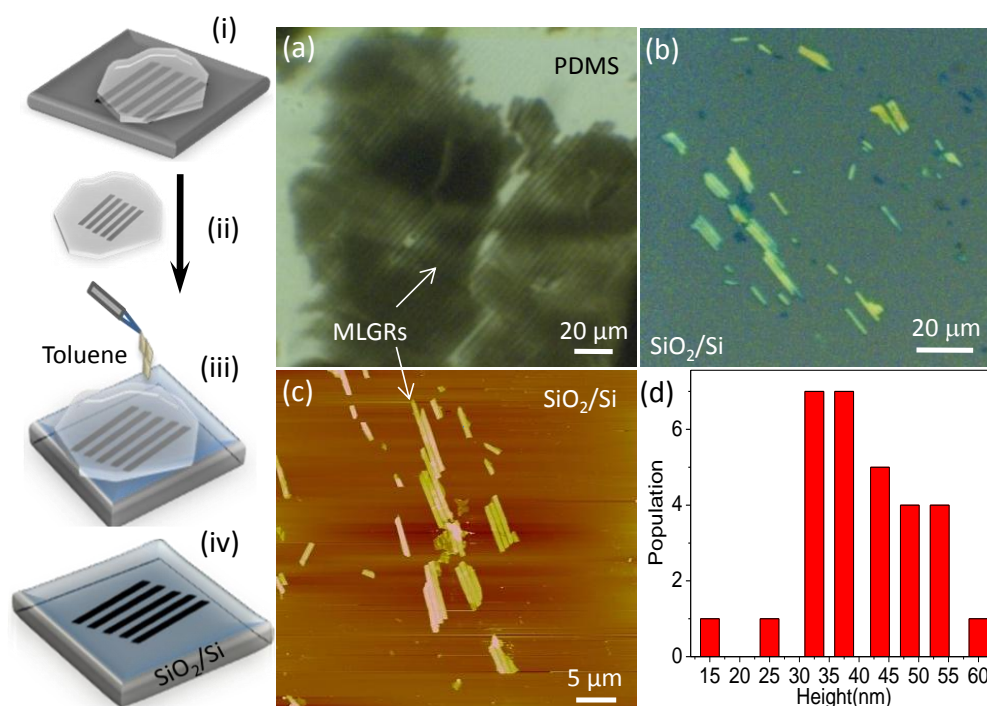
Figure IV.4 Left, schematic showing the steps involved in the transferring of G-ribbons on a desired substrate. Right, Optical micrographs of graphitic ribbons on the cured PDMS (a) and transferred onto SiO$_2$/Si (b). (c) AFM image of graphitic ribbons transferred on a SiO$_2$/Si substrate and (d) a histogram showing the distribution of heights of the transferred graphitic ribbons in (c).

The patterned regions from HOPG could be successfully transferred onto a desired substrate such as SiO_2/Si (Figure IV.4) using a known method [38, 39]. A small drop of the PDMS pre-polymer and curing agent (5:1) was drop coated on the HOPG surface covering the pattern, this was subjected to curing at 60 ºC overnight (Figure IV.4a). On gently peeling off the cured PDMS from the HOPG, the patterns came attached to the PDMS surface. The optical image in Figure IV.4a shows parallel sets of the ribbon-like structures adhering to the PDMS surface. The PDMS surface carrying the ribbons was then placed on a desired substrate (SiO_2/Si) while pouring few drops of toluene under gentle pressure. This procedure enables the swelling of PDMS (see the schematic in the left, Figure IV.4) followed by the release the ribbons from its surface. PDMS was then removed and the substrate was heated to 130 ºC to remove residual solvent. From the optical and AFM images shown in Figures IV.4b and c respectively, several individual and aligned ribbons can be seen lying on the SiO_2/Si substrate with relative orientation well maintained. The histogram of thickness distribution estimated using AFM height profiles (Figure IV.4d), indicates that most ribbons exhibit thickness in the range of 30-40 nm with only a few below 20 nm. Thus, the features are essentially multi-layer graphene ribbons (MLGRs). The widths of MLGRs are nearly 1.1 µm as expected.
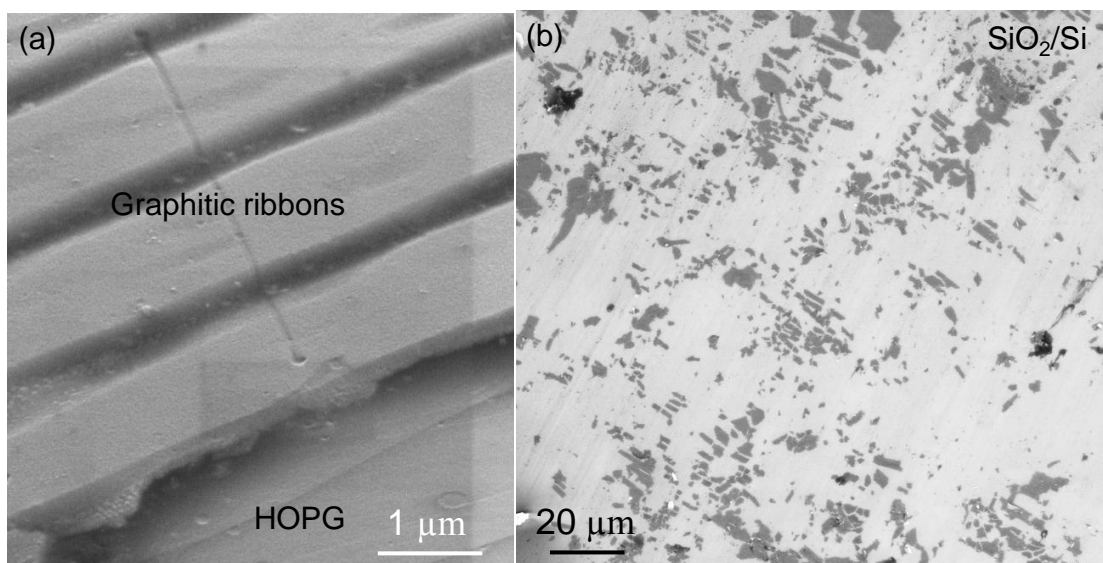

Figure IV.5 (a) SEM tilt image shows that the edge of the graphitic ribbon contains recrystallized carbon. The line drawn across the width is from electrochemcial etching using a biased AFM tip in a different experiment. (b) High throughput production of graphitic ribbons on SiO_2/Si.

The uneven edges of graphitic ribbons at some locations may arise during the transferring process (see Figure IV.5a). Biased AFM tip could etch the graphitic ribbons via local electrochemical oxidation (see Figure IV.5a). The above described transfer method enables high through-put production of MLGRs as illustrated in Figure IV.5b.

IV.1.4c Characterization of MLGRs

The Raman spectrum of HOPG (curve (i) in Figure IV.6a) has two major peaks at 1580 cm^{-1}(G -band) and 2690 cm^{-1} (2D band). The G band is due to in plane vibrations of sp^2 carbon network [40]. The D band at 1330 cm^{-1} arises due to disorder such as topological or functional defects in the large sp^2 carbon network. Though the D band is not seen at all locations on a HOPG surface, its overtone (2D band) is seen as it is very sensitive to the stacking order of graphite sheets along c-axis [41]. A Raman spectrum has been recorded on the HOPG grating (see red curve, (ii)) and it is similar to the HOPG (black curve). This indicates that under single shot mild irradiation (laser fluence ~ 1.1 J cm^{-2}), the pristine nature of graphite is well preserved [33]. The evolution of small D band in the MLGRs (see blue curve, (iii)) is essentially due to the edge defects. What is noteworthy is that the sp^2 crystallinity is highly preserved across the interior regions of the ribbon as the edges get formed during ablation.

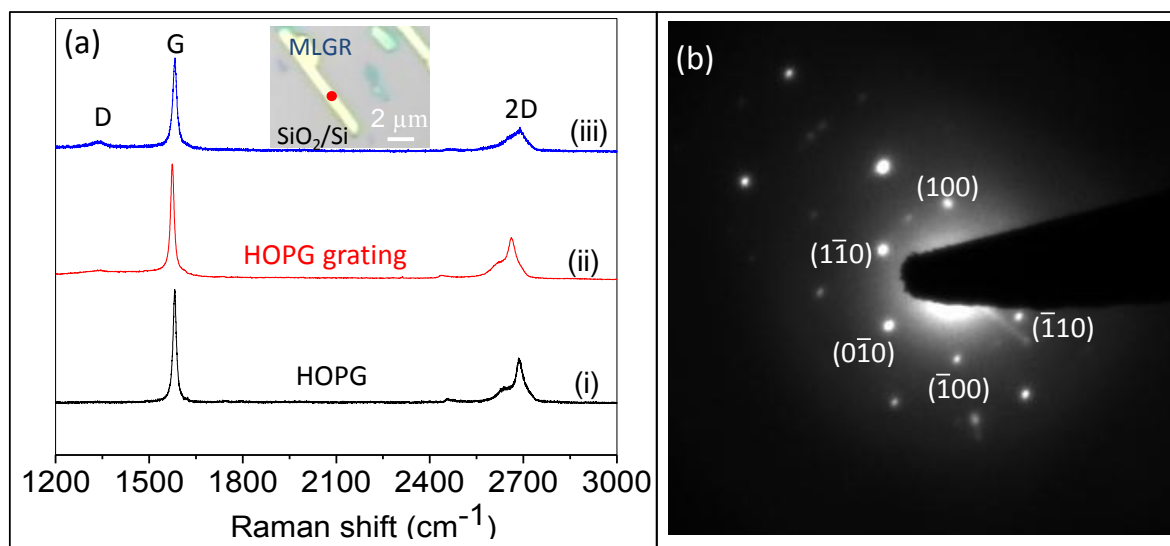**Figure IV.6** (a) The comparative (and normalized) micro Raman spectra (λ = 632.8 nm, spot diameter = 2 µm) of the HOPG (black curve, (i)), HOPG grating (red curve, (ii)) and the transferred graphitic ribbons on SiO$_2$/Si (blue curve, (iii)). Inset shows optical image of the ribbons on SiO$_2$/Si during Raman measurements, and (b) Electron diffraction pattern of the ribbon.

The transferring process using PDMS in the presence of mild solvents also do not seem to affect the crystallinity. The electron diffraction patterns collected at the different locations on a MLGR showed bright spots with the hexagonal symmetry (see Figure IV.6b). The mis-alignment of secondary set of hexagonal diffraction spots with respect to the inner set was observed. This occurs either due to the slight mis-orientation between A-B stacked graphene layers or due to incidence of the electron beam away from the normal [42].

On the other hand, multiple laser shots (5-10) may cause structural modification of the HOPG depending on the magnitude of laser fluence where the intensity of the D band is more than that of the G band, disrupting the c-axis periodicity [41] (see Figure IV.7).
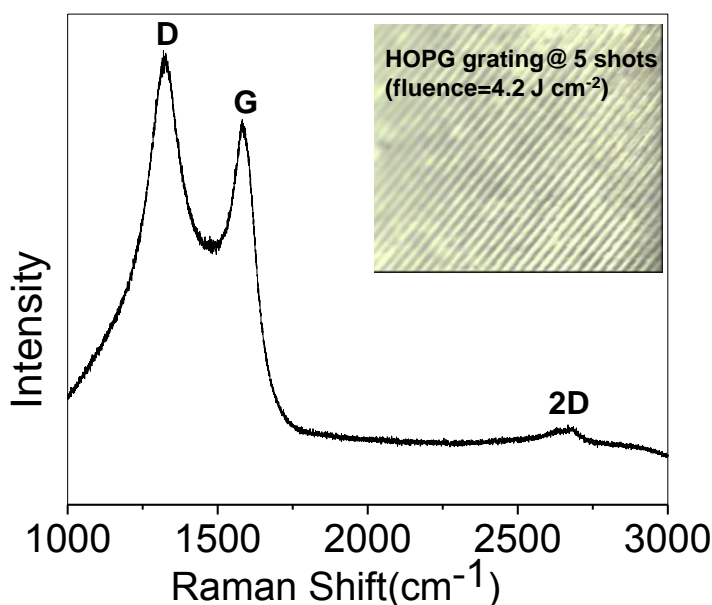
Figure IV.7 Raman spectrum on the HOPG grating created under laser irradiation(fluence = 4.2 J cm^{-2}) of 5 shots. The higher intensity of D band compared to the G band and changes in the shape of 2D band reveals those significant structural modifications to the HOPG. Inset shows the optical image of the HOPG grating.

The electrical nature of the MLGRs has been investigated. The in-plane I-V characteristics measured by placing a MLGR of thickness 25 nm across the Au gap electrodes on SiO$_2$/Si substrate (Figure IV.8a), showed a linear behavior with a resistance of ~1 kΩ which also includes the contact resistance from the gold-graphite interface (see bottom panel of Figure IV.8a). The two probe measurements have also been performed in the transverse direction (across the thickness of the MLGR). For this purpose, the MLGRs from PDMS were transferred onto a fresh HOPG surface which served as the bottom

electrode while a conducting atomic force microscopy tip was brought in contact as the top electrode. In order to minimize the contact resistance between the MLGR and HOPG, the sample has been heated at 200 ºC for 15 minutes, prior to cAFM measurement. Figure IV.8b shows the AFM topography image of MLGRs (thickness of 30 nm, 3 μm wide and 12 μm long) on HOPG substrate.
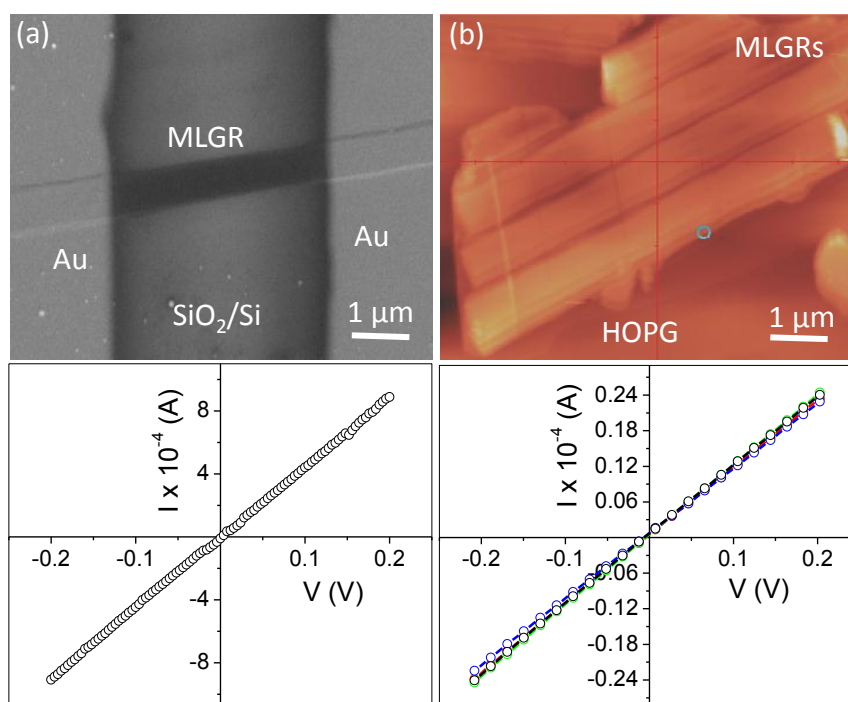
Figure IV.8 Two probe current-voltage characteristics MLGRs. (a) Top, FESEM image of single ribbon across gold contacts on SiO₂/Si substrate and bottom, in plane I-V measurement, and (b) AFM topography of ribbons on HOPG and the I-V curves acquired using CAFM in transverse geometry are shown below.

A number of I-V curves have been recorded by placing the conducting tip at different locations on the surface of the MLGRs (see bottom panel of Figure IV.8b). The average resistance of MLGR in the transverse geometry was found to be ~ 23 kΩ with unknown tip-sample contact resistance. These observations indicate that the MLGRs produced from the patterning process are well conducting and retain the graphitic character.

IV.1.4d Transferring and characterization of graphene ribbons

By optimizing the transferring conditions, it is possible to obtain quite thin and few layer graphene ribbons (FLGRs) (thickness ~ 2-3 nm) as shown in Figure IV.9.
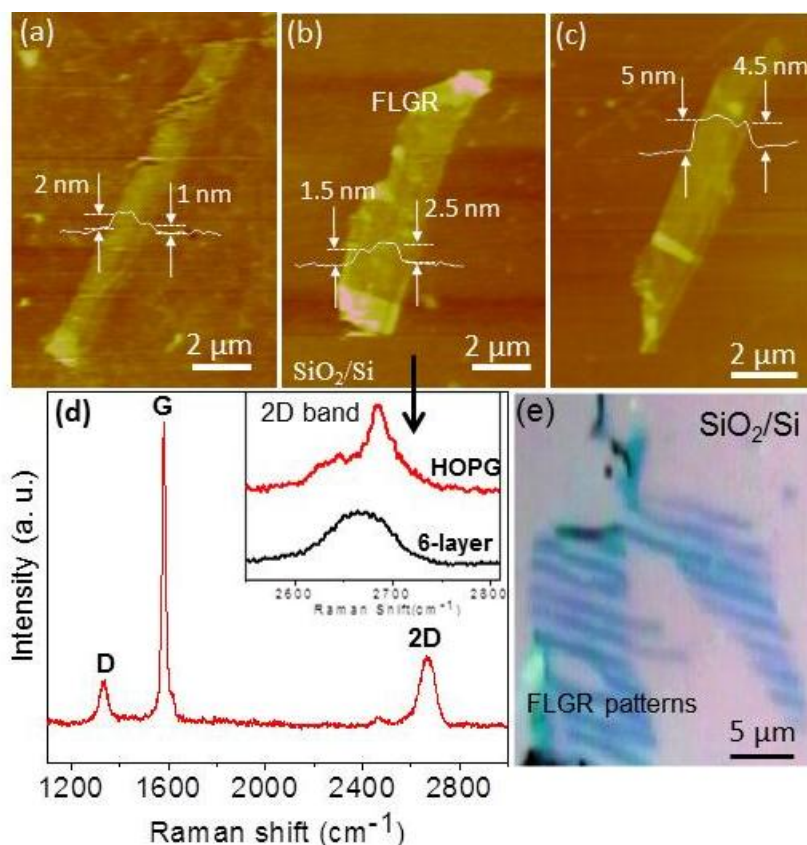
Figure IV.9 Transferring few layer graphene ribbons (FLGRs) onto SiO_2/Si substrate. AFM topography images revealing ribbons of different thicknesses, (a) 2 nm, (b) 2.5 nm and (c) 5 nm. The corresponding z-profiles are shown; ribbon width is ~ 1.2 μm. (d) Raman spectrum of the FLGR and the 2D band from the ribbon is compared with that from HOPG in the inset. (e) Optical micrograph showing the FLGR patterns after transferring onto the SiO_2/Si.

This was made possible by bringing HOPG in contact with PDMS while the latter was being cured at 120 ℃, instead of contacting prior to curing. This way, the adhesion of PDMS with HOPG could be controlled. After thinning the ribbons while being on the PDMS surface by repeated peel-off, the ribbons were transferred onto SiO_2/Si substrate by swelling the PDMS (see Figure IV.4).

The ribbons are relatively thin as seen from the AFM images and the associated profiles in Figure IV.9. The FLG ribbon in Figure IV.9b, for example, is ~ 2 nm thick containing ~ 6 graphene layers and its Raman spectrum in Figure IV.9d shows the D-band at 1380 cm^{-1}, G band at 1580 cm^{-1} and the 2D band at 2685 cm^{-1}. As the 2D band reflects the electronic band structure, the shape and position of 2D band is very sensitive to the number of graphene layers [43]. As shown in the inset of Figure IV.9d, the 2D band of the FLGRs consists of a broad single peak red shifted with respect to the HOPG 2D band,

which is a signature of 5-6 layer graphene [44]. The optical micrograph shows the transferred FLGR patterns on the SiO_2/Si substrate (see Figure IV.9e).

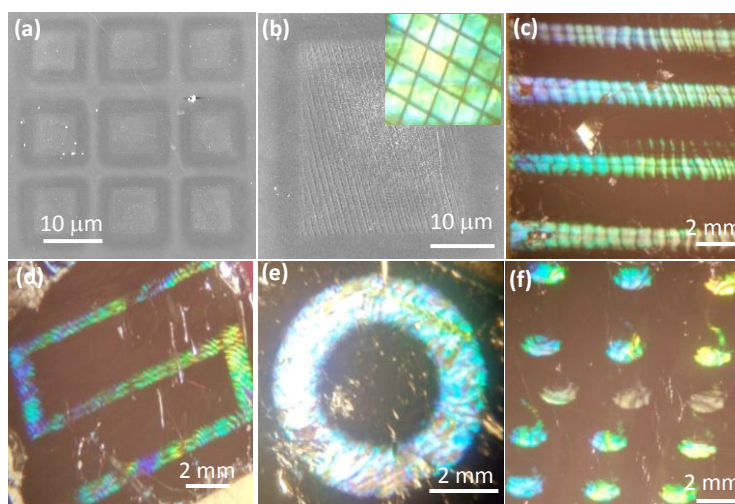### IV.1.4e HOPG gratings-other geometric patterns

Figure IV.10 Ultra-fast large area patterning of HOPG using shadow mask and transmitting phase masks or a combination of both, FESEM images of (a) the imprint of TEM grid on the HOPG (b) a block of line patterns in the laser irradiated regions (TEM grid was used in combination with the CD) and the optical micrograph shows square blocks of colors due to diffraction light from the grating features (see inset). Optical micrographs of laser ablative patterning of the HOPG (c) in continuous manner (d) raster fashion (e) circular and (f) well separated periodic manner using a motor controlled X-Y stage.

To explore the versatility of the presented lithography technique, HOPG was patterned with many functional geometrical shapes (shown in Figure IV.10) using a combination of a shadow mask and a transmitting phase mask. A second laser shot on a HOPG grating hosting a phase mask with its features running perpendicular, produced a check board pattern on the HOPG (Figure IV.11a). This is simply a superposition of the two sequential patterns. Similarly, an array of diamond like pits were patterned on HOPG (Figure IV.11b) after irradiating the single laser pulse (energy fluence = 4.2 J cm^{-2}) through the stack of two phase masks with their patterns aligned at an angle of 130º. This is a clear indication of modulating the laser intensity in the 2-dimensional manner to produce periodic array of holes whose shape depends on the orientation of the patterns of phase masks. Similar to the CD imprint on HOPG, digital videodisk (DVD) or anything similar can also serve as a transmitting phase mask (Figure IV.11c). In this case, obviously, the patterned features were much narrower, in conformity with grating parameters of the phase mask.
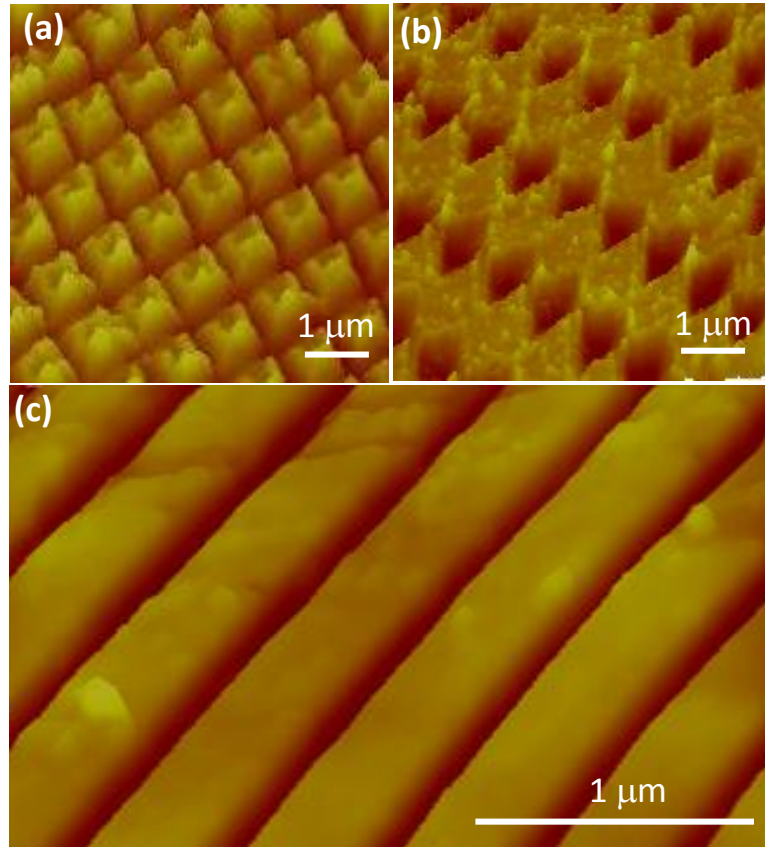
Figure IV.11 AFM images of various grating patterns on HOPG (a) a check board, (b) periodic diamond like pits (c) fine grating derived from using DVD as a transmitting diffraction grating.

In this study, the periodicity of the fabricated features on the HOPG does not primarily depend on the wavelength of the laser light used, but depends on the periodicity of the phase mask. A CD as a phase mask served ideally. The feature widths (~ 1.2 µm) are somewhat larger for edge effects to really dominate, yet small enough for miniaturization. Besides, the CD is flat and smooth and makes conformal contact with the substrate surface, important for large area patterning. The CD material, polycarbonate, absorbs only below 300 nm so that optical and UV lasers could be used. Unlike other UV transmission masks such as quartz gratings, a CD is inexpensive (also quartz is hard and may pose difficulty for conformal contact). The method uses rather simple laser geometry with a single pulse to imprint the periodic features of the mask via the near field. While this principle has been demonstrated in photolithography to create fine features [34, 35], in this study, it has been employed to imprint features on carbon (HOPG) surface by direct ablative patterning. It can be applied to the other surfaces (metals, semiconductors and insulators) as well. The patterning of HOPG is due to ablation of the carbon and not oxidation, as there was no

evidence for any oxy functional groups in Raman studies. A simple PDMS mediated transfer process produced ribbons from patterned regions. The Raman measurements along with TEM, SEM and AFM confirmed the graphitic nature of the ribbons with smooth surfaces. PDMS transfer process is not restricted to one time from a given region of HOPG, indeed it has been employed at least 5 to 6 times successfully from a patterned region, interestingly, using the same PDMS stamp. While some control on the ribbon thickness has been possible while transferring, very thin ribbons amounting to single layers has been somewhat difficult. Lowering the laser fluence to cause very mild ablation (to result in single layers while transferring) is also not viable, as the ablation took place only above a threshold fluence (1.1 J cm^{-2}) already causing a depth of 20-25 nm. This is due to the intrinsic optical properties of HOPG (skin depth = 20 nm, absorption coefficient = 5x10^5 cm^{-1}). Below the threshold energy, there will be no ablation and only electronic excitations of the material takes place. Leaving apart these few limitations, the method is ultra-fast and covers large areas and makes use of neither the expensive combinations of optics and lasers nor a number of process steps involving resists, developers and etchants as in photolithography. Using a combination of masks to generate interesting patterns is a simple extension.

IV.1.5 Conclusions

Ultra-fast, large area and direct patterning of HOPG surfaces have been realized using single shots of pulsed laser in presence of a transmitting diffraction grating. This is essentially a near field interference ablation process. The periodic modulation of laser beam intensity in the presence of a phase mask, ablates the material to produce the patterns on the HOPG. The patterned areas of HOPG were transferred to the desired substrates using PDMS as a transferring agent. The transferred areas contain few layer (5-6 layers) graphene ribbons with a width of ~ 1μm and a length of several microns. As the minimum depth of laser ablation is around 30-40 nm, the transferred regions contain high yield of 30-40 nm thick graphitic ribbons. The graphitic ribbons have been characterized through Raman, TEM and electrical measurements, confirming they are high quality and crystalline in nature**.**

IV.2 Few-layer graphene to graphitic films: Infrared photoconductive versus bolometric response

IV.2.1 Introduction

Graphene absorbs only 2.3% of visible radiation and has been employed as a transparent conductor in the solar cell applications [45-47]. Graphene absorbs over a wide range of electromagnetic radiation from infra-red (IR) to terahertz, due to the large strength of intraband and interband transitions involving the valence and conduction bands [45, 48]. Due to high mobility of charge carriers in graphene, single and also few layer graphene have been exploited in fabricating ultrafast photodetectors [49]. In addition, phototransistors have been fabricated using graphene nanoribbons [50]. Different studies have demonstrated the origin of photocurrent generation by studying the role of interfaces which mainly include single and bilayer regions [51], edge regions [52] and near metallic contacts [53]. The photoresponse from graphene based p-n junctions [54, 55], ultrafast hot carrier effects in graphene, electron-hole separation near the graphene-metal contacts and the generation of photocurrents have been investigated [56-58]. Position dependent photocurrents in reduced graphene oxide (RGO) films have demonstrated the role of the carbon-metal interface [59-61]. Hybrid structures of Au, ZnO and PbS quantum dots in combination with graphene have been fabricated to enhance the performance of phototransistors [62-65]. Recently, dual-gated bilayer graphene has been employed to fabricate a hot-electron bolometer [66]. In bolometric response, the resistance changes are due to thermal effects and not due to photoexcited holes and electrons [67]. Graphene based superconducting tunnel junctions showing bolometric response have been projected in ultrasensitive bolometry and calorimetry applications useful in fields such as astronomy and quantum information [68, 69]. In general, photoconductive and bolometric responses are dependent on the material properties such as absorption coefficient, thermal conductivity along with the nature of the material-electrode interface. Graphene for such purposes is usually obtained via mechanical exfoliation [49], epitaxially grown films [70], chemical vapor deposited graphene [62] and reduced graphene oxide films [59-61]. However, there is no systematic study on the photoresponse behavior of the graphene obtained from various methods and also in relation to the bulk graphite.

IV.2.2 Scope of the present investigation

There are no systematic studies in the literature discussing the influence of the number of graphene layers and defects on the IR photoresponse in relation to bulk graphite. Here, in this study, the IR photoconductive and bolometric response of FLG and bulk graphite were studied. The FLG films were grown directly on insulating substrates (quartz, SiO_2) by annealing sacrificial Ni thin films in the ambience of residual hydrocarbons of the vacuum chamber. Thus obtained FLG films showed a maximum photoresponse of 73%. The IR photoresponse of the FLG films obtained from PMMA as carbon source and also the transferred FLG films (CVD grown graphene and from mechanical exfoliation) have been compared. The IR response of the bulk graphitic films, on the other hand, was bolometric where the change in the resistance is due to thermal effects. Thus, by controlling the thickness and crystallite size of the graphene layers, one can tune the IR photoresponse from photoconductive to bolometric regime.

IV.2.3 Experimental Details

SiO_2 (300 nm)/Si substrates were cleaned by sonicating in acetone, isopropanol followed by a rinse in double distilled water for 2 minutes. Ni catalyst layer (30 nm) was deposited onto SiO_2/Si substrates by physical vapor deposition (PVD) at a chamber pressure of 6 x 10^{-6} Torr. At this vacuum, the substrate surface gets covered with adsorbed residual hydrocarbons (1 monolayer) within one second [71]. Vacuum annealing (P = 2 x 10^{-5} Torr) was carried out in the range 950-1050 ºC for 15 minutes. The steps involved in the formation of graphene films from the residual hydrocarbons are shown in Figure IV.12a. For the sake of comparison, other sources of graphene were also tried out. A 2 wt% of PMMA (molecular weight ~ 996 kDa) was spin coated on the SiO_2 surface at a spin speed of 5000 rpm for 60 s to form a thin film (20 nm). It was subjected to similar heat treatment as done for the residual hydrocarbons resulted in the formation of FLG. This is similar to the formation of FLG from solid carbon sources. In another experiment, a CVD grown graphene on Ni (Graphene Supermarket, Germany) was transferred onto a SiO_2 surface by an electrochemical delamination method [72]. Mechanically peeled graphene from HOPG (NT-MDT, mosaic spread ~ 0.8°) using the scotch tape technique also served as a source of FLG in another experiment. The scotch tape containing flakes of graphene was stamped against a SiO_2/Si surface followed by cleaning in hot acetone [2].

IV.2.4 Results and Discussion

Figure IV.12a illustrates the growth of few layer graphene (FLG) on insulating SiO_2/Si substrate with the aid of residual hydrocarbons abundant in the vacuum chamber. The vacuum chamber used in this study is pumped by an oil-based diffusion pump (at a base pressure of 10^{-5} Torr) which is backed by a rotary pump. These pumps liberate volatile hydrocarbon species into the vacuum chamber which get adsorbed onto the substrate surface. The adsorbed hydrocarbon species on the Ni/SiO_2/Si substrates, could get transformed into graphene upon vacuum annealing at the temperatures of 1050 ºC as evidenced from Raman analysis (see Figure IV.12b). The spectrum showed characteristic G and 2D bands at 1585 and 2690 cm^{-1} respectively. Thus, Ni acts as a catalyst layer to induce the growth of crystalline sp^2 carbon from the volatile residual hydrocarbons present in the vacuum chamber [73-75].

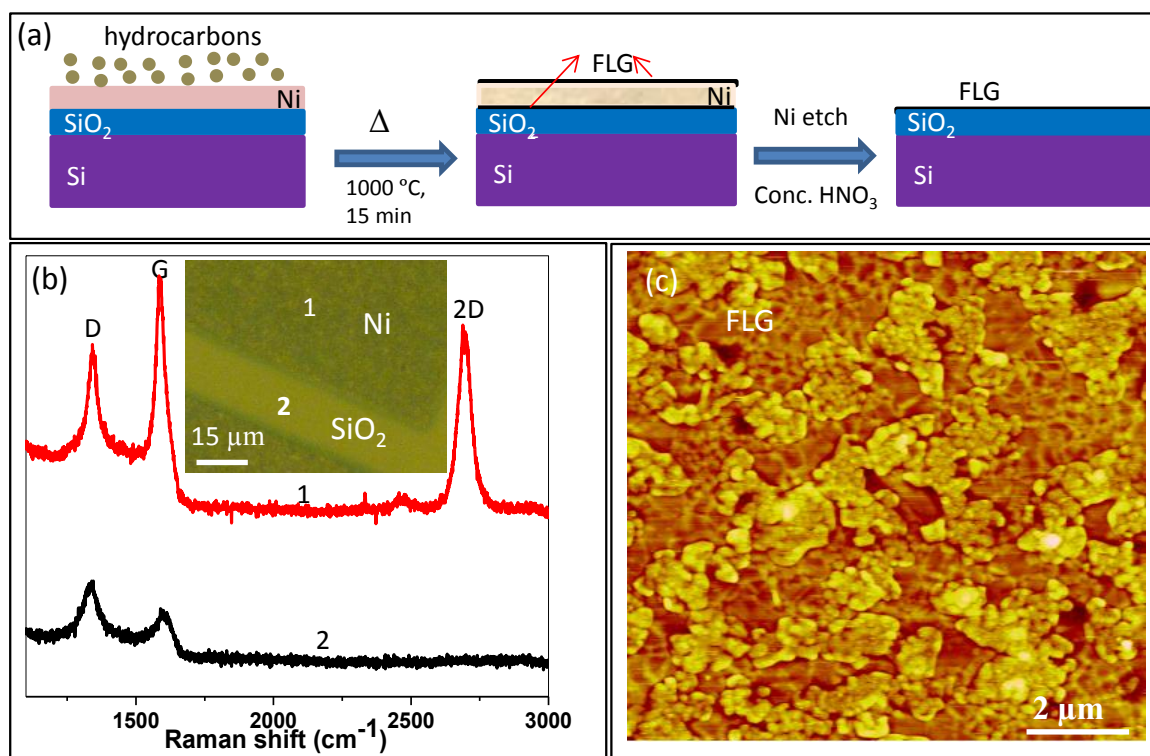**Figure IV.12** (a) Schematic illustration of direct growth of FLG on SiO_2/Si over large area using residual hydrocarbons of the vacuum chamber. (b) Raman spectra of the precipitated FLG and amorphous carbon from Ni (spectrum 1) and SiO_2 (spectrum 2) regions respectively. Inset shows the optical micrograph of Ni and SiO_2 regions. (c) AFM topography of the FLG features on SiO_2 surface.

The Raman spectrum of the graphitic deposits obtained after etching away the Ni layer consists of D (1350 cm^{-1}) and G (1585 cm^{-1}) bands (spectrum 1, Figure IV.12b) with line widths of 85 and 40 cm^{-1} respectively (I_D/I_G ratio of ~ 0.50). The 2D band appeared as a single peak (position ~ 2690 cm^{-1}) with a line width of 70 cm^{-1}. The I_G/I_{2D} ratio was found to be 1.5-2, indicating that the obtained graphene is of few layers [76]. Due to high solubility of carbon in Ni at the annealing temperature, the carbon atoms can diffuse through the Ni lattice and precipitate as graphene on the bottom SiO$_2$ surface (see the schematic in Figure IV12a) [77, 78]. Without the Ni overlayer, the carbon species hardly undergoes a change. The spectrum recorded from the SiO$_2$ region (without Ni layer) consists of only broad D and G bands with the 2D band being absent, indicating the amorphous nature of carbon unlike that from the Ni etched region (see spectrum 2, Figure IV.12b and the optical micrograph in the inset) [79, 80]. AFM topography in Figure IV.12c shows interconnected graphene features along with some residual Ni crystallites, which could not get etched away; perhaps they have been passivated with the graphene layers.
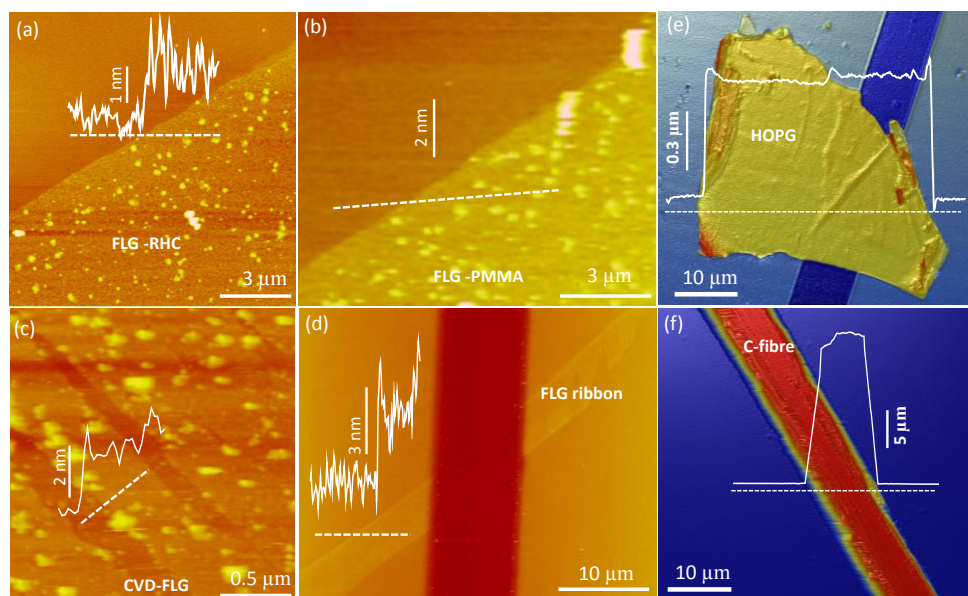
Figure IV.13 AFM topography of the FLG-RHC (thickness ~1.3 nm) (a), FLG-PMMA (~2.2 nm) (b), CVD-FLG (~2.5 nm) (c), scotch-FLG (~3 nm) (d), bulk graphite piece (~600 nm) (e) and carbon fibre (~18 μm) (f) respectively. The corresponding z-profiles are provided.

The AFM topography along with the z-profiles for the FLG and graphitic samples are shown in Figure IV.13. The typical thickness of FLG samples are in the range of 1-3 nm and the bulk graphitic samples of 0.6 and 18 μm were used for the photoresponse studies.

   The mobility values of the FLG samples are obtained from the field effect transistor (FET) measurements in which SiO_2 (300 nm) was used as bottom gate dielectric. All the FLG samples showed p-type behavior and hole mobilities were in the range of 550 to 8 cm^2/Vs (see Figure IV.14). The p-type doping is due to unintentional doping by the ambient water and oxygen molecules supported by the bottom SiO_2 surface. The defects present in the FLG may also support the adsorption of water molecules leading to the p-type behavior [77, 78, 81].
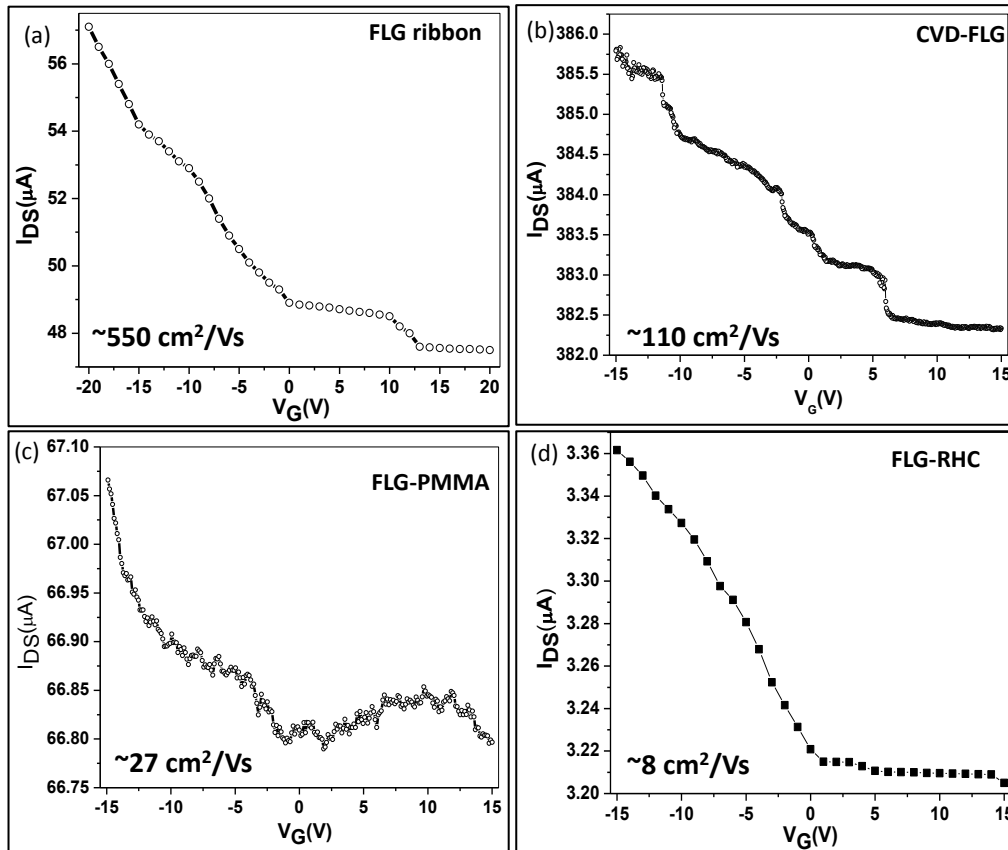
Figure IV.14 (a-d) Transfer curves for the FLG derived from different methods. Hole Mobilities are calculated from the transfer curves are found to be 550, 110, 27 and 8 cm^2/Vs for the FLG ribbon, CVD-FLG, FLG-PMMA and FLG-RHC respectively. SiO_2 (300 nm) was used as the bottom gate dielectric (specific capacitance, 12 nF/cm^2). Source-drain voltage (V_{DS}) was 0.1 V in all the measurements.

The mobilities are calculated from the transconductance values

$$g_m = (dI_{DS}/dV_G) = (W/L)\mu C_o V_{DS} \ \ldots\ldots(IV.2.1)$$

where W and L are the width and length of the channel.

μ is mobility and V_{DS} is the source-drain voltage.

C_o is the specific capacitance ~12 nF/cm^2.

Figure IV.15 (a) Two probe I-V characteristics of the FLG films (derived from the residual hydrocarbons) in the dark (black curve) and illuminated by IR laser (1064 nm) (red curve). (b) Plot showing the photoresponse behavior towards the IR beam. (c) Few cycles of response, and (d) the response with varying IR beam energy. The inset shows a plot of change in resistance versus laser beam energy. "on" is indicated with a green dot which indicates the time when the IR beam is turned on and at that moment the resistance starts decreasing. "Off" is indicated with a red dot, indicating the time when IR beam was turned off.
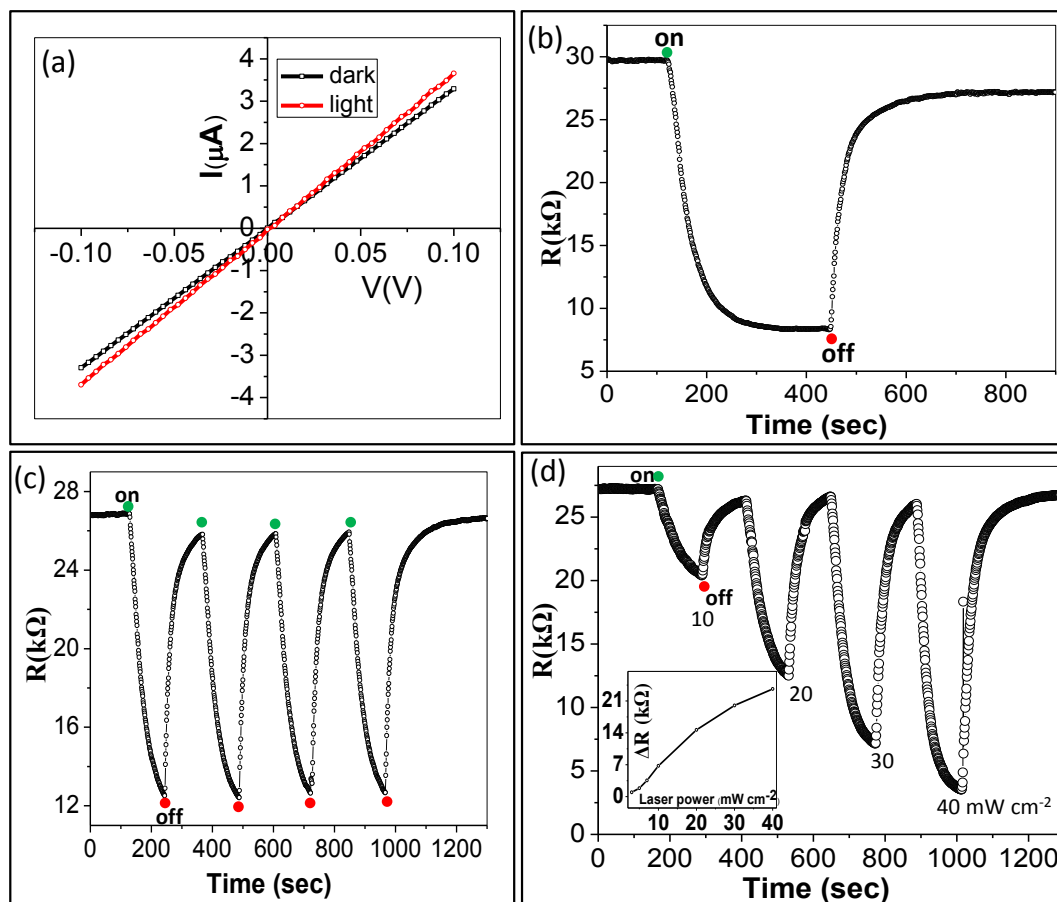
The photoresponse behavior of FLG derived from residual hydrocarbons (RHC-FLG) was examined under the IR source (Figure IV.15). From the I-V characteristics shown in Figure IV.15a, it is observed that the current in the circuit increases under IR illumination (red curve) relative to that obtained without illumination (black curve). This can be attributed to the generation of photoexcited charge carriers resulting in the enhanced photocurrent. When monitored with time (Figure IV.15b), the base resistance was found to decrease from ~ 30 to 9 kΩ within ~ 70 s under the IR beam (power, 20 mWcm^{-2}). The reduction in the resistance value is mainly due to the generation of photoexcited charge carriers and not due to photocurrent. The latter, which arises due to excitation of charge

carriers near the metal-graphene interface and their separation by the built-in electric field or local thermal fields, is typically of the order of nanoamperes. The dependence of resistance with photoexcited carrier density is given as, $\Delta R = (L/W) \, (1/e\mu) \, (1/\Delta n)$, where ΔR is the change in the resistance due to IR illumination, L and W are length and width of the FLG, e is the electron charge, μ is the mobility and Δn, is the change in the charge carrier concentration due to IR illumination. After substituting the values, a change in the carrier concentration of 3.7×10^{13} cm^{-2} for a given change of resistance of 21 kΩ in the FLG sample (equilibrium charge carrier concentration $\sim 2.6 \times 10^{13}$ cm^{-2} at room temperature) was observed. The resistance increased to nearly its original value at the moment when the IR beam was turned off (see Figure IV.15b). The estimated photoresponse based on the resistance values, is 73%, which qualifies RHC-FLG as IR detector. The stability of the circuit has been tested by turning the IR laser source on and off repeatedly for four cycles (Figure IV.15c). Accordingly, the changes in resistance were consistent in each cycle. There is a gradual decrease in the resistance with increasing the laser power from 10 to 40 mW cm^{-2} (Figure IV.15d). The change in the resistance is slightly non-linear (see inset in Figure IV.15d).

It may be noted that the photoresponse is lower compared to that from the graphene thin films derived from RGO [60]. In the present study, typical thickness of FLG is of the order of 1-3 nm (see Figure IV.13), i.e., ~ 4 orders of magnitude less, compared to that in reference 60, and correspondingly, its IR absorption is also less. The observed large photocurrent responses upto 1800% (in reference 60) at the metal-RGO interface has been attributed to the built-in electric fields and optically generated temperature gradients. The photoresponse has increased from 150% to 1800% with increasing laser power of 40 to 335 mW respectively [60]. Ghosh et al. have explained the enhanced photocurrents upto 193% for the reduced graphene oxide films (0.6 μm thick) using a Schottky barrier model [61]. Thus, the magnitude of photoresponse depends on the thickness of the graphene layers, the graphene-metal interface and the laser power [60, 61].

The time constants for the growth and decay of the photocurrent induced by the IR laser beam were calculated after fitting with exponential functions (see Figure IV.16) and they were found to be 41 and 50 seconds respectively. The time response is much slower

for these graphene films as compared to the crystalline graphene which could be in picoseconds [49]. The slower response times can be attributed to the presence of disorder and interfaces in the graphene films. The scattering of the charge carriers by the traps and boundaries can lead to a slower response. In this study, a shadow mask technique was used to deposit the electrode which is a 'clean' method unlike photolithography and electron beam lithography, which leave residues of resists behind and may influence the optoelectronic properties of FLG.
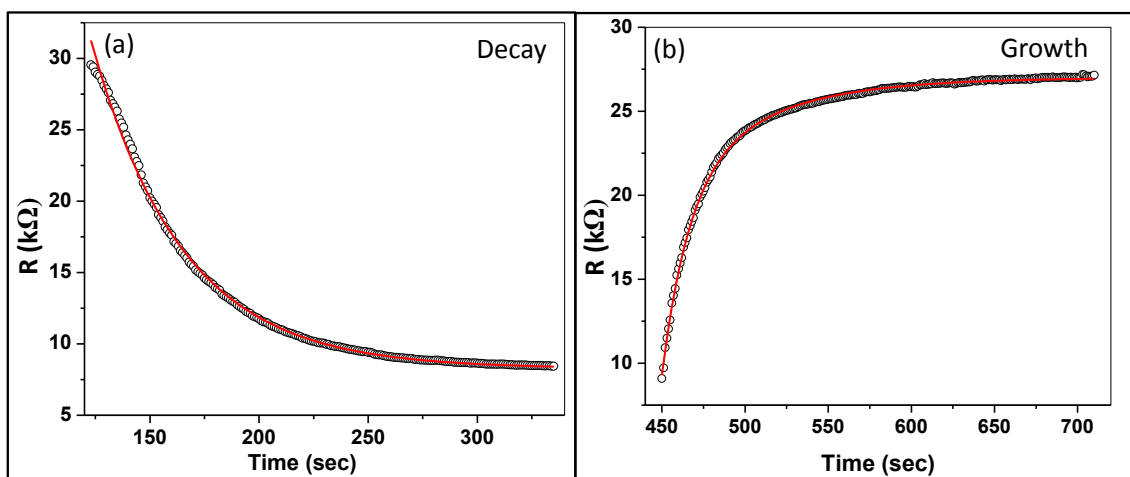
Figure IV.16 (a) and (b) Fall and rise of the resistance with respect to turning on and off of the IR beam.
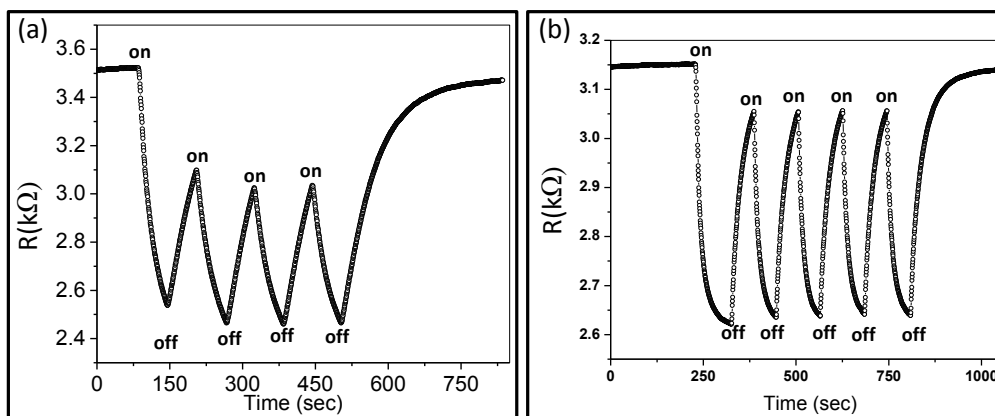

Figure IV.17 (a) and (b) IR photoresponse of the RHC-FLG on the quartz and sapphire substrates respectively. The photoresponses are found to be 37% and 25% respectively.

The IR photoresponse from the RHC-FLG deposited on the quartz and sapphire substrates is shown in Figure IV.17. The varied photoresponse of RHC-FLG films can be

attributed to the number of defects which is tunable through annealing temperature and annealing time.

The plot shown in Figure IV.18 illustrates the sensitivity of RHC-FLG with respect to IR radiation from an incandescent bulb. The temperature near the circuit was found to be 40-50 ℃. It is noteworthy that the FLG circuits showed a response to the IR radiation emitted from an incandescent bulb as well (surrounding temperature was ~ 40-50 ℃).
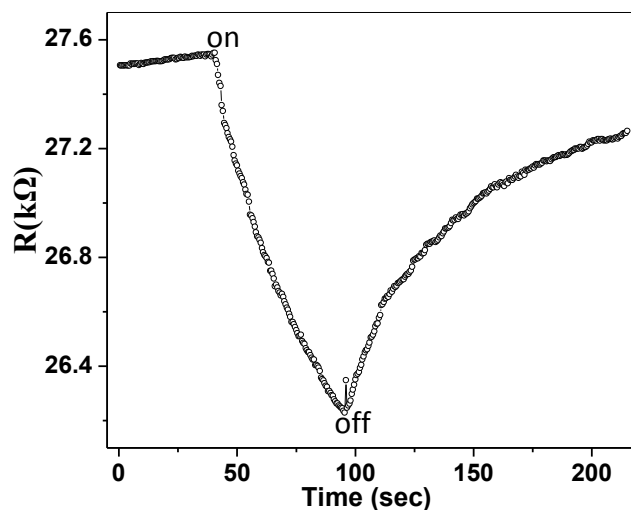
Figure IV.18 Decrease in the resistance of the FLG-RHCs towards the IR radiation (source: incandescent bulb, 60 W at a distance of 15 cm).

In order to examine the photoresponse behavior of the FLG obtained from other methods, PMMA was chosen as a solid carbon source, which was transformed into FLG by thermal treatment in presence of a Ni catalyst layer (see experimental section for details). The Raman spectrum recorded after washing away the Ni catalyst layer (Figure IV.19a) showed D, G and 2D bands at ~ 1350, 1587 and 2678 cm^{-1} respectively with I_D/I_G and I_G/I_{2D} ratios of 0.5 and 2.5, respectively. The AFM topography of the PMMA-FLG shows graphene sheets interconnected with each other over a large area (see inset in Figure IV.19a), similar to that observed with RHC-FLG (Figure IV.15c) [74, 75]. The PMMA-FLG film with a base resistance of 2.16 kΩ showed photoresponse of 21%, the temporal behavior is shown for four cycles (see Figure IV.19b). Similarly, the photoresponse of 16% observed for the PMMA-FLG film with a base resistance of 1.75 kΩ (see Figure IV.19c). It appears that the PMMA-FLG films were more conducting compared to the RHC-FLG films but the former exhibited lower photoresponse as compared to the latter.
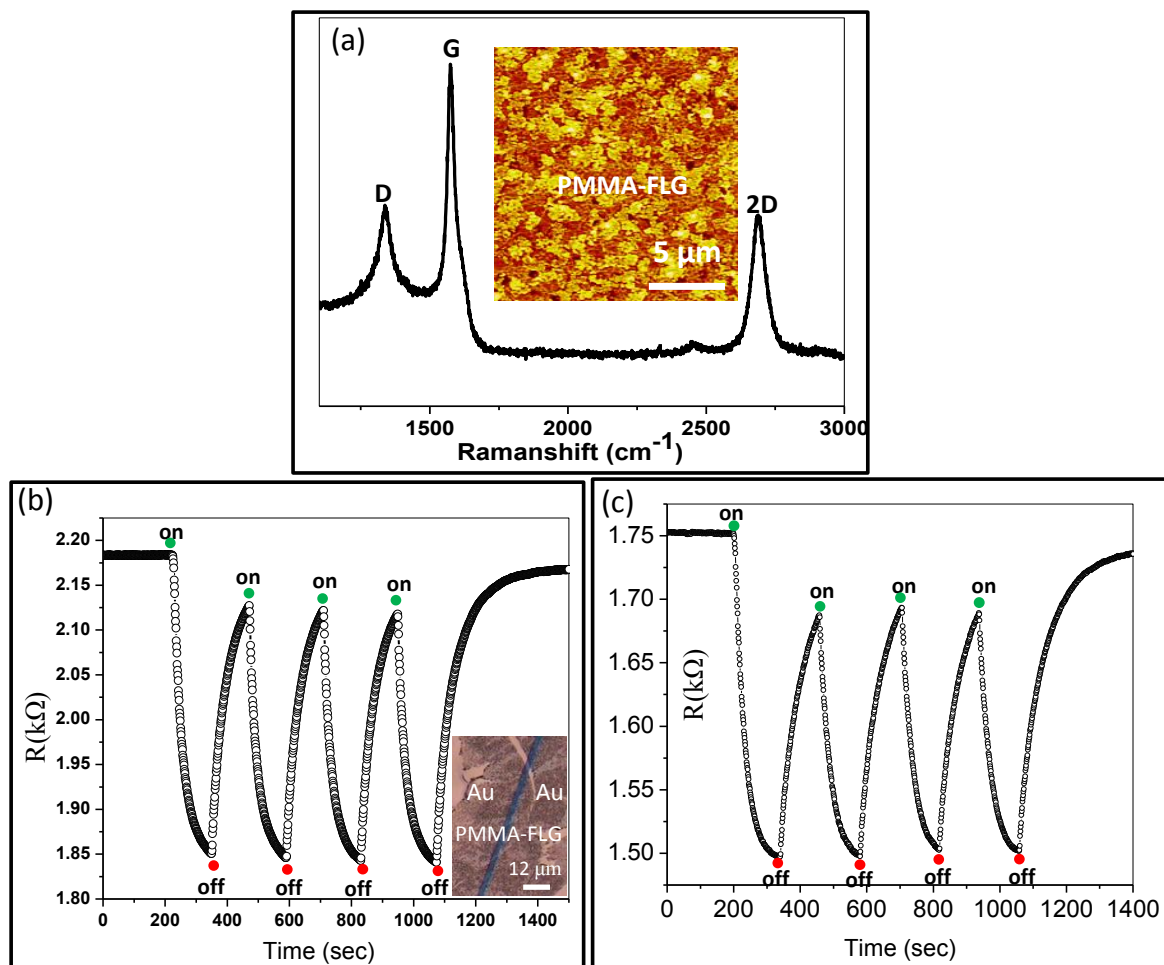
Figure IV.19 (a) Raman spectrum of the FLG derived from PMMA (FLG-PMMA), inset shows the AFM topography of the PMMA-FLG film on the SiO_2/Si surface. (b) and (c) IR photoresponse of two different circuits of PMMA-FLG. Inset is the optical micrograph of the circuit with Au contact pads.

The IR photoresponse properties of the FLG obtained from CVD and scotch tape methods have been illustrated in Figure IV.20. A decrease in the resistance after illuminating with the IR laser beam from 276 to 236 Ω corresponding to a photoresponse of 14% was observed (see Figure IV.20a). This value is comparable to that obtained with the PMMA-FLG films (see Figure IV.19).The temporal IR photoresponse of the CVD-graphene was shown in Figure IV.20b for few cycles. It was observed that the final resistance value (R_f) was not returning to the original base resistance (R_b) after turning off the IR beam which may be due to non-equilibration of photoexcited charge carriers. Another FLG circuit was made from the FLG ribbon obtained by scotch tape technique which was also exhibiting photoconductive response. The resistance of the FLG ribbon

was decreasing from 1.54 to 1.44 kΩ after illuminating with the IR beam, which corresponds to photoresponse of only 6% (see Figures IV.20c and d). The final resistance value (R_f) is found to be higher compared to the original base resistance (R_b) after turning off the IR beam which is due to the heating effect.
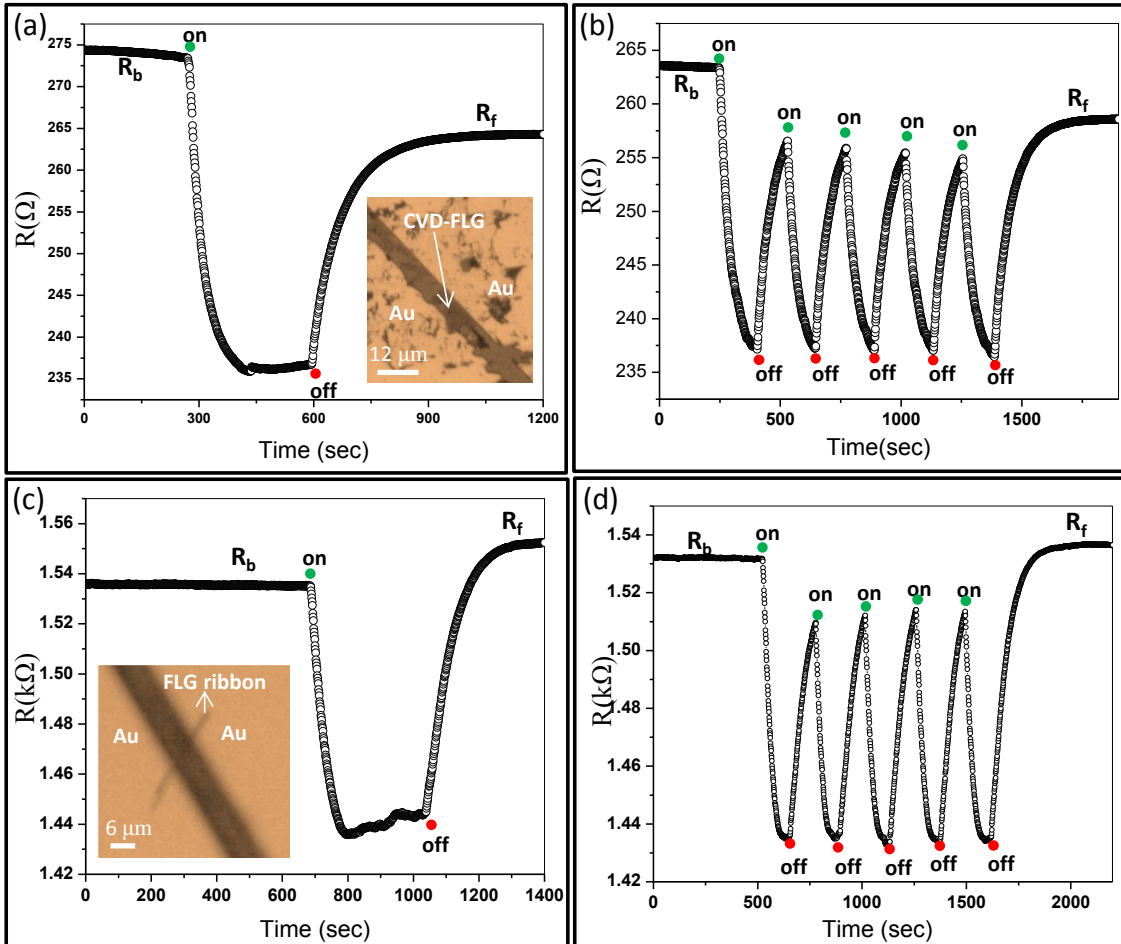
Figure IV.20 (a) and (b) IR photoresponse of the FLG transferred onto SiO$_2$ surface (CVD grown graphene film on the Ni surface). The inset shows the optical micrograph of FLG between two Au contact pads. (c) and (d) IR Photoresponse of the FLG obtained by scotch tape method. The inset shows the optical micrograph of the circuit containing FLG across 6 μm Au contact pads.

Figure IV.21 describes the IR photoresponse from the bulk graphitic films. The base resistance of the sample was found to be 15.8 Ω which was increased up to 18.2 Ω after illuminating with the IR beam (see Figure IV.21a). The increase in the resistance should be due to thermal energy imparted to the carbon lattice upon illuminating with the IR beam. Similar photoresponse behavior was observed for the carbon fibre which is also graphitic (many layers) in nature (see Figure IV.21b). The photoresponses were found to be 12 and

10% for bulk graphite and carbon fibre samples respectively.
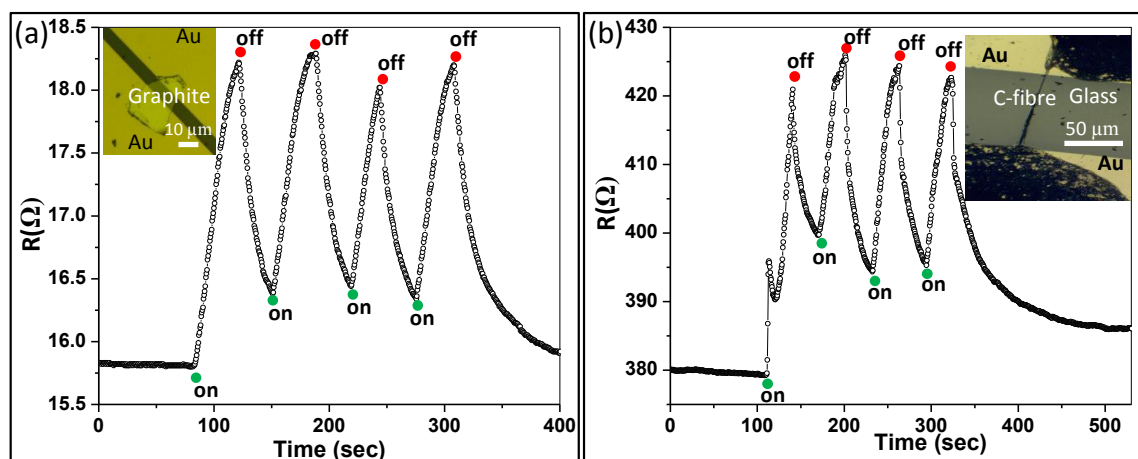
Figure IV.21 (a) Temporal photoresponse from the bulk graphite which is bolometric in nature with %R ~12%. Inset shows the optical micrograph of the HOPG piece between two Au contact pads. (b) The IR photoresponse from carbon fibre, cylces showing the increase and decrease in the resistance with respect to turning on and off of IR beam (%R=10%). Optical micrograph shows the carbon fibre circuit between Au contacts.

The time constants for the rise and fall of the resistance for the graphite sample are found to be ~21 and ~31 seconds respectively (see Figure IV.22). The response time is found to be rather high compared to that observed in suspended a SWNT film which is of the order of 50 ms [67]. Typically, the response time of a bolometer is limited by the ratio, $\tau = C/G$ where C is the heat capacity and G is the thermal conductance. It is obvious that the low thermal conductance and low heat capacity can minimize the response time. In the present study, the response was measured under ambient conditions giving rise to a high value of the response time. In the case of bulk graphite, the photoexcited charge carriers recombine in an ultra-fast (time scale of pico to femto seconds) manner which is a non-radiative decay producing heat in the graphite lattice. Thus, the absorbed IR radiation has transformed into heat leading to the temperature rise in the graphite lattice. The change in the resistance can be equated with the temperature change as, $\Delta R = (dR/dT)\Delta T$, where the temperature coefficient of resistance (dR/dT) is found to be 0.0165 Ω/K (from Figure IV.25b) and $\Delta R \sim$ 2.45 Ω is found from Figure IV.21a. Substituting these values in the above equation, ΔT comes out to be ~ 150 °C (laser power of 20 mWcm^{-2}). This way, the bolometric response can be tied to the temperature dependent resistance of the bulk graphitic films.
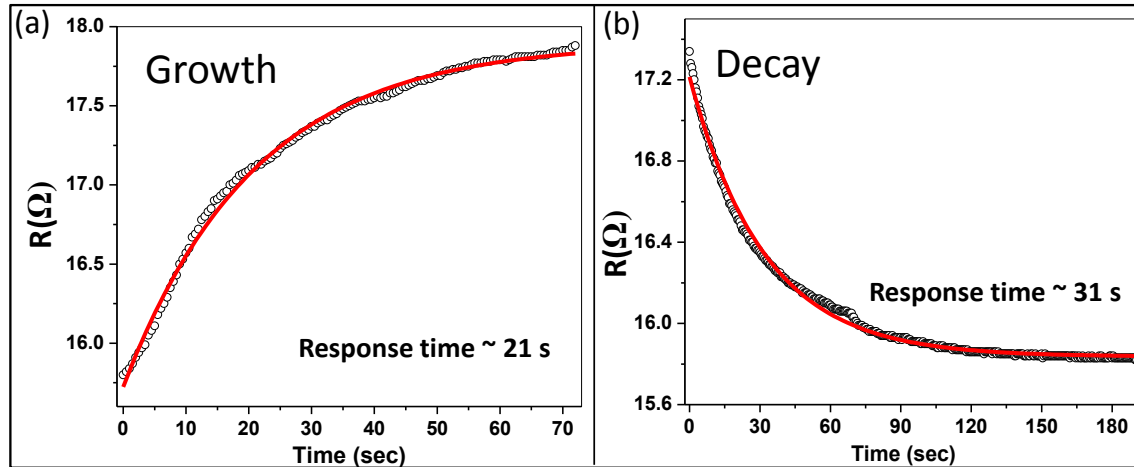
Figure IV.22 (a) Growth and (b) decay in the resistance of the bulk graphite samples with respect to turning on and off of the IR laser. Response times are found to be 21 and 31 seconds for the growth and decay respectively after fitting to exponential function.
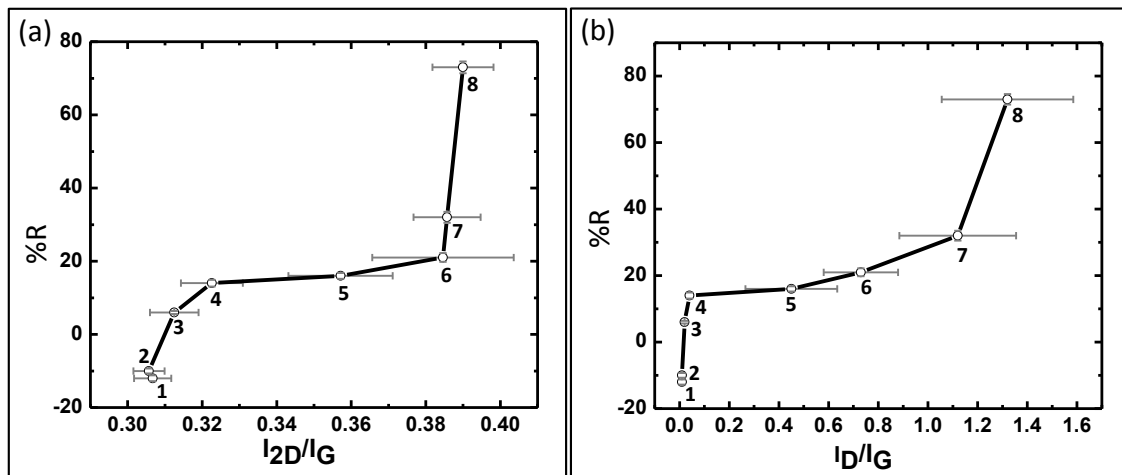
Figure IV.23 (a) and (b) IR photoresponse of the FLG and graphitic films with respect to I_{2D}/I_G and I_D/I_G ratios respectively. Points represent different FLG and graphitic samples (1, 2-bulk graphite; 3, 4-transferred graphene by scotch tape and CVD; 5, 6- PMMA-FLG; 7, 8- RHC-FLG).

In graphitic carbon, IR radiation causes intra-band transitions as well as lattice heating, which in terms of electrical transport have opposite effects. The intra-band transitions could generate photoexcited charge carriers while the thermal effects could rise the temperature, the latter being dominant, increase the resistance value which is nothing but a bolometric effect. The relative influence of these two effects on electrical transport depends on the 'thickness' of the graphitic carbon and accordingly, the IR response can be positive or negative. As the Raman intensities may be taken to indicate the 'thickness' and the nature of the carbon, the IR response from the various samples studied may be

correlated with the I_{2D}/I_G and I_D/I_G ratios as shown in the plot in Figure IV.23. In the case of bulk graphitic samples (HOPG and C-fibre), whose I_{2D}/I_G ratio is found to be ~ 0.31 (see points 1 and 2, Figure IV.23a), the IR response is bolometric (negative) in nature (%R, 10-12%). Clearly, thermal effects overcome the photoexcitation events due to high IR absorbance of the bulk graphitic species. Those from the CVD and the scotch tape methods exhibit a similar but positive response (%R, 6-14%) as the I_{2D}/I_G value increases (see points 3 and 4, Figure IV.23a), typical of FLGs. The IR response remains nearly steady for the FLGs derived from the PMMA although I_{2D}/I_G is relatively higher (up to 0.39). In this 'thickness' regime, the two opposing effects seem to balance each other! As I_{2D}/I_G further increases as in the case of FLGs from residual hydrocarbon (points 7 and 8, Figure IV.23a), the photoconductive nature takes over the bolometric behavior resulting in higher IR response (21% to 73%). Besides the number of layers, the presence of defects in the graphitic films can also influence the photoresponse (Figure IV.23b). A defect is essentially a scattering center contributing to increased electrical resistance. It is possible that the IR absorption can thermally activate the charge carriers to overcome the defect barriers giving rise to a higher photoresponse. Thus, the presence of defects, in a way, diverts part of the thermal energy away from bolometric process to photocurrent. The variation of %R with I_D/I_G (Figure IV.23b) is therefore quite striking and supports this view. It is noteworthy that the FLG with in-built defects is more like a self-doped system in contrast to graphene doped externally by metal or semiconductor nanoparticles in order to tune its photoresponse properties [62-65].

Based on the observed photoresponse from FLG and graphitic samples, photoconductive and bolometric behaviours can be explained using a schematic band level diagram shown in Figure IV.24. The FLG obtained from scotch tape and CVD methods is shown to have less number of localised defect states and accordingly, the change in the current (occupancy above E_F) is not significantly different after IR irradiation (Figure IV.24a). This is closer to being a bolometric than a photoconductive system. The extreme case is bulk graphite which exhibits only bolometric behaviour. The RHC-FLG, on the other hand (Figure IV.24b) may be represented by a discretised band diagram endowed with a large number of localised defect states. In this scenario, the current is less due to limited number of charge carriers. While the nature of conversion from photon to current is unclear [63], it

is likely that the defects aid the dissociation of excitons (produced by IR irradiation) into free carriers which can cross the defect potential barrier due to thermal energy leading to enhanced photoconductive response [61].
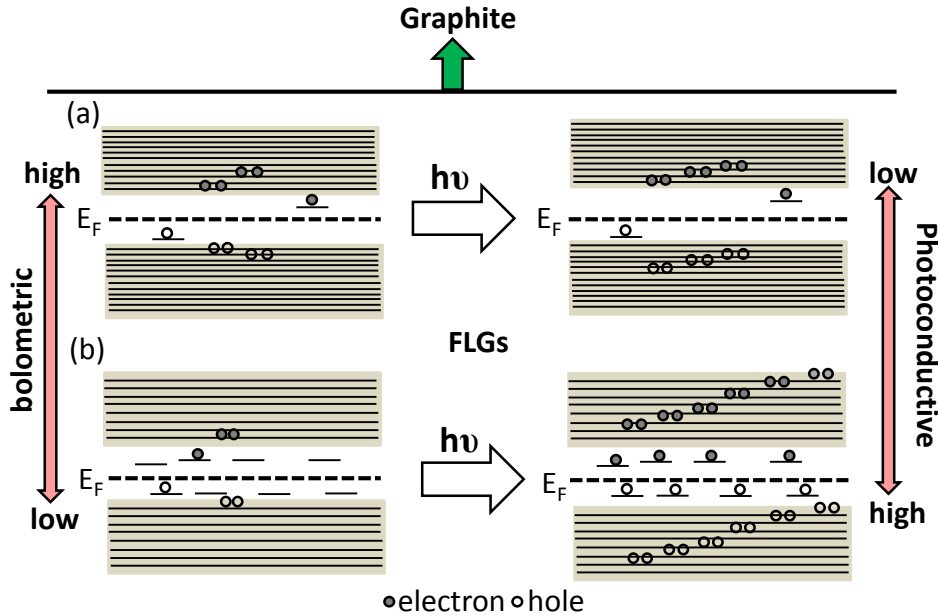
Figure IV.24 Schematic illustration of energy level diagrams and charge carrier excitations under an applied bias, for FLG with (a) less and (b) more number of localized defect states which are shown with short lines (-) above and below the E_F. The band gap is typically few meV. The situations favoring the photoconductive and bolometric responses are indicated.

In order to gain further insight of the interplay between charge trapping and recombination processes, measurement on temperature dependent resistance variation were investigated with and without IR illumination (see Figure IV.25). The FLG-RHC showed a decrease in the resistance with temperature (negative dR/dT) and the HOPG sample showed an opposite behavior (positive dR/dT) (see Figures IV.25a and b). Interestingly, the photoresponse ($\Delta R/R(300K)$) is found to vary nearly linear with temperature and higher photoresponse is observed at lower temperatures (compare %R ~ 50% at 100 K with %R ~ 10% at 400 K in Figure IV.25c). It is clear that the recombination rates are higher at higher temperatures leading to the diminished photoresponse. But at lower temperatures due to low recombination rates and enhanced trapping, the photoresponse is higher [82, 83]. Similar kind of temperature dependent photoconductive effects was observed in the case of disordered carbon aerogel systems [84]. The bolometric response showed weak temperature dependence as shown in Figure IV.25d with a variation of 3% in

the temperature range of 80-470 K, as the change of resistance with temperature [R(80 K)/R(470 K) = 0.86] is small [67].
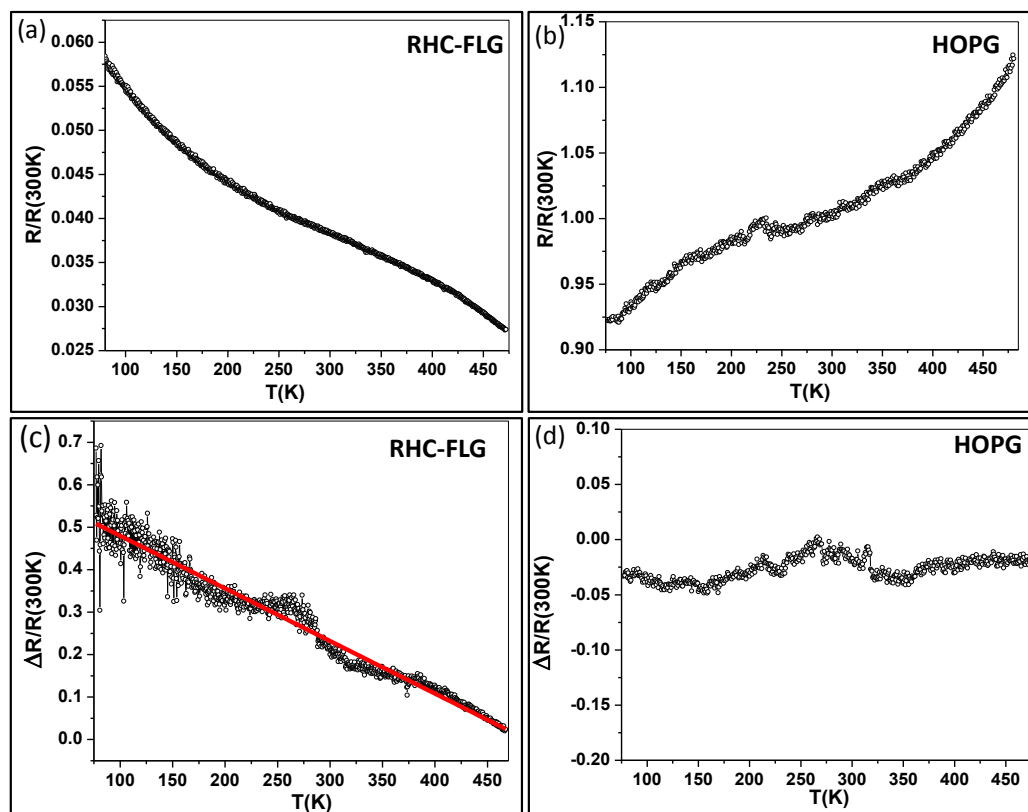
Figure IV.25 Temperature dependence resistance of FLG-RHC (a) and HOPG (b) with negative and positive temperature coefficients of resistance respectively. (c) and (d) are photoresponse of the FLG-RHC and HOPG samples with temperature respectively.

Photoconductive effects in a given system are guided by the interplay between trapping and recombination centers. Defect levels in a system can either act as trapping sites which assist the excitation of the electron into the conduction band or act as recombination sites for the holes as it is easier to capture the electron into these levels and release the hole into the valence band. Trapping is a one step process whereas recombination is a two-step process. Trapping centers increase the photoresponse while the recombination centers decrease the photoresponse.

The mutual cooperation of traps and recombination centers and their influence on the carrier mobility (lifetime) depends on the wavelength and intensity of illumination as well as on the temperature. The carrier recombination at the defect sites plays a dominant role in determining the carrier transport mechanism at different temperatures. Thus, the

temperature dependent photoconductive effects are quite complicated to understand. A modeling of the temperature dependent photoconductive effects may deserve a separate study requiring information about the temperature dependent mobility of the charge carriers which are influenced by the traps and the recombination centers in order to correlate with the observed photoresponse [82, 83].

IV.2.5 Conclusions

The IR photoresponse of FLGs obtained from different methods have been compared with that of bulk graphitic films. FLG films obtained through residual hydrocarbon source exhibited photoconductive response up to 73% due to generation of photoexcited charge carriers after illuminating with the IR beam. The FLG films obtained from CVD and scotch tape methods showed typical photoresponse of 6-12%. On the other hand, the photoresponse of the bulk graphitic films is bolometric in nature where the resistance changes are due to thermal effects. Thus, by controlling the thickness and defects of the graphitic films, it is possible to fabricate IR based photoconductive and bolometric detectors. The Raman data clearly elucidated the role of defects in the tunability of the IR response of the FLGs.

IV.3 Pencil-on-Paper based RC filters and FETs with Ion Gel Dielectric

IV.3.1 Introduction

Pencil writing on paper, which is a day-to-day practice since 16th century [85], deserves to be revisited in the light of recent developments in graphene research. Pencil is essentially a nanocomposite of graphite and a kaolin based clay, the latter acting as a binder to maintain the macroscopic continuity in the form of pencil rod [85-87]. Due to intercalated clay particles, the properties of the pencil are different compared to pure graphite [88, 89]. As pencil is moved on, the cellulose fibres constituting paper act abrasively to exfoliate the graphitic material from the pencil rod producing black deposits which form the 'pencil trace'. This *humble* deposit contains some interesting graphitic species, if not single or few layer graphene! It contains multi layers of graphene [90] which makes it reasonably conducting, in spite of the presence of insulating clay particles. Thus, pencil deposit on paper has made its way into various applications such as supercapacitors [90], piezoresistive sensors [91], air electrode of a Li-air battery [92] and also as electrode material for UV sensors [93, 94]. Recently, electro-kinetics of the fluid-flow has been studied with paper-and-pencil devices [95]. Paper based analytical devices have been developed for glucose biosensing using graphite pencil electrodes [96].

Although paper is not regarded as a suitable substrate, it is becoming popular in electronic and microfluidic applications due to its widespread availability [97-100]. Given its surface roughness, ensuring electrical continuity of a deposit (including pencil mark) and more so, its reproducibility, is indeed challenging [97, 100]. While paper has been employed in energy storage devices in combination with carbon nanotubes and metal nanowires [101, 102], it may not be well suited in devices such as field effect transistors (FETs) which generally require smooth dielectric layers with controlled thickness [97]. On the other hand, inorganic based dielectrics, which require high growth temperatures [103] but suffer from lower gate coupling efficiency, may not be suitable for fabricating FETs on a paper substrate [104]. To be compatible with paper, the dielectric has to be deposited near ambient room conditions yet possessing a high gate capacitance. Ionic liquids such as 1-ethyl-3-methylimidazolium bis(trifluoromethylsulfonyl)imide [EMITFSI], readily form electrochemical double layers (EDLs) and possess high thermal stability, non-volatility and high ion conductivity at room temperature (~0.02 S/cm), and therefore are used as

dielectric medium for low voltage operation of FETs [105, 106]. The gelation of ionic liquids with the block copolymers is also an approach for achieving high specific capacitance due to formation of EDLs, widely employed in fabricating flexible FETs [106-109].

IV.3.2 Scope of the present investigation

The electric field effect from turbostratic graphite has not been investigated in the literature. Here, in this study the electric field effect was realized from the pencil-traces on paper with the aid of iongel dielectric. The fabricated devices showed ambipolar electric field effect with carrier mobilities of around hundred cm^2/Vs under low operating voltages (< 3 V). The passive devices such as RC filters have been fabricated by employing pencil-trace as a resistor and ion gel as a capacitor dielectric.

IV.3.3 Experimental Details

Paper substrates used in this study are normal A4 sheets, thickness of 100 μm. Pencil used in this study is (HB grade, APSARA, India) with graphitic content of ~70%. Top gate dielectric used in this study ion gel based which is composed of polydimethylsiloxane and ionic liquid (1-butyl-3-methyl-imidazoliumoctyl sulfate) in the ratio 1:0.2, with typical capacitances of 0.3 μF/cm^2. Paper substrates with the pencil marks along with the Ag contacts and top gate dielectric were baked at 150 ℃ for 10-15 minutes.
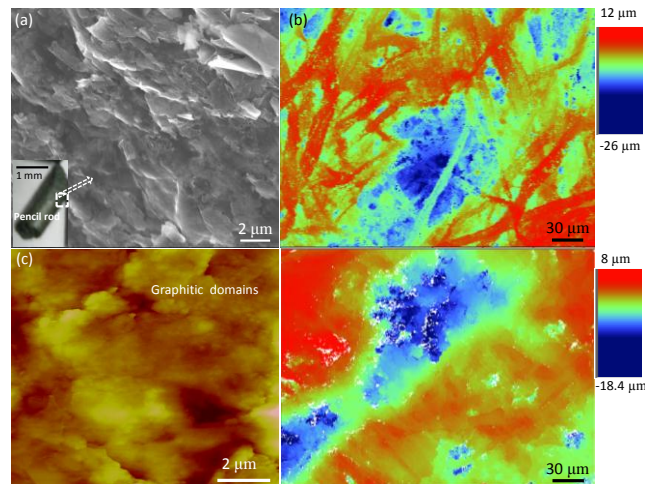
IV.3.4 Results and Discussion

Figure IV.26 (a) SEM image showing the surface morphology of the pencil rod, inset shows the optical micrograph of the pencil rod. (b) Optical profilometric image showing the cellulose fibres of the plane paper surface (c) AFM topography and (d) optical profiolometric images of the pencil trace on the paper.

The morphology of the pencil rod and its trace on paper surface has been examined through FESEM, optical profiler and AFM. The surface of the pencil rod appears to be corrugated with petal-like morphology of graphitic layers (see Figure IV.26a). The random alignment of the cellulose fibers of the paper was imaged using optical profiler (see Figure IV.26b). AFM topography and optical profilometric images of the pencil-trace on paper, revealing its domain structure (see Figures IV.26c and d).

While writing, the graphite layers get exfoliated and laid flat on the paper surface. Pencil-trace on paper thus contains interconnected graphitic domains with lots of edges and boundaries (see Figure IV.27a). The layer nature of the domains is apparent as shown in the inset of Figure IV.27a. The EDS spectrum is shown in Figure IV.27a, showing the signals for C, Fe, Ca and Mg. Energy dispersive spectroscopy (EDS) maps in Figure IV.27b show the distribution of the constituent elements, Fe, Ca and Mg, present in the graphitic matrix of the pencil-trace. TEM micrograph showing the nanocomposite constitution of the pencil powder where clay particles were seen among the graphitic layers (Figure IV.27c). The crystalline nature of the graphitic domains is evident from the electron diffraction pattern with hexagonal symmetry of the spots [110] (see inset of Figure IV.27c). Raman spectrum recorded from the pencil-trace made on a stainless steel substrate (Figure IV.27d, red curve) comprises of three prominent peaks at 1348, 1574 cm^{-1} and 2701 cm^{-1} which correspond to the D, G and 2D bands respectively. The G band arises from stretching of sp^2 bonded carbon lattice and D band originates from the presence of defects in the form of edges and grain boundaries. Using the estimated I_D/I_G ratio (~0.2), the average crystallite size of the graphitic domains was calculated [79] to be ~100 nm. The position, width and shape of 2D band provide information about number of layers, type of stacking along the c-axis of graphitic samples. In the case of pencil trace, the 2D band appears as a single symmetric peak at 2701 cm^{-1} with a width of 85 cm^{-1} (red curve, Figure IV.27d) which is quite different compared to asymmetric peak of HOPG (black curve, Figure IV.27d). The former is typical of turbostratic graphite, a close cousin of graphene [79, 80]. Due to mis-orientation of graphene layers along the c-axis, there is substantial electronic decoupling of the layers leading essentially to a 2D system.
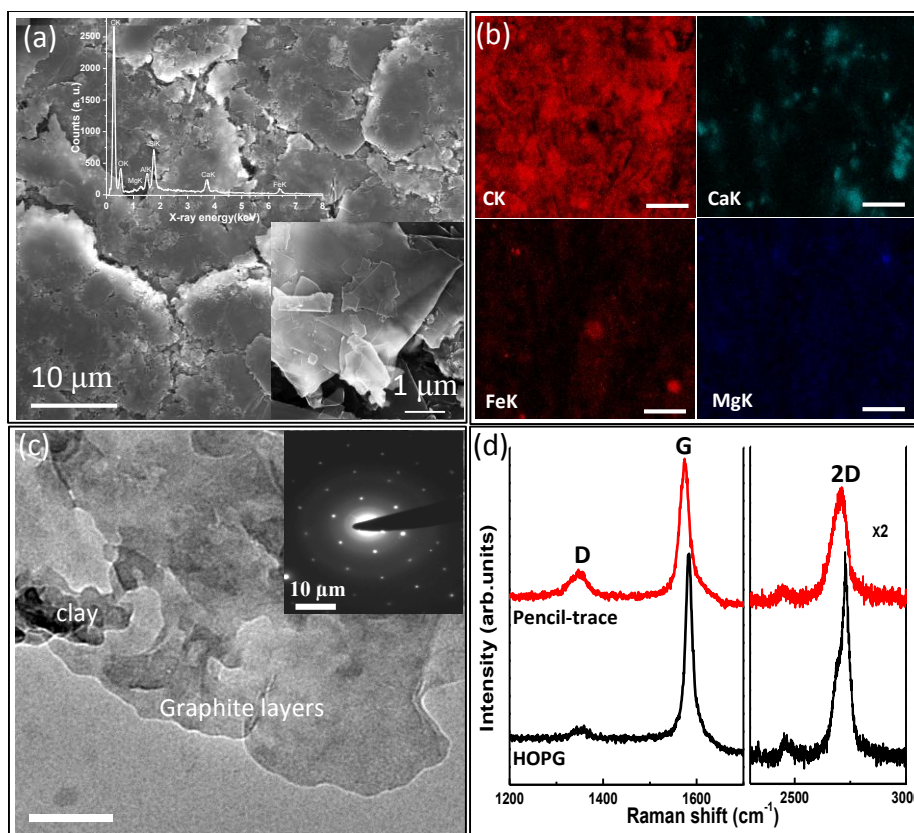
Figure IV.27 (a) FESEM images showing morphology of graphitic layers in pencil trace on paper along with the EDS spectrum. Inset shows a magnified view. The corresponding EDS maps of graphitic carbon (CK) along with the metallic elements present in the clay (FeK, CaK and MgK), scale bar 10 μm (b). (c) TEM micrograph of the graphitic layers, with the electron diffraction pattern in the inset, the sample for TEM was prepared by crushing a pencil rod into fine powder and dispersing it in chloroform followed by depositing on to a holey carbon grid. (d) Raman spectrum of the pencil trace (red curve) compared with HOPG (black curve). The 2D band intensities have been multiplied by two.

In order to investigate the electrical properties of the pencil trace on paper, its I-V characteristics were measured, which was found to be linear. A given trace with ~ 5 mm width showed a resistance of 12.5 kΩ (see Figure IV.28a). Typical resistance of the traces was in the order of few kΩs which of course depends on the length and thickness of the pencil trace. The resistance was found to vary linearly with length of the trace, confirming uniformity of the deposit (see inset of Figure IV.28b). Pencil drawing on paper could also be employed as a variable resistor (see inset of Figure IV.28b). Temperature dependent resistivity measurement was performed using a physical properties measurement system (see Figure IV.28c). The resistivity of the pencil trace decreases from 0.24 to 0.17 mΩ.m with increasing temperature, 20 to 250 K, indicating its semiconducting behavior. The

resistivity of the pencil-trace is $\sim$ 3 orders magnitude higher compared to that of bulk graphite ($\rho_{bulk} \sim 0.4~\mu\Omega.m$) [111].
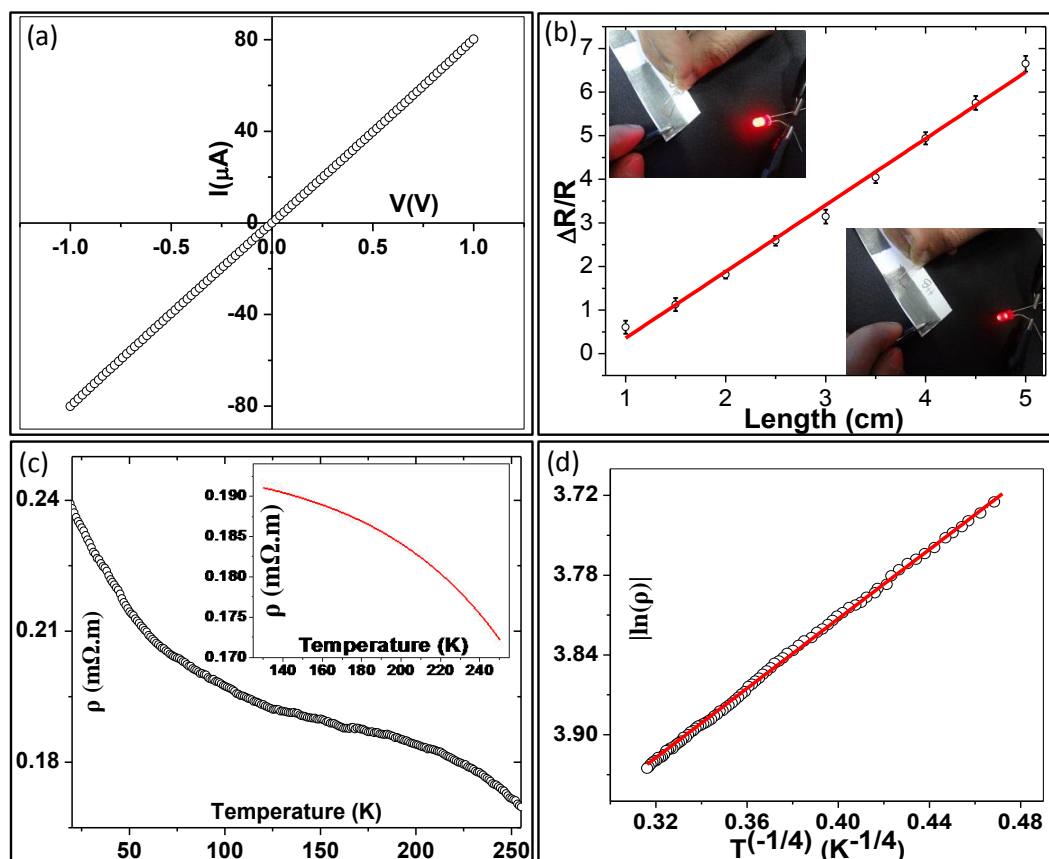
Figure IV.28 (a) Two probe current-voltage characteristics of a pencil-trace on paper substrate. (b) Normalized resistance of the pencil-trace on paper (width, 3 mm; thickness, 50 μm) over different lengths. Insets show photographs of varying brightness of a LED based on the resistance of the pencil-trace, (c) Four-probe resistivity of the pencil measured between 20 and 250 K. The distance between contacts was 1 mm with a width and thickness of the trace, $\sim$ 3 mm and 50 μm respectively. Inset plot showing the resistivity of the pencil-trace varying as $\rho \sim \exp((-T_0/T))$ above 100 K, where T_o is constant, T is the temperature. (d) $|\ln(\rho)|$ vs $T^{-1/4}$ plot, which is linear, characteristic of VRH model of electrical transport at low temperatures (20-100 K).

The higher resistivity of the pencil trace can be attributed to the scattering of the charge carriers by the intercalated clay particles, edges and boundaries of the interconnected graphitic domains. The transport being mesoscopic across the graphitic domains resembles a semiconductor behavior. As the graphite crystallites are interconnected with each other, the electrical transport at low temperatures (20-100 K) can be explained using the variable range hopping (VRH) model [112]. As shown in Figure IV.28d, $|\ln(\rho)|$ is seen varying linearly with $T^{-1/4}$ (in the 20-100 K range), characteristic of Mott type VRH which is

distinct from Efros-Shklovskii type VRH [113], implying that the Coulomb interactions are negligible in the conduction mechanism. At higher temperatures (above 100 K), resistivity decreases exponentially, characteristic of an activated transport behavior (see inset of Figure IV.28d).
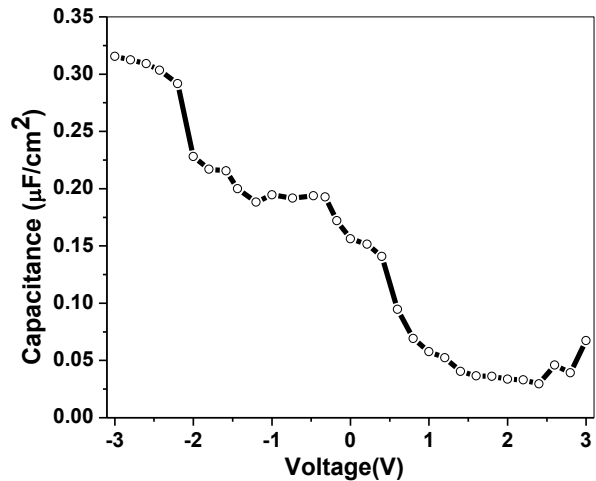
Figure IV.29 Specific capacitance-voltage characteristics of the ion gel at a frequency of 1 Hz.

Ion gel used as the dielectric was prepared by mixing PDMS with ionic liquid (1-butyl-3-methyl-imidazolium octylsulfate) in the ratio 5:1, which showed a typical dc specific capacitance of 0.3 $\mu F\ cm^{-2}$ (see Figure IV.29). The higher gate capacitance of the ion gel is due to the formation of electrochemical double layers [107].

Simple first-order passive filters were made by employing pencil-trace on paper as a resistor and ion gel (made of PDMS and ionic liquid) as dielectric between two Ag contacts as capacitor (Figure IV.30a). The Ag contacts were established using a tiny paint brush. The input signal (V_{in}) was applied using a function generator at voltage amplitude of 1 V, to the series combination (both the resistor and capacitor together) and the output signal (V_{out}) was measured using an oscilloscope across the capacitor (see Figure IV.30a). The resistance of the pencil-trace is found to be 350 kΩ. Figures IV.30b-d shows the voltage response of the filter at different frequencies, 100 Hz, 10 kHz, and 100 kHz respectively. The input signal is a square wave-shaped signal (blue curves in Figure IV.30) with almost vertical step input and the response of this integrator changed dramatically with increasing frequency.
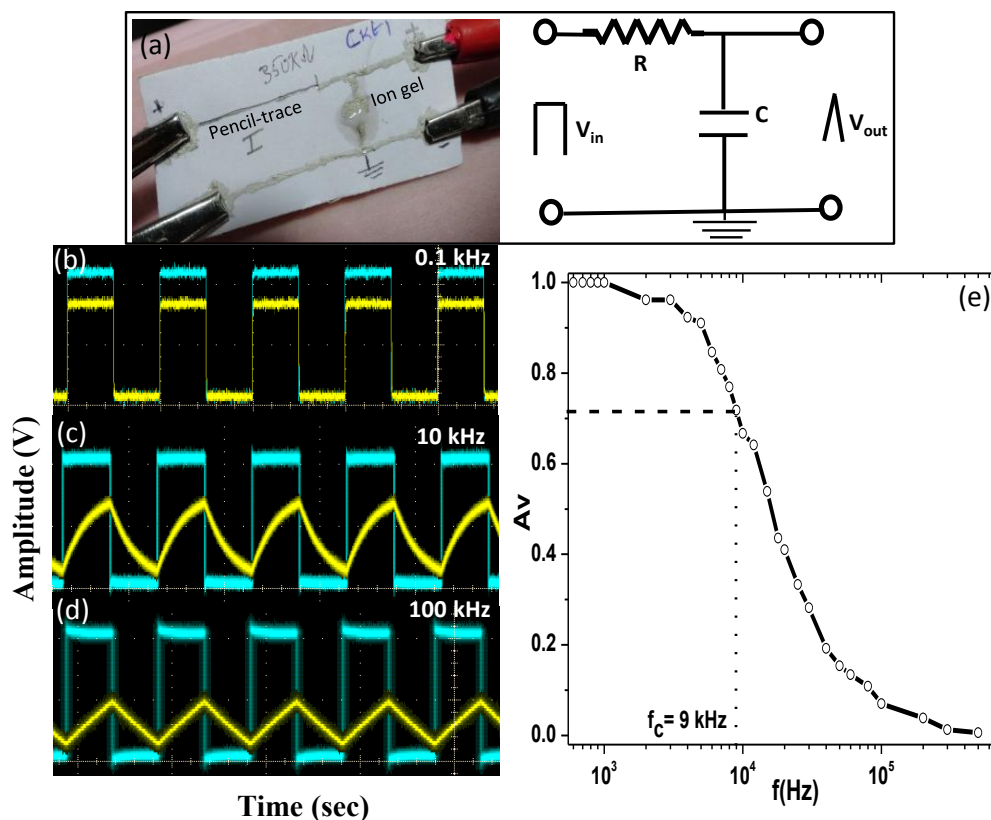
Figure IV.30 (a) Photograph showing a resistor-capacitor (RC) low pass filter on paper and its circuit diagram. The transient response from the filter at (b) 0.1 kHz, (c) 10 kHz and (d) 100 kHz. Input and output wave forms are shown with sky blue and yellow, respectively. (e) Normalized output voltage response with frequency of the RC low pass filter. The cut-off frequency corresponding to 0.707 of the maximum response is 9 kHz.

At low frequencies (100 Hz), the input and output wave forms are of similar shape except that the amplitude of the output is lower compared to the input due to charging of the capacitor (see Figure IV.30b). At higher frequencies (~ 10 kHz), the output voltage response converted to a triangular shaped waveform (yellow curve in Figure IV.30c) with respect to the input square wave signal. This shaping of the waveforms in the low pass RC circuits can be attributed to the frequency dependent reactance of the capacitor (see Figures IV.30c and d). A triangular waveform consisted of alternate but equal positive and negative ramps. At higher frequencies (~100 kHz), the output became a well shaped triangular wave (see Figure IV.30d). The performance of the circuit is as expected of a RC filter; the higher the input frequency, the lower will be the output amplitude due to decreasing capacitive reactance ($X_c = 1/2\pi fC$ where f is the frequency and C is the capacitnace). The normalized output voltage with frequency of the RC low pass filter is

shown in Figure IV.30e. The frequency corresponds to 0.707 level of the normalized output voltage is the cut-off frequency (f_c), which is found to be 9 kHz [114]. The time constant (τ) can be equated to the cut-off frequency (f_c) of the RC low pass filter by the following equation

$$f_c = 1/2\pi\tau = 1/2\pi RC....(IV.3.1)$$

The phase shift angle (φ) is given by the following equation

$$\phi = -arctan\ (2\pi f_c RC).....(IV.3.2)$$

At f_c, the phase angle is found to be -45°, out of phase with respect to the input signal. As the input voltage changes, the time taken by the capacitor for charging up results in an output voltage (the voltage across the capacitor) "lagging" behind the input signal. The higher the input frequency applied to the filter the more the capacitor lags and thus, the circuit goes "out of phase". The above study shows the possibility of making such circuit elements. Besides this integrator, a RC based differentiator circuit was also built simply by interchanging the positions of the resistor and capacitor of the integrator circuit (see Figure IV.31).
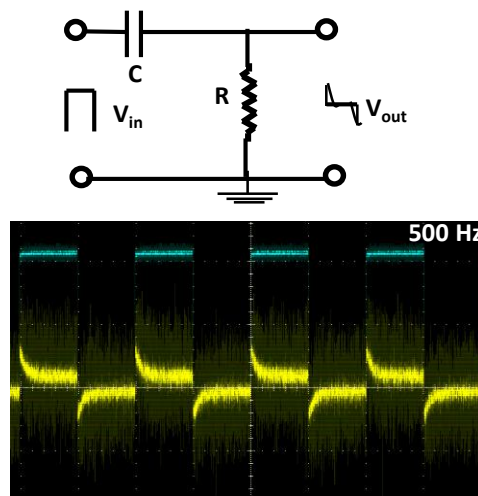
Figure IV.31 RC differentiator circuit and the voltage response at 500 Hz. Sky blue curve is the input signal and yellow curve is for the output signal.

Pencil trace on paper was then exploited as active element in field effect transistors. Ag paint was laid out with a paint brush forming source, drain electrodes on paper contacting the pencil trace. Initially, paper was used as gate dielectric in the in-plane geometry with Ag as gate electrode. Transistor characteristics recorded using a Keithley-4200

semiconductor characterization system produced no measurable field effect (see Figure IV.32), implying that paper on its own was not adequate as gate dielectric.
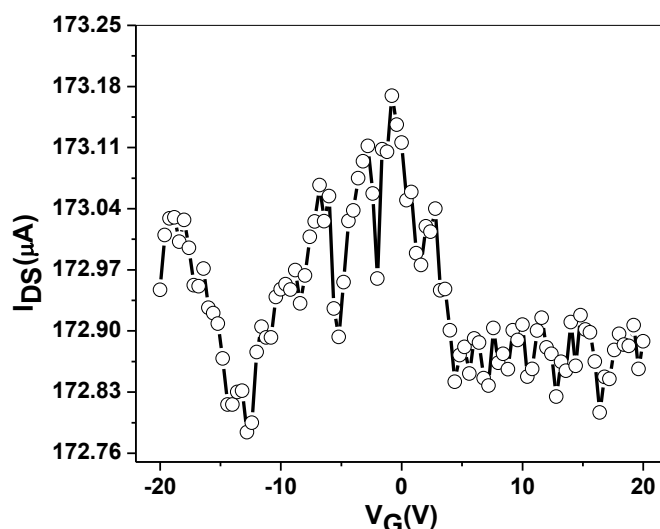
Figure IV.32 Transfer curve of the pencil-trace with the paper as gate dielectric, no field effect was observed.

A drop of the ion gel was placed on top of the pencil trace and baked for 15 minutes. While being hot, Ag paint was applied which dried instantly forming the gate electrode (see inset of Figure IV.33a). Figure 4a shows the output characteristics obtained, where the I_{DS} (source-drain current) varies linearly with V_{DS} (source-drain voltage) with a base resistance of ~11 kΩ for zero gate voltage ($V_G = 0$) indicating ohmic contact between the pencil-trace/Ag interface. The output characteristics showed increase in the current with varying gate voltages from 1.5 to -1.5 V (see Figure IV.33a). Transfer characteristics (Figure IV.33b) reflected the ambipolar nature where the positive and negative regions of gate voltage represent electron and hole transport respectively [104]. The asymmetry in the transfer curve indicates that the hole and electron mobilities are not equal. This may be attributed to the unintentional doping of pencil marks by the water molecules through capillaries of the paper which may suppress the electron mobility. The broad Dirac point minimum in the transfer curve can be attributed to the deriving of electric field effect from multilayers of graphene in the pencil trace [115]. The gate leakage current (see Figure IV.33b) is at least 2-3 orders of magnitude lower compared to the channel current.
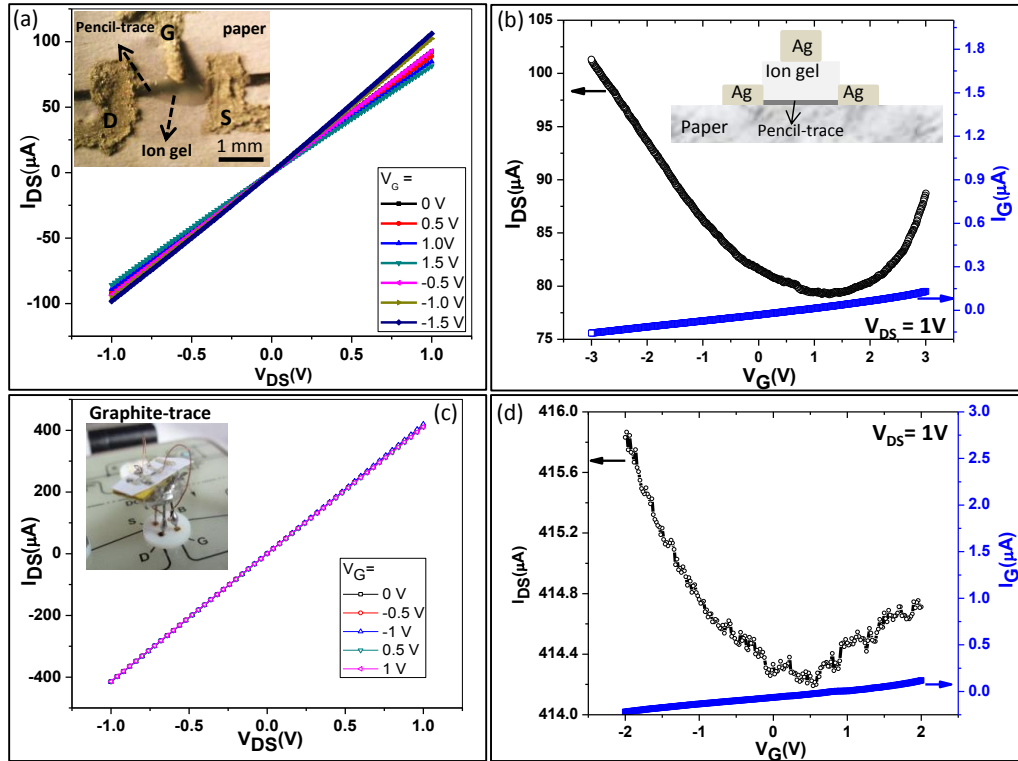
Figure IV.33 (a) Output and (b) transfer characteristics of the pencil trace on paper with PDMS-IL ion gel as top gate dielectric. Inset shows the optical micrograph of the pencil trace on a paper with the source, drain and gate as Ag paint and ion gel as top gate dielectric. The gate leakage current (blue curve) is also shown. Inset shows the geometry of the pencil-trace FET with ion gel as dielectric. (c) Output and (d) transfer characteristics of a HOPG trace on paper with ion-gel as gate dielectric, similar to the device shown above. Inset shows a photograph of a mounted paper FET device. The devices were baked at 150 °C for 15 minutes. All measurements were carried out in ambient conditions.

It is clear that the ion gel due to its high gate capacitance is effective in deriving the electric field effect from the pencil trace at such low operating voltages. The carrier (holes and electrons) mobilities (μ) were estimated from the channel transconductance ($g_m \sim 7$ and 3.9 μA/V for holes and electrons respectively) of the FET, $g_m = (dI_{DS}/dV_G) = (W/L)\mu C_o V_{DS}$ in the linear regime of the I_{DS}-V_G curve, where W/L is the width-to-length ratio of the channel and C_o is the gate capacitance per unit area [108]. Taking W/L as 0.2 and C_o as 0.3 μF/cm^2, the hole and electron mobilities were estimated to be $\mu_h \sim 106$ cm^2/Vs and $\mu_e \sim 59$ cm^2/Vs. In contrast to the turbostratic nature of the pencil trace, a HOPG trace (which is completely graphitic) was made on paper by rubbing and the FET characteristics were examined while using the same ion gel as dielectric. The output characteristics showed only a little dependence on the gate voltage (see Figure IV.33c) while the drain current at

zero gate bias was almost four times higher compared to the pencil trace (length and width are similar). The transfer curve (see Figure IV.33d) showed the ambipolar behavior with change in the I_{DS} of 1.5 µA and 0.5 µA for the hole and electron branches according to the applied gate voltages respectively. This indicates that electric field effect is less in the case of HOPG trace, which may be due to higher screening effects [104]. The pencil trace being turbostratic in nature with the intercalated clay particles, behaves like a 2D graphite system which is revealed through the observation of significant electric field effect induced by the gate.

Transfer characteristics of two more devices exhibited high mobility values but with some variation (~15%) (see Figure IV.34). Given that the substrate (paper) is rough and non-uniformity of pencil traces may cause the variation in the mobility values. The mobility values are less compared to the literature values obtained with graphite crystallites on SiO_2 surfaces [104], but are much higher compared to reduced graphene oxide based FETs [116]. However, the simple device reported here is not to be compared in terms of reproducible behavior and performance with a well-controlled single layer graphene device for example.
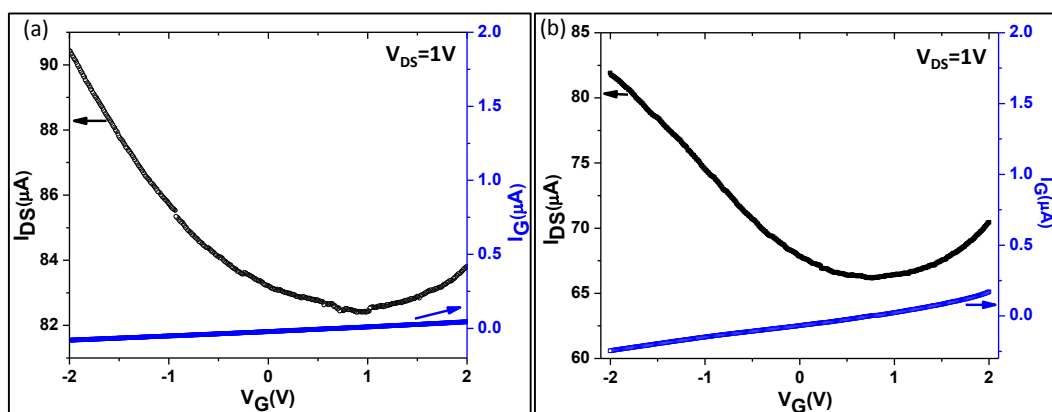
Figure IV.34 (a) and (b) Transfer curves of the pencil traces on the paper with ion gel as top gate dielectric. (hole and electron mobilities are found to be μ_h ~ 81, 112 and μ_e ~ 63, 69 cm^2/Vs for (a) and (b) respectively).

The electric field effect on the pencil-traces with varying resistances has also been investigated. It is observed that thicker pencil-traces with resistances up to 10 kΩ, showed a significant transconductance of 12-5 µS for holes and 4-2 µS for electrons (see marked region I, in Figure IV.35a). As the resistance of the pencil-trace increases upto 40 kΩ, the

transconductance gradually decreases (see region II, Figure IV.35a) and becomes negligible at higher channel resistance above 50 kΩ (region III, see Figure IV.35a). The corresponding SEM morphology of the pencil-traces in Figure IV.35b show that the low resistance thick trace is smooth and therefore the electrical transport is facile while the thinner pencil-traces may depend on percolative paths for electrical transport as the bottom cellulose fibers seem to intercept and disturbs the connectivity of the graphite domains of the pencil trace. Such scattering leads to lesser transverse electric field effect from the gate electrode (see Figure IV.35b).
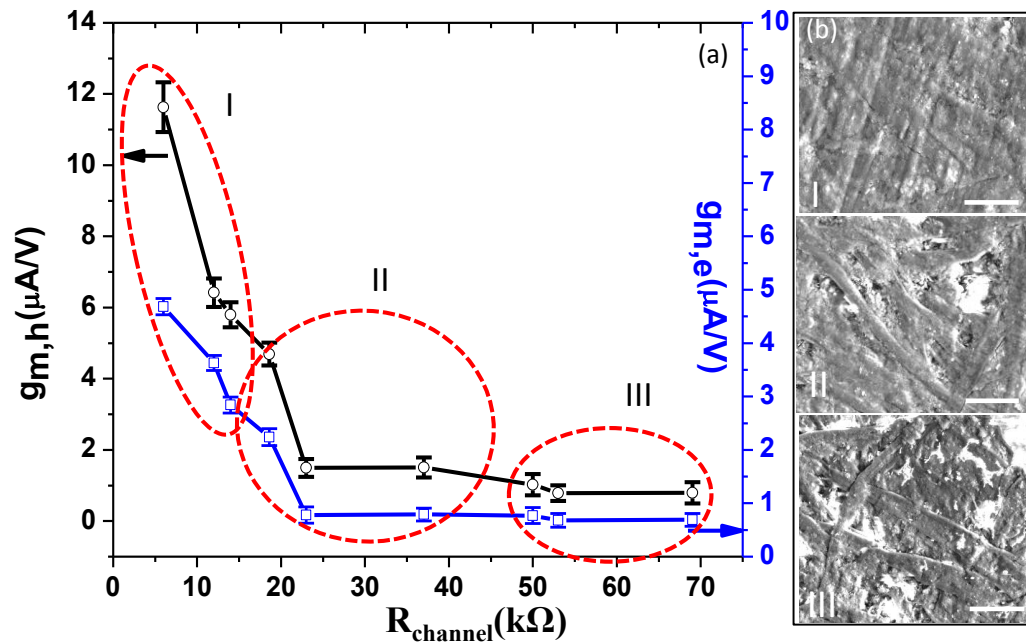
Figure IV.35 (a) Transconductance with respect to the varying resistance of the pencil-traces on paper. The corresponding SEM morphology of the pencil-traces (b). Scale bar, 50 μm.

The flexibility of the ion gel dielectric is demonstrated in Figure IV.36. The changes in the resistance of the channel and gate are normalised and plotted with respect to the bending angle in Figure IV.36a. It is observed that the resistance of the pencil mark changes significantly up to 160% at a maximum bending angle of 90º. The gate resistance, however, changes only up to 15% at a bending angle of 90º (see Figure IV.36b). Clearly, the ion gel dielectric is stable against substrate bending. Thus, the flexible ion gel based dielectrics can be explored as components for fabricating flexible electronic devices.
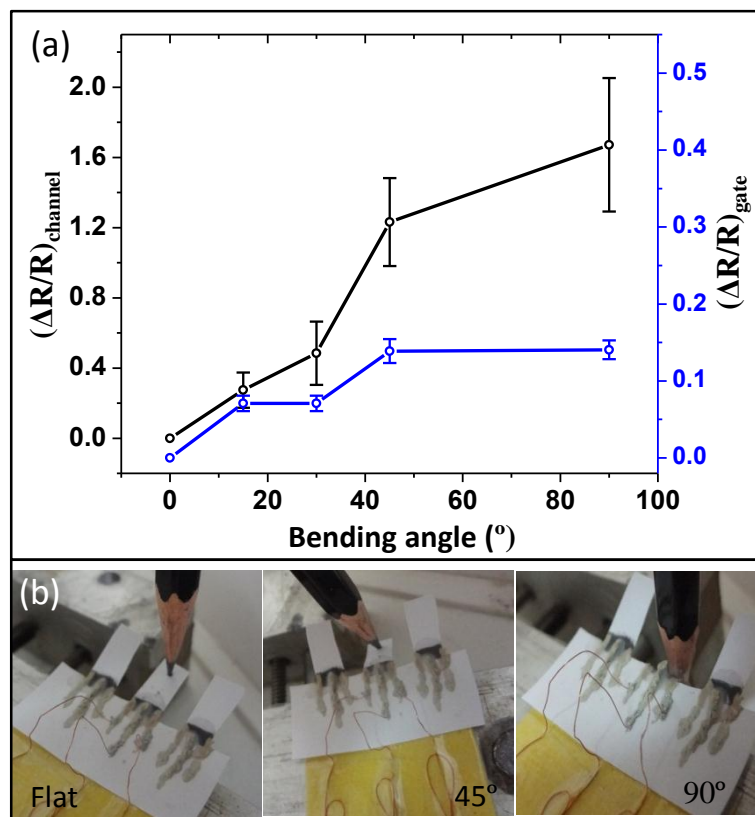
Figure IV.36 (a) Normalised resistance changes in the channel and the gate with respect to bending. The associated error bars are shown. (b) Photographs showing the extent of bending.

It is noteworthy that this study brings out clearly the turbostratic nature of the graphite in pencil trace and exploits it in making an active element of a field effect transistor. As substrate, common paper has been used which is attractive by all means. The dielectric properties of paper are supplemented by a PDMS based ion gel which could form conformal contact with the mating surface. Pencil traces with varied thicknesses and compositions can be obtained by applying different predefined pressures or by using pencils of different grades, which may offer interesting variations in device properties. The Ag electrodes may be screen or inkjet printed for the large area fabrication of pencil based FETs on paper. The passive circuits such as RC filters of higher orders can be built on a paper substrates in a cost effective manner.

IV.3.5 Conclusions

In conclusion, RC filters as well as FETs have been fabricated based on pencil markings on paper, with an ion-gel (1-butyl-3-methyl-imidazolium octylsulfate mixed with PDMS) as capacitor or gate dielectric. Graphite crystallites of the pencil-trace, which are turbostratic in nature, exhibited ambipolar electric field effect at low operating voltages. The carrier mobilities were found to be $\sim$ 106 and 59 cm^2/Vs for holes and electrons respectively. The RC filter exhibited a cut-off frequency of 9 kHz for a square wave input in the range of 100 Hz – 100 kHz, the output being a triangular wave. This approach offers a simple, solvent-free, low-cost method of fabricating filters and transistors on paper substrate, in use-and-throw applications not involving critical performance criteria. The fabrication of pencil-on-paper devices does not require any sophisticated facilities (clean room) and high end fabrication equipment. Being a direct-write method, it holds a great promise for graphite based electronic devices on paper. Future work may include the fabrication of large area pencil-trace based devices created using pencil plotters which may pave way to affordable and recycle electronics. This approach may also be used for fabricating higher order passive and active filters.

References

[1]   K. S. Novoselov, A. K. Geim, S. V. Morozov, D. Jiang, Y. Zhang, S. V. Dubonos, I. V. Grigorieva and A. A. Firsov, *Science*, 2004, **306**, 666.

[2]   A. K. Geim and K. S. Novoselov, *Nat. Mater.*, 2007, **6**, 183.

[3]   K. S. Novoselov, Z. Jiang, Y. Zhang, S. V. Morozov, H. L. Stormer, U. Zeitler, J. C. Maan, G. S. Boebinger, P. Kim and A. K. Geim, *Science*, 2007, **315**, 1379.

[4]   F. Bonaccorso, Z. Sun, T. Hasan and A. C. Ferrari, *Nat. Photon.,* 2010, **4**, 611.

[5]   Q. Bao and K. P. Loh, *ACS Nano,* 2012, **6**, 3677.

[6]   P. Avouris, *Nano Lett.,* 2010, **10**, 4285.

[7]   J. S. Bunch, A. M. van der Zande, S. S. Verbridge, I. W. Frank, D. M. Tanenbaum, J. M. Parpia, H. G. Craighead and P. L. McEuen, *Science*, 2007, **315**, 490.

[8]   A. A. Balandin, S. Ghosh, W. Bao, I. Calizo, D. Teweldebrhan, F. Miao and C. N. Lau, *Nano Lett.*, 2008, **8**, 902.

[9]   C. Lee, X. Wei, J. W. Kysar and J. Hone, *Science*, 2008, **321**, 385.

[10]   W. Bao, G. Liu, Z. Zhao, H. Zhang, D. Yan, A. Deshpande, B. LeRoy and C. Lau, *Nano Res.*, 2010, **3**, 98.

[11]   Y. B. Tang, C. S. Lee, Z. H. Chen, G. D. Yuan, Z. H. Kang, L. B. Luo, H. S. Song, Y. Liu, Z. B. He, W. J. Zhang, I. Bello and S. T. Lee, *Nano Lett.*, 2009, **9**, 1374.

[12] V. P. Gusynin and S. G. Sharapov, *Phys. Rev. Lett.*, 2005, **95**, 146801.

[13] K. S. Novoselov, E. McCann, S. V. Morozov, V. I. Fal'ko, M. I. Katsnelson, U. Zeitler, D. Jiang, F. Schedin and A. K. Geim, *Nat. Phys.*, 2006, **2**, 177.

[14] K. Nakada, M. Fujita, G. Dresselhaus and M. S. Dresselhaus, *Phys. Rev. B*, 1996, **54**, 17954.

[15] M. Ezawa, *Phys. Rev. B*, 2006, **73**, 045432.

[16] J. Bai, X. Duan and Y. Huang, *Nano Lett.*, 2009, **9**, 2083.

[17] G. Xu, C. M. Torres, J. Tang, J. Bai, E. B. Song, Y. Huang, X. Duan, Y. Zhang and K. L. Wang, *Nano Lett.*, 2011, **11**, 1082.

[18] At low length scales less than tens of nms, the band gap of graphene nanoribbons is inversely related to the width of the ribbon [9], due to edge states and quantum confinement. The mobility of the charge carriers decreases by 2-3 orders of magnitude with reduction in the lateral dimensions to sub tens of nanometers. But, the focus is on ribbons, well above this length scale.

[19] Y. Yang and R. Murali, *IEEE Electron Device Letters*, 2010, **31**, 237.

[20] K. S. Novoselov, D. Jiang, F. Schedin, T. J. Booth, V. V. Khotkevich, S. V. Morozov and A. K. Geim, *Natl. Acad. Sci. U.S.A.*, 2005, **102**, 10451.

[21] L. M. Viculis, J. J. Mack and R. B. Kaner, *Science*, 2003, **299**, 1361.

[22] D. A. Dikin , S. Stankovich , E. J. Zimney , R. D. Piner , G. H. B. Dommett , G. Evmenenko, S. T. Nguyen and R. S. Ruoff, *Nature*, 2007, **448**, 457.

[23] Y. Hernandez, V. Nicolosi, M. Lotya, F. M. Blighe, Z. Y. Sun, S. De, I. T. McGovern, B. Holland, M. Byrne, Y. K. Gun'Ko, J. J. Boland, P. Niraj, G. Duesberg, S. Krishnamurthy, R. Goodhue, J. Hutchison, V. Scardaci, A. C. Ferrari and J. N. Coleman, *Nat. Nanotechnol.*, 2008, **3**, 563.

[24] M. Lotya, Y. Hernandez, P. L. King, R. J. Smith, V. Nicolosi, L. S. Karisson, F. M. Blighe, S. De, Z. M. Wang, I. T. McGovern, G. S. Duesberg and J. N. Coleman, *J. Am. Chem. Soc.* 2009, **131**, 3611.

[25] C. A. Di, D. C. Wei, G. Yu, Y. Q. Liu, Y. L. Guo and D. B. Zhu, *Adv. Mater.*, 2008, **20**, 3289.

[26] X. Liang, Z. Fu and S. Y. Chou, *Nano Lett.*, 2007, **7**, 3840.

[27] L. Song, L. Ci, W. Gao and P. M. Ajayan, *ACS Nano*, 2009, **3**, 1353.

[28] X. Liang, A. S. P. Chang, Y. Zhang, B. D. Harteneck, H. Choo, D. L. Olynick and S. Cabrini, *Nano Lett.*, 2008, **9**, 467.

[29] D. S. Li, W. Windl and N. P. Padture, *Adv. Mater.*, 2009, **21**, 1243.

[30] M. Bieda, E. Beyer and A. F. Lasagni, *J. of. Eng. Mater. & Technol.*, 2010, **132**, 031015.

[31] A. F. Lasagni, J. L. Hendricks, C. M. Shaw, D. Yuan, D. C. Martin and S. Das, *Appl. Surf. Sci.*, 2009, **255**, 9186.

[32] T. Roch, E. Beyer and A. Lasagni, *Diamond and Related Materials*, 2010, **19**, 1472.

[33] A. Lasagni, R. Cross, S. Graham and S. Das, *Nanotechnology*, 2009, **20**, 245305.

[34] J. A. Rogers, K. E. Paul, R. J. Jackman and G. M. Whitesides, *J. Vac. Sci. Technol. B*, 1998, **16**, 59.

[35] J. A. Rogers, K. E. Paul, R. J. Jackman and G. M. Whitesides, *Appl. Phys. Lett.*, 1997, **70**, 2658.

[36] C. Larosa, E. Stura, R. Eggenhöffner and C. Nicolini, *Materials*, 2009, **2**, 1193.

[37] S. I. Kudryashov, A. A. Thikhov and V. D. Zvorykin, *Appl. Phys. A Mater. Sci & Processing*, 2010, **102**, 493-499.

[38] M. J. Allen, V. C. Tung, L. Gomez, Z. Xu, L. M. Chen, K. S. Nelson, C. W. Zhou, R. B. Kaner and Y. Yang, *Adv. Mater.*, 2009, **21**, 2098.

[39] K. S. Kim, Y. Zhao, H. Jang, S. Y. Lee, J. M. Kim, K. S. Kim, J.-H. Ahn, P. Kim, J.-Y. Choi and B. H. Hong, *Nature*, 2009, **457**, 706.

[40] M. S. Dresselhaus, A. Jorio, M. Hofmann, G. Dresselhaus and R. Saito, *Nano Lett.*, 2010, **10**, 751.

[41] M. A. Pimenta, G. Dresselhaus, M. S. Dresselhaus, L. G. Cancado, A. Jorio and R. Saito, *Phys. Chem. Chem. Phys.*, 2007, **9**, 1276.

[42] G. Jo, M. Choe, C. –Y. Cho, J. H. Kim, W. Park, S. Lee, W. –K. Hong, T.-W. Kim, S.-J. Park, B. H. Hong, Y. H. Kahng and T. Lee, *Nanotechnology*, 2010, **21**, 175201.

[43] J. Jiang, R. Saito, G. G. Samsonidze, A. Jorio, S. G. Chou, G. Dresselhaus and M. S. Dresselhaus, *Phys. Rev. B*, 2007, **75**, 035407.

[44] D. Graf, F. Molitor, K. Ensslin, C. Stampfer, A. Jungen, C. Hierold and L. Wirtz, *Nano Lett.*, 2007, **7**, 238.

[45] R. R. Nair, P. Blake, A. N. Grigorenko, K. S. Novoselov, T. J. Booth, T. Stauber, N. M. R. Peres and A. K. Geim, *Science*, 2008, **320**, 1308.

[46] G. Eda, G. Fanchini and M. Chhowalla, *Nat. Nanotechnol.*, 2008, **3**, 270.

[47] H. Bi, F. Huang, J. Liang, X. Xie and M. Jiang, *Adv. Mater.*, 2011, **23**, 3202.

[48] F. Wang, Y. Zhang, C. Tian, C. Girit, A. Zettl, M. Crommie and Y. R. Shen, *Science*, 2008, **320**, 206.

[49] F. Xia, T. Mueller, Y.-m. Lin, A. Valdes-Garcia and P. Avouris, *Nat. Nanotechnol.*, 2009, **4**, 839.

[50] V. Ryzhii, V. Mitin, M. Ryzhii, N. Ryabova and T. Otsuji, *Appl. Phys. Exp.*, 2008, **1**, 063002.

[51] X. Xu, N. M. Gabor, J. S. Alden, A. M. van der Zande and P. L. McEuen, *Nano Lett.*, 2009, **10**, 562.

[52] J. H. LeeEduardo, K. Balasubramanian, R. T. Weitz, M. Burghard and K. Kern, *Nat. Nanotechnol.*, 2008, **3**, 486.

[53] F. Xia, T. Mueller, R. Golizadeh-Mojarad, M. Freitag, Y.-m. Lin, J. Tsang, V. Perebeinos and P. Avouris, *Nano Lett.*, 2009, **9**, 1039.

[54] G. Rao, M. Freitag, H.-Y. Chiu, R. S. Sundaram and P. Avouris, *ACS Nano*, 2011, **5**, 5848.

[55] M. C. Lemme, F. H. L. Koppens, A. L. Falk, M. S. Rudner, H. Park, L. S. Levitov and C. M. Marcus, *Nano Lett.*, 2011, **11**, 4134.

[56] D. Sun, G. Aivazian, A. M. Jones, J. S. Ross, W. Yao, D. Cobden and X. Xu, *Nat. Nanotechnol.*, 2012, **7**, 114.

[57] J. C. W. Song, M. S. Rudner, C. M. Marcus and L. S. Levitov, *Nano Lett.*, 2011, **11**, 4688.

[58] J. Park, Y. H. Ahn and C. Ruiz-Vargas, *Nano Lett.*, 2009, **9**, 1742.

[59] B. Chitara, L. S. Panchakarla, S. B. Krupanidhi and C. N. R. Rao, *Adv. Mater.*, 2011, **23**, 5419.

[60] J. Loomis and B. Panchapakesan, *Nanotechnology* 2012, **23**, 265203.

[61] S. Ghosh, B. K. Sarker, A. Chunder, L. Zhai and S. I. Khondaker, *Appl. Phys. Lett.*, 2010, **96**, 163109.

[62] Y. Liu, R. Cheng, L. Liao, H. Zhou, J. Bai, G. Liu, L. Liu, Y. Huang and X. Duan, *Nat.Commun.*, 2012, **2**, 579.

[63] T. J. Echtermeyer, L. Britnell, P. K. Jasnos, A. Lombardo, R.V. Gorbachev, A. N. Grigorenko, A. K. Geim, A.C. Ferrari and K. S. Novoselov, nat. Commun., 2011, **2**, 458.

[64] H. Chang, Z. Sun, K. Yat-Fung Ho, X. Tao, F. Yan, W.-M. Kwok and Z. Zheng, *Nanoscale*, 2011, **3**, 258.

[65] G. Konstantatos, M. Badioli, L. Gaudreau, J. Osmond, M. Bernechea, F. P. G. de Arquer, F. Gatti and F. H. L. Koppens, *Nat. Nanotechnol.*, 2012, **7**, 363.

[66] J. Yan, M. H. Kim, J. A. Elle, A. B. Sushkov, G. S. Jenkins, H. M. Milchberg, M. S. Fuhrer and H. D. Drew, *Nat. Nanotecnol.*, 2012, **7**, 472.

[67] M. E. Itkis, F. Borondics, A. Yu and R. C. Haddon, *Science*, 2006, **312**, 413.

[68] H. Vora, P. Kumaravadivel, B. Nielsen and X. Du, *Appl. Phys. Lett.* 2012, **100**, 153507.

[69] K. C. Fong and K. C. Schwab, *Phys. Rev. X*, 2012, **2**, 031006.

[70] R. S. Singh, V. Nalla, W. Chen, W. Ji and A. T. S. Wee, *Appl. Phys. Lett.*, 2012, **100**, 093116.

[71] P. W. Atkins, Physical Chemistry; Oxford University Press: Oxford, U.K., 1990.

[72] L. Gao, W. Ren, H. Xu, L. Jin, Z. Wang, T. Ma, L.-P. Ma, Z. Zhang, Q. Fu, L.-M. Peng, X. Bao and H.-M. Cheng, *Nat. Commun.*, 2012, **3**, 699.

[73] A. J. Pollard, R. R. Nair, S. N. Sabki, C. R. Staddon, L. M. A. Perdigao, C. H. Hsu, J. M. Garfitt, S. Gangopadhyay, H. F. Gleeson, A. K. Geim and P. H. Beton, *J. Phys. Chem. C*, 2009, **113**, 16565.

[74] J. H. Chu, J. Kwak, T.-Y. Kwon, S.-D. Park, H. Go, S. Y. Kim, K. Park, S. Kang and S.-Y. Kwon, *ACS Appl. Mater. & Interfaces*, 2012, **4**, 1777.

[75] D. Kang, W.-J. Kim, J. A. Lim and Y.-W. Song, *ACS Appl. Mater. & Interfaces*, 2012, **4**, 3663.

[76] A. C. Ferrari, J. C. Meyer, V. Scardaci, C. Casiraghi, M. Lazzeri, F. Mauri, S. Piscanec, D. Jiang, K. S. Novoselov, S. Roth and A. K. Geim, *Phys. Rev. Lett.*, 2006, **97**, 187401.

[77] Z. Yan, Z. Peng, Z. Sun, J. Yao, Y. Zhu, Z. Liu, P. M. Ajayan and J. M. Tour, *ACS Nano*, 2011, **5**, 8187.

[78] Z. Peng, Z. Yan, Z. Sun and J. M. Tour, *ACS Nano*, 2011, **5**, 8241.

[79] M. A. Pimenta, G. Dresselhaus, M. S. Dresselhaus, L. G. Cancado, A. Jorio and R. Saito, *Phys. Chem. Chem. Phys.*, 2007, **9**, 1276.

[80] L. M. Malard, M. A. Pimenta, G. Dresselhaus and M. S. Dresselhaus, *Phys. Rep.*, 2009, **473**, 51.

[81] P. G. Collins, K. Bradley, M. Ishigami and A. Zettl, Science, 2000, **287**, 1801.

[82] H. –J. Shin, W. M. Choi, S. –M. Yoon, G. H. Han, Y. S. Woo, E. S. Kim, S. J. Chae, X. –S. Li, A. Benayad, D. D. Loc, F. Gunes, Y. H. Lee and J. –Y. Choi, *Adv. Mater.,* 2011, **23**, 4392.

[83] F. T. Vasko and V. Ryzhii, *Phys. Rev B*, 2008, **77**, 195433.

[84] G. A. M. Reynolds, Electronic transport and photoconductive properties of Resorcinol–Formaldehyde Based Carbon Aerogels, Ph.D. Thesis, MIT, 1995.

[85]   S. Cain, A. A. Cantu, R. Brunnelle and A. Lyter, *J. Forensic Sci.*, 1978, **23**, 643.

[86]   J. A. Zoro and R. N. Totty, *J. Forensic Sci.,* 1980, **25**, 675.

[87]   J. A. Denman, I. M. Kempson, W. M. Skinne and K. P. Kirkbride, *Forensic Sci. Int.,* 2008, **175**, 123.

[88]   M. S. Dresselhaus and G. Dresselhaus, *Adv. Phys.*, 2002, **51**, 1.

[89]   R. N. Bhowmik, *Composites: PartB*, 2012, **43**, 503.

[90]   G. Zheng, L. Hu, H. Wu, X. Xie and Y. Cui, *Energy Environ. Sci.*, 2011, **4**, 3368.

[91]   T.-L. Ren, H. Tian, D. Xie and Y. Yang, *Sensors*, 2012, **12**, 6685.

[92]   Y. Wang and H. Zhou, *Energy Environ. Sci.*, 2011, **4**, 1704.

[93]   A. J. Gimenez, J. M.Yáñez-Limón and J. M. Seminario*, J. Phys. Chem. C*, 2011, **115**, 282.

[94]   K. u. Hasan, O. Nur and M. Willander, *Appl. Phys. Lett.*, 2012, **100**, 211104.

[95]   P. Mandal, R. Dey and S. Chakraborty, *Lab Chip*, 2012, **12**, 4026.

[96]   M. Santhiago and L. T. Kubota, *Sens. Actuators B*, 2013, **177**, 224.

[97]   D. Tobjörk and R. Österbacka, *Adv. Mater.*, 2011, **23**, 1935.

[98]   Z. Nie, C. A. Nijhuis, J. Gong, X. Chen, A. Kumachev, A. W. Martinez, M. Narovlyansky and G. M. Whitesides, *Lab Chip*, 2010, **10**, 477.

[99]   D.-H. Kim, Y.-S. Kim, J. Wu, Z. Liu, J. Song, H.-S. Kim, Y. Y. Huang, K.-C. Hwang and J. A. Rogers, *Adv. Mater.*, 2009, **21**, 3703.

[100] A. Russo, B. Y. Ahn, J. J. Adams, E. B. Duoss, J. T. Bernhard and J. A. Lewis, *Adv. Mater.*, 2011, **23**, 3426.

[101] L. Hu, J. W. Choi, Y. Yang, S. Jeong, F. La Mantia, L.-F. Cui and Y. Cui, *Proc. Natl. Acad. Sci. U. S. A.*, 2009, **106**, 21490.

[102] K. Kordás, T. Mustonen, G. Tóth, H. Jantunen, M. Lajunen, C. Soldano, S. Talapatra, S. Kar, R. Vajtai and P. M. Ajayan, *Small*, 2006, **2**, 1021.

[103] Y. M. Lin, C. Dimitrakopoulos, K. A. Jenkins, D. B. Farmer, H. Y. Chiu, A. Grill and P. Avouris, *Science*, 2010, **327**, 662.

[104] A. Sagar, K. Balasubramanian, M. Burghard and K. Kern, *Appl. Phys. Lett.*, 2012, **100**, 203116.

[105] R. Misra, M. McCarthy and A. F. Hebard, *Appl. Phys. Lett.*, 2007, **90**, 052905.

[106] H. Yuan, H. Shimotani, A. Tsukazaki, A. Ohtomo, M. Kawasaki and Y. Iwasa, *Adv. Funct. Mater.*, 2009, **19**, 1046.

[107] J. H. Cho, J. Lee, Y. He, B. S. Kim, T. P. Lodge and C. D. Frisbie, *Adv. Mater.*, 2008, **20**, 686.

[108] J. H. Cho, J. Lee, Y. Xia, B. Kim, Y. He, M. J. Renn, T. P. Lodge and C. Daniel Frisbie, *Nat. Mater.*, 2008, **7**, 900.

[109] B. J. Kim, H. Jang, S.-K. Lee, B. H. Hong, J.-H. Ahn and J. H. Cho, *Nano Lett.*, 2010, **10**, 3464.

[110] Y. Hernandez, V. Nicolosi, M. Lotya, F. M. Blighe, Z. Sun, S. De, I. T. McGovern, B. Holland, M. Byrne, Y. K. Gun'Ko, J. J. Boland, P. Niraj, G. Duesberg, S. Krishnamurthy, R. Goodhue, J. Hutchison, V. Scardaci, A. C. Ferrari and J. N. Coleman, *Nat. Nanotechnol.*, 2008, **3**, 563.

[111] Setton, R., in Carbon Molecules and Materials, edited by R. Setton, P. Bernier, and S. Lefrant (Taylor and Francis, New York, 2002), p. 22.

[112] D. Yu, C. Wang, B. L. Wehrenberg and P. Guyot-Sionnest, *Phys. Rev. Lett.*, 2004, **92**, 216802.

[113] S. S. N. Bharadwaja, C. Venkatasubramanian, N. Fieldhouse, S. Ashok, M. W. Horn and T. N. Jackson, *Appl. Phys. Lett.*, 2009, **94**, 222110.

[114] B. Chen, T. Cui, Y. Liu and K. Varahramyan, *Solid State Electron.*, 2003, **47**, 841.

[115] K. Nagashio, T. Nishimura, K. Kita and A. Toriumi, *Appl. Phys. Express*, 2009, **2**, 025003.

[116] B. J. Kim, M. S. Kang, V. H. Pham, T. V. Cuong, E. J. Kim, J. S. Chung, S. H. Hur and J. H. Cho, *J. Mater. Chem.*, 2011, **21**, 13068.

Part V

Solar baked electrodes for the fabrication of high performance supercapacitors

Summary

This study introduces a new strategy for making electrodes for supercapacitors based on nanocrystalline Pd/carbon (nc-Pd/C) composite, obtained through thermolysing the thin film of Pd hexadecylthiolate under the concentrated sunlight. The nc-Pd/C composite exhibited a porous morphology and hydrophilic nature besides the good electrical conductivity (resistivity of ~ 2 $\mu\Omega$.m); confirmed through microscopy, contact angle and electrical measurements. The electrochemical performance of the nc-Pd/C composite was examined in aqueous (6M KOH), ion gel (PVA/H_3PO_4), ionic liquid (1M EMIMBF$_4$/ACN) and neutral (1M Na_2SO_4) electrolytes. Further, these nc-Pd/C composite electrodes were patterned by laser ablative lithography which enhanced the specific capacitance by 1.5 times compared to that of unpatterned films.

The autocatalytic nature of nc-Pd/C composite was exploited by depositing inexpensive pseudocapacitive material such as manganesedioxide (MnO_2) in an electroless manner. The electrochemical performance of MnO_2 coated nc-Pd/C composite was investigated by cyclic voltammetry (CV) and charge-discharge (CD) experiments in 1M Na_2SO_4 aqueous electrolyte, which showed a high specific capacitance of ~ 450 F/g. Further, an asymmetric supercapacitor was fabricated by employing MnO_2/nc-Pd/C as a positive electrode while the nc-Pd/C as a negative electrode, the potential window was extended up to 1.8 V, exhibited a maximum energy density of 86 Wh/kg. This synthesis protocol eludes processing involving high temperatures, multistep solution processes as well as the use of binders without compromising the electrochemical performance.

V.1 Introduction

There is a great deal of interest worldwide in developing electrochemical energy storage devices with the aim of achieving high energy and power densities [1-3]. Conventionally, batteries and fuel cells which work based on Faradaic processes [4], store high energy (~ 10 to 200 Wh/kg), but suffer from low power densities, low cyclability and discharge rates [3-6]. To circumvent these problems, alternative devices with higher power

densities are being developed which are known as electrochemical capacitors or supercapacitors [6-9]. Besides the high power density, long cycle life and fast discharge rates have made supercapacitors quite attractive in recent times [1, 7-9].

The electrode materials of a supercapacitor can be characterized by their high surface area and electrically conducting nature. The capacitance of a supercapacitor is superior to conventional capacitor due to the formation of electric double layers (EDLs) where the ions of the electrolyte get accumulated at the electrode/electrolyte interface upon the application of potential [3, 10, 11]. This double-layer capacitance generates a potential between the plates which gets harnessed in an external circuit [1, 3, 10, 11]. In this context, carbon based materials have been extensively explored as they possess large surface area, high electrical conductivity and excellent electrochemical stability; essential for a supercapacitor electrode [12-15]. The carbon materials have been activated through chemical, thermal and plasma methods in order to enhance porosity along with the tunable morphology [16-19]. Thus, activated carbons in the form of onions [20], nanoparticles [21], fibres [22] and nanotubes [23] have been explored as electrode materials in supercapacitors. Similarly, graphene and its derivatives such as curved [24], activated [25], solvated [26], doped graphene [27] as well as three dimensional graphene networks [28] have been employed as electrode materials in supercapacitors. It was found that the graphene layers tend to restack themselves with increasing number of cycles and this issue has been addressed by mixing the spacers such as CNTs and Au nanoparticles [29, 30].

The major challenge is to improve the energy density without sacrificing the power density, which translates to searching novel electrode materials involving balanced design of material composition, size and morphology, as well as employing suitable electrolytes [3, 31]. Pseudo capacitive coatings such as metal oxides (RuO_2, MnO_2, and NiO) [32-35], conducting polymers (polyaniline, polythiophenes and polypyrrole) [36, 37] and also hybrid electrodes [38, 39] in combination with the high surface area electrodes to attain the desired values of energy and power densities. However, supercapacitors based on carbon materials and pseudo capacitive coatings involve high temperature treatments, activation by the chemicals, multi-step complex solution processing and chemical vapor deposition techniques [16-39]. Implementation of additives such as polymer binders and conductive

adhesives may increase electrode stability but often cause degradation of the electrochemical performance [30-35].

V.2 Scope of the present investigation

The quest is to arrive at an optimized electrode material involving simple and inexpensive chemical recipes in a binder-free manner. Here, a new strategy was introduced in order to fabricate electrode materials of a supercapacitor which essentially consisting of nanocrystalline Pd/carbon composite (nc-Pd/C) derived from a molecular precursor subjected to mild thermolysis under the concentrated sunlight. Further, the autocatalytic nature of the nc-Pd/C composite could assist in depositing nanoscale MnO_2 features after dipping in neutral permanganate solution. The electrochemical performance was investigated in neutral 1M Na_2SO_4 electrolyte with a maximum specific capacitance of 450 F/g at a scan rate of 10 mV/s. Further, an asymmetric supercapacitor MnO_2/nc-Pd/C//nc-Pd/C was also designed which showed the maximum energy and power densities of 86 Wh/kg and 30 kW/kg, respectively. This synthesis protocol eludes processing involving high temperatures, multistep solution processing as well as the use of binders without compromising the electrochemical performance.

V.3. Experimental Details

Synthesis of nc-Pd/C composite

The synthesis procedure for the precursor, Pd hexadecylthiolate, $Pd(SC_{16}H_{33})_2$, is reported elsewhere [40]. Briefly, 100 mmol of hexadecylthiol (Sigma Aldrich) was added to 100 mmol of $Pd(OAc)_2$ (Sigma Aldrich) in toluene solution under stirring. The solution became viscous and color changed from orange to reddish orange. The glass substrates used for film formation were cleaned with deionized water and acetone followed by drying under N_2 flow. A 50 μl of 100 mM Pd hexadecylthiolate precursor solution was drop casted on a cleaned glass substrate which appears as orange color film. A convex lens with diameter of 8'' and a focal length of 50 cm was used for focusing sunlight which produces a temperature of 220 ℃ on the film, measured using a thermometer. During the heat treatments, the precursor decomposes leading to the formation of conducting nc-Pd/C composite within 30 minutes. Alternatively, nc-Pd/C was also obtained through heating on a hot plate (temperature ~ 220 °C) for 3 h.

Electroless deposition of MnO$_2$

      6 mM KMnO$_4$ in water solution was prepared and it was used as a precursor solution for depositing nanoscale MnO$_2$ features. Different loadings of MnO$_2$ were obtained at different dipping times (30 sec-10 min) followed by washing in distilled water to remove the unreacted permanganate.

Electrochemical characterization

Electrochemical double layer capacitor

      Supercapacitor is a commonly used term to a versatile class of energy storage devices that rely on the physical adsorption of ions at an electrode/electrolyte interface to form an electric double layer with a typical charge separation distance of ~ 1 nm. The geometry of the supercapacitors includes two identical porous carbon based electrodes separated by an ion permeable separator and electrolyte. The performance of supercapacitors can be investigated through cyclic voltammetry, charge-discharge and impedance measurements.

Cyclic voltammetry gives a voltammogram which is a measure of charge response with respect to changing voltage, estimating capacitance of a supercapacitor. The voltammogram records the current change with respect to the changing voltages at constant scan rate (dV/dt). The capacitance can be related to current (I) and scan rate (s) by the following equation

$$C = I/s\ldots..(V.1)$$

The specific capacitance was calculated from the equation $C_s = 2(1/m_t)(I/s)\ldots..(V.2)$

where m_t is the total mass of the electrodes (0.4-0.45 mg), I is the current in mA and s is the sweep rate in mV/sec (s = dV/dt).

The voltammogram for an ideal capacitor with no resistance would be of rectangular shape, but most real EDLC voltammograms would have the shape of parallelogram with irregular peaks. Prominent peaks at particular voltages are usually due to Faradaic processes (pseudocapacitive behavior). Higher scan rates correspond to charging and discharging of the supercapacitor at higher power levels. Typically, a set of cyclic voltammograms will be displayed at different scan rates in the same graph to determine the impact on charging characteristics at different power levels. The degree of reversibility of an electrode reaction can also be inferred from the voltammogram in which the reversible

and irreversible processes would have mirror image and two separate charge and discharge profiles respectively.

The energy and power densities of a supercapacitor can be estimated from after performing charge-discharge experiment at constant current. The voltage response can be obtained through charging or discharging the cell at a constant current. The equivalent series resistance (ESR) was calculated from the IR drop in the discharge curve. IR drop is the potential drop at the beginning of the discharge curve which arises due to the resistance of the electrodes, electrolyte and interfaces ($\Delta V = 2I_cR$ where I_c is the charging current and R is the ESR).

$$Energy\ (E) = \tfrac{1}{2}\ QV = \tfrac{1}{2}\ CV^2 \ldots\ldots(V.3)$$

The energy density was calculated from the formula

$$E = (1/2)C_s(V)^2 \ldots..(V.4)$$

where V is the working potential window of an electrolyte.

$$Power\ (P) = I \times V \ldots\ldots(V.5)$$

Power densities are calculated by multiplying different discharge current densities with the value of working potential (V). The maximum power density was calculated from the formula,

$$P_{max} = (V)^2/4Rm_t \ldots\ldots(V.6)$$

Electrical impedance spectroscopy (EIS) is a powerful method for evaluating the supercapacitor performance in the frequency domain. After applying a small AC voltage, the changes in magnitude and phase over a range of frequencies will be measured. The impedance can then be plotted on a Nyquist diagram where the imaginary part of impedance (-Z''(ohm)) is plotted against the real part (Z'(ohm)). For an ideal capacitor, a vertical straight line shifted on the real axis by its ESR is seen.

V.4 Results and Discussion

V.4a Fabrication of nc-Pd/C composite

Pd hexadecylthiolate is a novel precursor which upon mild thermolysis, produces nanocrystalline Pd in carbon matrix (nc-Pd/C) with tunable conducting property [41]. The precursor is amenable for patterning by various lithography techniques to achieve fine features of the nc-Pd/C [40-43]. This composite was previously employed in our laboratory as an active element in fabricating hydrogen [42] and strain sensors [41]. Drop coating of

Pd hexadecylthiolate precursor followed by drying of the solvent in air leaves orange colored film, which is insulating in nature (see Figure V.1). Now this film was baked under the sun light after focusing through a convex lens (diameter, 8'' and focal length of 50 cm) which could produce the maximum temperature of 220 ºC. The heat energy generated at the hot spot of the sunlight causes the decomposition of Pd hexadecylthiolate, leading to the liberation of volatile carbonaceous species. Subsequently, the Pd nanoparticles get nucleated leading to the formation of porous nc-Pd/C film within 30 minutes of irradiation (see Figure V.1). The multimeter display showing the two probe resistance value of nc-Pd/C film is of ~ 9 Ω. Even, similar kind of nc-Pd/C film can also be made through thermolysis of Pd hexadecylthiolate at 220 °C in air on a hot plate. The composite of nc-Pd/C was employed as a porous conducting electrode material in fabricating supercapacitors.

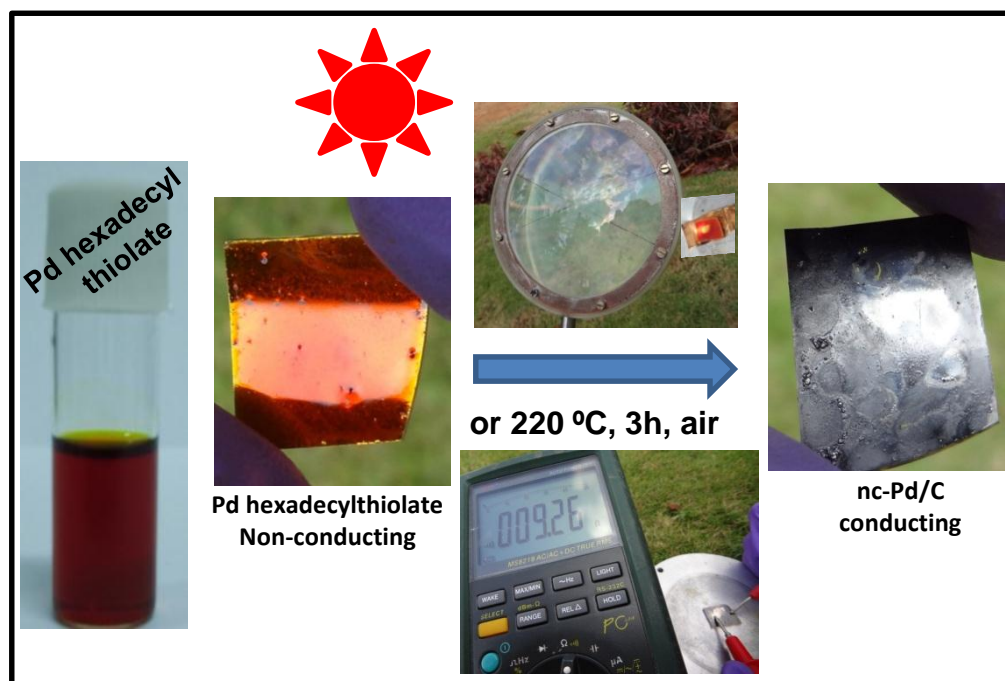**Figure V.1** Photograph showing the metal-organic precursor, Pd hexadecylthiolate. Thermolysis of Pd hexadecylthiolate (orange color) into nc-Pd/C (black color) using concentrated sunlight, obtained through focusing by convex lens. Focused spot of sunlight on the sample surface along with the lens is shown in the top. Bottom multimeter reading displaying the resistance value of the nc-Pd/C composite film.

V.4b Characterization of nc-Pd/C composite

The crystalline nature of nc-Pd/C was analyzed using the X-ray diffraction technique. The XRD pattern of the film showed peaks corresponding to metallic Pd, with the estimated particle size of ~16 nm (Fig. V.2). The Pd nanoparticles size can be calculated from (111) peak of XRD using Scherrer formula.

$$L = k\lambda/\beta\cos\theta.....(V.7)$$

where L = grain size

k = 0.9 (constant)

λ = wavelength (1.54Å)

β = (FWHM-FWHM for standard) * π/180

L = 0.9*1.54/ [(0.503)*(π/180)* cos(20.28*(π/180))]

= 158.2 Å

= 15.8 nm.

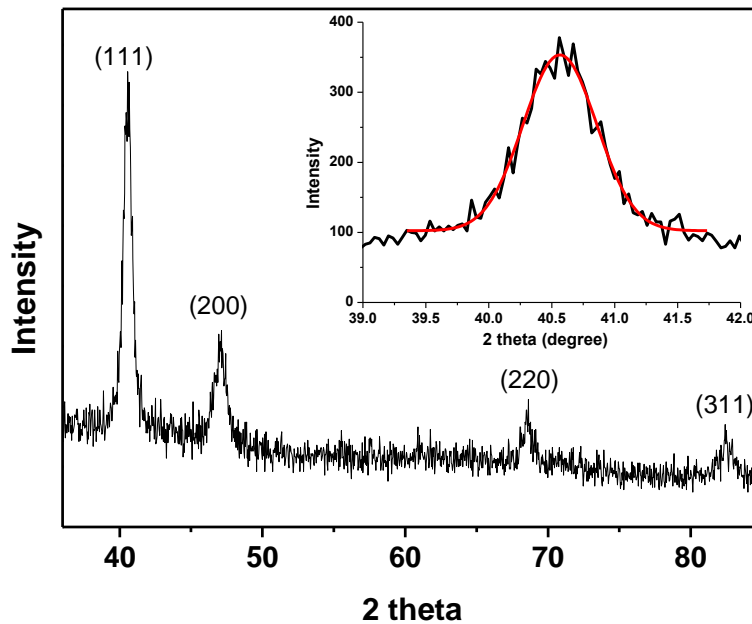**Figure V.2** XRD of nc-Pd/C composite film. The indexed peaks are matching well with metallic Pd. Inset shows the peak fitting for the calculation of particle size.

The morphology, composition and electrical nature of the nc-Pd/C composite were examined through microscopy and electrical measurements. This composite consists of densely packed, interconnected Pd nanoparticles (typical size, 15-20 nm) as seen in the

FESEM image (see Figure V.3a). The EDS spectra collected from different regions of the sample showed the presence of C and Pd in the atomic ratio, 1:2 (see inset of Fig V.3a). It is evident that the Pd hexadecylthiolate underwent decomposition leading to the formation of the Pd nanoparticles along with the carbonaceous species. The size of the Pd nanoparticles and the amount of the carbon content can be controlled through the annealing temperature [41]. The Pd particle size increases and the carbon content decreases with increase in the annealing temperature.
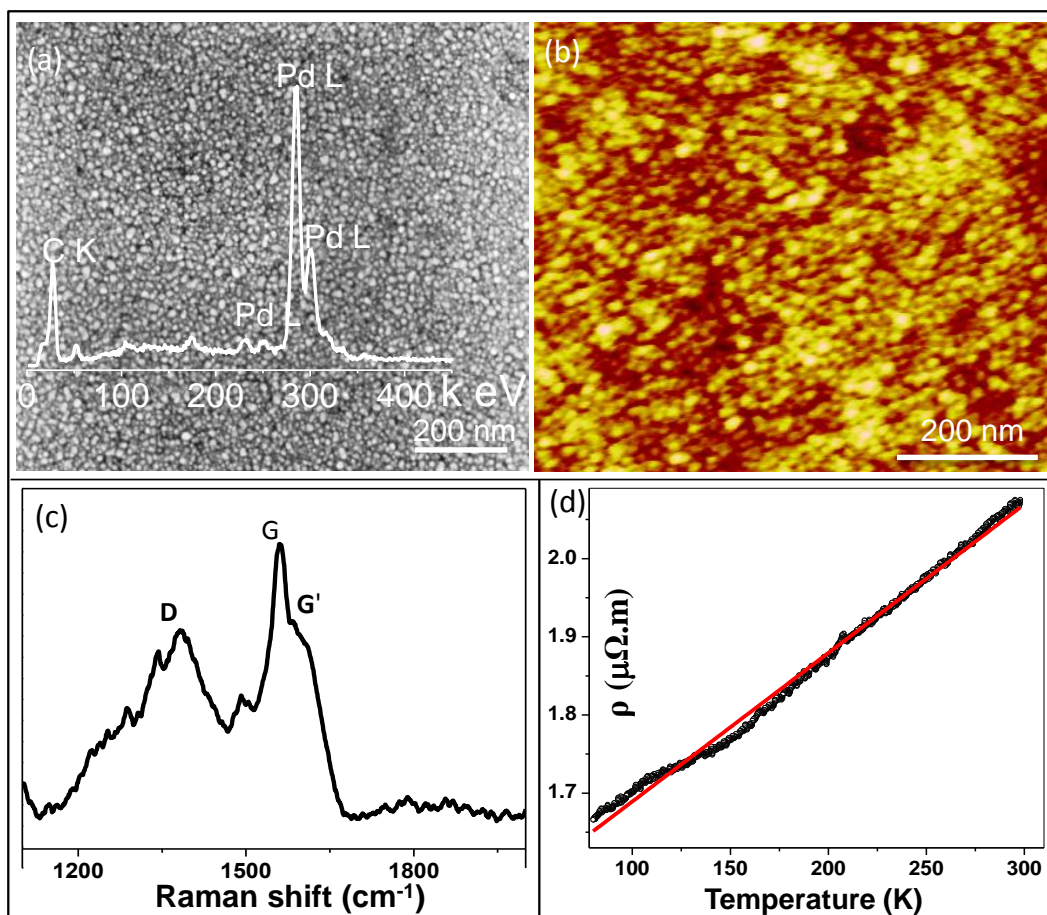
Figure V.3 (a) FESEM image showing the densely packed Pd nanoparticles, inset is the energy dispersive spectrum (EDS) showing Pd L and C K signals. (b) AFM topography and (c) Raman spectrum of the nc-Pd/C film showing the presence of functionalized amorphous carbon. (d) Temperature dependent resistivity of the film with near metallic behavior.

AFM topography of the nc-Pd/C film also showed the particle nature of the film (see Figure V.3b). In order to understand the nature of the carbon present in the nc-Pd/C film, Raman spectra was recorded from different regions of the film which showed the presence of broad D (position, 1377 cm^{-1}, width 185 cm^{-1}) and G bands (1564 cm^{-1}, width

38 cm^{-1}) with a shoulder at 1620 cm^{-1} corresponding to the G' band (width of 55 cm^{-1}), implying that the presence of functionalized amorphous carbon (see Figure V.3c) [44]. The electrical nature of the nc-Pd/C film was investigated through the temperature dependent resistivity measurements. The resistivity increased with increasing temperature, exhibiting metallic type behavior (see Figure V.3d). The room temperature resistivity was found to be ~ 2 μΩ.m, which reflects the highly conducting nature of the nc-Pd/C composite.
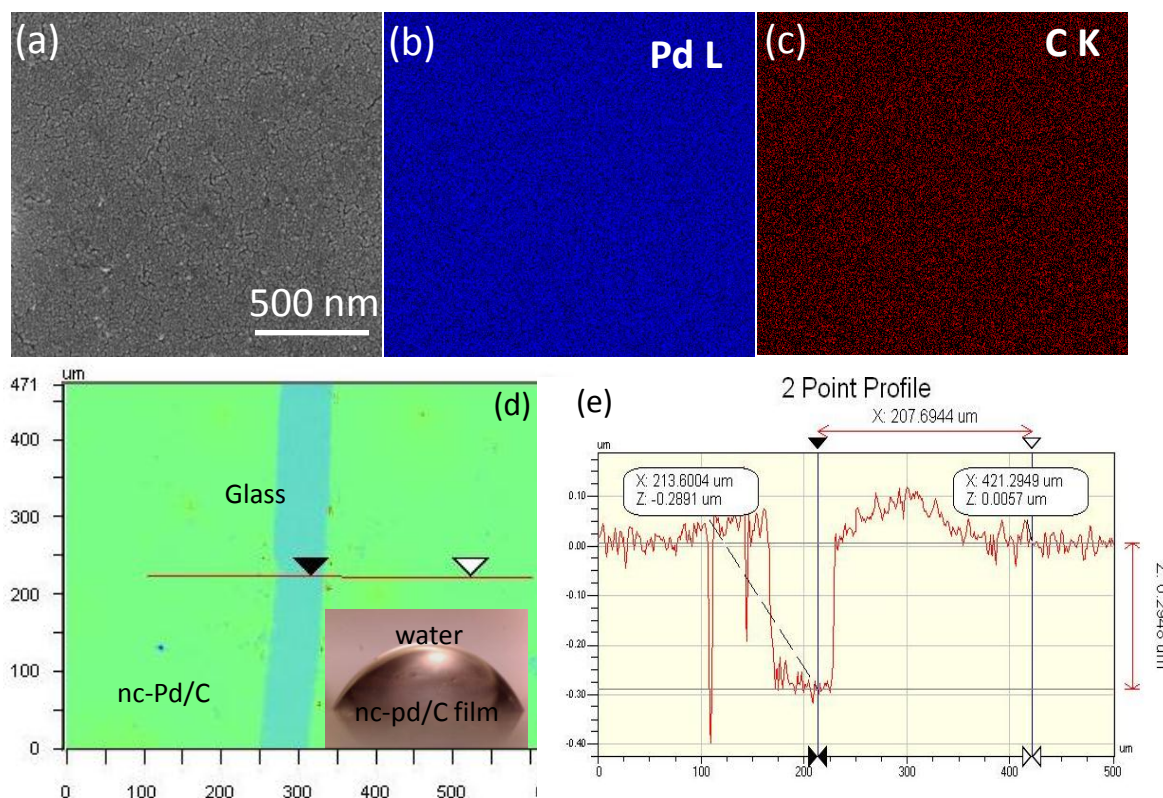

Figure V.4 EDS mapping of nc-Pd/C film on glass substrate. (a) SEM image of nc-Pd/C film in which mapping was done. (b) and (c) shows the presence of palladium and carbon uniformly over the substrate. (d) The optical profile image of prepared nc-Pd/C film over glass substrate to estimate thickness of the film. Inset shows the water contact angle on the nc-Pd/C film, found to be 49°, hydrophilic surface due to functionalized carbon. (e) the z-profile of the nc-Pd/C film on glass.

The uniformity of the Pd and carbon over the entire area of the nc-Pd/C film was investigated through EDS mapping (Figure V.4a, b, c). The PdL and CK maps showed the presence of carbon and Pd throughout the entire surface region mapped. The thickness of the nc-Pd/C films measured using profilometer with a typical thickness of ~ 300 nm (Figure V.4d, e). The water contact angle on the nc-Pd/C film is found to be 49°, indicating the hydrophilic nature of the surface due to presence of functional groups (see inset of Figure V.4d).

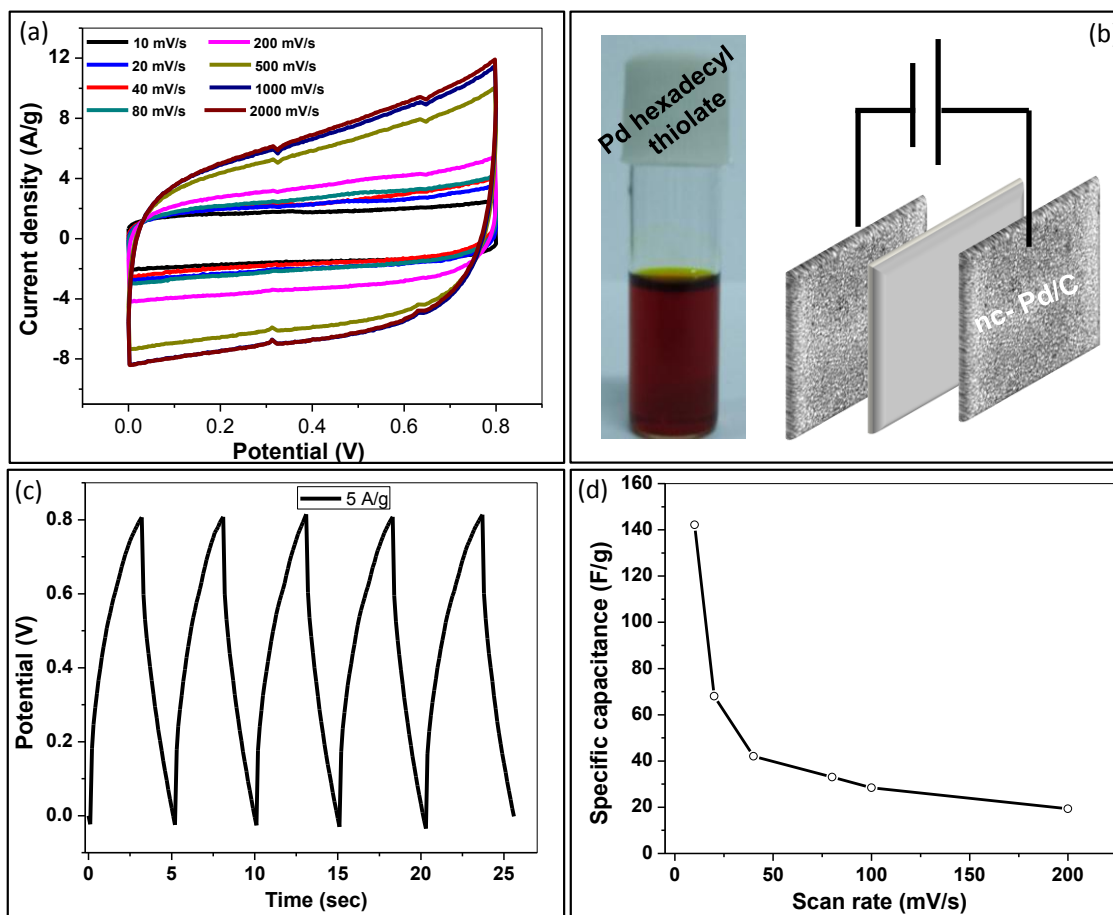## V.4c Electrochemical characterization of nc-Pd/C composites

Figure V.5 The performance of the nc-Pd/C electrochemical capacitor in aqueous 1M Na$_2$SO$_4$ solution. (a) Cyclic voltammograms (CV) at different scan rates, from 10 to 2000 mV/s. (b) Two-electrode configuration of the nc-Pd/C electrodes along with the separator. (c) Galvanostatic charge/discharge (CD) curves at a current density of 5 A/g. (d) Specific capacitance as a function of scan rate.

In order to examine the electrochemical properties, an assembly of two symmetric electrodes of nc-Pd/C composite (size, 1 x 1 cm) with a filter paper separator was immersed in 1M Na$_2$SO$_4$ aqueous electrolyte (5 ml). The electrochemical performance was analyzed through both cyclic voltammetry (CV) and galvanostatic charge/discharge (CD) experiments, as shown in Figure V.5. The CV curves are of nearly rectangular shape over scan rates of 10 to 2000 mV/s in the potential window of 0 - 0.8 V, indicating the formation of EDLs (Figure V.5a), which is an indication for the capacitive behavior of these nc-Pd/C electrodes. A galvanostatic charging/discharging (CD) test was conducted in the potential window of 0 - 0.8 V at a fixed current density of 5 A/g (see Figure V.5c). The CD curves show nearly triangular shape indicative of the formation of efficient EDLs

within the nc-Pd/C electrodes. The specific capacitance of ~ 140 F/g was observed at a low scan rate of 10 mV/s and deceasing with increasing scan rates (see Figure V.5d). Based on the value of specific capacitance, one can also estimate the active electrochemical surface area from the following equation.

$$\text{Specific capacitance } (C_i) = \varepsilon_o \varepsilon A_{el}/d \ldots\ldots \text{ (V.8)}$$

Where, ε_o – permittivity of free space = 8.85×10^{-12} F/m

ε - dielectric constant of the 1M Na_2SO_4 ~ 75

d- double layer thickness ~ 1 nm

C_i = 140 F/g

After substituting the above values, electrochemical active surface area (A_{el}) was found to be ~ 420 m^2/g.
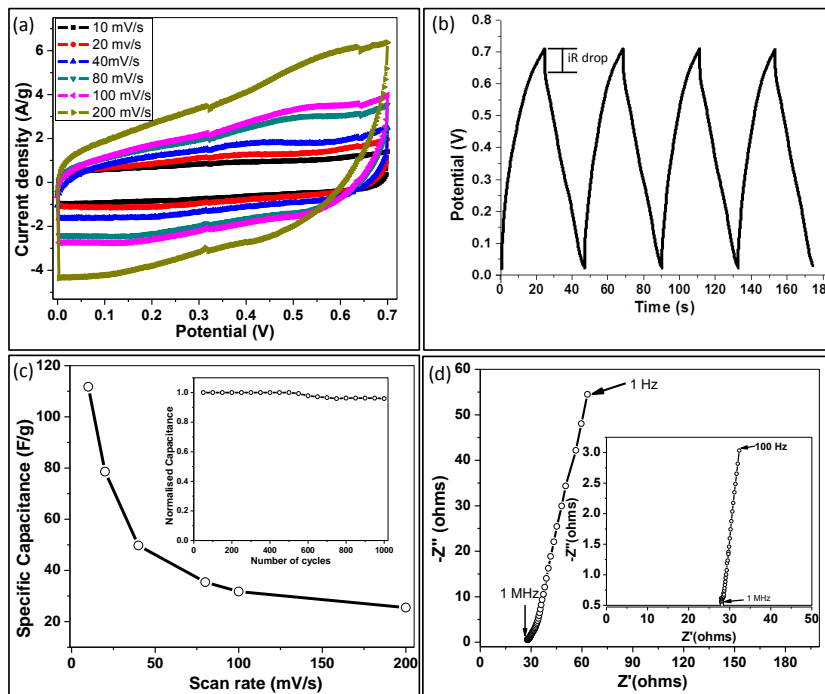
Figure V.6 The performance of the nc-Pd/C electrochemical capacitor in aqueous 6 M KOH solution. (a) Cyclic voltammetry (CV) curves at different scan rates, from 10 to 200 mV/s. A nearly rectangular shape of the CV curves indicates an efficient double-layer formation. (b) Galvanostatic charge/discharge (CD) curves at a current density of 2 A/g. (c) Specific capacitance as a function of scan rate, inset shows the Normalized capacitance versus number of cycles. (d) The Nyquist impedance plot of nc-Pd/C supercapacitor in the frequency range 1 MHz to 1 Hz, with the inset showing the high-frequency region.

The electrochemical performance of the nc-Pd/C electrodes were also examined in 6M KOH aqueous electrolyte. The CV curves are nearly rectangular in shape over scan

rates of 10 to 200 mV/s in the potential window of 0 - 0.7 V, indicating the capacitive behavior (Figure V.6a). CV curves contain a small peak at around 0.4 V which may be a redox peak corresponding to the functional groups of the amorphous carbon matrix. On the other hand, the presence of functional groups is advantageous in that the wetting of the electrolyte solution is enhanced while the Pd nanoparticles along with amorphous carbon bring in the desired porosity to the electrode. Neither a separate metal electrode as current collector nor any binder (or electro-active additives) was used. The nc-Pd/C composite along with the functionalized carbon species supports the formation of EDLs and also as a current collector. A galvanostatic charging/discharging (CD) test was conducted in the potential window of 0 - 0.7 V at a fixed current density of 2 A/g (see Figure V.6b). The CD curves show nearly triangular shape indicative of the formation of efficient EDLs within the nc-Pd/C electrodes. In addition, the CD curves show only a small voltage drop of 0.06 V at the start of the discharge curve, indicating that the device had a low equivalent series resistance (ESR) of the order of 30 Ω (Figure V.6b). The specific capacitance decreased from 110 to 25 F/g with increasing scan rate, 10 to 200 mV/s (see Figure V.6c). The long term cycling stability of the nc-Pd/C supercapacitor was tested through a cyclic CD curves at a fixed current density of 2 A/g (see inset of Figure V.6c). The capacitance remained at 95% of the initial capacitance after 1000 CD cycles, demonstrating its excellent long term cycling stability. Further, the electrochemical impedance measurements for the nc-Pd/C composite electrodes were performed in order to understand the frequency response. Nyquist plot in Figure V.6d shows the imaginary component (Z'') of impedance against the real component (Z') as the frequency of the ac voltage is varied from 1 Hz to 1 MHz. The intersection of the curve at the X-axis corresponding to higher frequency region, represents the equivalent series resistance (ESR) which in this case was found to be ~ 29 Ω, which determines the rate at which the supercapacitor can be charged or discharged. The vertical nature of the curve at lower frequencies reflects the capacitive behavior indicating facile ion diffusion in the electrode structure [10].

A solid state supercapacitor of nc-Pd/C was designed using PVA/H_3PO_4 gel electrolyte (see Figure V.7). The cyclic voltammograms for different scan rates (20 - 400 mV/s) show nearly rectangular shape, indicating the EDL formation (see Figure V.7a). The specific capacitance was found to be ~ 45 F/g at a scan rate of 10 mV/s. In the case of

PVA/H_3PO_4 gel, the mobility of the ions is restricted due to presence of PVA matrix unlike the case of aqueous KOH electrolyte. The specific capacitance decreased from 45 to 5 F/g with increasing scan rate from 10 to 400 mV/s (see Figure V.7b). The galvanostatic charge-discharge curves showed the triangular shape which is an indication of the EDL formation. The voltage drop corresponds to the ~ 0.09 V (see Figure V.7c). The capacitance retention test conducted over 1000 cycles demonstrated the excellent stability of the supercapacitor (see Figure V.7d).
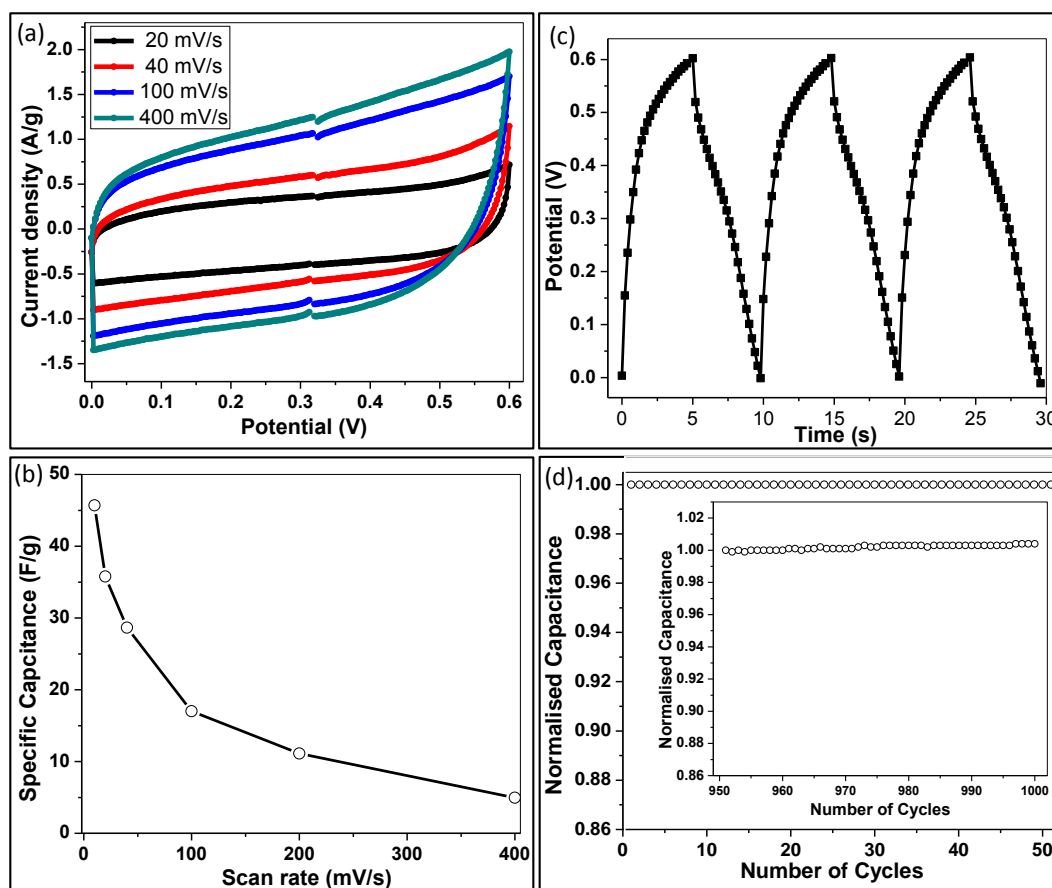
Figure V.7 Solid state supercapacitors based on nc-Pd/C films using PVA/H_3PO_4 gel electrolyte. (a) Cyclic voltammetry (CV) curves at different scan rates ranging from 20 to 400 mV/s. (b) Specific capacitance as a function of scan rate. (c) Galvanostatic charge/discharge (CD) curves at a current density of 3 A/g. (d) Normalized capacitance versus number of cycles, inset is for the higher cycle numbers.

The electrochemical performance of the nc-Pd/C film has also been investigated in 1M EMIMBF$_4$ in acetonitrile (Figure V.8). The CV curves are of nearly rectangular shape over scan rates of 10 to 400 mV/s in the potential window of 0 – 1.5 V, indicating the formation of EDLs (Figure V.8a), which is an efficient capacitive behavior. A

galvanostatic charging/discharging (CD) test was conducted in the potential window of 0 – 1.5 V at a fixed current density of 10 A/g (see Figure V.8b).
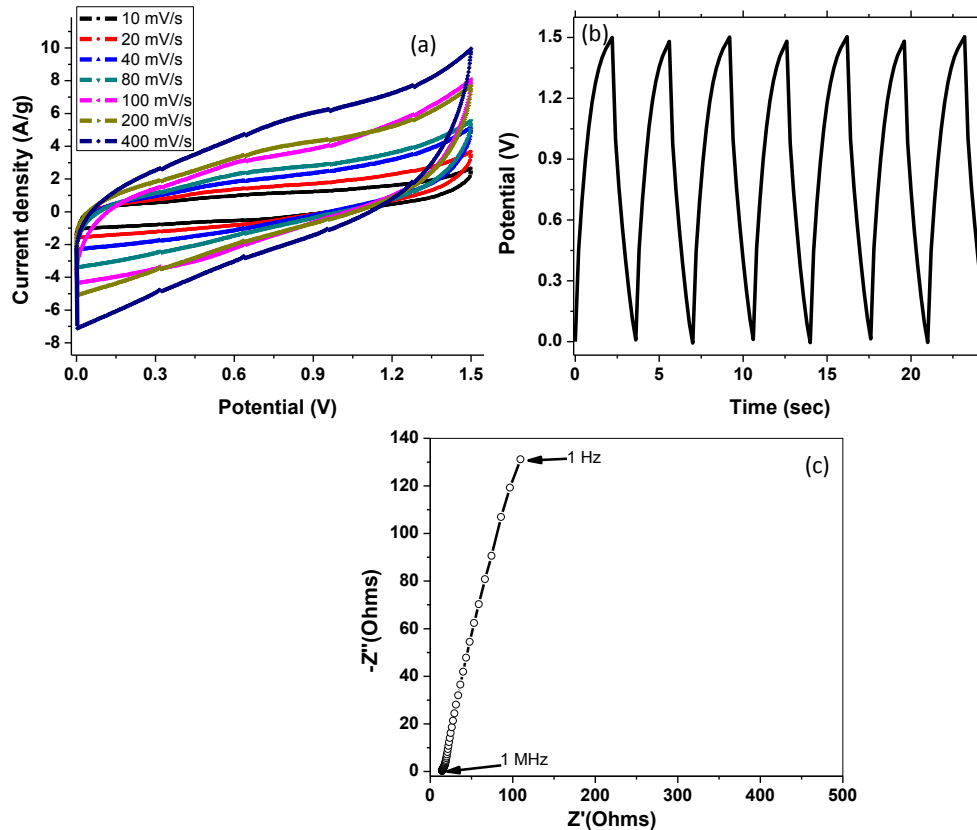
Figure V.8 (a) CV and (b) CD curves for the nc-Pd/C films using the ionic liquid electrolyte 1M EMIMBF$_4$ in acetonitrile (current density of 5 A/g). (c) Nyquist impedance plot of the nc-Pd/C in ionic liquid electrolyte.

The CD curves show nearly triangular shape indicative of the formation of efficient EDLs within the nc-Pd/C electrodes. Further, the electrochemical impedance measurements for the nc-Pd/C composite electrodes were performed in order to understand the frequency response. Nyquist plot in Figure V.8c shows the imaginary component (Z'') of impedance against the real component (Z') as the frequency of the ac voltage is varied from 1 Hz to 1 MHz. The vertical nature of the curve at lower frequencies reflects the capacitive behavior indicating facile ion diffusion in the electrode structure [10].

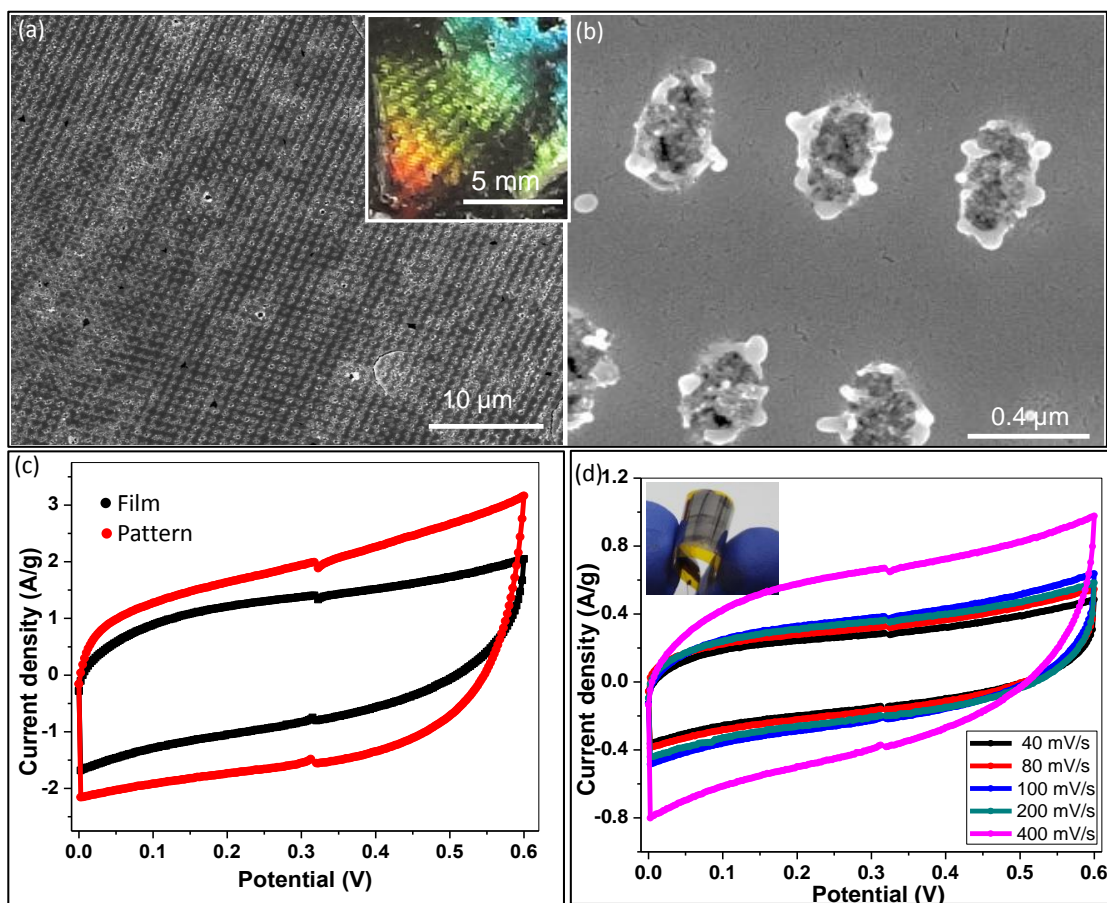**Figure V.9** (a) FESEM images of the periodic pits on the nc-Pd film over a large area, inset shows the diffraction of the light from the nc-Pd/C grating. (b) Zoom-in view of the pits on the nc-Pd film. (c) Comparison of the specific capacitance of the nc-Pd/C film (black) with the patterned (red) film in PVA/H_3PO_4 gel at a scan rate of 400 mV/s. (d) CV curves for the nc-Pd film over the flexible kapton substrate at different scan rates. Inset shows the flexible nc-Pd/C film over kapton sheet.

Pd hexadecylthiolate is amenable for patterning by various lithography techniques such as electron beam lithography, soft lithography and nanoimprint lithography [40, 41, 43, 44]. Near-field laser ablative patterning was employed to create periodic pits on the nc-Pd/C film over a large area by using combination of phase masks. Previously, this method has been used on graphite to make graphene ribbons [45]. Single shot laser ablation of the nc-Pd/C film through two DVD phase masks resulted in the formation of periodic pits over a large area (see Figure V.9a). The pits are typically 200 nm wide and 100 nm deep (see Figure V.9b). Specific capacitance was found to be 1.5 times higher compared with the plane nc-Pd/C films (scan rate of 400 mV/s, see Figure V.9c). This indicates that the periodic pits on the nc-Pd/C film helps in the formation of greater number of EDLs due to

increase in the effective surface area, leading to an increment in specific capacitance. The nc-Pd/C films are electrically stable against bending [41]. These films could be formed on flexible kapton sheets and the electrochemical performance was examined in the PVA/H$_3$PO$_4$ gel. The CV curves recorded at different scan rates, from 40 to 400 mV/s, are nearly rectangular, indicating the capacitive nature of the nc-Pd/C electrodes (see Figure V.9d).

V.4d Pseudocapacitive MnO$_2$ coating and electrochemical characterization

MnO$_4^-$ ions can be spontaneously reduced to MnO$_2$ on a functionalized carbon surfaces based on the following reaction [46, 47].

$$4MnO_4^- + 3C + H_2O \longrightarrow 4MnO_2 + CO_3^{2-} + 2HCO_3^- \quad .....(V.9)$$

Reduction of permanganate ion (MnO$_4^-$) to MnO$_2$ on carbon is pH dependent. The electrically conducting nature of nc-Pd/C helps in the spontaneous reduction of permanganate ions into manganese dioxide. Neutral permanganate solution leads to the formation of thin films of MnO$_2$, while acidic solution would result in the formation of large agglomerated MnO$_2$ particles [46]. It has been shown that the nc-Pd/C surface exhibits autocatalytic property which could assist the spontaneous growth of Cu, ZnO, polyaniline [47]. MnO$_2$ is a very cheap and good pseudocapacitve material which was brought onto the nc-Pd/C surface in an electroless manner after dipping in neutral permanganate solution. The typical morphology of the MnO$_2$ was found to be petal-like vertical growth which is very good for the formation of double layers besides its pseudocapacitive behavior. The electrolyte ions can thus access the entire surface of the vertical petals which should lead to enhanced capacitance. The amount of MnO$_2$ deposited on the nc-Pd/C surface was controlled depending on the dipping time (30 sec-10 min).

The growth conditions of MnO$_2$ on the nc-Pd/C surface were optimized. Dipping of nc-Pd/C substrates in neutral permanganate solution for 30 seconds resulted in the less dense deposits while dipping for longer times (10 minutes) resulted in the formation of thicker deposits (see Figures V.10a-e). It was found that the deposition time of 2 minutes resulted in the optimal coverage of MnO$_2$ where the bottom the nc-Pd/C surface is also seen (see Figure V.10c). The Raman spectrum of the MnO$_2$ is characterized by one sharp peak at 638 cm^{-1} and two weak peaks at around 290 and 347 cm^{-1} respectively (see Figure V.10f). The peak at 638 cm^{-1} may be assigned to the symmetric Mn-O stretching vibration

of MnO_6 octahedra group [49]. The low-frequency bands at 290 cm^{-1} and 347 cm^{-1} are assigned to the bending modes of Mn-O. The bands in the Raman spectrum of MnO_2 are closely matching to that of γ-MnO_2 [49].
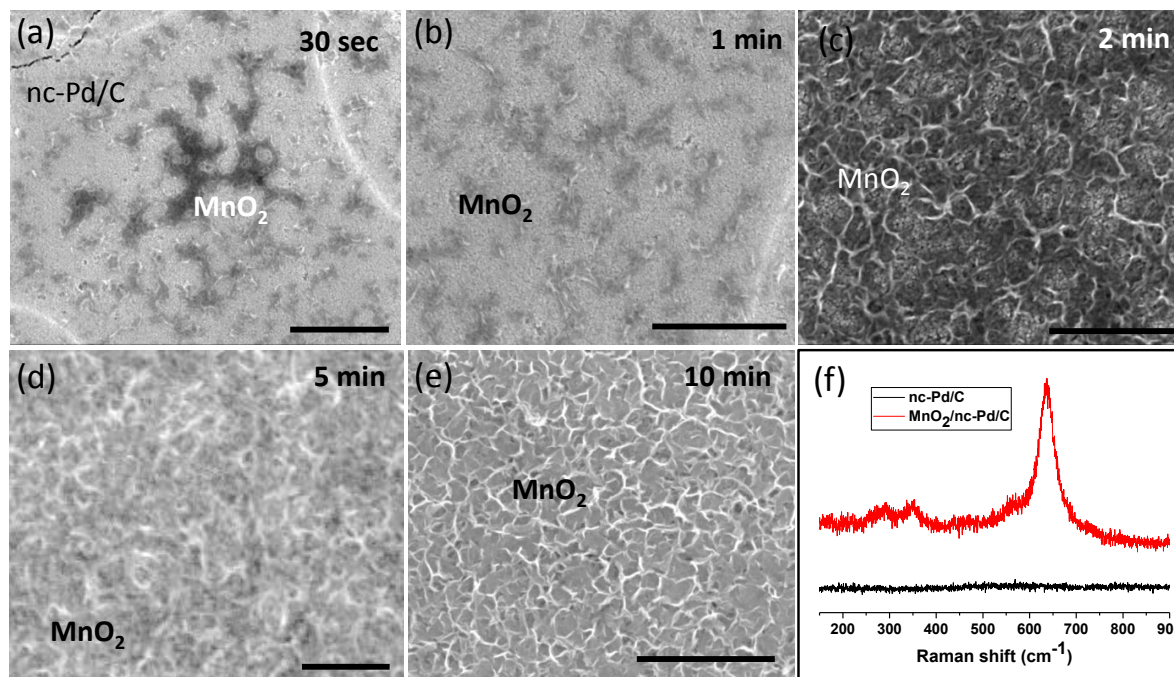

Figure V.10 Electroless deposition of MnO_2 nanowall structures on the autocatalytic nc-Pd/C surface. (a-e) FESEM images of the MnO_2 nanowall structures after dipping in neutral permangante solution for 30 sec, 1 min, 2 min, 5 min and 10 minutes respectively. (f) Raman spectra of the MnO_2 in comparision with palne surface. Scale bar, 1 μm.

Cyclic voltammetry (CV) measurements were performed for the MnO_2/nc-Pd/C composites for different mass loadings of MnO_2. All the electrochemical measurements were performed in two electrode configuration in 1M Na_2SO_4 solution. Figure V.11a shows the scan rate dependent CVs for 30 seconds deposited MnO_2 on nc-Pd/C surface at different scan rates of 10-500 mV/s, with a potential window of 0-0.8 V. The current values of CVs for 5 min deposited MnO_2 on nc-Pd/C are found to be higher and good symmetrical rectangular shape for CVs at various scan rates were observed showing the capacitive behavior of MnO_2/nc-Pd/C electrodes (see Figures V.11a-d).
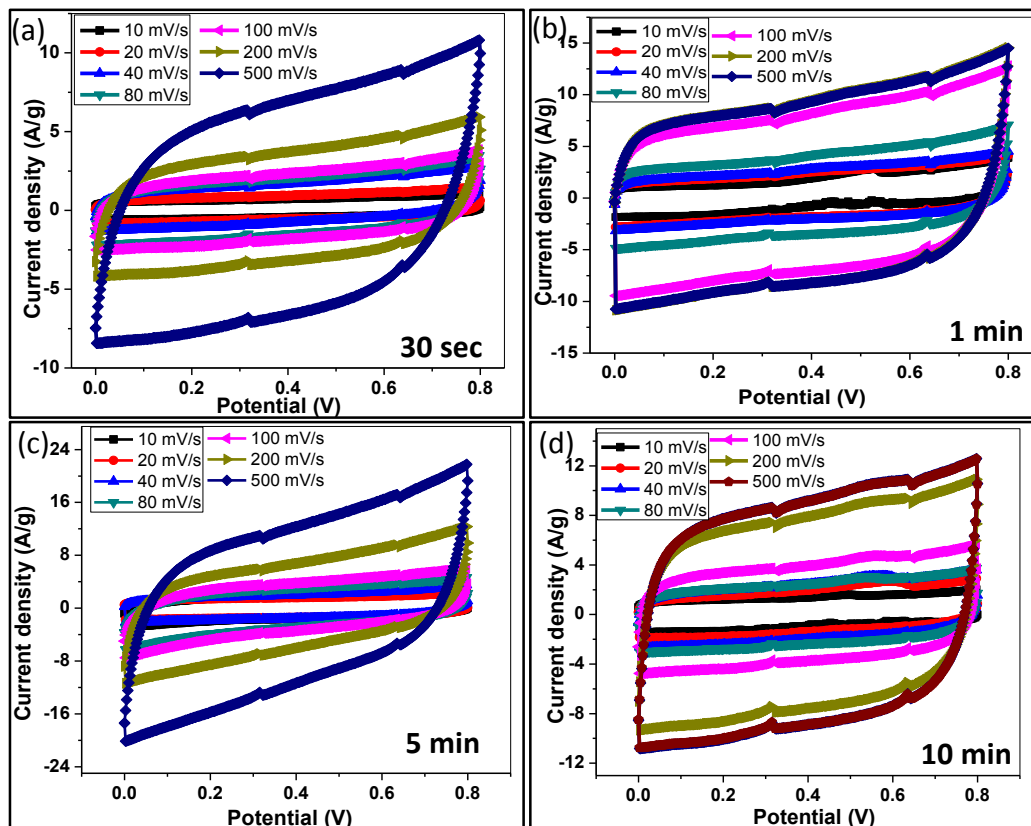
Figure V.11 (a-d) Cyclic voltammetry curves for MnO_2/nc-Pd/C structure at different scan rates (10-500 mV/s) with different MnO_2 deposition times of 0.5, 1, 5 and 10 min, respectively.

Figure V.12a shows the scan rate dependent CVs for 2 min MnO_2/nc-Pd/C at scan rates of 10-200mV/s, with a potential window of 0-0.8 V. The current values of CVs were higher than those of plane nc-Pd/C and also different deposition times of MnO_2 at the same scan rates (see Figures V.11 and 12a). The galvanostatic charge/discharge curves at different current densities are shown in Figure V.12b. The triangular nature of the of charge and discharge curves revealing that the good capacitive characteristics of the device. The specific capacitance for different amounts of MnO_2 on nc-Pd/C was plotted against the scan rate (see Figure V.12c). It was found that the 2 minutes deposited MnO_2 showed the maximum specific capacitance of 450 F/g at a scan rate of 10 mV/s. In other words, the optimal coverage of MnO_2 increases the specific capacitance from 140 F/g (plane nc-Pd/C without MnO_2) to 450 F/g (see Figure V.12d). As MnO_2 is an insulating material, thicker deposits result in the higher resistivity for electron transfer, leading to the decreased specific capacitance values at longer deposition times. The optimal coverage of

MnO$_2$ over nc-Pd/C is required for obtaining better performance which in this case found to be depositing time of 2 minutes.
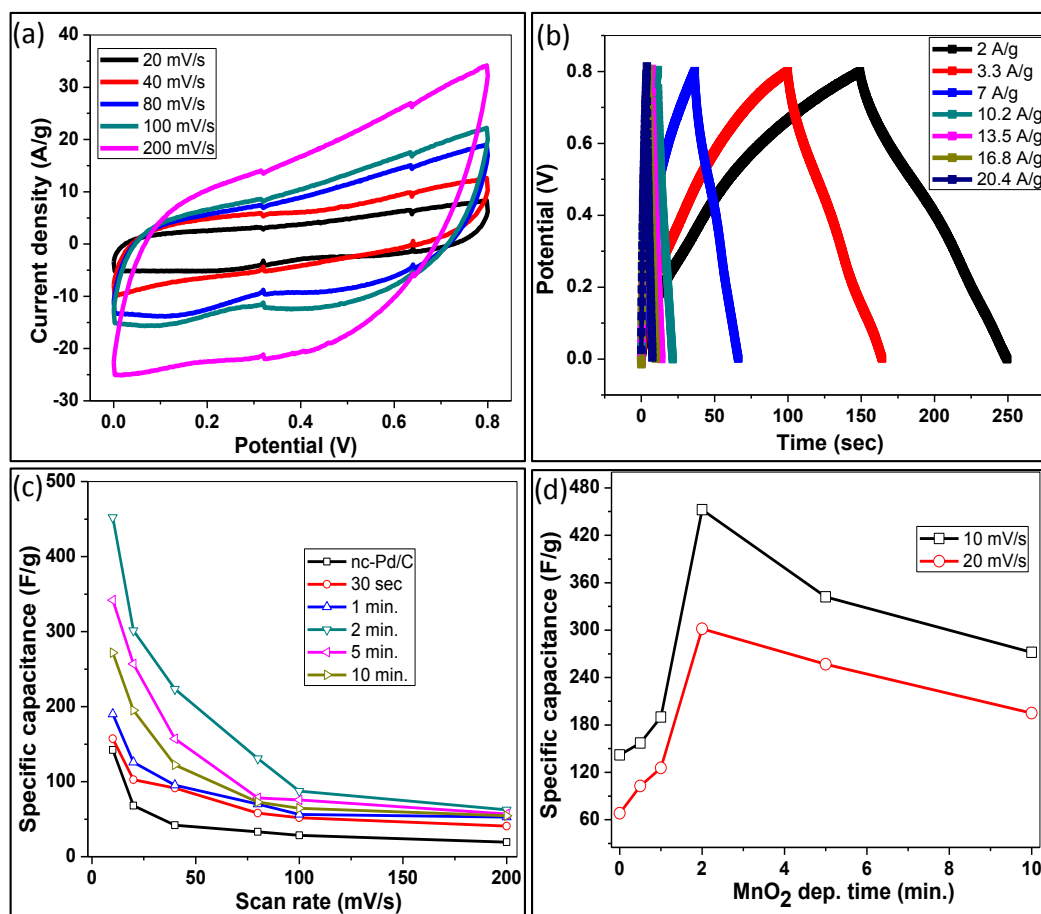

Figure V.12 (a) Cyclic voltammetry curves for (2 min) MnO$_2$/nc-Pd/C at different scan rates ranging from 5 to 100 mV/s. (b) Galvanostatic charging/discharging curves at different current densities. (c) Specific capacitance versus scan rates at varied mass loadings of MnO$_2$ in comparison to the plane nc-Pd/C. (d) Plot of specific capacitance with respect to MnO$_2$ deposition times at scan rates of 10 and 20 mV/s.

V.4e Asymmetric supercapacitor

As the energy density is directly proportional to specific capacitance and square of the operating potential window (E = ½ C$_i$V^2), broadening of the total potential range and increases the energy density through an asymmetric configuration of electrodes. Here, in this study, ASC was made by connecting MnO$_2$/nc-Pd/C//nc-Pd/C to the positive and negative electrodes respectively in 1M Na$_2$SO$_4$ solution. The CV curves for MnO$_2$/nc-Pd/C//nc-Pd/C ASC at different scan rates in the potential window of 0-0.8 V showed

rectangular curves (see Figure V.13a). Further, the CV curves were recorded at a scan rate of 80 mV/s via extending the potential range up to 1.8 V which showed rectangular curves, indicating that the stable electrochemical window of the ASC till 1.8 V (see Figure V.13b). In order to further evaluate the performance of the cell, the galvanostatic charge and discharge was performed at a current density of 7 A/g by extending the potential window from 0.8 V to 1.8 V (see Figure V.13c). The electrochemical stability of the ASC was tested by performing charge-discharge cycles over 1000 times at a current density of 7 A/g.
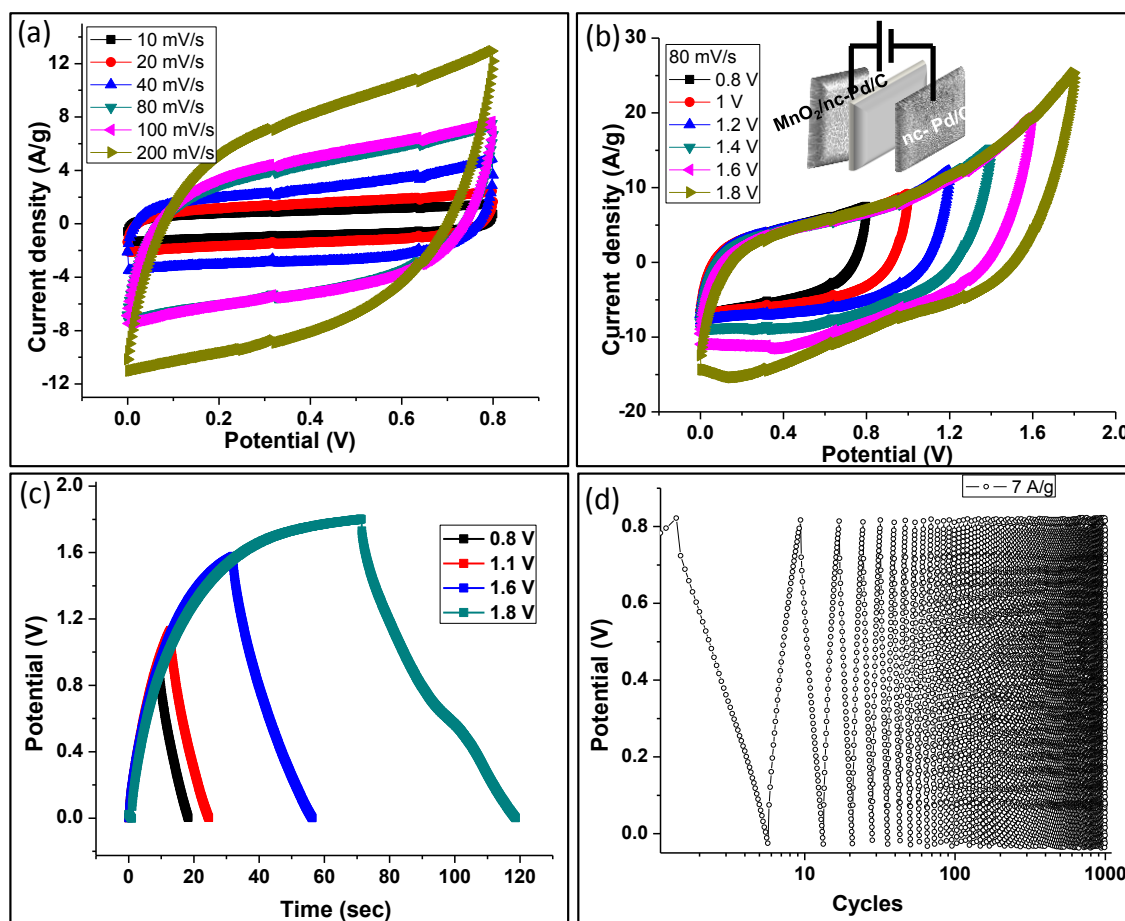
Figure V.13 (a) CV curves of (2 min) MnO_2/nc-Pd/C//nc-Pd/C asymmetric supercapacitor (ASC) measured at different scan rates between 0 and 0.8 V. (b) CV curves of optimized (2 min) MnO_2/nc-Pd/C//nc-Pd/C ASC measured at different potential windows at a scan rate of 80 mV/s. (c) galvanostatic charge–discharge curves at 7 A/g in different potential windows. (d) Cycling stability of a ASC over 1000 cycles of charge-discharge at a current density of 7 A/g.

Figure V.14 Ragone plots for nc-Pd/C, MnO$_2$/nc-Pd/C and MnO$_2$/nc-Pd/C//nc-Pd/C ASC in 1M Na$_2$SO$_4$. Inset shows the red LED glowing after connecting to three cells in series.

In order to compare the electrochemical performance of nc-Pd/C, MnO$_2$/nc-Pd/C and MnO$_2$/nc-Pd/C//nc-Pd/C ASCs, the corresponding energy densities are plotted against power densities as shown in the Ragone plot (see Figure V.14). The Ragone plot is a graphical representation of 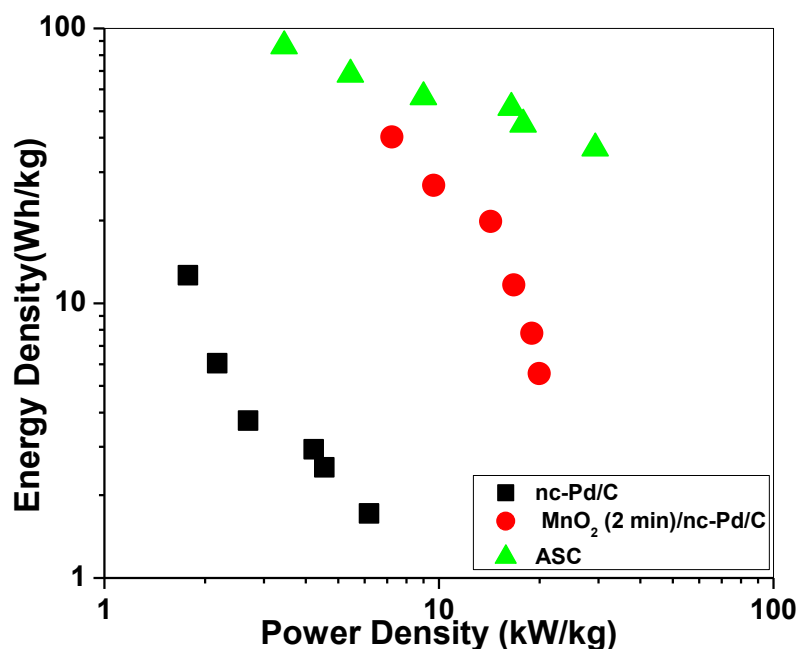the energy density against power density of the energy storage devices [10]. Typically, it is represented in log-log plot for making a comparison among various energy storage devices or the same device in different electrolytes or both. The maximum energy density obtained for the MnO$_2$/nc-Pd/C//nc-Pd/C ASCs reaches 86 W h/kg at a power density of 3 kW/kg and reaches to 36 Wh/kg at a power density of 29 kW/kg which is much higher than the commercially available supercapacitor devices (energy density: 1–10 Wh/kg and power density: 2–10 kW/kg), which are mainly based on porous activated carbon [21]. Further, the performance of the ASC made in this study was either comparable or better when compared with the previous literature reports, mentioned below. The energy density of various ASC such as MnO$_2$//activated carbon (<28.8 W h/kg) [50], MnO$_2$/graphene//graphene (30.4 W h/kg) [51], K$_{0.27}$ MnO$_2$.0.6H$_2$O//AC (25.3 W h/kg) [52], MnO2//polyaniline (5.86 W h/kg) [53], MnO$_2$//polypyrrole (7.37 W h/kg) [53], MnO$_2$//poly(3,4-ethylenedioxythiophene) (13.5 Wh/kg) [53] and 3D porous

graphene/MnO$_2$ nanorod//graphene/Ag hybrid (50.8 Wh/kg) [54] have been fabricated. The symmetric supercapacitor based on MnO$_2$/nc-Pd/C electrodes showed a maximum energy density of 40 Wh/kg with a maximum power density of 20 kW/kg. Plane nc-Pd/C electrodes have a maximum energy density of 12 Wh/kg with a maximum power density of 6 kW/kg. The inset shows the demonstration of the working of the ASC for glowing a 1.5 V LED. Series connections of 3 cells (each cell of size of 1x2 cm) were charged at 1.5 V for 30 seconds, to glow the LED for ~ 2 minutes.

It is worthwhile to mention few merits of the nc-Pd/C composites as electrodes for designing supercapacitors. This method offers a way to fabricate the metal nanoparticle/carbon composites via solution processable route in which the decomposition of the metal-organic precursors leading to the nucleation of the metal nanoparticles along with the functionalized carbon. While being porous, this composite is highly conducting, assisting the formation of EDLs. The functionalized nature of the carbon matrix to excellent wetting property of the electrolyte, a critical factor for the functioning of a supercapacitor. By employing the appropriate metal organic precursors, it is possible to fabricate the supercapacitors based on metal nanoparticle/carbon composites. An additional advantage offered is the low thermolysis temperatures (<250 ℃) which can be easily obtained by simply focusing sunlight. The performance of the electrode materials can be improved via patterning as the initial metal organic precursors are amenable for patterning by various lithography techniques such as nanoimprint lithography, electron beam lithography and soft lithography. It is also possible to fabricate planar and micro supercapacitors based on metal nanoparticle-carbon composites from metal-organic precursors.

V.5 Conclusions

In conclusion, a simple strategy to fabricate electrode materials for supercapacitors has been demonstrated using nc-Pd/C composites which is essentially a single step thermolysis of Pd hexadecylthiolate under the focused sunlight in ambient conditions. The electrochemical performance of the nc-Pd/Carbon composites has been tested in aqueous, ion gel and ionic liquid electrolytes. The electrochemical performance of the nc-Pd/C composites has been tested in aqueous, ion gel and ionic liquid electrolytes. The nanostructures of MnO$_2$ were grown spontaneously on the autocatalytic nc-Pd/C surface by

dipping in neutral permanganate solution. Maximum specific capacitance of 450 F/g was achieved for 2 minutes growth of MnO_2. Asymmetric supercapacitors with the design, MnO_2/nc-Pd/C//nc-Pd/C, which showed maximum energy density of 86 Wh/kg, higher compared to symmetric MnO_2 supercapacitor (40 Wh/kg). Power densities of 20 and 30 kW/kg were achieved for the symmetric and asymmetric supercapacitors respectively. The performance the ASC based on MnO_2/nc-Pd/C//nc-Pd/C design showed much higher performance than the commercially available activated carbon based supercapacitors.

References

[1]   M. F. El-Kady, V. Strong, S. Dubin and R. B. Kaner, *Science.*, 2012, **335**, 1326.
[2]   C. Largeot, C. Portet, J. Chmiola, P.-L. Taberna, Y. Gogotsi and P. Simon, *J. Am. Chem. Soc.*, 2008, **130**, 2730.
[3]   P. Simon and Y. Gogotsi, *Nat. Mater.*, 2008, **7**, 845.
[4]   Y. Zhu, S. Murali, M. D. Stoller, K. J. Ganesh, W. Cai, P. J. Ferreira, A. Pirkle, R. M. Wallace, K. A. Cychosz, M. Thommes, D. Su, E. A. Stach and R. S. Ruoff, *Science*, 2011, **332**, 1537.
[5]   Y. Zhai, Y. Dou, D. Zhao, P. F. Fulvio, R. T. Mayes and S. Dai, *Adv. Mater.*, 2011, **23**, 4828.
[6]   M. Winter and R. J. Brodd, *Chem. Rev.*, 2004, **104**, 4245.
[7]   C. Meng, C. Liu, L. Chen, C. Hu and S. Fan, *Nano Letters.*, 2010, **10**, 4025.
[8]   B. G. Choi, J. Hong, W. H. Hong, P. T. Hammond and H. Park, *ACS Nano.*, 2011, **5**, 7205.
[9]   J. J. Yoo, K. Balakrishnan, J. Huang, V. Meunier, B. G. Sumpter, A. Srivastava, M. Conway, A. L. Mohana Reddy, J. Yu, R. Vajtai and P. M. Ajayan, *Nano Lett.*, 2011, **11**, 1423.
[10] B. E. Conway, Electrochemical Supercapacitors, Scientific, Fundamentals and Technological Applications, Plenum: New York, 1999.
[11] J. R. Miller and P. Simon, *Science,* 2008, **321**, 651.
[12] Y. Huang, J. Liang and Y. Chen, *Small*, 2012, **8**, 1805.
[13] H. Nishihara and T. Kyotani, *Adv. Mater.*, 2012, **24**, 4473.
[14] S. L. Candelaria, Y. Shao, W. Zhou, X. Li, J. Xiao, J. G. Zhang, Y. Wang, J. Liu, J. Li and G. Cao, Nano *Energy.,* 2012, **1**, 195.
[15] G. Wang, L. Zhang and J. Zhang, *Chem. Soc. Rev.*, 2012, **41**, 797.
[16] L. L. Zhang, X. Zhao, M. D. Stoller, Y. Zhu, H. Ji, S. Murali, Y. Wu, S. Perales, B. Clevenger and R. S. Ruoff, *Nano Lett.*, 2012, **12**, 1806.
[17] J. Chmiola, C. Largeot, P. L. Taberna, P. Simon and Y. Gogotsi, *Science.,* 2010*, **328**, 480.
[18] L. Hu, J. W. Choi, Y. Yang, S. Jeong, F. La Mantia, L.-F. Cui and Y. Cui, *Proc. Natl. Acad. Sci. USA.,* 2009, **106**, 21490.

[19] V. L. Pushparaj, M. M. Shaijumon, A. Kumar, S. Murugesan, L. Ci, R. Vajtai, R. J. Linhardt, O. Nalamasu and P. M. Ajayan, *Proc. Natl. Acad. Sci. USA.,* 2007, **104**, 13574.

[20] D. Pech, M. Brunet, H. Durou, P. Huang, V. Mochalin, Y. Gogotsi, P. L. Taberna and P. Simon, *Nat. Nanotechnol.,* 2010, **5**, 651.

[21] A. G. Pandolfo and A. F. Hollenkamp, *J. Power Sources.,* 2006, **157,** 11.

[22] E. Frackowiak and F. Béguin, *Carbon.,* 2001, **39**, 937.

[23] G. Xiong, K.P.S.S. Hembram, R.G. Reifenberger and T.S. Fisher, *J. Power Sources.,* 2013, **227**, 254.

[24] C. G. Liu, Z. Yu, D. Neff, A. Zhamu and B. Z. Jang, *Nano Lett.,* 2010 **10**, 4863.

[25] Y. Zhu, S. Murali, M. D. Stoller, K. J. Ganesh, W. Cai, P. J. Ferreira, A. Pirkle, R. M. Wallace, K. A. Cychosz, M. Thommes, D. Su, E. A. Stach and R. S. Ruoff, *Science.*, 2011, **332**, 1537.

[26] X. Yang, J. Zhu, L. Qiu and D. Li, *Adv. Mater.,* 2011, **23**, 2833.

[27] H. M. Jeong, J. W. Lee, W. H. Shin, Y. J. Choi, H. J. Shin. J. K. Kang and J. W. Choi, *Nano Lett*. 2011, **11**, 2472.

[28] X. Cao, Y. Shi, W. Shi, G. Lu, X. Huang, Q. Yan, Q. Zhan and H. Zhang, *Small.,* 2011, **7**, 3163.

[29] V. Sridhar, H.-J. Kim, J.-H. Jung, C. Lee, S. Park and I.-K. Oh, *ACS Nano.,* 2012, **6**, 10562.

[30] Z. Niu, J. Du, X. Cao, Y. Sun, W. Zhou, H. H. Hng, J. Ma and X. Chen and S. Xie, *Small.*, 2012, **8**, 3201.

[31] M. G. Hahm, A. Leela Mohana Reddy, D. P. Cole, M. Rivera, J. A. Vento, J. Nam, H. Y. Jung, Y. L. Kim, N. T. Narayanan, D. P. Hashim, C. Galande, Y. J. Jung, M. Bundy, S. Karna, P. M. Ajayan and R. Vajtai, *Nano Lett.*, 2012, **12**, 5616.

[32] J. M. Miller, B. Dunn, T. D. Tran and R. W. Pekala, *J. Electrochem. Soc.,* 1997, **144**, L309.

[33] G. Yu, L. Hu, M. Vosgueritchian, H. Wang, X. Xie, J. R. McDonough, X. Cui, Y. Cui and Z. Bao, *Nano Lett.,* 2011, **11**, 2905.

[34] L. Yuan, X.-H. Lu, X. Xiao, T. Zhai, J. Dai, F. Zhang, B. Hu, X. Wang, L. Gong, J. Chen, C. Hu, Y. Tong, J. Zhou and Z. L. Wang, *ACS Nano.*, 2012, **6**, 656.

[35] C.Yuan, X. Zhang, L. Su, B. Gao and L. Shen, *J. Mater. Chem.,* 2009, **19**, 5772.

[36] Q. Wu, Y. Xu, Z. Yao, A. Liu and G. Shi, *ACS Nano.*, 2010, **4**, 1963.

[37] L. Yuan, X. Xiao, T. Ding, J. Zhong, X. Zhang, Y. Shen, B. Hu, Y. Huang, J. Zhou and Z. L. Wang, *Angew. Chem. Int. Ed.,* 2012*,* **51**, 4934.

[38] H. Jiang, C. Li, T. Sun and J. Ma, *Nanoscale*, 2012, **4***,* 807.

[39] J. Zhang, J. Jiang, H. Li and X. S. Zhao, *Nanoscale,* 2011, **4**, 4009.

[40] T. Bhuvana and G. U. Kulkarni, *ACS Nano.,* 2008, **2**, 457.

[41] B. Radha, A. A. Sagade and G. U. Kulkarni, *ACS Appl. Mater. Interfaces.,* 2011, **3**, 2173.

[42] A. A. Sagade, B. Radha and G. U. Kulkarni   *Sensors and Actuators B: Chemical.,* 2010, **149**, 345.

[43] B. Radha and G. U. Kulkarni, *Small.*, 2009, **5**, 2271.

[44] B. Radha, S. H. Lim, M. S. M. Saifullah and G. U. Kulkarni, 2012 *Scientific Reports (Nature).*, accepted for publication.

[45] N. Kurra, A. A. Sagade and G. U. Kulkarni, *Adv. Funct. Mater.,* 2011, **21***,* 3836.

[46] S. W. Lee, J. Kim, S. Chen, P.T. Hammond and Y.S. Horn, *ACS Nano,* 2010, **4**, 3889.

[47] X. Jin, W. Zhou, S. Zhang and G. Z. Chen, *Small*, 2007, **3**, 1513.

[48] B. Radha, G. Liu, D. J. Eichelsdoerfer, G. U. Kulkarni and C. A. Mirkin, ACS Nano, 2013, **7**, 2602.

[49] F. Buciuman, F. Patcas, R. Craciun and D. R. T. Zahn, *Phys. Chem. Chem. Phys.*, 1999, **1**, 185.

[50] T. Brousse, P. -L. Taberna, O. Crosnier, R. Dugas, P. Guillemet, Y. Scudeller, Y. Zhou, F. Favier, D. Bélanger and P. Simon, *J. Power Sources*, 2007, **173**, 633.

[51] Z.-S. Wu, W. Ren, D.-W. Wang, F. Li, B. Liu and H.-M. Cheng, *ACS Nano*, 2010, **4**, 5835.

[52] Q. Qu, L. Li, S. Tian, W. Guo, Y. Wu and R. Holze, *J. Power Sources*, 2010, **195**, 2789.

[53] V. Khomenko, E. Raymundo-Pi~ nero, E. Frackowiak and F. Béguin, *Appl. Phys. A: Mater. Sci. Process.*, 2006, **82**, 567.

[54] Y. Shao, H. Wang, Q. Zhang and Y. Li, *J. Mater. Chem. C*, 2013, **1**, 1245.

Outlook

"Be a scientist, save the world"- Richard Smalley

The thesis is about exploring the 2D nanocarbon materials in terms of their functional aspects and device fabrication. In Part II, the carbonaceous deposits obtained by electron beams are indeed fascinating in that they serve as a local dielectric and also as a source for obtaining graphene in a selective manner. This technique can be utilized in growing various graphene structures in the form of nanoribbons and nanomeshes with controlled electronic and optoelectronic properties. Further, AFM bias lithography on these carbonaceous platforms (Part-III) turned out to be interesting in terms of observing various kinds of nanoscale phenomenon such as nucleation of water droplets, electrochemical modifications and charge patterning depending on the experimental conditions adopted. Mesoscopic graphitic islands could be carved on the graphite surface by AFM bias lithography which showed unusual charge storage properties. This idea may be extended to graphene to control the charge transport behavior by creating charge islands and studying the phenomenon at low temperatures will be interesting to study quantum/nanoscale phenomenon.

A laser patterning technique is detailed out in part IV for fabrication of graphene ribbons of uniform shapes can be generalized to other layered materials such as MoS_2, WS_2, etc. to pattern them in a direct manner. Patterning of metallic films similarly, may lead to the formation of metallic photonic crystals, which is of current interest in developing photonic devices. Pencil on paper is a simple approach for the fabrication of various kinds of active and passive electronic devices. Higher order passive devices may be possible which can be integrated with the active device components to achieve the desired functionality based on simple pencil-on-paper devices. In part-V, supercapacitors were designed out of nc-Pd/C composites, obtained by thermolysing the metal-organic precursors under the concentrated sunlight. This technique can be generalized to other metal-organic precursors in order to obtain metal nanoparticle-carbon composites which are highly conducting and autocatalytic in nature to assist the spontaneous growth of the psuedocapacitive coatings for fabrication of high performance supercapacitors in a simple manner.

List of Publications

From Thesis work

1. **Narendra Kurra** and G. U. Kulkarni "Pencil-on-paper:Electronic devices", *Lab Chip*, **2013**, 13, 2866-2873.

2. **Narendra Kurra**, D. Dutta, and G. U. Kulkarni "Field effect transistors and RC filters from pencil-trace on paper" Physical Chemistry Chemical Physics, **2013**, 15, 8367-8372.

3. **Narendra Kurra**, Venkata Srinu Bhadram, Chandrabhas Narayana, and G. U. Kulkarni "Few layer graphene to graphitic films: Infrared photoconductive versus bolometric response" Nanoscale, **2013**, 5, 381-389.

4. **Narendra Kurra**, Venkata Srinu Bhadram, Chandrabhas Narayana, and G. U. Kulkarni "Nanocrystalline graphene: Field effect transistors and Infrared photodetectors" *Nanotechnology,* **2012**, 23, 425301.

   (Research highlight **on this article appeared in Nanotech web 2012).**

5. **Narendra Kurra**, Venkata Srinu Bhadram, Chandrabhas Narayana, and G. U. Kulkarni "Field-Effect Transistors Based on Thermally Treated Electron Beam-Induced Carbonaceous Patterns" *ACS Appl. Mater. Interf*., **2012**, 4, 1030-1036.

6. **Narendra Kurra**, Abhay A. Sagade, and G. U. Kulkarni "Ultrafast Direct Ablative Patterning of HOPG by Single laser pulses to produce graphene ribbons" *Adv. Funct. Mater. 2011,* 21, 3836–3842.

   (*Research highlights* **on this article appeared in Materials view, Nature India, 2011)**

7. **Narendra Kurra**, Gyan Prakash, S Basavaraja, Timothy S Fisher, G U Kulkarni and Ronald G Reifenberger "Charge storage in mesoscopic graphitic islands fabricated using AFM bias lithography" *Nanotechnology* **2011**, 22, 245302.

   (*Research highlights* **on this article appeared in Nanotech web, Nature India, 2011)**

8. **Narendra Kurra**, T. Vijaykumar, and G. U. Kulkarni "CNT Manipulation: Inserting a Carbonaceous Dielectric Layer Beneath Using Electron Beam Induced Deposition" *J. Nanosci. Nanotech.* **2011**, 11, 1025-1029.

9. **Narendra Kurra**, Adina Scott, and Giridhar U. Kulkarni "Electrocondensation and Evaporation of Attoliter Water Droplets: Direct Visualization Using Atomic Force

Microscopy" *Nano Res.* **2010**, 3, 307-316.

10. **<u>Narendra Kurra</u>**, S.Kiruthika, and G. U. Kulkarni "Solution processed sun baked electrodes for the fabrication of high performance flexible supercapacitors" 2013, Submitted.

11. **<u>Narendra Kurra</u>** "Tunable Atomic force microscopy bias lithography on Electron beam induced carbonaceous platforms" **2013**, submitted.

12. **<u>Narendra Kurra</u>**, Ronald G Reifenberger and G. U. Kulkarni "AFM bias lithography on nanocarbon surfaces", **2013**, review article, submitted.

Manuscript under preparation

13. **<u>Narendra Kurra,</u>** S.Kiruthika and G. U. Kulkarni "MnO$_2$/pencil-trace based paper supercapacitors", **2013, under preparation**.

14. S. Kiruthika, **<u>Narendra Kurra</u>**, and G. U. Kulkarni "Asymmetric supercapacitors based on Co$_3$O$_4$ and nc-Pd/C composites", **2013** (under preparation).

Other publications

15. T. Vijaykumar, **<u>Narendra Kurra</u>** and G. U. Kulkarni "Electron beam induced carbonaceous deposition as a local dielectric for CNT circuits" *International Journal of Nanoscience,* **2011**, 10, 935.

16. K. D. Mallikarjuna Rao, T. Bhuvana, B. Radha, **<u>Narendra Kurra</u>** and G. U. Kulkarni "Metallic conduction in NiS$_2$ nanocrystalline structures" *J. Phys. Chem. C*, **2011**, 21, 10462.

Patent Filed

17. Graphene Nanoribbons and Methods for their Preparation and Use
    Narendra Kurra, Abhay A Sagade and G.U. Kulkarni
    US patent, Application No.: 13/599,810
    Date of Filing - August 30, 2012.